Dissertation zur Erlangung des Doktorgrades
der Fakultät für Chemie und Pharmazie
der Ludwig-Maximilians-Universität München

Development and Application of Mass Spectrometry-Based Proteomic Approaches for Investigating Intercellular Signaling

Jonathan Johannes Swietlik

aus

Karlsruhe, Deutschland

2024

Erklärung

Diese Dissertation wurde im Sinne von § 7 der Promotionsordnung vom 28. November 2011 von Herrn Prof. Dr. Matthias Mann betreut.

Eidesstattliche Versicherung

Diese Dissertation wurde eigenständig und ohne unerlaubte Hilfe erarbeitet.

Boston, 03.03.2025

Jonathan Johannes Swietlik

Dissertation eingereicht am 12.12.2024

1. Gutachter: Prof. Dr. Matthias Mann

2. Gutachter: Prof. Dr. Felix Meissner

Mündliche Prüfung am 17.02.2025

Summary

Exploring the molecular mechanisms of cell communication deepens our understanding of biology and lays the groundwork for precision medicine. Proteins, the central players in intercellular signaling, act as both signals and receptors, making mass spectrometry (MS)-based proteomics a powerful tool for their study. Nonetheless, important aspects of cell communication remain understudied due to unresolved technical challenges. In this work, I employed state-of-the-art proteomics to investigate intercellular signaling in the immune system and cancer, and focused on developing new approaches to address questions that remain elusive with current methods.

A primary goal of my thesis was to advance methods for analyzing intercellular communication within complex, heterocellular environments. Cell-selective protein labeling with non-canonical amino acids for bioorthogonal enrichment has emerged as a promising strategy to study cells in their native context. I developed workflows that substantially increased sensitivity and specificity by overcoming critical challenges in click chemistry enrichment and the MS analysis of cell-selective azidonorleucine labeling experiments. This more than doubled the proteomic coverage compared to previous studies and, for the first time, enabled deep, cell type-resolved investigations of extracellular signaling proteins in tissues. When applied to pancreatic ductal adenocarcinoma (PDAC) models, these methods offered novel insights into the intricate cross-talk between cancer cells, stromal cells in the tumor microenvironment, and host cells at distant sites.

Beyond the profiling of intercellular signals, understanding protein-protein interactions at the cell surface that mediate signal reception and transduction is essential for deciphering intercellular signaling pathways and their regulatory mechanisms. Here, I developed a proximity labeling (PL)-based approach to capture ligand-receptor interactions and map the lateral environments of receptors on living cells. A novel strategy to modulate labeling radii significantly enhanced the spatial resolution and distinguished captured proteins based on their spatial relationships to the PL source, overcoming a long-standing challenge in the field.

The findings and developments presented in this thesis fill previous technological gaps and offer novel capabilities for the in-depth characterization of cells, signaling proteins, and their interactions in their native environment. Application of these methods revealed novel insights into cell communication in pancreatic cancer and innate immunity. Collectively, these advancements lay a foundation for a better understanding of complex biological systems.

Table of Contents

1. Introduction

1.1 Proteomic analysis of intercellular signaling

Communication between cells through the exchange of signaling cues is a fundamental process in biology. In multicellular organisms, intricate intercellular communication networks orchestrate complex tasks that surpass the capabilities of solitary cells. This cellular coordination is essential for guiding development, maintaining homeostasis, and responding to environmental changes. Moreover, given the central role of cell non-autonomous processes in diseases, a progressively detailed molecular understanding of intercellular signaling also lays a foundation for innovation in therapeutic treatments and clinical diagnostics. A quintessential example is cancer.

1.1.1 The significance of intercellular signaling in disease, exemplified by cancer

While early molecular cancer research was centered on investigating cell-autonomous processes driving cellular transformation, there has been a growing emphasis on understanding the tumor microenvironment (TME) as our knowledge has advanced[7,8]. In addition to cancer cells, tumors comprise a diverse network of non-transformed stromal cells, like fibroblasts, endothelial cells, pericytes, adipocytes, neurons, and immune cells, embedded in a remodeled extracellular matrix (ECM)[5,9] (Figure 1).

Today, it is widely recognized that the tumor-associated stroma is integral to tumorigenesis and disease progression, significantly contributing to the hallmark capabilities of cancer[7,8]. Research has demonstrated that even the most fundamentally defining features of cancer cells, such as their capacity for sustained growth, emerge not solely from cancer cell-intrinsic mechanisms but also through heterocellular interactions with stromal cells within the TME[10]. Cancer-associated fibroblasts (CAFs), for example, can strongly contribute to sustained proliferative signaling as a major source of paracrine growth factors like fibroblast growth factors (FGF), hepatocyte growth factor (HGF), and epithelial growth factor (EGF)[11]. CAFs are crucial and often abundant components of the TME, exhibit remarkable heterogeneity and plasticity, and fulfil a wide array of functions[12]. Among their key roles, they are major producers of matrix components, playing a critical

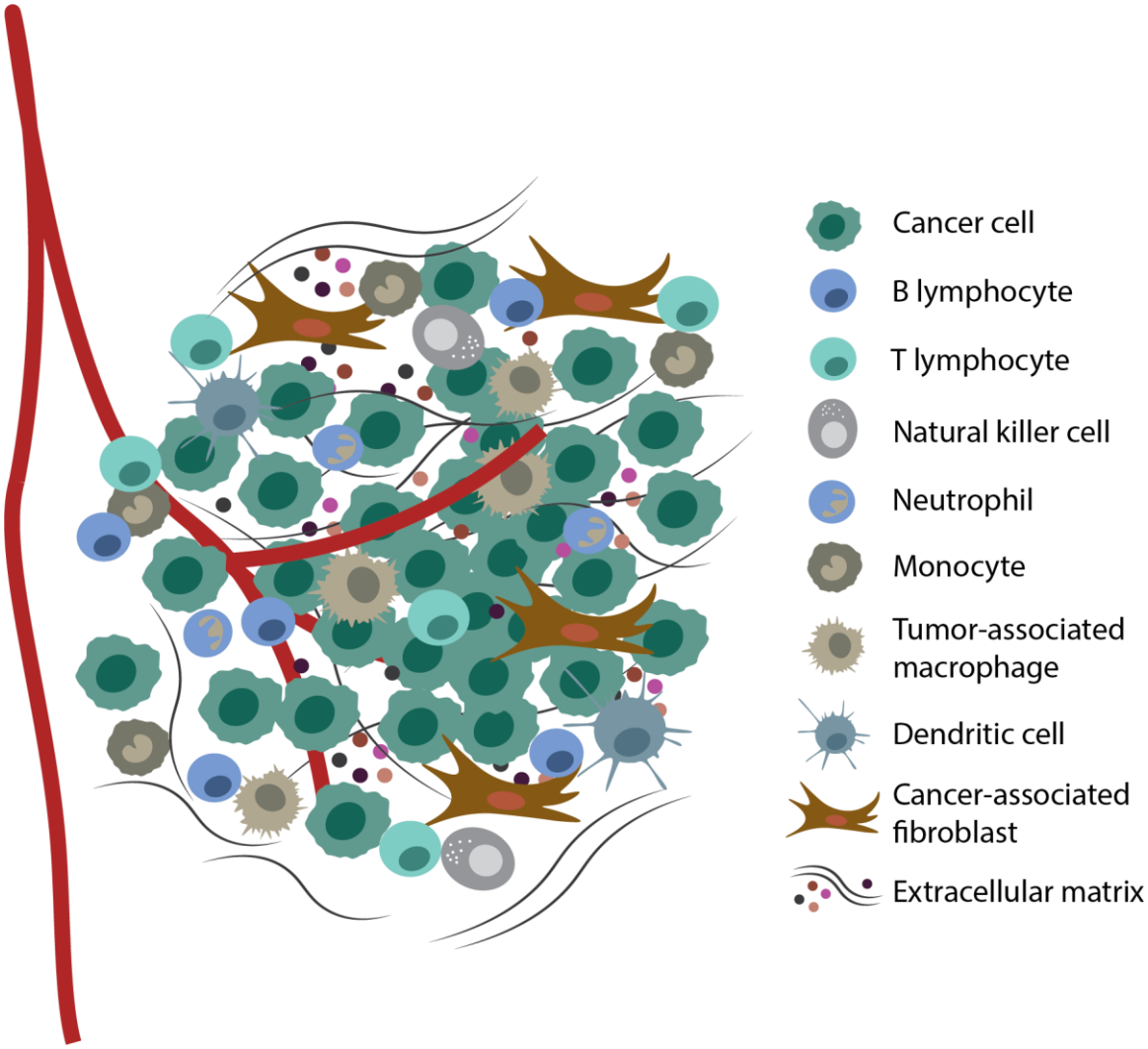

Figure 1: Components of the tumor microenvironment. Tumors comprise heterogeneous populations of cancer cells and non-transformed resident or recruited stromal cells, which collectively shape the tumor microenvironment (TME), a dynamic ecosystem central to disease progression. Among others, key stromal components include fibroblasts, diverse cell types of the innate and adaptive immune system, and endothelial cells lining tumor-associated blood vessels. Cells in the TME play dualistic roles, with both host-protective and tumor-supportive functions. The composition and functional states of these cells vary widely across cancers, individual tumors, and disease stages. Immersed in a complex network of aberrant intercellular signals - mediated, for example, by cell-cell contacts, paracrine messengers like growth factors, chemokines, and cytokines, and environmental factors like hypoxia – TME cells engage in reciprocal interactions that drive their dynamic co-evolution, profoundly impacting tumor progression, prognosis, and therapy response[5]. Figure adapted from[5,6].

part in the extensive remodeling of the ECM within the TME, they have significant

immunomodulatory capacity, and stimulate angiogenesis[5,13]. To support continuous growth, tumors devise angiogenic signaling pathways, such as vascular endothelial growth factor (VEGF) signaling[14], and induce new blood vessels that supply oxygen and nutrients and remove waste products[15]. In many solid tumors, chronic and unbalanced pro-angiogenic signaling leads to the formation of chaotic vessel networks, uneven blood flow, vessel leakage, and an increased interstitial fluid pressure, promoting metastasis and hampering drug delivery[16,17].

In the microenvironment of virtually all tumors, there is dynamic crosstalk and interaction with immune cells. The immune system continuously monitors the body's tissues and efficiently detects and eliminates most neoplastic cells, alerted by features like "danger" signals and tumor antigens[18]. Immunosurveillance thereby serves as a critical defense barrier against cancer. However, beyond protective function, the selective pressure applied by immune effector cells also shapes the evolutionary trajectory of tumors. It can eventually lead to the outgrowth of cancer cells with diminished immunogenicity that are fit for survival in immunocompetent hosts[19,20]. To evade immune destruction, cancer cells exploit various escape routes, ranging from cell-intrinsic mechanisms that reduce tumor antigen presentation to the active modulation of the host's immune response via secretion of intercellular signals like cytokines[21,22]. Moreover, the TME fosters the recruitment and functional reprogramming of immune cells toward protumorigenic phenotypes. Tumor-associated macrophages, for example, are among the most extensively studied immune cells in the TME[23] and key regulators of tumor-associated chronic inflammation. Inflammation is considered an enabling hallmark of cancer, driving many other hallmark capabilities, including suppression of adaptive immune responses, sustained growth signaling, and promotion of angiogenesis, invasion, and metastasis[7,24,25].

Perhaps the most life-threatening aspect of cancer lies in its capacity for spreading beyond the primary tumor site to distant parts of the body. In a series of complex cell biological steps, cancer cells can acquire the ability to invade surrounding tissue, enter circulation through lymphatic or blood vessels, survive as circulating tumor cells, arrest at a distant secondary site, extravasate, and colonize new environments to establish metastases[26,27]. While interactions with stromal cells play critical roles throughout the process, intercellular communication is a crucial enabler of metastasis even before cancer cells disseminate. In 1889, Stephen Paget described metastatic organotropism and proposed that cancer does not spread randomly but selects congenial sites for secondary growth, a concept known as the "seed and soil" hypothesis[28]. Later research

discovered that tumors selectively induce remodeling of tissues at sites of future metastasis, establishing environments that support cancer cell survival and growth, termed pre-metastatic niches (PMNs)[29,30].

A deepening understanding of the interactions between cancer cells and their microenvironment has illuminated synergies and mechanisms of drug resistance, paving the way for novel therapeutic strategies. Targeting pro-tumorigenic alliances within the TME rather than cancer cells directly has yielded some of the most substantial advancements in cancer therapy to date. In 2013, *Science* selected cancer immunotherapy as the Breakthrough of the Year[31], highlighting the substantial clinical impact of immune checkpoint inhibition (ICB), specifically therapies targeting the inhibitory receptors cytotoxic T-lymphocyte associated protein 4 (CTLA4) and programmed cell death protein 1 (PD-1) on T-cells, and promising advances in chimeric antigen receptor (CAR) T-cell therapy. This innovative approach was further recognized in 2018, when James Allison and Tasuku Honjo were awarded the Nobel Prize in Physiology or Medicine for their pioneering work in discovering and characterizing CTLA-4 and PD-1 pathways[32-35]. While marking a paradigm shift in oncology treatment, the clinical translation of strategies targeting the TME has also underlined significant knowledge gaps and posed numerous unresolved questions. ICB has proven extremely effective for specific cancers and patient populations; however, the majority of patients do not respond[23]. Mechanisms for treatment resistance are complex and incompletely understood, and accurate prediction of ICB efficacy is often difficult with current diagnostic means[36,37].

The successes and limitations of immunotherapy emphasize the value of a comprehensive understanding of cellular communication and interaction in cancer to address unmet clinical needs. In-depth studies that elucidate mechanisms linking cancer genotypes and phenotypes with the intercellular signals shaping the TME are fundamental for discovering new treatment targets, and biomarkers that can stratify patients to make current treatments more effective[23,38]. However, some questions in cancer communication networks remain hard to study due to technical limitations. For example, developing new approaches for the effective cell type-resolved characterization of extracellular signaling proteins in tissues will likely accelerate a deeper mechanistic understanding of cellular communication in the TME and illuminate processes like PMN formation, opening ways for targeted prevention of metastasis[30].

1.1.2 The Landscape of Intercellular Signaling Proteins

Investigations into the underlying molecular foundations of intercellular signaling have revealed diverse signal transmission modalities between cells, ranging from chemical messengers such as metabolites and nucleic acids to mechanical cues. However,

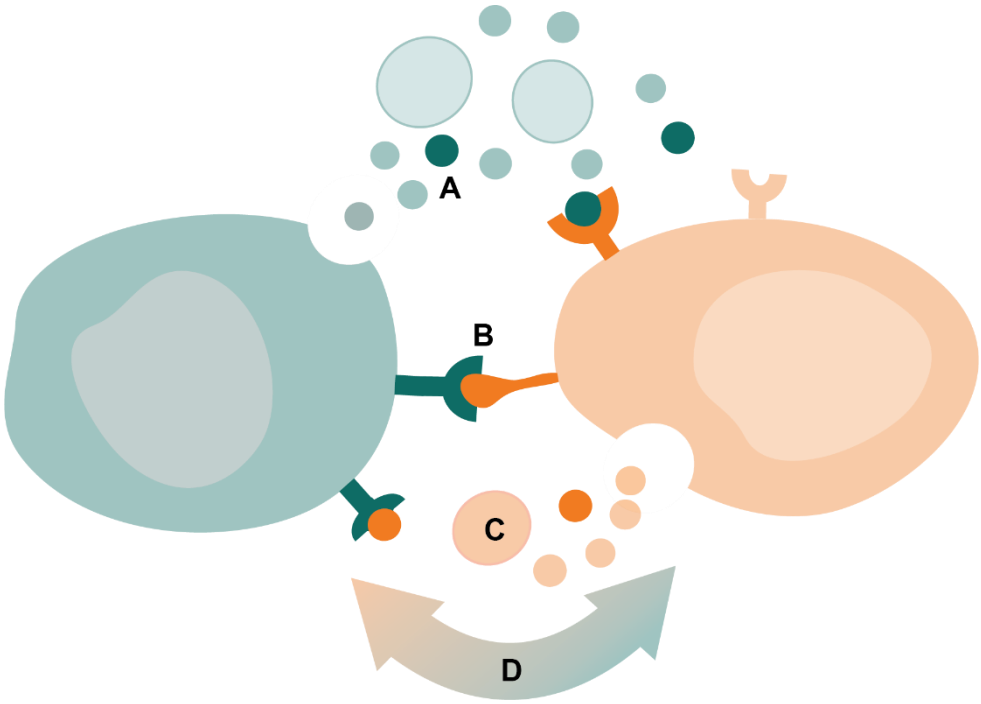

Figure 2: Protein-mediated cell communication. Cell communication involves the exchange of signals, predominantly mediated by proteins through specific ligand-receptor interactions. (A) Ligands, like growth factors or cytokines, are secreted, diffuse through the extracellular environment, and bind to their respective receptors on the same cell (autocrine signaling) or neighboring cells (paracrine signaling). (B) Other forms of signaling, for example, rely on direct contact between membrane-bound proteins (juxtacrine signaling) or (C) transfer through extracellular vesicles. (D) Signaling is typically reciprocal, with cells dynamically responding and adapting to each other's signals. Figure adapted from[4].

proteins dominate the primary means of cellular communication, acting both as key messengers and as the principal agents for signal reception (Figure 2). To advance our comprehension of human physiology and disease, it is critical to explore the molecular mechanisms of protein-based intercellular communication networks in detail.

1.1.2.1 Diverse pathways facilitate and modulate the transmission of protein-mediated intercellular signals

Signal-transmitting cells typically initiate protein-based intercellular signaling by releasing diffusing signal proteins. At a given time and context, a single cell type expresses often hundreds of such messenger proteins with known intercellular signaling function[39-41]. Most of these proteins are marked by a signal sequence, trafficked through the endoplasmatic reticulum (ER), the Golgi apparatus, and across the plasma membrane via secretory vesicles or granules. The sorting signal sequence that marks proteins for this conventional secretion pathway has features that computational methods can predict. Combined evidence from multiple prediction tools suggests that approximately 10 - 15 % of human protein-coding genes encode secreted proteins[39,42].

Important subsets of intercellular signaling proteins, however, lack a conventional secretion signal sequence (often referred to as 'leaderless' secretory proteins) and exit cells via unconventional secretion pathways. For example, interleukin-1β, a cytokine and crucial modulator of immune responses, is expressed as a cytosolic inactive precursor protein. Upon caspase-1-controlled maturation by cleavage, the active cytokine can be released directly through plasma membrane pores formed by gasdermin D (GSDMD), a key mediator of pyroptosis[43,44]. Other pore formation-independent protein export routes have also been proposed[45-47].

Another important immune regulator, tumor necrosis factor alpha (TNF-α), is initially expressed as an integral transmembrane protein and subsequently cleaved by the membrane-bound protease TNF-α-converting enzyme (TACE) to release the extracellular domain as soluble TNF-α[48-50]. Both the soluble cytokine and membrane-bound forms have biological activity. The latter engages with receptors on adjacent cells, exemplifying cell-contact-dependent communication through juxtacrine signaling. Besides releasing active signaling proteins from membrane-bound precursors, cell-surface protein ectodomain cleavage (often referred to as "shedding") can also neutralize signaling proteins by releasing decoy receptors[51,52].

When released, even proteins with unrelated intracellular functions can become signals in the intercellular space. For example, high-mobility group box 1 (HMGB1) is primarily a nuclear protein engaged in various DNA-associated processes. Yet, upon active secretion by immune cells or passive release from dying cells, it assumes the role of an alarmin and exerts potent immunomodulatory effects by interacting with pattern recognition receptors

(PRRs)[53,54].

1.1.2.2 The identity, quantity, and organization of signal receptor proteins at the cell surface are critical determinants of cellular responses

With some notable exceptions, such as proteins transmitted between cells via extracellular vesicles or gap junctions, intercellular signaling proteins cannot penetrate the plasma membrane. Instead, they are recognized by transmembrane receptors of signal-receiving cells through specific interaction with surface-exposed ligand-binding domains. Most transmembrane receptors can be broadly categorized into three groups based on their distinct mechanisms for relaying signals into the intracellular space:

Ion channel-linked receptors (also known as ligand-gated ion channels) mediate ligand binding-controlled changes in membrane ion permeability, converting chemical signals into electrical ones, an essential mechanism for rapid neuronal signal transmission[55]. Ligand engagement with *enzyme-linked receptors* regulates the intrinsic catalytic activity of intracellular receptor domains or receptor-associated enzymes. For example, most growth factors are recognized by receptor tyrosine kinases, which typically oligomerize upon ligand binding, autophosphorylate, and initiate signal propagation by recruitment and activation of intracellular enzymes and adaptor proteins with Src homology-2 (SH2) and phosphotyrosine-binding (PTB) domains[56-58]. Many cytokine receptors are tyrosine-kinase-associated receptors and signal through members of the Janus kinase (JAK) family[59,60]. With over 800 encoding genes, *G-protein-coupled receptors (GPCRs)* exhibit extensive genetic diversity and form the largest family of human cell surface receptors[61,62]. They respond to a wide range of signals, including hormones, neurotransmitters, and chemokines, and mediate key sensory functions like vision and smell[63]. Likewise, the intracellular signal-transduction pathways triggered by GPCRs are highly diverse, including canonical GPCR signaling via heterotrimeric G proteins, and G protein-independent mechanisms, for example, via PDZ scaffolds, non-PDZ scaffolds and arrestins[61].

The nature, quantity, and spatial organization of receptors displayed at the cell surface are key determinants of the capacity of a cell to respond to a specific intercellular signaling protein. Ligand-receptor interactions are usually not strictly exclusive - a single ligand can often bind to multiple receptors, and various ligands can modulate a receptor's activity. For example, three human epidermal growth factor receptors are activated by a group of

ligands encoded by at least 13 different genes[58,64]. Additionally, most receptors do not operate as simple binary switches but instead demonstrate a range of varied response patterns influenced by multiple context factors. Specific ligands can have different efficacies ranging from full and partial agonism (increase of signaling activity above basal level), to neutral antagonism (no direct effect on activity, but blocks other ligands), to inverse agonism (reduction of signaling activity below basal level of unliganded receptor)[63]. Moreover, different ligands engaging the same receptor can trigger qualitatively distinct signaling responses, referred to as biased agonism or functional selectivity. Most extensively studied for GPCRs, ligands can stabilize unique conformational states of receptors, affecting signal transduction, for example, by favoring particular effector systems over others[61,65]. Besides biased agonism, differential expression and localization of co-receptors, signal transducers, and other interactors introduce a system bias, significantly contributing to the variability of cellular responses to the same signal[65].

Large signaling protein clusters like the immunological synapse, a critical gateway for adaptive immunity formed between a T cell and an antigen-presenting cell, underscore the complexity of molecular interactions used by cells to communicate. The detailed characterization of context-dependent expression, spatial organization, and interactions of signaling proteins refines our understanding of intercellular signaling mechanisms and builds the foundation for databases and models that infer communication networks in complex heterocellular systems[66-68]. Hence, high-throughput protein analysis techniques are invaluable for advancing the field.

1.1.3 MS-based proteomics provides discovery tools for studying intercellular signaling from molecular interactions to systems biology

The collective of all proteins expressed by humans, referred to as the human proteome, is a vast and intricate compilation of biomolecules with a large diversity of structures, chemical properties, and biochemical functions. The decoding of the human genome has revealed around 20,000 protein-coding genes[69]. However, transcripts are commonly modified by mechanisms like RNA editing, trans-splicing of mRNA molecules, and, affecting more than 93 % of all human genes[70,71], alternative splicing of exons and introns, greatly expanding the plurality of gene products. Transcript variants produce different protein isoforms (proteins translated from distinct mRNA sequences derived from a single gene[72-74]). Despite sharing the same genetic origin, isoforms can have divergent and even

opposing roles in cellular physiology[75], exemplified by canonical proangiogenic VEGF-A isoforms that activate VEGFR-2, and alternative splice variants that bind the same receptor as partial agonists and do not induce angiogenesis[76]. Protein diversity again drastically increases by modification after translation, yielding distinct proteoforms (all different molecular forms of a protein from a single gene, including splice isoforms and post translational modifications (PTMs)[74]), often with critical functional consequences. Therefore, the number of all different proteins in the human proteome varies depending on definition and ranges from around 20,000 representative proteins for each protein-coding gene, more than 70,000 protein splice variants, to hundreds of thousands of proteoforms with PTMs taken into account[77]. This, however, is still not counting the vast numbers of protein variants produced, for example, by somatic recombination in adaptive immune cells[77], or proteins arising from mutation.

The complexity of proteomes poses a significant analytical challenge for technologies that provide a comprehensive view of proteins in biological processes. Today's leading technology for large-scale analyses of complex protein mixtures relies on mass spectrometry (MS), as detailed in Chapter 1.2. Modern mass spectrometers can quantify thousands of proteins within just a few minutes of analysis time[78], providing deep insights into cellular phenotypes. Additionally, the resolution of specific subproteomes can be further enhanced by combining MS-based proteomics with biochemical enrichment techniques. PTM-specific enrichment, for example, allows for detailed analyses of intracellular signal transduction dynamics[79,80], and sheds light on the mechanisms of action of chemical compounds in drug discovery[81-84].

Advances in MS-based proteomics have opened unparalleled opportunities for exploring cellular communication networks. Specialized workflows enable the dissection of intercellular signaling across multiple layers with great precision and depth (Figure 3), as reviewed in Article 1. For example, secretomics methods facilitate the comprehensive profiling of extracellular proteins, elucidating cell secretion patterns and their dynamic changes in response to stimuli[40], and allowing the inference of communication channels between different cell types[68]. The largely selection bias-free detection enables the discovery of signaling proteins in unexpected contexts or even ascribe function to proteins with previously unknown roles in intercellular communication[85]. Moreover, secretomics detection is independent of protein exit routes, effectively capturing conventionally and unconventionally secreted proteins, as well as shed receptors (see, for example, Article 5).

Additionally, the capacity of MS-based methods to distinguish proteoforms illuminates the roles of PTMs in modulating the signaling activity of proteins like chemokines[86].

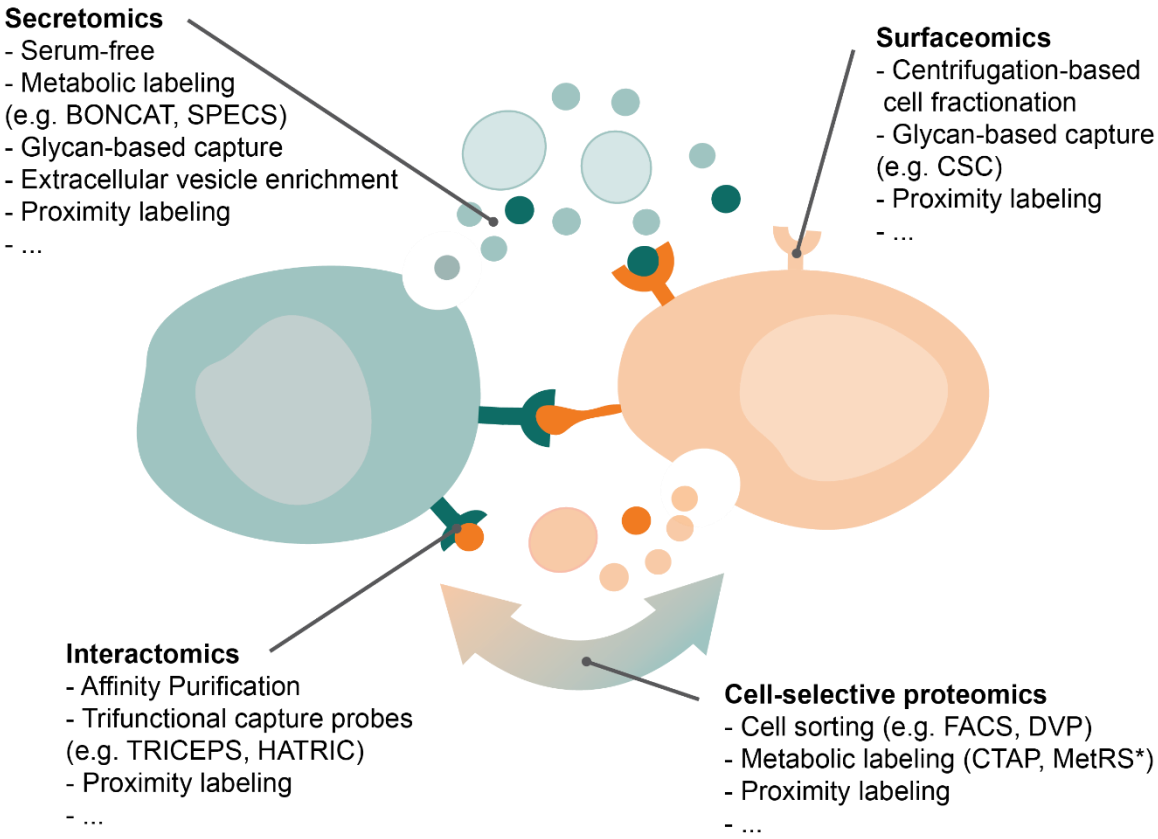

Figure 3: MS-based proteomics methods elucidate mechanisms of intercellular signaling. Proteomics provides a powerful framework for dissecting molecular mechanisms of cell communication signaling. Specialized workflows allow focusing the analytical bandwidth on protein groups of interest. For example, secretomics methods offer comprehensive insights into released signaling proteins, while surfaceomics methods facilitate the detailed characterization of membrane-bound ligands and receptor proteins, together forming a crucial foundation for inferring context-dependent intercellular communication channels. Other workflows can specifically capture interactions between signaling proteins and thereby deepen our understanding of molecular signaling mechanisms. Cell-selective proteomics techniques allow the study of reciprocal responses of directly interacting cells within heterocellular model systems like co-cultures or tissues. Figure adapted from[4].

Similar to secreted proteins, specialized MS-based proteomics methods facilitate detailed studies of proteins exposed on the cell surface membrane, collectively referred to as the surfaceome. Like secreted proteins, the expression and trafficking of plasma membrane proteins are often intricately regulated at the post-transcriptional level. This leads to a

lower-than-average correlation between mRNA and protein abundances, making transcriptomics approaches less reliable for predicting their presence[40,87-89]. Techniques like cell surface capture (CSC) proteomics that provide direct protein level quantification with spatial specificity are therefore essential to accurately understand the physiological composition of the cell surface[90]. CSC has been used to systematically map proteins on the surface of many different cell types[88], creating invaluable resources for the inference of cell communication and the selection of cell type and state-specific markers. This information is also crucial for developing novel therapeutic approaches, particularly in the development of cell type-selectively targeted antibody drug conjugates (ADCs)[91]. Moreover, combining CSC surfaceomics with cross-linking mass spectrometry has revealed disease-specific surface protein conformers, such as an acute myeloid leukemia (AML)-selective integrin β_2 conformation, that may serve as highly specific targets for chimeric antigen receptor (CAR) T cell immunotherapy[92,93].

However, some aspects of intercellular signaling remain elusive with current methods. For instance, challenges persist in the cell-selective profiling of cell communication, particularly of secreted proteins, directly within complex tissue environments.

1.1.4 Cell-selective proteomic analysis of intercellular signals in tissues

While MS-based proteomics can quantify thousands of proteins within a single biological sample, it cannot inherently discern their cell type origins in convoluted mixtures like tissue lysates. To link proteomic data to specific cellular contexts in complex heterocellular environments, MS-based proteomics is typically paired with cell sorting techniques. However, metabolic and chemical labeling methods are emerging as highly complementary approaches, especially for studying intercellular communication mechanisms.

1.1.4.1 Cell-selective proteomics by cell isolation and sorting techniques

The most commonly employed strategy for cell type-resolved analyses of tissues involves extracting individual cells through mechanical dissociation and digestion of ECM components with collagenases and other proteases. After filtration to remove cell clusters

and debris, the cells are washed and stained with labeled antibodies directed against specific surface markers. The labeled antibodies facilitate the sorting of isolated cells using techniques such as fluorescence-activated cell sorting (FACS) or magnetic-activated cell sorting (MACS). This well-established approach is accessible to many laboratories, and customized marker panels provide high flexibility, often enabling a precise distinction of cell types. After sorting, cells can be directly analyzed or cultured and manipulated further *in vitro*, for example, in stimulation experiments. As a fundamental component of countless studies across key fields of biomedical research and a cornerstone of single-cell techniques, FACS is a critical enabler in deepening our understanding of biological processes.

Nonetheless, classical cell sorting has limitations that make some experiments challenging and leave crucial layers of information inaccessible. For example, depending on the tissue and cell type of interest, extracting intact cells can be difficult and may necessitate harsh treatment. Exposure to stress factors and environmental changes during the extraction and sorting process can alter cell states and significantly reduce cell viability, diminishing yields and potentially limiting downstream applications. Notably, less resilient cell types or subpopulations may be disproportionally depleted, biasing the observed tissue cell type composition and phenotypes[94]. Furthermore, cell sorting removes extracellular proteins and spatial context information, which are highly valuable for understanding cellular interactions and communication structures in tissues.

Exciting new opportunities have emerged from the significant advancements in high-sensitivity MS-based proteomics[95,96] and its recent integration with high-resolution microscopy, machine learning-guided cell classification, and automated cell isolation by laser microdissection, collectively known as deep visual proteomics (DVP)[97]. DVP gives access to the vast resources of formalin-fixed and paraffin-embedded patient samples stored in biobanks and links cell- or subcell-selective proteomic data with their corresponding spatial context in intact tissue, providing a powerful platform for studying complex, highly heterogeneous cell systems like tumors down to the single cell-shape level[98].

1.1.4.2 Cell-selective proteomics by metabolic or chemical protein labeling

Metabolic and chemical protein labeling methods offer new approaches to cell-selective proteomics. Compared to traditional cell sorting techniques, they provide unique advantages for studying intercellular communication, such as resolving rapid cell signaling processes at the PTM level, and comprehensively profiling protein secretion dynamics.

In a pioneering study, Jorgensen *et al.* used stable isotope labeling by amino acids in cell culture (SILAC)[99] to pre-label HEK293 cells engineered to express either the ephrin receptor EphB2 or its corresponding surface-bound ligand ephrin-B1, before allowing them to interact for ten minutes in co-culture[100]. SILAC labeling facilitated combined lysis, phospho-site enrichment, and analysis without the need for prior cell separation, effectively preserving cell states while avoiding temporal lag and sorting-related artifacts. Mass differences arising from SILAC enabled the deconvolution of cell type-specific protein abundances via mass spectrometry, revealing asymmetric reciprocal signaling events in both cell types upon contact. Moreover, cell responses to unidirectional stimulation, for example, through cytoplasmatic truncation of ephrin ligand or receptor, or stimulation with soluble ligand variants, showed significant differences to co-cultures with bi-directional signaling. This elegantly demonstrated non-cell-autonomous portions of intracellular signaling responses to intercellular communication signals, which are not accurately captured in simplified models but resolved by cell-selective labeling-based analyses of directly interacting cells.

A major limitation of SILAC in co-culture systems is the rapid dilution of labeled proteins when differentially labeled cells are mixed and cultured without a continuous supply of heavy amino acids. Cell type-specific labeling using amino acid precursors (CTAP) addresses this challenge by engineering cells to produce biosynthetic enzymes for L-lysine, an essential amino acid in vertebrae[101]. By introducing genes for lysine racemase (lyr) or diaminopimelate decarboxylase (DDC), transgenic cells can convert the precursors D-lysine or 2,6-diaminopimelic acid (DAP) into L-lysine. This allows for continuous growth and selective labeling of two cell types in lysine-deficient media supplemented with isotopically labeled precursors, effectively maintaining label fidelity over extended periods[102]. Tape *et al.* used CTAP to elucidate the propagation of oncogene-driven signals

across heterocellular systems, shedding light on reciprocal signaling processes between cancer cells and surrounding stromal cells[103].

Notably, cell-selective labeling extends to secreted proteins, making them traceable to their cellular origins even when dispersed over significant distances. The capability to delineate cell type contributions to extracellular proteins within heterocellular environments overcomes a fundamental constraint inherent to cell sorting and most biomolecular analysis methods, and can greatly enhance our understanding of intercellular signaling processes. Gauthier *et al.* demonstrated a proof-of-concept and successfully used CTAP to resolve cell type origins of proteins detected in supernatants from two different cell types in co-culture[101]. However, like unlabeled secretomics experiments, CTAP requires the collection of secreted proteins in serum-free media to avoid dynamic range issues. The presence of highly abundant serum proteins can obscure low-abundance proteins during MS analysis, thereby hindering the deep characterization of cell secretomes. In addition to labeling competition from natural amino acids, a high abundance of proteins expressed by non-labeled cells may also hinder the effectiveness of CTAP *in vivo*, particularly if the cells of interest constitute a relatively small fraction of the tissue composition.

Emerging technologies based on metabolic labeling of proteins through the residue-specific incorporation of non-canonical amino acids (ncAAs) with functional groups suitable for bioorthogonal chemical enrichment elegantly address dynamic range challenges. Bioorthogonal non-canonical amino acid tagging (BONCAT), for example, uses L-azidohomoalanine (Aha), an azide group-containing L-methionine (Met) analog recognized by the endogenous protein synthesis machinery and incorporated into proteins as a methionine substitute[104]. Proteins with Met-Aha substitutions can be effectively enriched through click chemistry-based affinity purification methods, which drastically enhances the detection limits of labeled proteins within predominantly unlabeled backgrounds. Originally designed to differentiate newly synthesized proteins from preexisting ones and study proteome-wide synthesis dynamics[104], BONCAT has proven highly valuable for secretomics analyses. The specific enrichment of Aha-labeled proteins facilitates comprehensive analyses of cell-secreted proteins in serum-containing culture media, avoiding serum-starvation, which can rapidly affect cell phenotypes[105]. Moreover, engineered aminoacyl-tRNA synthetases (aaRS) expand the repertoire of incorporable ncAAs beyond those recognized by endogenous enzymes, thereby enabling cell-selective labeling. While various pairs of modified aaRS and ncAAs have been successfully

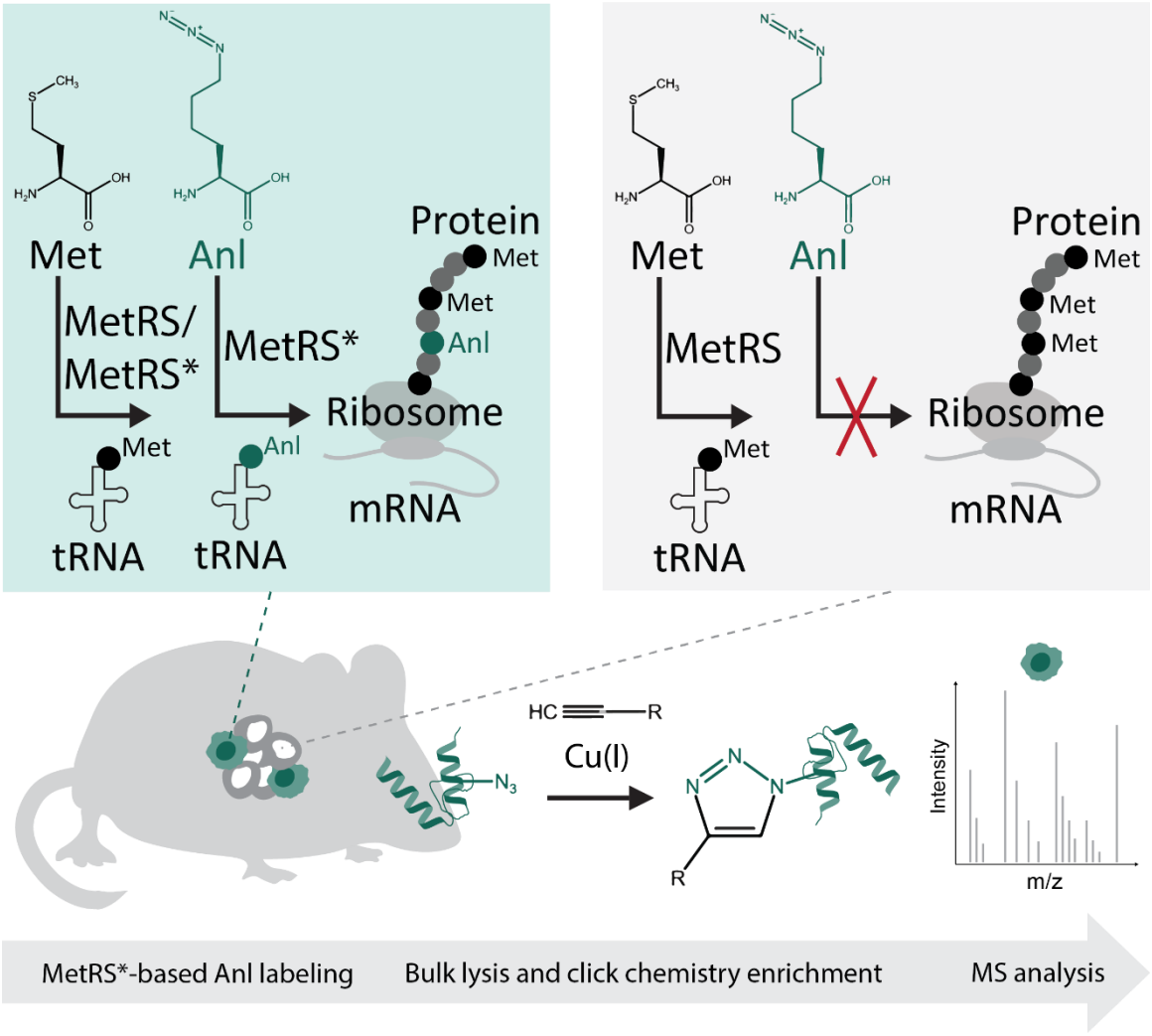

Figure 4: MetRS*-based cell-selective proteomics. The non-canonical amino acid azidonorleucine (Anl) is taken up by cells when supplied but is not utilized by the endogenous translation machinery. However, it can be activated by an engineered methionyl-tRNA synthetase (MetRS*). In MetRS*-expressing cells, Anl is incorporate into nascent proteins as a methionine substitute. Anl-labeled proteins can then be selectively enriched through click chemistry workflows, for example, using immobilized alkynes. The enriched proteins are subsequently analyzed by quantitative MS-based proteomics to gain cell-selective insights into protein expression (see chapter 1.2). Figure adapted from[1-3].

developed and tested for cell-selective proteomics experiments, such as L-azidotyrosine and L-azidophenylalanine with their corresponding aaRSs[106], the most widely adopted methods are based on the incorporation of L-azidonorleucine (Anl) by a modified methionyl-tRNA synthetase[107] (Figure 4).

Compared to Aha, Anl has a two-carbon longer side chain, allowing it to be taken up by cells but not activated by the endogenous methionyl-tRNA synthetase (MetRS). However,

engineered murine methionyl-tRNA synthetase (MetRS*), which contains an L274G point mutation that enlarges the amino acid binding pocket, charges Anl to $tRNA^{Met}$[108]. As a result, the expression of MetRS* enables cell-selective labeling in the presence of Anl through Met-Anl substitutions. Successful cell-selective labeling via MetRS* has been demonstrated in various cell types and tissues of model organisms without significant toxicity, including the brains of fruit flies and mice[109,110]. This suggests broad applicability for both *in vitro* and *in vivo* studies.

The advantages of cell-selective labeling and enrichment of labeled proteins have primarily been utilized in neurobiology to profile cells like neurons, which are notoriously difficult to extract from tissue and sort[1,111]. However, the proteome coverage achieved in previously published MetRS*-based proteomics experiments falls short of that obtained in standard proteomics studies using comparable instrumentation[1,108,110,112-114]. Furthermore, the high potential of MetRS*-based labeling for investigating cellular communication in complex heterocellular systems through cell type-resolved analyses of extracellular proteins has yet to be explored. Despite its benefits, its comparably low labeling efficiency is a critical challenge that has likely hindered the broader and more effective adoption of MetRS*-based cell-selective proteomics. It has been demonstrated that MetRS*-mediated Anl incorporation is significantly slower than the non-cell-selective Aha incorporation by the endogenous MetRS[115], and that MetRS* still activates Met around four-fold faster than Anl[108]. Consequently, Anl labeling is typically substoichiometric and strongly dependent on MetRS* expression levels, local Anl concentration, and Met competition, with substitution rates of only a few percent even under very favorable conditions[2]. To boost labeling rates, *in vitro* experiments are typically conducted in Met-free media, and in some cases, mice have been fed chow with low Met content[1,110]. Previous work has been primarily focused on establishing the method in model systems and optimizing labeling rates, which is important for the success of MetRS*-based experiments. However, there haven't been focused efforts to systematically evaluate and optimize the downstream sample preparation workflow, which is critical for Anl-protein extraction, recovery, and enrichment specificity, and may strongly improve the performance and scope of MetRS*-based methods.

Beyond metabolic protein labeling, chemical labeling techniques like proximity labeling (PL) have come into focus within cell-selective proteomics. PL methods are based on the spatially restricted activation of affinity probes around specific proteins or structures of interest and have emerged as powerful methods for profiling sub-cellular compartments

and protein interactomes, as described in more detail in Chapter 1.1.5.1. However, recent studies have adapted PL using promiscuous biotin ligases such as BioID or TurboID for broad, cell-selective protein labeling and analyses[116-119]. Although successfully implemented in both cell culture and animal models, the protein coverage that met quality control standards for high-confidence cell specificity was relatively low[116-119]. Nonetheless, these initial results highlight promising avenues for further method development to refine PL workflows, enabling comprehensive proteomic profiling of cell types within complex tissues. Notably, several groups recently provided proof-of-concept for PL-based *in vivo* cell-selective secretomics analysis, revealing, for example, an increased abundance of hepatocyte-derived betaine-homocysteine S-methyltransferase (BHMT) in blood plasma of mice on a high fructose, high sucrose diet[120-123].

1.1.5 Proteomics analysis of intercellular signaling protein interactions

After decoding the human genome[69,124], the comprehensive mapping of human protein-protein interactions (PPIs), commonly referred to as the human interactome, has risen as a key objective in biological research. Early efforts systematically characterized pathway-specific interactomes[125] and evolved to proteome-wide investigations[126-128]. Large-scale studies leverage technical advances in high throughput PPI detection technologies, like yeast two-hybrid (Y2H)[129,130] and affinity purification-mass spectrometry (AP-MS)[131-134], and provide experimental evidence for tens to hundreds of thousands of PPIs. The continuous increase of cumulative knowledge on eukaryotic interactomes is cataloged and curated in databases such as HPRD134, BioGRID135, and MIntAct[135].

Nonetheless, after more than two decades of research, our understanding of global, proteome-scale PPI networks is still fragmented[136]. Truly comprehensive PPI mapping remains elusive for several reasons, including technical and logistical challenges due to the vast number of proteins and proteoforms in the human proteome, biochemical properties of specific protein classes, transient interactions, and context-dependence of protein expression and interactions[134,137].

PPIs involving extracellular proteins and transmembrane signaling receptors are among the most underrepresented interaction types in typical high throughput screens[137-139]. Their extracellular localization, comparably low abundance, the amphipathic nature of transmembrane proteins, requirements for proper ectodomain folding, the context-

specificity of signaling interactions, and often weak affinity of monovalent binding events that need clustering for increased binding avidity collectively impede effective characterization by conventional PPI detection methods[140]. However, the central role of extracellular signaling protein interactions in biomedical research motivates great efforts to overcome these challenges with specialized techniques.

Single-pass receptor ectodomains can maintain ligand-binding function when recombinantly expressed in soluble form[140,141]. Therefore, biochemical high throughput screens with receptor ectodomain libraries are used to systematically probe pairwise interactions with extracellular proteins. Avidity-based extracellular interaction screens (AVEXIS)[142] detect even transient interactions and have led to significant discoveries such as neuropilin-2 as a long-sought human cytomegalovirus receptor in epithelial and endothelial cells[143], and basigin as a receptor for PfRh5, a ligand expressed by *Plasmodium falciparum* with essential function in erythrocyte invasion and pathogenesis of malaria[144]. Similar methods identified interleukin-34 as a previously undescribed extracellular signaling protein and new ligand for colony-stimulating factor 1 receptor[145]. Other approaches utilize genetic screening methods such as CRISPR/Cas9 technology[146,147] to explore ligand-receptor interactions. Cell-based genome-scale studies of “loss of binding” phenotypes can identify receptors of ligands-of-interest and provide additional information on essential proteins in pathways necessary for functional receptor presentation at the cell surface[148,149].

While such screening methods offer significant insights, the scale required is often impractical and cost-prohibitive for research groups with more confined research questions. Moreover, unresolved conceptual limitations underscore the need for continued innovation in technical approaches. Intact cell-based capture techniques, combined with MS-based proteomics, have emerged as particularly versatile and effective tools for analyzing protein-protein interactions at the cell surface. For example, Bernd Wollscheid and colleagues pioneered chemoproteomic methods dedicated to the deorphanization of extracellular ligands without known receptors: The ligand-based receptor capture (LRC) methods, TRICEPS[150,151] and HATRIC[152], utilize trifunctional compounds designed to covalently modify a ligand-of-interest. The modified ligand then guides a glycan-dependent capture reaction between the capture compound and ligand-corresponding target receptors on living cells. Upon cell lysis, cross-linked ligands and receptors are specifically enriched and analyzed by mass spectrometry. The *in situ* capture of receptors within their native cellular environment effectively mitigates many of

the technical challenges inherent to the analysis of extracellular PPIs. Notably, the covalent cross-linking of interaction partners also enables LRC methods to capture even low-affinity binding events. TRICEPS and HATRIC successfully identified novel cell surface ligand-receptor interactions, such as tyrosine-protein kinase Mer (MERTK) as a contributor to endothelial HDL binding[153], and VISTA as an acidic pH-selective ligand for PSGL-1[154]. Limitations of TRICEPS and HATRIC include their dependence on modified sugar residues, which must be accessible within a certain range and orientation on target proteins. Sugar oxidation can also alter the interaction properties of some targets, potentially affecting the results.

Moreover, recent studies have demonstrated significant potential for systematically exploring PPIs at the cell surface using proximity labeling (PL) proteomics techniques.

1.1.5.1 Proximity labeling proteomics

The common concept of PL methods involves tethering a catalytic moiety to proteins of interest, which, upon activation, convert inert probe molecules into highly reactive ones, typically open-shell species or electrophiles. The activated probe molecules then diffuse around the emitting catalyst and covalently bind to nearby biomolecules, creating a chemical tag for selective enrichment. Tagged and enriched proteins can be identified and quantified using MS. Developed to explore the spatial organization and interactions of proteins in their native cellular contexts, PL proteomics offers unique advantages and experimental capabilities that were previously hard to achieve. Pioneering methods are based on biotin ligases and peroxidases (Figure 5), and remain the most prevalent in the field.

Roux and colleagues introduced the PL strategy BioID in 2012, employing a promiscuous mutant of BirA (BirA*), a biotin ligase from *Escherichia coli*[155]. While the wild-type BirA enzyme catalyzes the formation of highly reactive biotinoyl-5'-AMP (bioAMP) from ATP and biotin, followed by the stringent sequence-selective biotinylation of specific substrate proteins, BirA* exhibits a significantly reduced affinity for bioAMP. This leads to the release of bioAMP from the active site and spontaneous reaction with primary amines, such as lysines of nearby proteins. Due to the low reaction rates of BirA* in standard cell culture biotin concentrations[155], the BioID method allows time-controlled PL through biotin supplementation. Further enzyme development yielded important enhancements. For example, the directed evolution of TurboID[156] markedly increased its catalytic efficiency,

reducing BioID-typical labeling times from 16 hours and more[157] to as brief as 10 minutes. MiniTurbo is a more compact variant, decreasing the enzyme's size from 35 kDa to 28 kDa, which may reduce potential fusion artifacts that can affect function and protein trafficking[156]. While most BioID and related PL-based studies were focused on intracellular experiments, recent publications demonstrate the applicability to the cell surface[158-162].

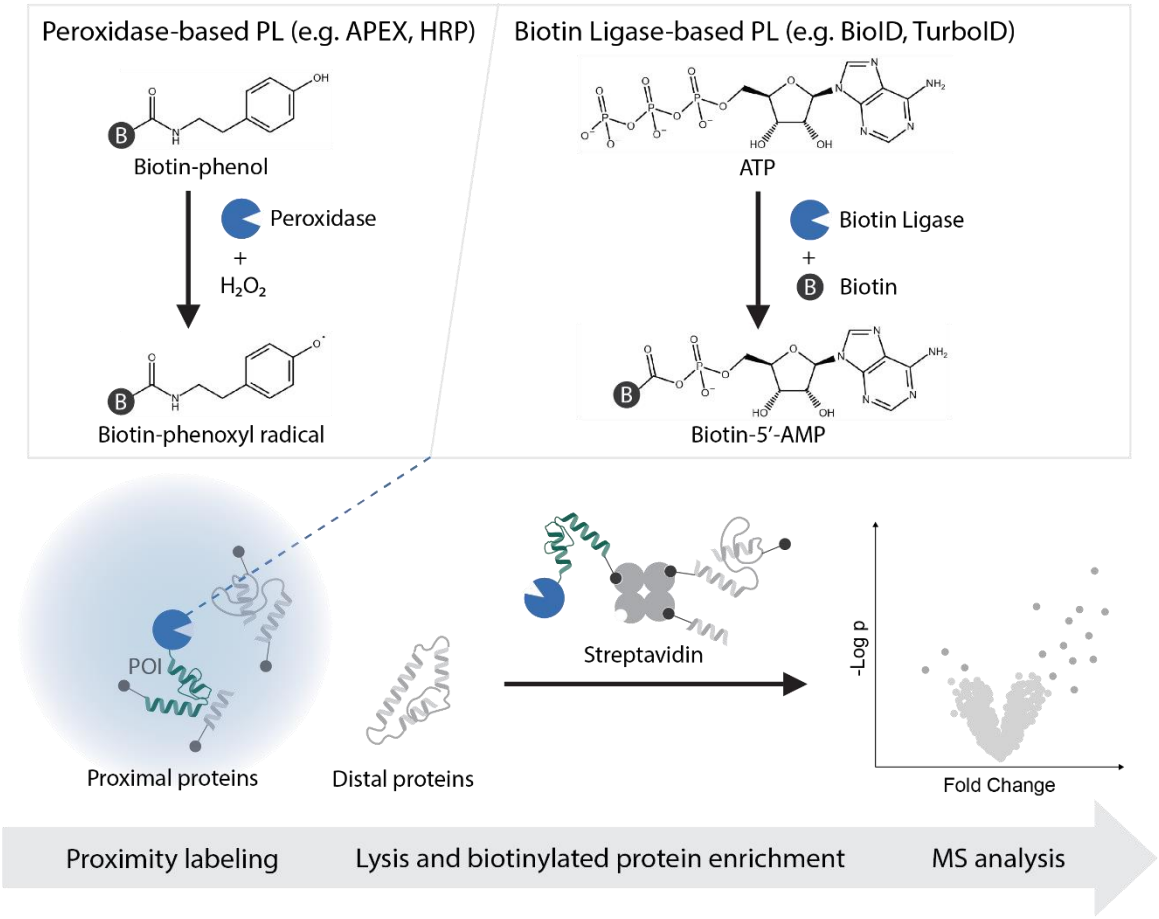

Figure 5: Proximity labeling proteomics. To capture proteins in close spatial proximity, a protein of interest is fused to a catalyst capable of activating reactive probe molecules with an enrichment handle, typically biotin. Activated probes covalently tag proteins within the effective labeling radius, determined by their half-life in the given environment. Tagged proteins are then selectively enriched, analyzed by MS-based proteomics (see chapter 1.2), and quantitatively compared to controls.

One year after the public release of BioID, Alice Ting and colleagues demonstrated effective PL proteomics using engineered ascorbate peroxidase (APEX), a 28 kDa peroxidase previously employed as a genetically encoded reporter for electron microscopy[163,164]. In the presence of H_2O_2, APEX oxidizes biotin-phenol derivates to phenoxyl radicals, which covalently bond with electron-rich amino acids like tyrosine,

tryptophan, histidine, and cysteine in proximate proteins[165]. Similar to BioID's advancements, subsequent directed evolution further improved APEX, leading to the development of APEX2 with significantly enhanced reaction kinetics, thermal stability, and H_2O_2 resistance[166]. While cytotoxicity of H_2O_2 limits peroxidase-based PL applications *in vivo*, the fast kinetics facilitate efficient labeling within very short time frames, often around one minute and less. High sensitivity and superior temporal resolution compared to BioID-type methods have made APEX particularly valuable for analyzing rapid signal transduction events that were previously challenging to study. For example, APEX has played an important role in exploring dynamic GPCR interactomes following receptor activation, including studies on the δ- and μ-opioid receptors[164,167], angiotensin II type 1 receptor, and β2 adrenoceptor[168].

Like APEX, horseradish peroxidase (HRP) is an effective catalyst for PL, but it is unsuitable for use in the cytosol and reducing environments due to its calcium dependence and essential disulfide-bridges[163]. However, HRP is a valuable tool in the secretory pathway and extracellular space, offering even higher activity than APEX2. Techniques like enzyme-mediated activation of radical sources (EMARS)[169], selective proteomic proximity labeling using tyramine (SPPLAT)[170], and biotinylation by antibody recognition (BAR)[171] are based on PL through antibody-HRP conjugates. Guided against cell surface structures of interest, such approaches have been successfully employed to characterize functionally integrated membrane protein assemblies around cell surface receptors such as the B cell receptor[170], as well as protein composition in plasma membrane microdomains like the axon initial segment[172], which are intractable for conventional biochemical separation techniques. Moreover, newly developed membrane-impermeable biotin phenol substrates effectively suppress background labeling from intracellular protein pools, thereby improving surface-specific PL using membrane protein-HRP-fusion constructs[173]. This has enabled cell type-selective and time-resolved surfaceome analyses in intact tissues, revealing, for example, LRP1 as a key regulator of neural circuit assembly in *Drosophila*[174], and a critical role of Armh4 in Purkinje cell dendrite morphogenesis in mice[175].

The spatial range and resolution of PL methods are dependent on the half-life of the emitted reactive species[176,177]. In living cells, effective labeling radii of biotin ligase- and peroxidase-based PL have been estimated to be in the tens of nanometers range[163,178]. However, as probe half-lives are influenced by environmental factors, such as quencher concentrations and macromolecular crowding[179,180], and other factors like tether lengths play a role, estimates should not be generalized throughout biological compartments and

contexts. At the cell surface, with fewer radical quenchers, experimentally determined HRP labeling radii have been observed to exceed 200 nanometers[177,181]. Notably, HRP-based PL is sufficiently precise to capture proteins within spatially defined yet physically open cellular domains such as synaptic clefts with high specificity[173]. Yet, differentiating proteins that are co-clustering and functionally interacting from a potentially large number of co-localized but not directly related proteins within the same cellular compartment can be a significant challenge. Tailored control designs, applied on a case-by-case basis, aid in deconvolving PL data, facilitating successful discovery and validation of previously unknown interactors of signaling receptors[164,167]. Nonetheless, there is a significant need for technical solutions that control the range of PL methods to simplify data interpretation, and provide means to confidently identify interactor candidates.

Recent advancements in photocatalyst-based PL methods have substantially improved the spatial resolution for cell surface applications. LUX-MS, for example, uses small-molecule singlet oxygen generators (SOG) for light-controlled oxidation of proximal proteins[182]. Under typical labeling conditions, singlet oxygen species produced by LUX-MS have brief half-lives in the microsecond range[183], tuneable with deuterated buffers. Photo-oxidized amino acids formed by PL, primarily 2-oxo-histidine, are biotinylated with biotin hydrazide probes. The advantages of the tighter labeling radius are highlighted by a direct comparison of LUX-MS and HRP PL in an anti-CD20-guided experiment on human B-cells. While both methods successfully captured the direct target receptor and known lateral receptor interactors, LUX-MS resulted in fewer significantly co-enriched proteins[182]. Moreover, the small catalyst size of LUX-MS (< 1 kDa) ensures broad ligand compatibility, opening new applications that are intractable with larger tags due to steric hindrance. For example, LUX-MS enabled the target identification of the small molecule drug CG1, whereas HRP conjugation interfered with target engagement[182].

Even more precise cell surface labeling was achieved with MicroMap (µMap). The µMap workflow leverages the nanosecond lifespans of carbenes in water, which react rapidly with biomolecules by insertion into C-H bonds[184]. Protein-of-interest-coupled iridium-catalysts are excited by blue light and activate diazirine probes via Dexter energy transfer, generating carbenes within 0.1 nm of the catalyst. Rapid quenching by water confines carbene diffusion to an estimated maximum of 4 nm[185], making the µMap labeling radius so small that it is primarily dictated by the tether-length[177]. Applied to antibody-guided PL at the living cell surface, µMap facilitates highly selective labeling and enrichment of direct targets (PNAS and Science paper). Since interaction networks of interest may span larger

distances than effectively captured by µMap, the authors evaluated additional probe types and developed new variants of µMap with intermediate labeling radii[177], bridging the gap to peroxidase PL.

1.2 Quantitative MS-based proteomics

Mass spectrometry (MS) is today's leading analytical method for systematically analyzing complex protein mixtures. Key scientific achievements, including genome sequence databases[69,186,187], soft ionization methods for biological macromolecules[188-190], and software for automated spectra interpretation[191-193], have enabled MS-based methods for high throughput quantification of proteins without prior target selection, allowing discovery-driven proteome-wide analyses of biological samples.

Proteins can be measured directly by MS (top-down proteomics), which allows for the precise identification and quantification of proteoforms with their specific combinations of pre- and post-translational modifications. However, the analysis of intact proteins poses significant technical challenges, such as in chromatographic separation, ionisation, and the interpretation of the typically very complex mass spectra[194]. Despite technical advances that enhance the scalability of top-down proteomics[195], its comparably low throughput, proteome coverage, and sensitivity have predominantly limited its applications to purified proteins or low complexity mixtures.

In bottom-up or "shotgun" proteomics, protein level information is inferred from MS analyses of cleavage products after digestion with specific proteases rather than measuring intact proteins directly. Although this approach introduces ambiguities at the peptide level, hampering the clear distinction of specific proteoforms, the significant technical advantages of analyzing peptides and the resulting gains in sensitivity, throughput, and coverage strongly outweigh this loss of information for many research questions. Bottom-up proteomics has evolved over decades of continuous development and has established itself as the gold standard for the comprehensive analysis of complex biological samples. A typical workflow is summarized in Figure 6 and described in more detail in the following chapters.

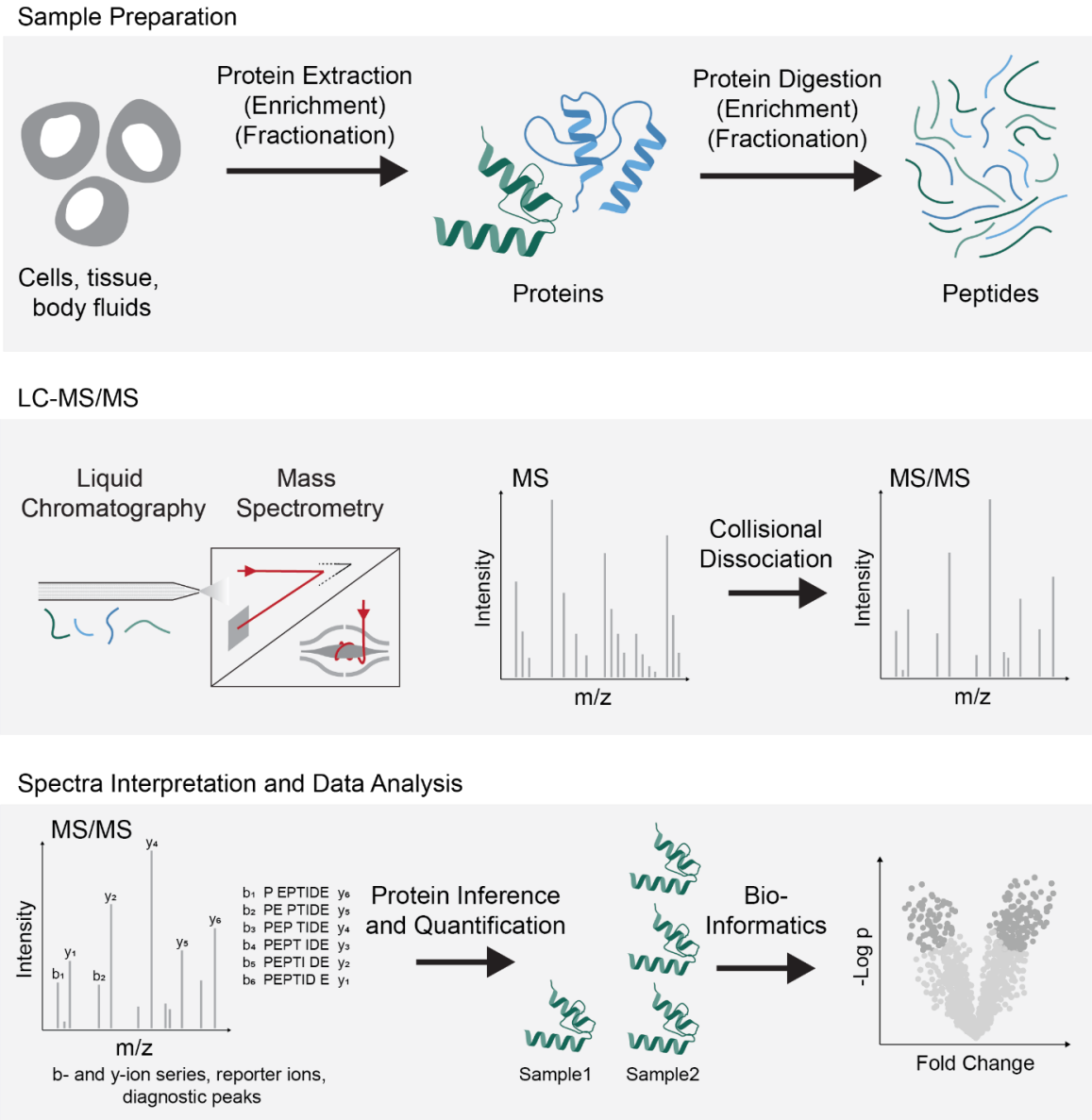

Figure 6: Bottom-up proteomics. In bottom-up proteomics experiments, proteins are extracted from samples, denatured, and digested by specific proteases. Selective enrichment at the protein or peptide level facilitates focused analyses of specific sub-proteomes. Peptide samples are cleaned and then separated by online-liquid chromatography, before being electrosprayed into a mass spectrometer. Peptide ions are analyzed in multiple stages to collect spectra that facilitate their identification via database matching algorithms, their quantification, and ultimately the inference of protein abundances in the original sample. Differences between sample groups are assessed using bioinformatic methods. Figure adapted from[196].

1.2.1 Sample preparation for bottom-up "shotgun" LC-MS/MS analyses

Typical sources for samples in biomedical research range from purified proteins over simple cell monolayers cultured *in vitro* to fresh model organism tissues, body fluids, and formalin-fixed paraffin-embedded (FFPE) biopsies of patients. In principle, any type of sample can be analyzed by MS-based proteomics as long as proteins can be extracted, and samples can be cleaned from MS-incompatible chemicals. Basic workflows for global proteomics analyses require only a few principal steps.

Cell and tissue samples are homogenized and lysed in buffers typically containing detergents and/ or chaotropic agents like urea or guanidine salts, facilitating efficient protein extraction and denaturation. Homogenization is often aided by mechanical cell disruption procedures like grinding in bead-mills or sonication, which also shears genomic DNA and thereby reduces the viscosity of concentrated samples. Reducing agents like DTT or TCEP and alkylation agents like chlor- or iodoacetamide are used to break disulfide bridges and irreversibly block cysteine side chains. For shotgun proteomics analyses, proteins are then digested with sequence-specific proteases.

Several important advantages have made trypsin digestion the gold standard: Trypsin has high enzymatic activity, remains stable in various buffer conditions with high tolerances for denaturing reagents, and cleaves proteins after the basic amino acids arginine and lysine with extremely high specificity[197]. Tryptic peptides have an average length of 8.4 amino acids (*in silico* digestion of the yeast proteome[198]) and at least two positive charges in acidic solution (at the N-terminus and the c-terminal amino acid side chain), which facilitates effective fragmentation by collision-induced dissociation (CID) (see below) and generally yields well interpretable MS^2 spectra with high mass y-ion series[197,199,200]. Lys-C, a second endopeptidase that mediates sequence-specific cleavage after lysine, is often used in conjunction with trypsin. It can cleave sequence motives that suppress trypsin activity, such as lysins followed by a proline, and decrease the overall rate of missed cleavages, improving protein quantification accuracy and coverage[201]. Alternative proteases can provide complementary information and increase the sequence coverage of proteins of interest.

After digestion, peptide samples undergo solid phase extraction to remove salts and other components that could suppress peptide ionization and interfere with the MS analysis. Alternative clean-up protocols, such as solid-phase-enhanced sample-preparation (SP3),

can further enhance chemical compatibility and offer elegant solutions for automating liquid handling[202].

Depending on the start material or research question, details of this principal workflow can vary significantly. For example, tissue proteomics experiments often benefit from harsh mechanical and chemical treatment to ensure thorough homogenization, efficient protein extraction, and comprehensive proteome coverage[203,204]. In contrast, affinity purification MS (AP-MS) protein-protein interaction studies usually rely on mild lysis conditions with low detergent and salt concentrations to preserve protein folding and interactions as much as possible[205]. AP-MS also requires workflow extensions, typically a bead-based pulldown of a bait protein in complex with potential interactors. Overall, MS-based proteomics is an incredibly versatile platform that can be combined with various complementary biochemical techniques to elucidate specific aspects of biology in great detail. Workflows for specific enrichment of often low abundant post-translationally modified peptides such as phosphopeptides or ubiquitinylated peptides greatly expand their coverage, allowing, for example, in-depth investigation of intracellular signaling. Likewise, sophisticated biochemical techniques make it possible to track protein subcellular localisation[206], find targets of drugs and drug candidates[40], or dissect intercellular signaling by MS-based proteomics, as discussed in previous chapters and Article 1.

1.2.2 Online liquid Chromatography

In typical MS-based proteomics experiments, peptide mixtures are separated by liquid chromatography (LC) systems that are directly coupled to the mass spectrometer before they are ionized and analyzed. Chromatographic separation reduces the complexity of analytes entering the mass spectrometer at a given time, greatly enhancing the number of peptides that can be identified and quantified in a single sample.

Currently, the most common setups use nano-high performance liquid chromatography (HPLC) systems with very narrow columns (inner diameters often in the sub-100 µm range) and low flow rates of a few hundred nl/min, which grants significantly improved sensitivity and ionization efficiency compared to standard HPLC[207]. Peptides are separated by reverse phase chromatography at low pH with a hydrophobic stationary phase, typically silica particles coated with long aliphatic C18 chains, and gradually

increasing hydrophobicity in the mobile phase, typically aqueous buffers with a volatile acid like formic acid and increasing acetonitrile concentrations.

To further enhance the proteomic analysis depth, samples can be pre-fractionated offline using an orthogonal chromatographic technique. This allows for quantifying an even larger number of peptides but requires more input material, increases MS analysis time, and complicates protein quantification[208,209].

1.2.3 Electrospray ionization tandem mass spectrometry (ESI-MS/MS)

MS instruments measure the abundance and mass-to-charge ratios of ions. Therefore, a prerequisite for MS analysis is the ionization and transfer of intact analytes into the gaseous state, a significant challenge for larger, non-volatile biomolecules like proteins or peptides. In the 1980s, matrix-assisted laser desorption ionization (MALDI)[190], the closely related soft laser desorption[189], and electrospray ionization (ESI)[188] overcame the technical hurdles for soft ionization of large biomolecules. For their development, Koichi Tanaka and John Fenn were awarded shares of the 2002 Nobel Prize in Chemistry. MALDI ionizes and transfers analytes from solid into the gas phase by laser pulses after being embedded in a crystalline matrix of low molecular weight molecules with high absorption in range of the laser's wavelength[210]. ESI, in turn, ionizes analytes directly from solution and produces ions continuously. This allows for direct coupling to LC systems, providing a crucial technological foundation for modern MS-based proteomics.

Until today, ESI persists as by far the most used ionization technique in proteomic research. A high voltage (kilovolts) potential is applied between the MS inlet and the analyte solution within a spray needle, often the pulled tip of the fused silica chromatographic column[211]. The high electric field induces the formation of a Taylor cone at the tip of the needle[212], and leads to the emission of finely dispersed and highly charged droplets. Evaporation of solvent shrinks droplets and eventually yields desolvated analyte ions[213].

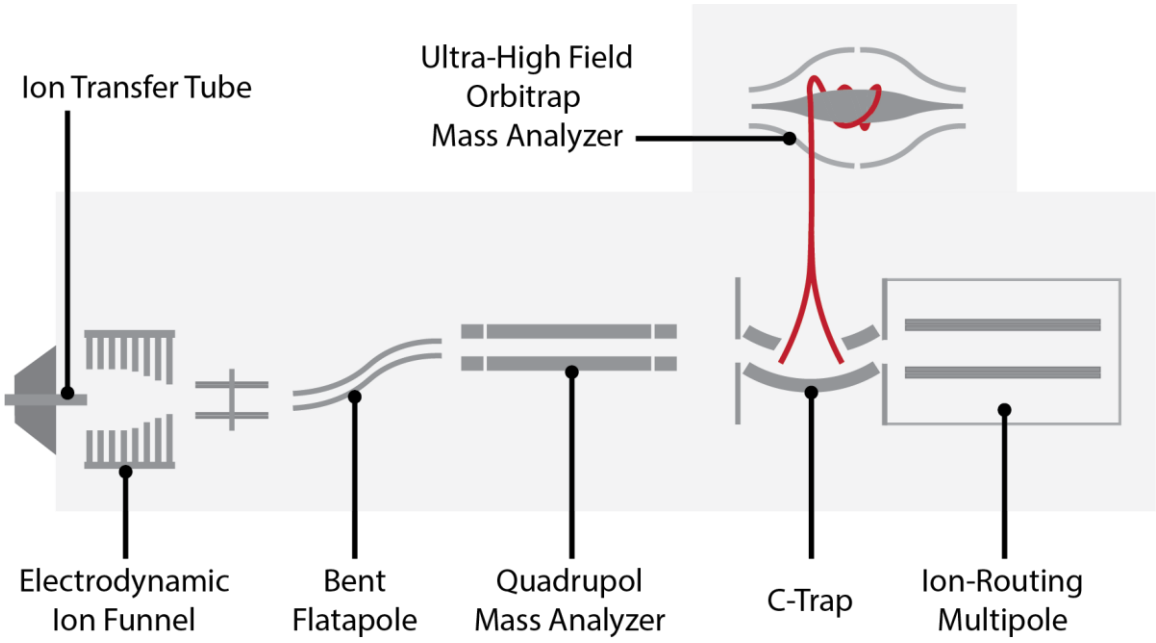

Figure 7: Scheme of a Thermo Scientific Orbitrap Exploris 480 mass spectrometer. The primary instrument used in this thesis was a Thermo Scientific Orbitrap Exploris 480 quadrupole-orbitrap hybrid mass spectrometer. Analytes are ionized by ESI and enter the instrument through the orifice of a heated ion transfer tube along a decreasing pressure gradient. Ions are focused and transmitted by ion optics, including a bent flatapole that diverges the ions from neutral particles and remaining solvent droplets, and guides them to a linear quadrupole mass filter. RF and DC voltages applied to the quadrupole rods determine transmitted m/z ranges and are adjusted for each scan. Ions are slowed down in the gas-filled C-Trap from where they are passed into the orbitrap mass analyzer or the ion-routing multipole for fragmentation by Higher Energy Collisional Dissociation (HCD). Figure adapted from[214].

Upon entering the orifice of the mass spectrometer, ions are guided by electric fields across a sequence of principal instrument components (Figure 7). In addition to an ion source, mass spectrometers comprise at least one mass analyzer and detector. For proteomic experiments, hybrid mass spectrometers with two or more m/z separation components of different types, and instruments with very high mass accuracy and resolution termed high resolution accurate mass (HRAM) systems, are preferred.

Typically, a quadrupole is used as a first-stage mass analyzer. Quadrupoles consist of four parallel and equally spaced rods, with opposing rods electrically connected. By applying a combination of direct current (DC) and radio frequency (RF) voltages to the rods, a quadrupole can be tuned to transmit all incoming ions or selectively allow ions within a specific m/z range to pass through[215]. The currently most popular instruments for

proteomics experiments use quadrupoles in conjunction with either Time-of-flight (TOF) or Orbitrap[216] mass analyzers. TOF analyzers accelerate ions through an electric field into a field-free flight tube towards a detector and distinguish ions by their velocities, which are influenced by their m/z. Orbitrap analyzers capture ions between an outer barrel-like electrode and an inner spindle-shaped electrode. Trapped ions orbit around the inner electrode, and the image current induced by their movement is deconvoluted by Fourier Transformation and used to derive their m/z. Progress in MS technology continues to drive innovation in proteomics research. This is exemplified by new mass analyzers such as the asymmetric track lossless (Astral) analyzer, pushing the boundaries of mass spectrometry, including significant improvements in scan speed and sensitivity[78,96].

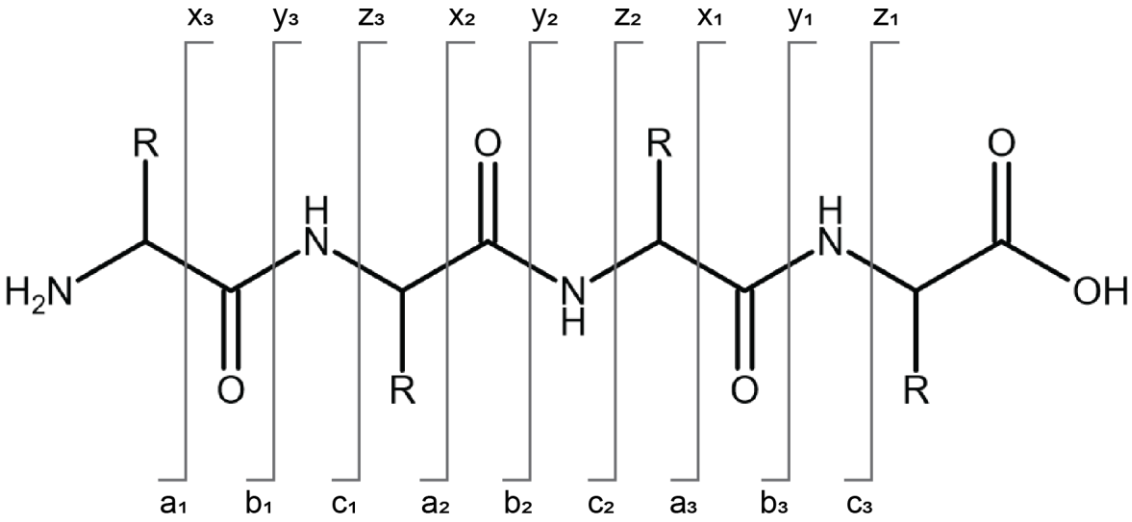

Figure 8: Fragment ion classification in peptide mass spectra. The Roepstorff-Fohlmann-Biemann nomenclature is a widely adopted system for describing backbone fragmentation in MS/MS analyses of peptides. Ions are classified based on the location of the break and the portion of the peptide (N- or C-Terminus) retained in the fragment. Collision-induced dissociation methods commonly used in proteomics experiments predominantly produce fragments with breaks of the peptide bond, yielding b- (retaining the N-terminus) and y-ions (retaining the C-terminus). Fragment ions are sequentially numbered from to the respective terminus. Figure adapted from[217].

In complex proteome digests, peptide masses alone are often insufficient to conclusively identify specific peptides. For more detailed sequence insights, peptides are fragmented within the mass spectrometer[218-220]. The predominant fragmentation techniques, collision-induced dissociation (CID) and higher-energy collisional dissociation (HCD) expose

selected precursor ions to collisions with a neutral gas like nitrogen or helium. These collisions lead to the conversion of kinetic energy to internal energy that can induce breakage of covalent bonds[221]. Fragmentation patterns of peptides depend on the chosen method, with CID and HCD primary yielding highly predictable b and y ion series (Figure 8), which arise from the cleavage of the amide backbone. The generated fragment ions are subsequently analyzed in a follow-up mass spectrometry scan, typically referred to as MS/MS or MS2 scan.

1.2.4 Data acquisition modes and computational proteomics

Modern mass spectrometers acquire high resolution and accurate mass data for peptide precursors and their fragments at rates of hundreds of scans per second[78,95,96]. As MS hardware continues to advance, scan modes evolve concurrently, with different approaches to optimizing the usage of measuring time for confident peptide identifications and accurate quantification.

Targeted acquisition methods, such as selected reaction monitoring (SRM) or parallel reaction monitoring (PRM), facilitate highly specific, sensitive, and robust detection of predetermined sets of peptides[222]. Advanced approaches, for example, use real-time calibration of masses and retention times to target thousands of peptides per run[223,224], or spike-in triggered acquisition combined with sample multiplexing[225]. However, exploring the proteome as comprehensively as possible is a fundamental goal in proteomics research. Bottom-up MS-based proteomics enables discovery methods without the need for analyte preselection, aiming to quantify the widest possible range of peptides present within a sample. The predominant acquisition modes in discovery proteomics are data-dependent acquisition (DDA) and data-independent acquisition (DIA).

In DDA mode, the MS instrument cycles through sequential MS/MS scans, narrowly isolating specific precursor ions detected in initial MS1 survey scans that span the entire m/z range of interest. Given that the number of different peptides in typical biological proteome samples greatly exceeds the number of scans a mass spectrometer can practically acquire, only a selection of peptides can be analyzed by DDA. Survey scan data is processed in real-time to select precursor ions for fragmentation, using criteria designed to maximize the yield of informative MS/MS scans. For example, selection algorithms typically prioritize precursors with the highest abundance (commonly termed

“topN”), and specific charge states, while excluding precursors that have been analyzed in previous scans (“dynamic exclusion”)[226].

In contrast, DIA methods use predefined scan patterns, independent of the spectra being acquired. Instead of isolating individual precursor ions for MS/MS scans, all ions within wider m/z windows are collectively fragmented and analyzed. Moreover, the MS/MS windows are positioned to cover the whole m/z range of interest in each scanning cycle, collecting fragment scan data for all precursor ions within these boundaries. A primary challenge of DIA methods is the deconvolution of the complex spectra arising from co-fragmenting multiple precursors. Experimental parameters such as the width and placement of precursor isolation windows are tuned to optimize the balance between cycle time and spectral complexity for optimal peptide identification and quantification, and DIA acquisition schemes remain a highly active area of development[227]. While initially trailing the proteome coverage achieved by DDA[228], DIA with modern HRAM instruments and advanced analysis software now supersedes typical label-free DDA experiments in many key areas, including deeper analytical coverage, greater data completeness, and more accurate and precise quantification[193,229,230]. Furthermore, advances in MS instrumentation, enabling fast scans at high resolution, mass accuracy, and sensitivity, facilitate effective DIA experiments with extremely narrow isolation windows across a wide m/z range, blurring the lines between DIA and DDA[78].

In MS-based proteomics, raw data is computationally processed to perform automated feature detection, peptide identification, quantification, and data rollup for protein inference. These core functionalities often incorporate additional features such as nonlinear recalibration of masses and retention times, abundance normalization across runs, identification of pre-defined peptide modifications, and calculating their site-specific localization probabilities[231]. The most common approach for identifying peptides from DDA data involves a spectrum-centric search, comparing measured precursor fragmentation spectra against target fragmentation spectra databases[231,232]. Such databases typically contain all known or anticipated protein sequences expressed by the organism under study. These are then digested and fragmented *in silico* to mimic the expected cleavage patterns of enzyme(s) and peptide dissociation techniques used during the sample preparation and MS analysis. Search engines compute peptide spectrum match (PSM) scores for all theoretical and experimental precursor fragmentation spectra combinations. The highest-scoring PSMs for experimental fragment spectra are then filtered to control the false discovery rate (FDR) of peptide

identifications, often using a target-decoy method to define thresholds[233]. Many proteomics software solutions implement machine learning algorithms for various workflow functions to improve performance, including PSM scoring and FDR estimation[193,234,235]. Various strategies for deconvoluting DIA fragmentation spectra have been introduced, including algorithms that reconstruct DDA-like pseudo-spectra[236], making them compatible with established DDA search engines. However, the most effective current methods employ target spectral library-based peptide-centric approaches to extract quantitative data from DIA spectra. Spectral libraries can be acquired empirically, for example, through auxiliary DDA experiments, or predicted in silico[193,237-239].

Similar to methods for data acquisition, there are several classes of proteomics quantification strategies, each offering distinct advantages depending on the research questions and aims. Approaches can be broadly classified in label-free and label-based methods and vary in sample throughput, accuracy and precision of quantification, and effects on spectral complexity, among other factors. Label-free methods quantify peptides based on the intensities of MS1 precursors, MS2 fragments, or both. Different samples are measured sequentially, and relative peptide and protein abundances are compared across runs. In contrast, label-based quantification strategies require labeling with stable isotopes at the protein or peptide level during sample preparation, and allow multiplexed MS analysis of pooled samples. Non-isobaric labeling, such as stable isotope labeling by amino acids in cell culture (SILAC)[99] or dimethyl labeling[240], produces distinct precursor mass shifts that allow quantification of label ratios at MS1 level. Isobaric-labeling methods like tandem mass tags (TMT)[241] or EASI-tag[242] result in precursors that have identical m/z values at the MS1 level, but yield differentiating ions upon fragmentation in MS2 spectra, which are used for quantification.

Many peptides generated in bottom-up proteomics workflows are not unique but shared among multiple proteins. This establishes many-to-many relationships and introduces ambiguities in mapping peptides back to their protein sources. While there are different approaches to dealing with this protein inference problem, common procedures use parsimonious models based on the principle of Occam's razor[243], aiming to identify the minimal set of proteins that can account for all observed peptides[231]. Proteins that are not distinguishable by the identified peptides are combined into protein groups. To limit errors of protein inference, different methods are used to estimate and control the FDR at the protein level[231,244]. Protein group abundances are compared across sample groups using

bioinformatical methods to reveal quantitative differences and evaluate statistical significance, offering comprehensive insights into biological processes[232,245,246].

2. Aims of the thesis

Technological progress has substantially enhanced the tools available for investigating the molecular mechanisms of cell communication. MS-based proteomics, in particular, offers an exceptional platform for dissecting intercellular signaling by comprehensively identifying proteoforms, quantifying their dynamic expression and secretion, capturing their molecular interactions, and profiling phenotypic changes in response (as reviewed in Article 1). Despite these advances, limitations remain, often restricting cell communication research to simplified models that cannot accurately capture important layers of biological complexity and leave fundamental questions unanswered. The overarching goal of my thesis was to deepen our understanding of context-dependent intercellular signaling dynamics and to devise new technical solutions that extend our capabilities in areas where current state-of-the-art methods fall short. Specifically, my work addressed three major aims:

Methionyl-tRNA synthetase (MetRS)-based azidonorleucine (Anl) labeling holds significant promise for cell-selective proteomics applications due to its broad applicability in live tissue. However, its sensitivity and proteome coverage have lagged behind conventional proteomics approaches, severely limiting its potential for discovery and broader utility beyond proof-of-concept studies. A central aim of my thesis was to identify and overcome key challenges of this approach to enable comprehensive cell-selective proteomics in complex biological model systems. Through extensive method development, I increased labeled protein recovery, enrichment specificity, and proteome coverage, substantially expanding the capabilities and scope of this method. Leveraging these gains in sensitivity, I then sought to adapt the workflows for secretomics analyses in heterocellular environments like co-cultures and tissues to facilitate in-depth study of reciprocal intercellular signaling networks (Articles 2 and 3).

I used these newly developed cell-selective proteomic workflows along with established state-of-the-art secretomics methods to investigate cell communication in cancer and the immune system, aiming to enhance our understanding of disease processes and support the development of therapy and diagnostics. Collaborating closely with the Saur group at the Center for Translational Cancer Research (TranslaTUM) in Munich, my research focused on characterizing intercellular signaling in pancreatic ductal adenocarcinoma, one of today's leading causes of cancer-related deaths. Comparative analyses revealed critical differences between the classical epithelial and the highly aggressive

mesenchymal PDAC subtypes, contributing to their urgently needed molecular characterization and providing important insights for novel targeted therapy approaches (Articles 2 and 4). Additionally, I contributed to a group-internal project exploring signaling protein release mechanisms in pyroptosis, a form of programmed cell death with key roles in inflammation (Article 5).

Even for otherwise well-described signaling proteins, interactions with cell surface receptors, co-receptors, and other regulators of signal transduction are often underexplored because they are difficult to study with conventional methods. Proximity labeling (PL) has emerged as a powerful approach for capturing even transient protein interactions under near-native conditions. However, PL interactomics experiments are prone to high false positive rates through co-enrichment of unrelated proteins localized in the same subcellular compartment, necessitating extensive follow-up experiments to validate large numbers of interactor candidates. I aimed to develop PL-based workflows to systematically evaluate extracellular signaling protein interactions at the cell surface and map proteins in the lateral receptor environment. A novel PL analysis strategy, employing scavengers to modulate the labeling radius, enabled the effective differentiation of known interactors and high-confidence candidates from the background, addressing a key challenge in the field (Article 6).

3. Publications and manuscripts

Article 1: Dissecting intercellular signaling with mass spectrometry-based proteomics

Curr. Opin. Cell Biol. 63, 20–30 (2020).

Jonathan J. Swietlik[1#], Ankit Sinha[1,2#], Felix Meissner[1]

[1] Experimental Systems Immunology Laboratory, Max-Planck Institute of Biochemistry, Martinsried, Germany

[2] Institute of Translational Cancer Research and Experimental Cancer Therapy, Klinikum Rechts der Isar, TU München, Munich, Germany

[#] These authors contributed equally to the work.

Modern MS instrumentation, proteomics methods, and software enable the unsupervised detection of thousands of proteins in a single sample within minutes of analysis time. Additionally, the ability of MS to distinguish between proteoforms offers unique insights into molecular mechanisms that regulate protein function. Specialized workflows capitalize on this broad and distinctive analytical scope to dissect intercellular signaling mechanisms and have established MS-based proteomics as a fundamental tool for studying cellular communication.

In this review article, we highlight recent advancements in MS-based proteomics methods that elucidate different layers of intercellular signaling. Our focus is techniques that comprehensively characterize cell-released signaling proteins, signaling proteins and receptors at the cell surface, protein-protein interactions at the cell surface, and methods that resolve cell type-specific signals in heterocellular environments. For each application, we describe leading approaches, highlight their benefits and challenges, and guide the reader through the current landscape of this dynamic field. Methods like proximity labeling, featured as emerging techniques for profiling intercellular signals, have since gained significant impact and popularity. The techniques described here were focal points and crucial enablers for my work in this thesis.

Contribution:

Together, Ankit Sinha, Felix Meissner, and I reviewed the current literature and collaboratively authored the manuscript.

Available online at www.sciencedirect.com

ScienceDirect

Current Opinion in Cell Biology

Dissecting intercellular signaling with mass spectrometry–based proteomics

Jonathan J. Swietlik[1,a], Ankit Sinha[1,2,a] and Felix Meissner[1]

Abstract

Physiological functions depend on a coordinated interplay of numerous different cell types. Proteins serve as major signaling molecules between cells; however, their comprehensive investigation in physiologically relevant settings has remained challenging. Mass spectrometry (MS)–based shotgun proteomics is emerging as a powerful technology for the systematic analysis of protein-mediated intercellular signaling and regulated post-translational modifications. Here, we discuss recent advancements in cell biological, chemical, and biochemical MS-based approaches for the profiling of cellular messengers released by sending cells, receptors expressed on the cell surface, and their interactions. We highlight methods tailored toward the mapping of dynamic signal transduction mechanisms at cellular interfaces and approaches to dissect communication cell specifically in heterocellular systems. Thereby, MS-based proteomics contributes a unique systems biology perspective for the identification of intercellular signaling pathways deregulated in disease.

Addresses

[1] Experimental Systems Immunology Laboratory, Max-Planck Institute of Biochemistry, Martinsried, Germany

[2] Institute of Translational Cancer Research and Experimental Cancer Therapy, Klinikum Rechts der Isar, TU München, Munich, Germany

Corresponding author: Meissner, Felix (meissner@biochem.mpg.de)

[a] These authors contributed equally to this work.

Current Opinion in Cell Biology 2020, 63:20–30

This review comes from a themed issue on **Cell Signalling**

Edited by **Andrea Ablasser** and **Jeremy W. Thorner**

For a complete overview see the Issue and the Editorial

Available online 9 January 2020

https://doi.org/10.1016/j.ceb.2019.12.002

Keywords

Proteomics, Mass spectrometry, Intercellular, Signaling, Cell non-autonomous, Posttranslational modification, PTM, Sender, Receiver, Messenger, Interactions, Heterocellular, Paracrine, Autocrine, Receptor, Ligand, Interaction.

Introduction

Cells exchange information with neighboring cells and the extracellular environment to coordinate physiological processes ranging from tissue development to protective immunity. Intercellular communication relies on various classes of biomolecules, with proteins playing a major role in both transmission and reception of signals. Immune responses are a hallmark example in which motility, differentiation, and fate of numerous cell types are cell non-autonomously controlled by secreted proteins such as cytokines as well as cell surface receptors. As key determinants of complex multicellular behavior, intercellular signaling proteins are the largest target group of Food and Drug Administration–approved drugs [1,2]. Knowledge of the cell- and context-specific utilization of intercellular messenger proteins therefore does not only advance our understanding of metazoan biology but also enables the discovery of disease modifying signaling pathways and targets for drug development.

Secreted and cell surface proteins undergo multiple processing steps determining their cellular localization, structure, and activity [3]. Different proteoforms (all protein molecules arising from a single gene by genetic variation, splicing, and post-translational modifications (PTMs) [4]) can have distinct functions, exemplified by the proteolytic inactivation of CXCL10 or activation of IL-1B cytokines as well as modified signaling of receptors such as the ErbB family of proteins through PTMs such as glycosylation [5–7]. Therefore, direct information at the protein level is crucial for the assessment of protein-mediated intercellular signaling. Antibody-based methods are widely used to quantify proteins, including enzyme-linked immunosorbent assays, cytometric bead arrays, as well as flow and mass cytometry. Although antibodies allow the quantification of defined sets of proteins with high sensitivity and throughput, the availability, cost, and varying specificity of antibodies limit their universal applicability and discovery potential for systems-wide investigations [4,8].

In recent years, MS-based proteomics has emerged as a powerful technology for the unsupervised and comprehensive quantification of proteins. Modern instruments, workflows, and computational analysis platforms enable the identification of thousands of proteins from a single sample in less than an hour, providing the depth and throughput required for systems biology investigations [9,10]. Accordingly, MS-based proteomics has significantly influenced biomedical research by, for example, characterizing proteome dynamics in physiological or

pathological processes [11]. Owing to its ability to detect proteoforms, for example, covalently modified amino acids within a protein's sequence, MS-based proteomics has also become a key discovery tool for PTMs such as phosphorylation [12,13]. While MS-based approaches to study intracellular signal transduction mechanisms have become streamlined and are widely used, intercellular signaling has been less systematically studied because of various technical challenges. These include the low concentration of secreted messengers in typically protein-rich biological matrices, amphiphilic properties of membrane proteins hampering efficient extraction, and frequently weak protein interactions at cellular interfaces.

Recently developed cellular, chemical, and biochemical techniques now make multiple facets of intercellular signaling accessible to systems-level investigations by proteomics. Here, we discuss recent and promising MS-based shotgun proteomics strategies to profile sequential steps of intercellular signal transduction, starting from messaging entities (such as secreted proteins) released by the source cells to receiving entities (such as receptors present on the cell surface) of target cells. We highlight how unique MS-based approaches enable the elucidation of dynamic signal transduction mechanisms at the interface of communicating cells and bidirectional cell-specific signaling in heterocellular systems (Figure 1).

Intercellular signaling proteins in the extracellular space

The entirety of secreted proteins (referred to as the secretome) of a single cell type often consists of hundreds of messengers. Unsupervised and comprehensive characterization of secretomes by MS can reveal the complex dynamics of signals that are transmitted to neighboring or remote cells and enables the discovery of key drivers for cell nonautonomous processes, as well as marker proteins, for example, in cancer. Furthermore, different proteoforms of secreted proteins can be detected, frequently revealing distinct biological activities. However, many signaling proteins such as cytokines fulfill their physiological function at very low concentrations (picogram/ml range). In primary bodyfluids or experimental *in vitro* systems with serum supplements, the MS-based detection of secreted signaling proteins is hampered by the presence of highly abundant proteins of the biological matrix (such as albumin with 35–50 mg/mL in serum), a limitation well known as the dynamic range issue [14]. We highlight selected methods to study intercellular messengers in the extracellular space that circumvent the dynamic range issue, summarized in Table 1.

Resource-intensive biochemical fractionation approaches can improve the detection of lower abundance proteins in a protein-rich biological matrix [15]. However, they are limited by low throughput and impractical for testing multiple biological hypotheses. Instead, the main strategy for comprehensive secretomics analyses *in vitro* relies on decreasing sample complexity by culturing cells for defined time periods in serum-free media. Cell supernatants without serum supplements are harvested and directly processed for shotgun MS, allowing high-throughput analyses of secretomes in multiwell plate formats from only a few hundred thousand cells and enabling the quantification of sometimes more than 50 cytokines [16]. This strategy revealed, for example, previously undescribed roles for MFAP5 in tongue squamous cell carcinoma, EPDR1 as a novel batokine, IL-10 family members in anti-inflammatory feedback loops, and TGF-β family ligands mediating cellular senescence [17–20*].

Because serum depletion can alter cellular physiology, serum-free secretomics experiments require careful optimization of incubation times and/or supplementation of defined growth factors, hormones, and surfactants to minimize starvation artifacts [21]. In case serum starvation is not an option, strategies based on metabolic labeling of proteins with noncanonical, click chemistry compatible amino acids provide promising alternatives. In these experiments, for example, azidohomoalanine (AHA) is added to serum-supplemented medium *in vitro* and incorporated into nascent proteins as a methionine surrogate. AHA-labeled secreted proteins can then be enriched from serum-supplemented cell supernatants using click chemistry. By this means, Eichelbaum *et al.* [22] demonstrated the detection of low abundant secreted cytokines and extensive ectodomain shedding in serum-containing media. However, AHA labeling is usually carried out under methionine depletion to increase incorporation efficiency into cellular proteins, which may alter cellular physiology. Moreover, owing to incomplete protein labeling and biochemical enrichment, millions of cells are required as starting material [23]. Hence, the most suitable strategy should be thoroughly evaluated for each experimental model system, with special regards to tolerance for serum or methionine depletion and cellular starting material.

Maintaining high cell viability is crucial for secretomics experiments, as distinguishing 'truly' secreted proteins from proteins that leaked from dying cells is challenging. Most secreted proteins are processed through the ER–Golgi–dependent secretory pathway, which enables their prediction, for example, based on respective signal sequences by computational tools such as SignalP [24]. Although such strategies are often used as a filter criterion in secretome analyses [20], secretomics is particularly powerful for the discovery of bona fide intercellular signals released through unconventional routes such as cytokines similar to IL-1B, damage-

associated molecular patterns (such as HMGB1), or cell surface receptors (e.g. IL-4Rα) by ectodomain shedding [25,26]. Experimental and analytical strategies, for example, pharmacological or genetic perturbation of cellular protein release pathways and evaluation of proteins leaked from dying cells by osmoprotectants, membrane stabilizing agents [27], or secretome to total proteome correlation further help to define high confidence released proteins, as well as their cellular exit routes [21]. A subgroup of unconventionally released proteins is transported as cargo from the cytoplasm to the extracellular compartment via extracellular vesicles

Figure 1

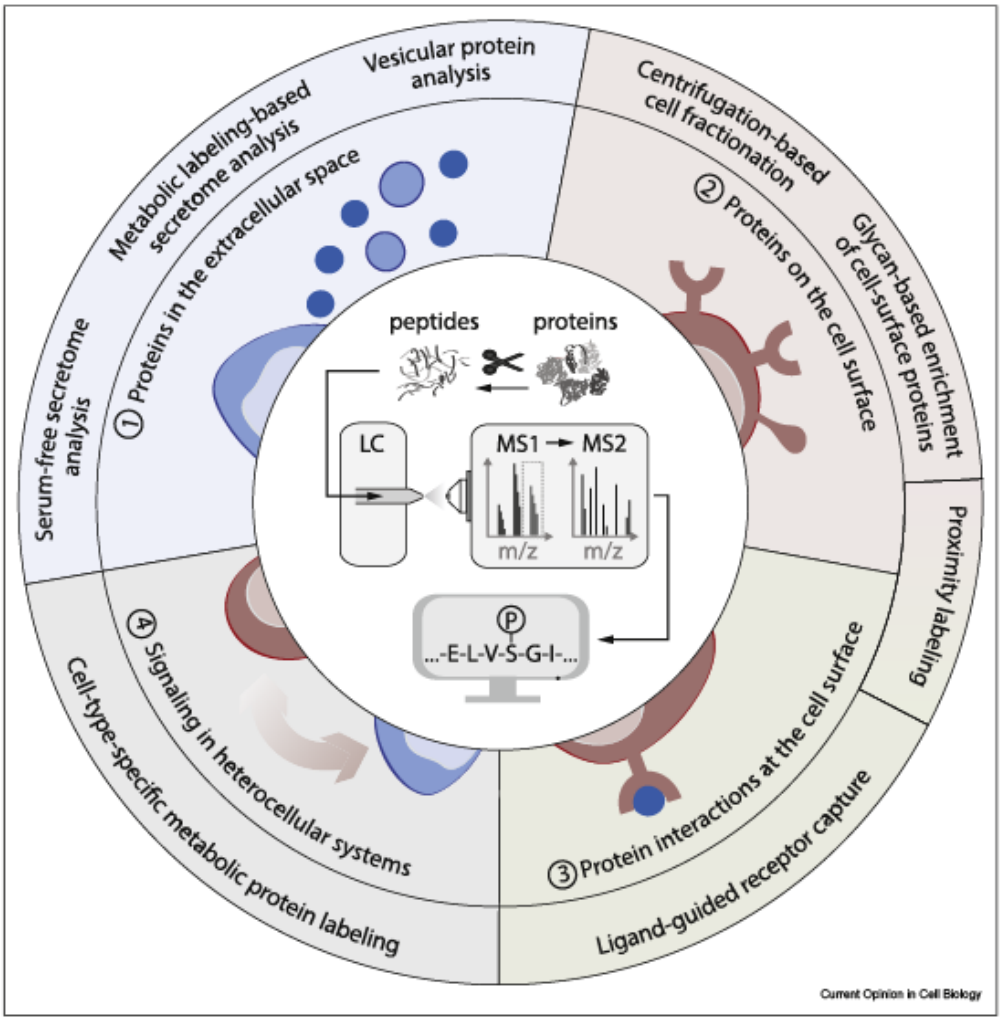

Overview of MS-based proteomics strategies for characterizing various facets of intercellular signaling. Intercellular signaling can be analyzed using distinct cellular and biochemical strategies. This includes the characterization of **(1)** intercellular signaling proteins in the extracellular space, **(2)** intercellular signaling proteins at the cell surface, **(3)** signaling protein interactions, and **(4)** intercellular signaling in heterocellular systems. (Center) For all described approaches, proteins are analyzed by shotgun proteomics. Briefly, proteins are extracted from biological samples and digested into peptides. The peptides are chromatographically separated based on hydrophobicity and analyzed in the mass spectrometer. Peptide intensities and masses, as well as fragmentation patterns are recorded, from which peptide sequences and post-translational modifications are determined. A detailed description of the facets of proteomics workflows is reviewed elsewhere [78]. Modern MS technology can detect stable and abundant post-translationally modified sites of proteins in standard shotgun proteomics experiments [11,12]. Comprehensive PTM analyses, however, require specialized workflows to enrich specific proteins under investigation or low abundant and substoichiometric proteoforms such as glycosylated or proteolytically processed proteins or peptides [79,80]. PTM, post-translational modifications

Table 1

MS-based proteomic strategies for profiling intercellular signaling proteins in the extracellular space.

Strategy	Method	Typically required cell numbers (as reported in references)	Sample preparation throughput	Serum compatibility	Features and caveats	References (PMID)
Serum-free secretome analysis	Serum depletion	~10^5	1–2 day protocol, workflow highly parallelizable in multiwell format, low handling time	No	- Requires optimization of medium supplements and duration to minimize effects of serum starvation - Very high coverage of low abundance signaling proteins	29177865
Metabolic labeling–based secretome analysis	BONCAT (Bioorthogonal noncanonical amino acid tagging)	~10^7	3–4 day protocol with high handling time for concentration of cell supernatants, bead-based enrichment and extensive washing protocol	Yes	- Requires optimization of pulse-labeling duration, AHA concentration and methionine depletion - High coverage of low abundance signaling proteins - Cell type–specific analysis with MetRS*-mediated ANL labeling (26991063) - Covers only proteins synthesized within the labeling period	23000932 30816242
Vesicular protein analysis	Centrifugation-based enrichment, Immunoaffinity enrichment	Typically millions to hundreds of millions, yields vary strongly with cell type and isolation techniques	2–3 day protocol, depending on isolation method, for example, long centrifugation steps can limit throughput	No	- Requires serum starvation or EV depleted serum - Assessment of purity/heterogeneity of EVs, for example, by electron microscopy or nanoparticle tracking analysis - Affinity enrichment requires prior knowledge of specific EV subtype markers	30951670 26194179

EV, extracellular vesicle; AHA, azidohomoalanine; ANL, Azidonorleucine.

(EVs). EVs can be enriched specifically from cellular supernatants or primary bodyfluids by centrifugation or affinity purification, reviewed elsewhere [28,29]. Proteomic analysis of tumor-derived EVs revealed the association of exosomal integrin patterns with metastatic tropism to specific organs or annexin A6 as a potential prometastatic regulator during chemotherapy [30,31].

Intercellular signaling proteins on the cell surface

Plasma membrane–associated proteins act both as ligands and receptors for intercellular signal transduction. Thus, the protein composition of the cellular surface controls messages transmitted via direct cell–cell contacts and defines which signals can be received by the cell. Plasma membrane proteins have relatively low abundance in the cellular proteome and their amphiphilic nature complicates efficient extraction and solubilization [32]. For this reason, specialized enrichment strategies have been developed to facilitate the comprehensive analysis of cell surface proteins by MS-based proteomics, reviewed comprehensively elsewhere [33,34]. Here, we highlight selected methods, summarized in Table 2.

Centrifugation-based methods are commonly used for subcellular fractionation and isolation of plasma membrane proteins. These methods, however, typically suffer from contamination through coisolation of proteins from other compartments [33]. Hence, modern variants assign proteins to all major subcellular compartments including the plasma membrane by their distribution across different centrifugation fractions and thereby facilitate quantitative subcellular mapping of the proteome [35,36].

As most cell surface–associated proteins are glycosylated, glycans can be targeted for affinity-based or chemoselective enrichment [37]. For example, lectins bind glycans and enable the purification and detection of cell surface proteins with simple and high throughput compatible workflows [38]. Alternatively, glycans are mildly oxidized to form aldehydes, which are enriched by covalent capture on a solid phase using hydrazone or oxime ligation [39–41]. Using this strategy, Cogger *et al.* [42] identified novel cell surface marker proteins for pancreatic progenitor cells differentiated from human pluripotent stem cells. As these methods also enrich intracellular glycosylated proteins, Wollscheid *et al.* [41] advanced this principle by developing a cell surface capturing technology with exclusive specificity for surface glycoproteins. Here, glycomoieties are oxidized on intact cells and subsequently modified with affinity probes, preventing intracellular glycoproteins from being captured. This cell surface capturing technology was used to establish a cell surface atlas of 41 human and 31 mouse cell lines comprising 1492 human and 1296 mouse cell surface proteins [43].

Proximity labeling techniques such as APEX [44] and BioID [45], which have been very successfully applied for the investigation of intracellular protein interactions and mapping of proteins in defined intracellular compartments [46], are now emerging as powerful tools to characterize cellular surfaces. In these approaches, proteins are tagged with enzymes that label interacting and neighboring proteins with reactive affinity probes within a short radius. Target proteins can be tagged by genetic fusion or antibody-horseradish peroxidase conjugates [47, 48, 49] to identify functional surface protein clusters or to generate proteomic proximity maps of the cell, including the plasma membrane [50]. Recently, Loh *et al.* [51**] used plasma membrane–horseradish peroxidase fusion proteins in combination with a novel non-membrane permeable affinity probe for exclusive labeling of cell surface proteins on the extracellular side of the membrane. This enabled the profiling of specific synaptic cleft types of primary neurons revealing novel synaptic proteins. Li *et al.* [52**] extended this highly enabling approach for the temporally resolved and cell type–specific mapping of the cell surface proteome of a *Drosophila* neuron subtype *in vivo*.

Signaling protein interactions at the cell surface

Knowledge of biochemical interactions between soluble or membrane-bound signaling proteins and surface receptors is a prerequisite to elucidate signaling pathways between cells. As surface receptors often engage in transient binding events and usually require their physiological membrane environment for full biological activity, interactions on the cell surface are underrepresented in most conventional protein–protein interaction studies [53,54]. Accompanied by advancements in high-throughput screening approaches, such as large-scale screens with reverse transfection microarray technology or genome-scale CRISPR knockout screens as reviewed elsewhere [55], recently developed MS-based proteomics methods facilitate the systematic investigation of extracellular protein interactions. We highlight selected methods, summarized in Table 3.

A specialized family of proteomics methods provides an easily applicable, yet highly efficient procedure for the targeted identification of surface receptors that recognize a given soluble or membrane-bound ligand under near physiological conditions. First, ligands are tagged with specially designed trifunctional capture molecules. Guided by the ligand, the capture molecules covalently bind to target receptors on the surface of living cells and provide a handle for subsequent enrichment and identification by MS. This strategy was originally introduced with TRICEPS, a trifunctional molecule that uses the aforementioned surface glycan oxidation and hydrazone ligation reaction for capturing the receptor [56]. Sobotzki *et al.* [57**] recently developed HATRIC, a

Table 2

MS-based proteomic strategies for profiling intercellular signaling proteins on the cell surface.

Strategy	Method	Scope	Typically required cell numbers (as reported in references)	Enrichment principle	Features and caveats	References (PMID)
Centrifugation-based cell fractionation	Dynamic Organellar Maps, LOPIT-DC (localization of organelle proteins by isotope tagging after differential ultracentrifugation)	Global mapping of proteins to subcellular compartments	~10^7–10^8	Sequential ultracentrifugation of cell lysates for crude enrichment of subcellular fractions	- Computational assignment of proteins to subcellular locations including the plasma membrane according to fractionation profiles - All major cellular compartments analyzed simultaneously	28903049 30659192
Glycan-based enrichment of cell surface proteins	Lectin-based enrichment	Global glycoprotein characterization	~10^6 (or ~ 100 µg digested peptides)	Lectin-mediated capture of glycopeptides from trypsin digested cell lysates or bodyfluids	- Analysis based on PNGaseF eluted formerly N-glycosylated peptides - High throughput compatible workflow - No discrimination between internal or surface glycoproteins - Potential bias from binding selectivities of lectins	20510933
	SPEG (solid phase extraction of glycopeptides)	Global glycoprotein characterization	~10^7	Oxidation of glycans in lysates or bodyfluids and enrichment of oxidized glycoproteins by hydrazide-derivatized resins	- Analysis based on PNGaseF eluted formerly N-glycosylated peptides - No discrimination between internal or surface glycoproteins	12754519 17406594
	CSC (cell surface capture)	Cell surface glycoprotein characterization	~10^8	Oxidation of glycans on the surface of intact cells and derivatisation of oxidized glycoproteins with hydrazide enrichment probes	- Analysis based on PNGaseF eluted formerly N-glycosylated peptides of cell surface proteins - Very high specificity, almost exclusive identification of bona fide membrane proteins	19349973

(*continued on next page*)

Current Opinion in Cell Biology 2020, 63:20–30

Table 2. (*continued*)

Strategy	Method	Scope	Typically required cell numbers (as reported in references)	Enrichment principle	Features and caveats	References (PMID)
Proximity labeling	HRP fusion protein-mediated proximity labeling	Characterization of colocalized surface proteins and interactors	~10^7	Genetic fusion of HRP to extracellular terminus of bait membrane proteins; labeling of neighboring proteins with affinity probes activated by HRP in presence of H_2O_2	- Demonstrated to be applicable for global surface proteome or functional membrane subdomain characterization - Enables cell type–specific analysis *in vivo* - Membrane impermeable affinity probe decreases background - Short labeling duration (1 min) provides high temporal resolution	27565350
	HRP antibody–mediated proximity labeling	Characterization of colocalized surface proteins and interactors	~10^7	Targeting of bait membrane proteins with antibody HRP conjugates; labeling of neighboring proteins with affinity probes activated by HRP in presence of H_2O_2	- Depends on availability and specificity of primary antibody - Applicable for fixed tissues or living cells - Short labeling duration (minutes) provides high temporal resolution	25829300 22106087 29256494
	PUP-IT (pupylation-based interaction tagging)	Characterization of colocalized surface proteins and interactors	~10^7–10^8	Genetic fusion of PafA to bait membrane proteins; coexpression with bio-PUP(E), a small, biotinylated protein that can be ligated by PafA to lysine residue of nearby proteins	- Very small labeling radius, since activated PUP does not diffuse from the enzyme - Requires long labeling durations (≥24 h)	30104635

HRP, horseradish peroxidase.

www.sciencedirect.com

Table 3

MS-based proteomic strategies for ligand-guided receptor capture.

Strategy	Method	Typically required cell numbers (as reported in references)	Enrichment principle	Features and caveats	References (PMID)
Trifunctional capture molecules	TRICEPS	~5×10^7	NHS-mediated tagging of ligand with TRICEPS, oxidation of glycans present the surface of target cells and ligand-guided capture of target receptors by hydrazone ligation	- Capture reaction at pH 6.5, which can reduce ligand–receptor affinity - Peptide-centric workflow (quantification exclusively based on glycosylated prey peptide)	22983091
	HATRIC	~$5–20 \times 10^6$ recommended, but down to 1 million cells	NHS-mediated tagging of ligand with HATRIC, oxidation of glycans present the surface of target cells and ligand-guided capture of target receptors by catalyzed hydrazone ligation	- Capture reaction at physiological pH - Protein-centric workflow (quantification based on whole prey protein) - Click chemistry enrichment prevents streptavidin peptide contamination upon on bead digestion	29666374
	Photoaffinity probes	~10^8	NHS-mediated tagging of ligand with trifunctional photoaffinity probe, ligand-guided diazirine-mediated capture of target receptors on cells upon irradiation with UV light	- Glycan independent capture - High number of potential side reactions, for example, self-reaction of the probe–ligand complex that can reduce sensitivity	30514721

refined version of the workflow and capture molecule with broader applicability and increased sensitivity. Since TRICEPS and HATRIC require the presence and accessibility of oxidized glycans on target receptors, glycan-independent capture molecules based on photochemical cross-linking have been developed. However, their applicability and discovery potential is not well explored yet [58].

Alternatively, proximity labeling methods introduced previously show great potential for detecting transient and weak interactions on the cell surface and can also be applied for the identification of extracellular ligand–receptor interactions. This was demonstrated, for example, by Liu *et al.* [59*], who showed specific IL2-based proximity labeling of IL2R with pupylation-based interaction tagging, a novel approach based on a bacterial ubiquitination-like system. Proximity labeling concepts open exciting avenues for investigations of intercellular signal propagation by the characterization of dynamic receptor signaling complex compositions in physiologically relevant settings [60].

Communicating cells are often inferred *in silico* from the cell type–specific usage of respective soluble or membrane-bound ligands or receptors. Although mass cytometry and RNA sequencing studies establish intercellular communication networks at the single-cell level, for example, of tissue resident cells [61–64], MS-based strategies provide comprehensive and protein-based intercellular signaling networks of cell populations. The latter is exemplified by Rieckmann *et al.* [65*] who revealed understudied signaling proteins and channels between immune cells. Data gained from comprehensive proteomic mapping of intercellular protein interactions as described above will provide in situ evidences on physiological or pathophysiological communication channels between cell types. To add spatial resolution, for example, in tissue microenvironments, laser capture dissected cells in tissues can be profiled by proteomics [66].

Intercellular signaling in heterocellular systems

Intercellular signaling is often highly interactive, with cells reciprocally regulating each other's phenotypes in heterocellular systems. As most techniques cannot resolve cell type–specific signals in cellular mixtures, these aspects of intercellular signaling are often disregarded, despite their importance [67]. MS-based approaches are particularly powerful to deconvolute interdependencies of cellular phenotypes by metabolic 'barcoding' of proteins from distinct cells with stable isotopes [68]. This is demonstrated, for example, by Jørgensen *et al.* [69] who show that EphR–ephrin signaling mutually alters cellular physiology of directly interacting cells. A variation of this concept enables the analysis of protein transfer between cells by trans-stable isotope labeling with amino acids in cell culture (SILAC) [70]. Cell type–specific labeling with amino acid precursors (CTAP) expands this concept to continuous coculture experiments by the cell type–specific expression of enzymes that facilitate isotopic 'barcoding' of proteomes [71,72]. Using CTAP, Tape *et al.* [73] showed the reciprocal signaling between cancer cells and fibroblasts. Moreover, engineered tRNA Ssynthetases allow cell type–specific incorporation of click chemistry compatible noncanonical amino acids [74] enabling cell type–specific proteome enrichments and analyses *in vivo*. By this means, Alvarez-Castelao *et al.* [75**] identified differential regulation of more than 200 proteins in hippocampal excitatory neurons.

Outlook

MS-based proteomics provides powerful discovery tools for all levels of intercellular signaling. It enables the characterization of cell and context-specific secretory programs, identification of unexplored extracellular protein functions, for example, of damage-associated molecular patterns or moonlighting proteins, as well as their corresponding receptors or receptor-associated proteins. In addition, it provides the unique advantage to detect proteoforms and specific extracellular PTMs. Novel developments enable the spatial and dynamic *in situ* proteome mapping of signaling complexes in membranes and at cellular interfaces between neighboring cells. In combination with methods that allow cell type–resolved proteomic analysis in heterocellular mixtures, key regulatory processes in the extracellular space can be studied in physiological relevant systems such as organoids or, for example, in tissue microenvironments *in vivo*. Like single-cell sequencing methods resolve intratissue heterogeneity on the nucleic acid level, anticipated MS technology developments will enable the analyses of intercellular signaling between rare primary cell types or even at the single-cell level in the future [76,77].

Funding support

The work is supported by the Max Planck Society for the Advancement of Science, German Research Foundation SFB1335 and European Molecular Biology Organization (EMBO) Long Term Fellowship (ALTF 539–2018) to AS.

Conflict of interest statement

Nothing declared.

References

Papers of particular interest, published within the period of review, have been highlighted as:

- * of special interest
- ** of outstanding interest

1. Law V, *et al.*: **DrugBank 4.0: shedding new light on drug metabolism**. *Nucleic Acids Res* 2014, 42:D1091–D1097.

2. Uhlen M, *et al.*: **Proteomics. Tissue-based map of the human proteome**. *Science* 2015, **347**:1260419.

3. Lippincott-Schwartz J, Roberts TH, Hirschberg K: **Secretory protein trafficking and organelle dynamics in living cells**. *Annu Rev Cell Dev Biol* 2000, **16**:557–589.

4. Aebersold R, *et al.*: **How many human proteoforms are there?** *Nat Chem Biol* 2018, **14**:206–214.

5. Afonina IS, *et al.*: **Proteolytic processing of interleukin-1 family cytokines: variations on a common theme**. *Immunity* 2015, **42**: 991–1004.

6. Bronger H, *et al.*: **Proteolytic chemokine cleavage as a regulator of lymphocytic infiltration in solid tumors**. *Cancer Metastasis Rev* 2019, **38**:417–430.

7. Ferreira IG, *et al.*: **Glycosylation as a main regulator of growth and death factor receptors signaling**. *Int J Mol Sci* 2018, **19**: 580.

8. Edwards AM, *et al.*: **Too many roads not taken**. *Nature* 2011, **470**:163–165.

9. Kelstrup CD, *et al.*: **Performance evaluation of the Q exactive HF-X for shotgun proteomics**. *J Proteome Res* 2018, **17**: 727–738.

10. Riley NM, Hebert AS, Coon JJ: **Proteomics moves into the fast lane**. *Cell Sys* 2016, **2**:142–143.

11. Aebersold R, Mann M: **Mass-spectrometric exploration of proteome structure and function**. *Nature* 2016, **537**:347–355.

12. Larance M, Lamond AI: **Multidimensional proteomics for cell biology**. *Nat Rev Mol Cell Biol* 2015, **16**:269–280.

13. Humphrey SJ, *et al.*: **High-throughput and high-sensitivity phosphoproteomics with the EasyPhos platform**. *Nat Protoc* 2018, **13**:1897–1916.

14. Hortin GL, Sviridov D: **The dynamic range problem in the analysis of the plasma proteome**. *J Proteom* 2010, **73**:629–636.

15. Dey KK, *et al.*: **Deep undepleted human serum proteome profiling toward biomarker discovery for Alzheimer's disease**. *Clin Proteonomics* 2019, **16**:16.

16. Anderson NL, Anderson NG: **The human plasma proteome: history, character, and diagnostic prospects**. *Mol Cell Proteom* 2002, **1**:845–867.

17. Principe S, *et al.*: **Proteomic analysis of cancer-associated fibroblasts reveals a paracrine role for MFAP5 in human oral tongue squamous cell carcinoma**. *J Proteome Res* 2018, **17**: 2045–2059.

18. Acosta JC, *et al.*: **A complex secretory program orchestrated by the inflammasome controls paracrine senescence**. *Nat Cell Biol* 2013, **15**:978–990.

19. Meissner F, *et al.*: **Direct proteomic quantification of the secretome of activated immune cells**. *Science* 2013, **340**: 475–478.

20. * Deshmukh AS, *et al.*: **Proteomics-based comparative mapping of the secretomes of human Brown and white adipocytes reveals EPDR1 as a novel batokine**. *Cell Metabol* 2019, **30**: 963–975 e7.
comparatively analysed the secretomes of human brown and white adipocytes and discovered novel candidate batokines including EPDR1.

21. Frauenstein A, Meissner F: **Quantitative proteomics of secreted proteins**. *Methods Mol Biol* 2018, **1714**:215–227.

22. Eichelbaum K, *et al.*: **Selective enrichment of newly synthesized proteins for quantitative secretome analysis**. *Nat Biotechnol* 2012, **30**:984–990.

23. Shin J, *et al.*: **Comparative analysis of differentially secreted proteins in serum-free and serum-containing media by using BONCAT and pulsed SILAC**. *Sci Rep* 2019, **9**:3096.

24. Almagro Armenteros JJ, *et al.*: **SignalP 5.0 improves signal peptide predictions using deep neural networks**. *Nat Biotechnol* 2019, **37**:420–423.

25. Rabouille C: **Pathways of unconventional protein secretion**. *Trends Cell Biol* 2017, **27**:230–240.

26. Lichtenthaler SF, Lemberg MK, Fluhrer R: **Proteolytic ectodomain shedding of membrane proteins in mammals-hardware, concepts, and recent developments**. *EMBO J* 2018, **37**. art. no. e99456.

27. Chan AH, Schroder K: **Inflammasome signaling and regulation of interleukin-1 family cytokines**. *J Exp Med* 6 January 2020, **217**:e20190314.

28. Jeppesen DK, *et al.*: **Reassessment of exosome composition**. *Cell* 2019, **177**:428–445 e18.

29. * Lobb RJ, *et al.*: **Optimized exosome isolation protocol for cell culture supernatant and human plasma**. *J Extracell Vesicles* 2015, **4**:27031.
discovered pro-metastatic chemotherapy-elicited extracellular vesicles derived from primary tumors and identified annexin A6 as a driver of pre-metastatic niche formation.

30. Hoshino A, *et al.*: **Tumour exosome integrins determine organotropic metastasis**. *Nature* 2015, **527**:329–335.

31. Keklikoglou I, *et al.*: **Chemotherapy elicits pro-metastatic extracellular vesicles in breast cancer models**. *Nat Cell Biol* 2019, **21**:190–202.

32. Vuckovic D, *et al.*: **Membrane proteomics by high performance liquid chromatography-tandem mass spectrometry: analytical approaches and challenges**. *Proteomics* 2013, **13**: 404–423.

33. Li Y, Qin H, Ye M: **An overview on enrichment methods for cell surface proteome profiling**. *J Sep Sci* 2019:1–21.

34. Kuhlmann L, *et al.*: **Cell-surface proteomics for the identification of novel therapeutic targets in cancer**. *Expert Rev Proteomics* 2018, **15**:259–275.

35. Geladaki A, *et al.*: **Combining LOPIT with differential ultracentrifugation for high-resolution spatial proteomics**. *Nat Commun* 2019, **10**:331.

36. Itzhak DN, *et al.*: **A mass spectrometry-based approach for mapping protein subcellular localization reveals the spatial proteome of mouse primary neurons**. *Cell Rep* 2017, **20**: 2706–2718.

37. Zhu R, *et al.*: **Glycoprotein enrichment analytical techniques: advantages and disadvantages**. *Methods Enzymol* 2017, **585**: 397–429.

38. Zielinska DF, *et al.*: **Precision mapping of an in vivo N-glycoproteome reveals rigid topological and sequence constraints**. *Cell* 2010, **141**:897–907.

39. Kolmel DK, Kool ET: **Oximes and hydrazones in bioconjugation: mechanism and catalysis**. *Chem Rev* 2017, **117**: 10358–10376.

40. Zhang H, *et al.*: **Identification and quantification of N-linked glycoproteins using hydrazide chemistry, stable isotope labeling and mass spectrometry**. *Nat Biotechnol* 2003, **21**: 660–666.

41. Wollscheid B, *et al.*: **Mass-spectrometric identification and relative quantification of N-linked cell surface glycoproteins**. *Nat Biotechnol* 2009, **27**:378–386.

42. Cogger KF, *et al.*: **Glycoprotein 2 is a specific cell surface marker of human pancreatic progenitors**. *Nat Commun* 2017, **8**:331.

43. Bausch-Fluck D, *et al.*: **A mass spectrometric-derived cell surface protein atlas**. *PLoS One* 2015, **10**. art. no. e0121314.

44. Rhee HW, *et al.*: **Proteomic mapping of mitochondria in living cells via spatially restricted enzymatic tagging**. *Science* 2013, **339**:1328–1331.

45. Roux KJ, *et al.*: **A promiscuous biotin ligase fusion protein identifies proximal and interacting proteins in mammalian cells**. *J Cell Biol* 2012 Mar 19, **196**:801–810.

46. Kim DI, Roux KJ: **Filling the void: proximity-based labeling of proteins in living cells**. *Trends Cell Biol* 2016, **26**:804–817.

50. Go CD, *et al.*: **A proximity biotinylation map of a human cell.** *bioRxiv* 2019.

47. Jiang S, *et al.*: **A proteomics approach to the cell-surface interactome using the enzyme-mediated activation of radical sources reaction.** *Proteomics* 2012, **12**:54–62.

48. Rees JS, *et al.*: **Selective proteomic proximity labeling assay using tyramide (SPPLAT): a quantitative method for the proteomic analysis of localized membrane-bound protein clusters.** *Curr Protein Pept Sci* 2015, **80**. 19 27 1-18.

49. Bar DZ, *et al.*: **Biotinylation by antibody recognition-a method for proximity labeling.** *Nat Methods* 2018, **15**:127–133.

51. ** Loh KH, *et al.*: **Proteomic analysis of unbounded cellular compartments: synaptic clefts.** *Cell* 2016, **166**:1295–1307 e21.
mapped proteins of synaptic clefts using spatially restricted HRP-mediated proximity labeling on the cell surface of living neurons and discovered novel synaptic protein candidates.

52. ** Li J, *et al.*: **Cell-surface proteomic profiling in the fly brain uncovers new wiring regulators.** *bioRxiv* 2019.
developed a cell-type specific proximity labeling approach to profile cell-surface proteomes *in vivo* and monitored the characteristic changes of the projection neuron surface proteome during maturation in *Drosophila*.

53. Huttlin EL, *et al.*: **The BioPlex network: a systematic exploration of the human interactome.** *Cell* 2015, **162**:425–440.

54. Wright GJ: **Signal initiation in biological systems: the properties and detection of transient extracellular protein interactions.** *Mol Biosyst* 2009, **5**:1405–1412.

55. Wood L, Wright GJ: **Approaches to identify extracellular receptor-ligand interactions.** *Curr Opin Struct Biol* 2019, **56**: 28–36.

56. Frei AP, *et al.*: **Direct identification of ligand-receptor interactions on living cells and tissues.** *Nat Biotechnol* 2012, **30**: 997–1001.

57. ** Sobotzki N, *et al.*: **HATRIC-based identification of receptors for orphan ligands.** *Nat Commun* 2018, **9**:1519.
introduce HATRIC, a trifunctional molecule that is used for the identification of target receptors for orphan ligands on living cells. Compared to previous generations of this technology, HATRIC offers click-chemistry based enrichment and receptor capture at physiological pH as well as a protein-centric workflow.

58. Muskens FM, *et al.*: **Design, synthesis, and evaluation of a diazirine photoaffinity probe for ligand-based receptor capture targeting G protein-coupled receptors.** *Mol Pharmacol* 2019, **95**:196–209.

59. * Liu Q, *et al.*: **A proximity-tagging system to identify membrane protein-protein interactions.** *Nat Methods* 2018, **15**:715–722.
developed pupylation-based interaction tagging (PUP-IT), a novel proximity labeling strategy for the identification of membrane protein interactions.

60. Bausch-Fluck D, Milani ES, Wollscheid B: **Surfaceome nanoscale organization and extracellular interaction networks.** *Curr Opin Chem Biol* 2019, **48**:26–33.

61. Vento-Tormo R, *et al.*: **Single-cell reconstruction of the early maternal-fetal interface in humans.** *Nature* 2018, **563**:347–353.

62. Cohen M, *et al.*: **Lung single-cell signaling interaction map reveals basophil role in macrophage imprinting.** *Cell* 2018, **175**:1031–1044. e18.

63. Goltsev Y, *et al.*: **Deep profiling of mouse splenic architecture with CODEX multiplexed imaging.** *Cell* 2018, **174**:968–981. e15.

64. Schapiro D, *et al.*: **histoCAT: analysis of cell phenotypes and interactions in multiplex image cytometry data.** *Nat Methods* 2017, **14**:873–876.

65. * Rieckmann JC, *et al.*: **Social network architecture of human immune cells unveiled by quantitative proteomics.** *Nat Immunol* 2017, **18**:583–593.
established an experimental and computational framework to map intercellular signaling networks based on ligand-receptor and receptor–receptor interactions, and provide a healthy state reference for the identification of intercellular immune signals associated with pathology.

66. Coscia F, *et al.*: **A streamlined mass spectrometry-based proteomics workflow for large scale FFPE tissue analysis.** *bioRxiv* 2019:779009.

67. Tape CJ: **Systems biology analysis of heterocellular signaling.** *Trends Biotechnol* 2016, **34**:627–637.

68. Terzi F, Cambridge S: **An overview of advanced SILAC-labeling strategies for quantitative proteomics.** *Methods Enzymol* 2017, **585**:29–47.

69. Jorgensen C, *et al.*: **Cell-specific information processing in segregating populations of Eph receptor ephrin-expressing cells.** *Science* 2009, **326**:1502–1509.

70. Rechavi O, *et al.*: **Trans-SILAC: sorting out the non-cell-autonomous proteome.** *Nat Methods* 2010, **7**:923–927.

71. Gauthier NP, *et al.*: **Cell-selective labeling using amino acid precursors for proteomic studies of multicellular environments.** *Nat Methods* 2013, **10**:768–773.

72. Tape CJ, *et al.*: **Cell-specific labeling enzymes for analysis of cell-cell communication in continuous co-culture.** *Mol Cell Proteom* 2014, **13**:1866–1876.

73. Tape CJ, *et al.*: **Oncogenic KRAS regulates tumor cell signaling via stromal reciprocation.** *Cell* 2016, **165**:910–920.

74. Mahdavi A, *et al.*: **Engineered aminoacyl-tRNA synthetase for cell-selective analysis of mammalian protein synthesis.** *J Am Chem Soc* 2016, **138**:4278–4281.

75. ** Alvarez-Castelao B, *et al.*: **Cell-type-specific metabolic labeling of nascent proteomes in vivo.** *Nat Biotechnol* 2017, **35**: 1196–1201.
developed a transgenic mouse line with inducible cell-type specific expression of mutant MetRS and demonstrate MS-based analysis of specific neuronal subtype proteomes after *in vivo* labeling with azidonorleucine.

76. Marx V: **A dream of single-cell proteomics.** *Nat Methods* 2019, **16**:809–812.

77. Specht H, Slavov N: **Transformative opportunities for single-cell proteomics.** *J Proteome Res* 2018, **17**:2565–2571.

78. Cox J, Mann M: **Quantitative, high-resolution proteomics for data-driven systems biology.** *Annu Rev Biochem* 2011, **80**: 273–299.

79. Ke M, *et al.*: **Identification, quantification, and site localization of protein posttranslational modifications via mass spectrometry-based proteomics.** *Adv Exp Med Biol* 2016, **919**: 345–382.

80. Yang Y, Franc V, Heck AJR, Glycoproteomics: **A balance between high-throughput and in-depth analysis.** *Trends Biotechnol* 2017, **35**:598–609.

Article 2: Cell-selective proteomics segregates pancreatic cancer subtypes by extracellular proteins in tumors and circulation

Nat Commun 14, 2642 (2023)

Jonathan J. Swietlik[1#], Stefanie Bärthel[2,3,4#], Chiara Falcomatà[2,3,4#], Diana Fink[5], Ankit Sinha[6], Jingyuan Cheng[1], Stefan Ebner[5], Peter Landgraf[7], Daniela C. Dieterich[7,8], Henrik Daub[9], Dieter Saur[2,3,4], Felix Meissner[1,5]

[1] Experimental Systems Immunology, Max Planck Institute of Biochemistry, Martinsried, Germany

[2] Division of Translational Cancer Research, German Cancer Research Center and German Cancer Consortium, Heidelberg, Germany

[3] Chair of Translational Cancer Research and Institute of Experimental Cancer Therapy, University Hospital Rechts der Isar, School of Medicine, Technical University of Munich, Munich, Germany

[4] Center for Translational Cancer Research (TranslaTUM), School of Medicine, Technical University of Munich, Munich, Germany

[5] Institute of Innate Immunity, Department of Systems Immunology and Proteomics, Medical Faculty, University of Bonn, Bonn, Germany

[6] Department of Proteomics and Signal Transduction, Max Planck Institute of Biochemistry, Martinsried, Germany

[7] Institute for Pharmacology and Toxicology, Otto-von-Guericke-University Magdeburg, Magdeburg, Germany

[8] Center for Behavioral Brain Sciences, Magdeburg, Germany

[9] NEOsphere Biotechnologies GmbH, Martinsried, Germany

[#] These authors contributed equally to the work.

Non-canonical amino acid labeling techniques hold significant promise for the detailed and accurate analysis of cell states and interactions in heterocellular environments like tissues. Specifically, incorporating azidonorleucine (Anl) via a modified methionyl tRNA-synthetase (MetRS*) demonstrates remarkable specificity and broad compatibility with animal models, with minimal side effects under typical labeling regimens. Anl-labeled proteins synthesized by MetRS*-expressing cells can be enriched from complex backgrounds through bioorthogonal azide-alkyne cycloaddition, commonly referred to as “click chemistry”. Chemical protein separation for cell-selective analyses offers unique advantages over conventional cell sorting techniques: By allowing samples to be snap-frozen and lysed in bulk, this approach avoids sorting-related artifacts and better preserves sensitive cell types. Proteins synthesized during labeling pulses can be

distinguished from pre-existing ones. Crucially, non-canonical amino acid labeling also allows extracellular proteins to be traced back to their cellular origin. However, previous studies that combined Anl-labeling and enrichment with MS-based proteomics have yielded low proteome coverage, limiting the approach to simple experimental designs and restricting the information gained primarily to highly abundant proteins.

We were eager to adapt this technology to gain the first cell-selective *in vivo* secretomics insights in mouse models. Yet, despite significant affords, we initially failed to obtain convincing data, even from large numbers of cells cultured and labeled under favorable conditions *in vitro*. Consequently, we set out to thoroughly evaluate key workflow steps and identified critical enhancements, particularly around the click reaction, that significantly increased Anl-protein recovery and enrichment specificity. This enabled the development of robust methods for the in-depth characterization of cell-selective proteins, more than doubling the proteomic coverage of previous studies. For the first time, it also facilitated comprehensive, cell-selective analysis of secreted intercellular signaling proteins in the extracellular space *in vivo*.

Encouraged by the new opportunities this technology provides, we started a tight collaboration with the Saur group at the translaTUM in Munich to explore how interactions between cancer cells and stromal cells shape pancreatic ductal adenocarcinoma (PDAC) phenotypes. Historically, studies of PDAC have largely overlooked the vast heterogeneity of this complex disease, limited by the lack of technologies that allow cell-selective analyses, and model systems that accurately reflect distinct PDAC subtypes. Recently, the Saur group has revealed a critical role of mutant KRAS allelic imbalance in driving the mesenchymal PDAC subtype[247], characterized by a unique stromal composition[248], particularly high lethality, and resistance to current forms of therapies, highlighting a significant unmet clinical need.

Here, we used azidonorleucine labeling-based cell-selective proteomics to compare intercellular crosstalk between models of classical epithelial and highly aggressive mesenchymal PDAC. We identified differences in cancer cell-released immunomodulatory signaling proteins and linked these to distinct tumor immune cell infiltration patterns. Moreover, we offer novel insights into the extracellular matrix (ECM) in PDAC tumors, which has long been recognized as a crucial factor for tumor progression and therapy response. While early studies have shown the dualistic roles of ECM components, recent research demonstrated that matrix proteins explicitly derived from cancer cells, as opposed to those from stromal cells, are associated with poor prognosis and may

represent promising targets for drug development[249-251]. Our approach offers the first comprehensive characterization of cancer cell- and PDAC subtype-specific tumor ECM proteomes in fully immunocompetent mice. We discovered distinct expression patterns of matrix and matrix-associated proteins across PDAC subtypes. This includes strongly elevated secretion of EMT-associated proteins like fibrillar collagens and lysyl oxidases by the mesenchymal subtype, which have been linked to the promotion of metastasis and pre-metastatic niche formation. Notably, we captured over 1600 cancer cell-derived proteins in the serum of tumor-bearing mice, underlining the technology's potential for studying cell communication across large distances, as well as for identifying disease biomarkers and novel therapeutic targets.

Contribution:

I designed and conducted experiments, with the exception of mouse breeding, cell implantations and mouse treatment, FACS analyses, and the initial characterization of PDAC cell lines. I analysed and visualised data for all figures except Figure 4a. Felix Meissner and I co-wrote the manuscript, with contributions from Dieter Saur, Stefanie Bärthel, and Chiara Falcomatà.

nature communications

Article

https://doi.org/10.1038/s41467-023-38171-8

Cell-selective proteomics segregates pancreatic cancer subtypes by extracellular proteins in tumors and circulation

Received: 6 August 2022

Accepted: 14 April 2023

Published online: 08 May 2023

Check for updates

Jonathan J. Swietlik[1,10], Stefanie Bärthel[2,3,4,10], Chiara Falcomatà[2,3,4,10], Diana Fink[5], Ankit Sinha[6], Jingyuan Cheng[1], Stefan Ebner[5], Peter Landgraf[7], Daniela C. Dieterich[7,8], Henrik Daub[9], Dieter Saur[2,3,4] ✉ & Felix Meissner[1,5] ✉

Cell-selective proteomics is a powerful emerging concept to study heterocellular processes in tissues. However, its high potential to identify non-cell-autonomous disease mechanisms and biomarkers has been hindered by low proteome coverage. Here, we address this limitation and devise a comprehensive azidonorleucine labeling, click chemistry enrichment, and mass spectrometry-based proteomics and secretomics strategy to dissect aberrant signals in pancreatic ductal adenocarcinoma (PDAC). Our in-depth co-culture and in vivo analyses cover more than 10,000 cancer cell-derived proteins and reveal systematic differences between molecular PDAC subtypes. Secreted proteins, such as chemokines and EMT-promoting matrisome proteins, associated with distinct macrophage polarization and tumor stromal composition, differentiate classical and mesenchymal PDAC. Intriguingly, more than 1,600 cancer cell-derived proteins including cytokines and pre-metastatic niche formation-associated factors in mouse serum reflect tumor activity in circulation. Our findings highlight how cell-selective proteomics can accelerate the discovery of diagnostic markers and therapeutic targets in cancer.

Cells in multicellular organisms adapt their phenotypes and function by crosstalk with other cell types. Short- and long-ranged intercellular signals are an integral part of organismal homeostasis and, when altered, drive the pathogenesis of diverse diseases. For example, in cancer, vivid interactions between transformed cells and non-transformed stromal cells promote or inhibit tumor development, metastasis, and the efficacy of drugs.

A rising incidence and high lethality make pancreatic ductal adenocarcinoma (PDAC) one of the leading causes of cancer-related deaths[1]. Since PDAC is typically discovered in advanced stages and refractory to most treatment modalities, there is a pressing need for more effective therapy and biomarkers that allow early detection. However, hallmark features of PDAC, such as a dense and fibrotic stroma, an immunosuppressive tumor microenvironment (TME), and often low neoplastic cellularity, exacerbate its molecular characterization and therapy development[2,3]. Based on the transcriptional profile and pathological features, PDAC is stratified into two major molecular subtypes[4]. Classical PDAC is characterized by a well-

[1]Experimental Systems Immunology, Max Planck Institute of Biochemistry, Martinsried, Germany. [2]Division of Translational Cancer Research, German Cancer Research Center and German Cancer Consortium, Heidelberg, Germany. [3]Chair of Translational Cancer Research and Institute of Experimental Cancer Therapy, University Hospital Rechts der Isar, School of Medicine, Technical University of Munich, Munich, Germany. [4]Center for Translational Cancer Research (TranslaTUM), School of Medicine, Technical University of Munich, Munich, Germany. [5]Institute of Innate Immunity, Department of Systems Immunology and Proteomics, Medical Faculty, University of Bonn, Bonn, Germany. [6]Department of Proteomics and Signal Transduction, Max Planck Institute of Biochemistry, Martinsried, Germany. [7]Institute for Pharmacology and Toxicology, Otto-von-Guericke-University Magdeburg, Magdeburg, Germany. [8]Center for Behavioral Brain Sciences, Magdeburg, Germany. [9]NEOsphere Biotechnologies GmbH, Martinsried, Germany. [10]These authors contributed equally: Jonathan J. Swietlik, Stefanie Bärthel, Chiara Falcomatà. ✉e-mail: dieter.saur@tum.de; felix.meissner@uni-bonn.de

differentiated histopathology and epithelial gene expression signature. In contrast, mesenchymal (basal-like) PDAC shows an undifferentiated, non-glandular histology, a mesenchymal gene expression profile, and is associated with a poor prognosis and high resistance to standard-of-care chemotherapy compared to the classical subtype[5–9]. Despite the substantial clinicopathological differences between the two PDAC subtypes, the underlying differences in the intercellular signaling of cancer cells with their TME have not been studied systematically so far.

Important insights into tumor cell composition and phenotype have been gained by systems-wide transcriptional approaches. However, the correlation between mRNA and protein copy numbers can vary widely[10,11], especially for proteins with roles in intercellular crosstalk[12,13]. Therefore, systems-wide and unbiased tools for comprehensive quantitative protein analyses can provide unique perspectives on the context-dependent crosstalk of cancer cells with their microenvironment[14]. Mass spectrometry (MS)-based proteomics is today's gold standard for high throughput protein analysis and has significantly improved our understanding of cancer pathogenesis[15–18]. The combination of proteomics with cell-selective metabolic protein labeling strategies promises to resolve context-dependent cell behavior and interaction in complex heterocellular systems like tumors. One of the emerging methods uses the specially engineered methionyl-tRNA-synthetase^{L274G} (MetRS*), which enables the time-controlled and cell-specific introduction of the non-canonical amino acid azidonorleucine (Anl) into proteomes[19–21]. Azide-alkyne click chemistry allows the subsequent extraction of MetRS*-expressing cell-derived proteins from cell mixtures. Successful application in living

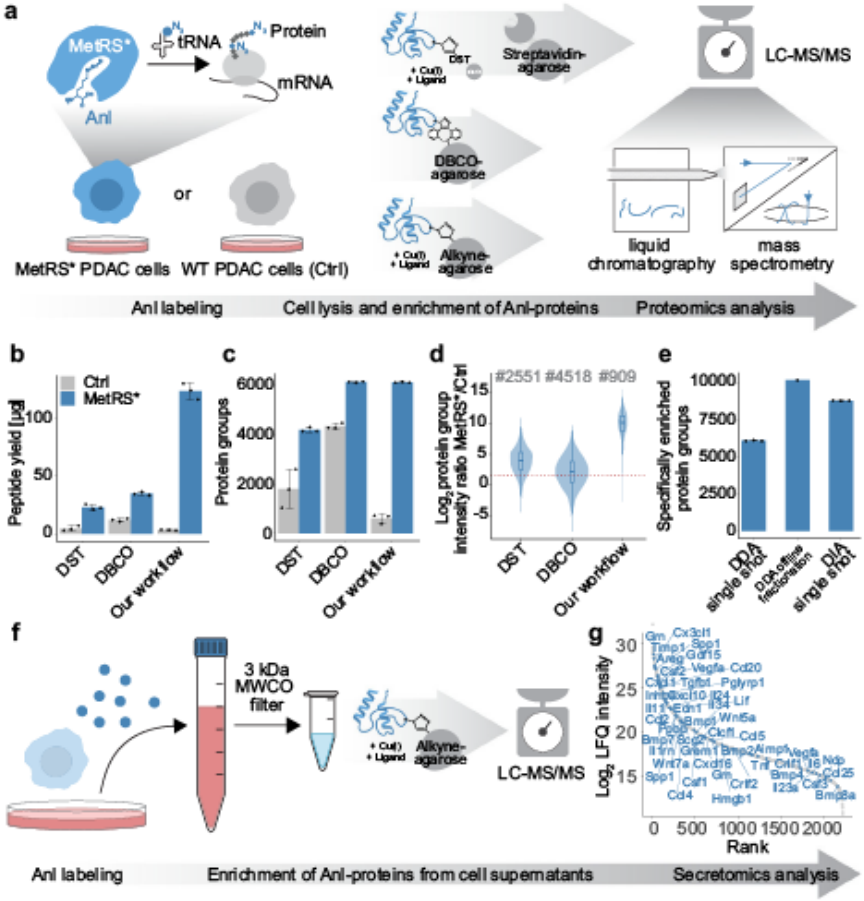

Fig. 1 | A sensitive workflow for comprehensive cell type-selective proteomics and secretomics. a Scheme of cell-selective proteomics workflows: The methionyl-tRNA synthetase^{L274G} (MetRS*) activates azidonorleucine (Anl) by loading it onto methionyl-tRNAs. MetRS*-expressing cells incorporate Anl as a methionine substitute into newly synthesized proteins. Lentivirally transduced primary MetRS*-expressing or wild-type (Ctrl) PDAC cells isolated from mouse tumors with a conditional pancreatic expression of Kras^{G12D} were grown for 8 h in Met-depleted medium supplemented with 4 mM Anl. 1×10^7 MetRS* and Ctrl cells were processed by DST enrichment, DBCO enrichment, and our improved alkyne-agarose CuAAC enrichment protocols ($n = 3$, workflow replicates). **b** Peptide yields (mean ± SD) determined by absorbance at 280 nm after enrichment, digestion, and solid phase peptide extraction. **c** Identified protein groups (mean ± SD) after MS-based analysis using 2 h chromatographic gradient length and data-dependent acquisition (DDA). **d** Intensity ratios of proteins identified in MetRS* and Ctrl samples. Counts of overlapping identifications with ratios are indicated. **e** Specifically enriched protein groups (exclusive or >3-fold higher intensity compared to Ctrl samples) identified after alkyne-agarose enrichment and single run DDA, DDA analysis of 16 fractions separated by offline high-pH reverse phase chromatography, or single run data-independent acquisition (DIA) (mean ± SD, fractionation $n = 1$, single shots $n = 3$, workflow replicates). The latter was used for all further experiments. **f** Scheme of cell-selective secretomics workflow: MetRS* and Ctrl 8661 PDAC cells were cultured for 8 h in 5% FBS containing Met-depleted medium with 4 mM Anl ($n = 3$, workflow replicates). MetRS*-expressing cell-derived Anl-proteins were enriched from cell supernatants after buffer exchange and concentration. **g** Specifically-enriched PDAC cell-released proteins ranked by label-free quantification (LFQ) intensity. Proteins with cytokine function are indicated. Source data are provided as a Source Data file.

animals provided evidence for broad tissue compatibility[22] and revealed, for example, differential expression of 200 proteins in hippocampal excitatory neurons in mice exposed to an enriched environment[23]. In contrast to cell-sorting-based strategies such as FACS or MACS, intact tissues are snap-frozen directly after harvesting and subsequently lysed without cell dissociation. This effectively avoids cell-damage-related losses, selection bias for more robust cell populations, and potential protein expression or modification state artifacts by stresses and environmental changes during the enzymatic and mechanical treatment necessary to extract cells from tissues[24–27]. However, the achieved proteome coverage has generally been low, and even the deepest studies remained under 4000 specifically enriched proteins[23,28], leaving open the feasibility of comprehensive Anl enrichment-based proteomics analysis.

Here, we developed an improved workflow that enables an unprecedented proteomics depth for cell type-specific cellular proteome and secretome profiling in vitro and in vivo. This vastly increased the detection capacity of often low abundant intercellular signaling proteins such as secreted cytokines or receptors and therefore raised the potential for MetRS*/ Anl-based cellular communication analyses. We applied our approaches in the context of primary PDAC co-culture and orthotopic transplantation models and demonstrated unique advantages in capturing extracellular proteins compared to conventional cell sorting-based proteomics. We used the strength of our comprehensive cell-type specific proteomics workflow to reveal functional differences between classical and mesenchymal PDAC subtypes in tumors and circulation, such as context-specific secretion of cancer cell-derived EMT-promoting molecules and immunomodulators that correlated with differential immune cell recruitment in vivo, as well as distinct qualitative and quantitative contributions of cancer cell-derived proteins to the tumor extracellular matrix (ECM).

Results

An improved workflow enables highly efficient and specific cell-selective enrichment of proteins

Conceptually, methionyl-tRNA synthetase^{L274G} (MetRS*)-based azidonorleucine (Anl) labeling offers unique possibilities for analyzing intercellular interactions in complex heterocellular systems. However, the achieved proteomic depth in our initial experiments and previously published MetRS*-based studies did not exceed 4000 proteins[23,28] and was therefore significantly lower than state-of-the-art with modern mass spectrometers and software[29], limiting the discovery potential. Hence, we set out to identify and overcome technical bottlenecks.

We first evaluated the Anl-incorporation rates of MetRS*-expressing cells in vitro by conventional MS-based shotgun proteomics without specific enrichment. Quantifying Anl-containing peptides compared to their unmodified counterparts showed that Anl incorporation was indeed highly specific to MetRS*-expressing cells but much slower than the incorporation of methionine (L-methionine-methyl-$^{13}C,d_3$) or the MetRS*-independent Met-substitute azidohomoalanine (Aha) (Supplementary Fig. 1a, b). Furthermore, Anl labeling is strongly dosage-dependent and reduced with methionine competition, as shown in previous studies[19,30,31]. We reasoned that the Anl-protein abundance would be very low in most applications, especially in vivo, considering often pronounced cell type heterogeneity and limited Anl bioavailability in tissues. Consequently, the demands for both recovery and specificity of the enrichment workflow are very high when aiming for deep proteomics analyses. We chose a straightforward copper(I)-catalyzed azide-alkyne cycloaddition (CuAAC) and alkyne agarose-based strategy for scalability and high reaction rates[32] as the basis for protocol optimization. We individually evaluated key experimental steps to improve protein extraction from tissue and click chemistry efficiency by systematic implementation of previous findings[33,34] and empirical testing of reactant ratios, buffer components, and new reagents, including next-generation Cu(I)-stabilizing agents[35].

A direct comparison of our improved alkyne-agarose CuAAC protocol with frequently used dibenzocyclooctyne (DBCO) resin- and cleavable disulfide biotin alkyne-tag (DST)-based procedures (Fig. 1a) demonstrated substantial advantages: Using MetRS*-expressing and negative control wild-type primary PDAC cells that were both incubated in Anl-containing media, our protocol showed minimal unspecific background and a drastically increased yield of specifically enriched peptides (Fig. 1b). This advantage translated well into the MS analysis: While DST-based enrichment provided good specificity but reduced overall coverage, DBCO-based enrichment led to many identifications in both MetRS* and negative control samples, concordant with higher side reactivity of strained alkynes[32,36]. In contrast, our protocol yielded deep proteome coverage but with the fewest identifications in negative controls (Fig. 1c). The technical reproducibility was equal to or better than alternative protocols, with 84% of all MetRS* sample identifications quantified in all three replicates and a median precursor coefficient of variation (CV) of 11.5% (Supplementary Fig. 2a, b). Importantly, low overlap and high-intensity differences of proteins identified in both MetRS* samples and controls demonstrated very low background interference from unspecific enrichment with our workflow (Fig. 1d). We defined proteins as specifically enriched if they were exclusively identified in MetRS* samples or quantified with at least threefold higher intensity than in negative controls and excluded all other proteins from further analysis, as described by Alvarez-Castelao et al.[23,37]. Accordingly, our workflow identified a total of 6576 specifically enriched protein groups (compared to 4416 and 4736 with DST- or DBCO-based enrichment, respectively), including almost all proteins covered with both other methods together plus 1039 exclusive identifications (Supplementary Fig. 3).

To optimize deep proteomics investigations, we combined our workflow with offline high pH reverse phase fractionation of peptides after enrichment and digestion, resulting in the identification of 10,146 specifically enriched protein groups, demonstrating exceptional proteome coverage (Fig. 1e). Furthermore, using a data-independent acquisition (DIA) method, we achieved an average of 8770 specifically enriched protein groups per sample in 2-h runs without fractionation. The use of DIA also improved data completeness between replicates and decreased precursor CVs compared to data-dependent acquisition (DDA) (Supplementary Fig. 2c, d).

To further evaluate the technical reproducibility of our enrichment, we repeated the experiment with ten negative control replicates, confirming the previously observed high signal-to-noise ratio between specifically enriched proteins and unspecific background (Supplementary Fig. 4a, c). While the very low signal intensity in negative controls caused more stochastic identifications than in MetRS* samples (Supplementary Fig. 4b), results remained very consistent when control samples were divided into groups of three and used separately to evaluate background interference in MetRS* samples (Supplementary Fig. 4c). The vast majority of proteins with sparse identifications in controls had high ratios far above our chosen specificity cutoff (Supplementary Fig. 4d). Conversely, the majority of proteins with lower MetRS*/Ctrl ratios had very high data completeness. Thus, not only were there a very limited number of proteins with higher background interference overall, but the controls were also effective in capturing most of these proteins consistently.

We applied the described filtering strategy to all subsequent MetRS* experiments in this study, using at least three experiments with wild-type cells as negative controls for corresponding MetRS* sample groups to define specifically enriched proteins and ensure high confidence in cell selectivity. To enable both very deep and MS time-efficient analysis with high throughput for larger-scale experiments, we used our enrichment workflow together with DIA single-shot analyses.

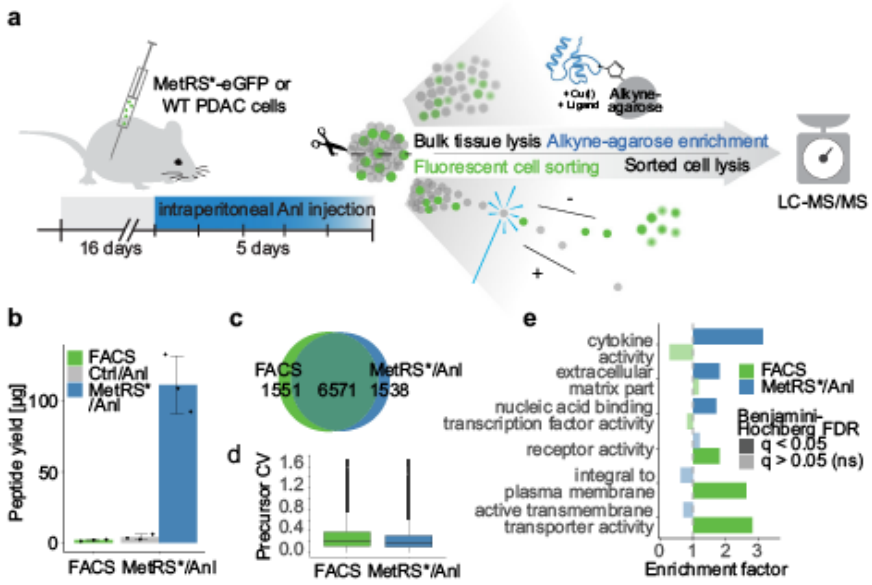

Fig. 2 | MetRS*- and FACS-based cancer cell-selective proteomics in vivo. **a** Scheme of PDAC transplantation for cell-selective proteomics: MetRS*-eGFP expressing 8661 PDAC (>90% eGFP-positive cells before transplantation, see Supplementary Fig. 5a) and wild-type (Ctrl) cells were orthotopically transplanted into fully immunocompetent syngeneic mice ($n = 3$, biological replicates). After a 16 days tumor growth period, mice were interperitoneally injected with Anl twice daily for 5 days. Afterward, tumors were harvested and cut in half. One half was snap-frozen for subsequent click chemistry enrichment, the other half was used fresh for cell dissociation and eGFP-FACS. **b** Peptide yields (mean ± SD) determined by absorbance at 280 nm. **c** Exclusively identified and overlap of (specifically enriched) cancer cell-derived protein groups with either method. **d** Distribution of precursor coefficients of variation (CVs) between biological replicates. **e** Analysis of enriched GO annotations (Fisher's exact test) within exclusively identified proteins with either method compared to all other identified proteins (full list in Supplementary Data 4). Source data are provided as a Source Data file.

Comprehensive cell-selective secretomics analysis in serum-containing media

Encouraged by the strongly increased specific peptide recovery, we next aimed to adapt our methods for investigations of intercellular signaling, specifically for the comprehensive analysis of secreted proteins. Previously, non-cell-selective incorporation of azide amino acids has improved the detection of comparably low abundant secreted cellular proteins in the presence of highly abundant serum proteins in serum-containing conditioned media[38]. MetRS*-based Anl-labeling could expand this concept for cell-selective analyses in heterocellular systems such as co-culture experiments. To establish proof-of-concept for in-depth secretomics with our enrichment protocol, we analyzed supernatants of primary PDAC cells in the presence of 5% serum (Fig. 1f). This yielded deep coverage of PDAC cell-released proteins, with a total of 2229 specifically enriched protein groups and 788 protein groups annotated with UniProtKB Keywords "secreted" and/or "signal." Of those, 103 protein groups are known ligands for intercellular communication according to CellPhoneDB[39], including 46 with described cytokine function (Fig. 1g). Despite their often small size and low abundance, 83 (81%) and 41 (89%) of the detected intercellular signaling proteins and cytokines were identified with at least two peptides.

Increased yields and extracellular protein coverage of MetRS*-based cell-selective proteomics compared to FACS in vivo

A key feature of MetRS*-based Anl labeling is its applicability in living animals. As shown previously in Falcomatà and Bärthel et al.[40], we modeled molecular PDAC subtypes in vivo by orthotopic transplantation of primary low-passaged cancer cells in the pancreas of fully immunocompetent syngeneic mice. We evaluated our enrichment workflow with tissue samples from this model by directly comparing Anl-based enrichments with conventional fluorescence-activated cell sorting (FACS) from MetRS* and eGFP co-expressing cells. After cell injection and an initial tumor growth period, we supplemented Anl by intraperitoneal injection and then used one-half of each tumor for Anl-enrichment or FACS (Fig. 2a). In total, 13–17% of the dissociated cells were cancer cells, as indicated by eGFP-fluorescence (Supplementary Fig. 5).

Peptide yields revealed striking differences with an over 50-fold higher average recovery of cancer cell-derived proteins by click chemistry enrichment compared to FACS, indicating significant cell losses during the dissociation and sorting procedure (Fig. 2b). However, both methods yielded a sufficient peptide amount for single-shot proteomics analyses with modern MS instrumentation. Both methods resulted in more than 8100 protein groups, with a lower median coefficient of variation between replicates for Anl-enrichment samples, indicating better quantitative precision (Fig. 2c, d). While around 70% of the identified protein groups overlapped between both FACS and Anl-enrichment-based analysis (Fig. 2c), exclusive identifications with each method revealed distinct strengths. Flow cytometry-sorted samples showed, for example, enrichment of transmembrane proteins, likely facilitated by strong ionic detergent-based lysis, which enhances transmembrane protein extraction and digestion[41,42] but can interfere with CuAAC reactions[34]. Conversely, cell-selective labeling captured proteins released by cells, such as ECM components and cytokines, specifically well (Fig. 2e). We primarily attribute this to the enrichment of proteins from the interstitial space in tumors, which are accessible for MetRS*-based cell-selective proteomics but lost in tissue-dissociation and sorting-based protocols.

Co-culture promotes inflammatory responses of PDAC cells and polarization of primary macrophages

After closing the gap to state-of-the-art proteomics performance and extending Anl labeling applications to in-depth cell-selective secretomics, we applied our toolkit to study pancreatic cancer biology. Both

https://doi.org/10.1038/s41467-023-38171-8

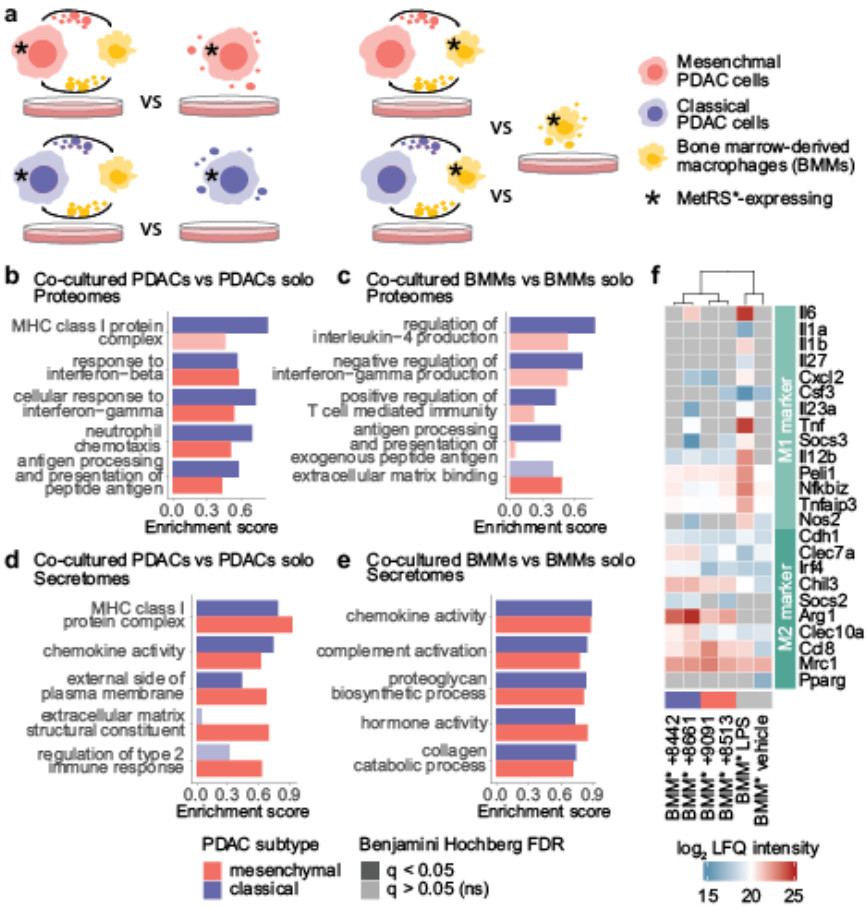

Fig. 3 | Co-culture of cancer cells with primary macrophages induces bidirectional adaptions. a Scheme of PDAC and primary macrophage cells in co-culture. Wild-type (WT) or MetRS*-expressing mesenchymal (8513 and 9091) or classical (8442 and 8661) PDAC cells and BMMs were cultured in isolation or co-culture for 36 h with AnI labeling during the last 8 h ($n = 3$, workflow replicates). Asterisks indicate MetRS* expression. **b–e** Strongly enriched gene ontology (GO) terms and UniProtKB keywords in upregulated proteins after PDAC–BMM co-culture compared to each cell type in isolation (two-sided 1D annotation enrichment[28] (full list in Supplementary Data 4)). **f** Heatmap of protein intensities associated with macrophage polarization states in BMM proteomes and secretomes.

the coverage of lower abundant proteins and cell type-resolved information on released signaling proteins are invaluable for understanding intercellular communication. In cancer, complex interactions between transformed cells and tumor stromal cells shape each other's phenotypes and the overall tumor biology. Macrophages, for example, are a major component of solid tumors and are among the earliest tumor-infiltrating immune cells in PDAC[43,44]. To evaluate the potential of MetRS*-based cell-type specific proteomics for the molecular dissection of such intercellular crosstalk, we explored the bidirectional interaction between PDAC cells and macrophages in a controlled in vitro setting. All primary PDAC cell cultures were derived from a genetically engineered $Kras^{G12D}$ -driven autochthonous mouse PDAC model[45]. They are representative of the classical subtype, displaying an epithelial morphology ("8661" and "8442"), or of the basal-like mesenchymal subtype ("8513" and "9091"), characterized by increased oncogenic *Kras* gene dosage (*Kras-mut* iGD) and a particularly unfavorable prognosis. By generating LysM-Cre-MetRS* mice, which specifically express MetRS* in the myeloid compartment, we were able to obtain primary MetRS*-expressing bone marrow-derived macrophages (BMMs). We then cultured the four PDAC lines, and the BMMs alone or in co-culture (Fig. 3a) and cell type-selectively analyzed proteins from cells and cell supernatants. Principal component analyses (PCAs) showed reciprocal adaptions of cancer cells and BMMs to co-culture with changes in both global proteome expression and protein secretion, although less clear for PDAC secretomes (Supplementary Fig. 6). PCAs further indicated distinct differences between PDAC subtypes and PDAC line-specific BMM responses.

We first investigated broad trends and processes in the proteome and secretome dynamics between each cell type in isolation and co-culture. A gene ontology (GO)[46] enrichment analysis showed increased expression of antigen-presentation and major histocompatibility complex (MHC) class I-associated proteins in classical, and to a lesser degree in mesenchymal PDAC cells (Fig. 3b), which was previously observed in breast cancer cells co-cultured with macrophages in transwell systems[47]. Interaction with BMMs also induced strong upregulation of chemokine production and interferon response signatures in both classical and mesenchymal PDAC cells, while, in particular, mesenchymal cells strongly increased structural matrix protein deposition (Fig. 3b, d). Secretomics analysis at the individual protein level revealed secretion of complex immunomodulatory signals with pronounced differences between PDAC subtypes and significant changes upon interaction with macrophages (68 signaling proteins with cytokine function and significant abundance differences (ANOVA, FDR = 5%, S0 = 0.1) between subtypes and culture conditions, see

https://doi.org/10.1038/s41467-023-38171-8

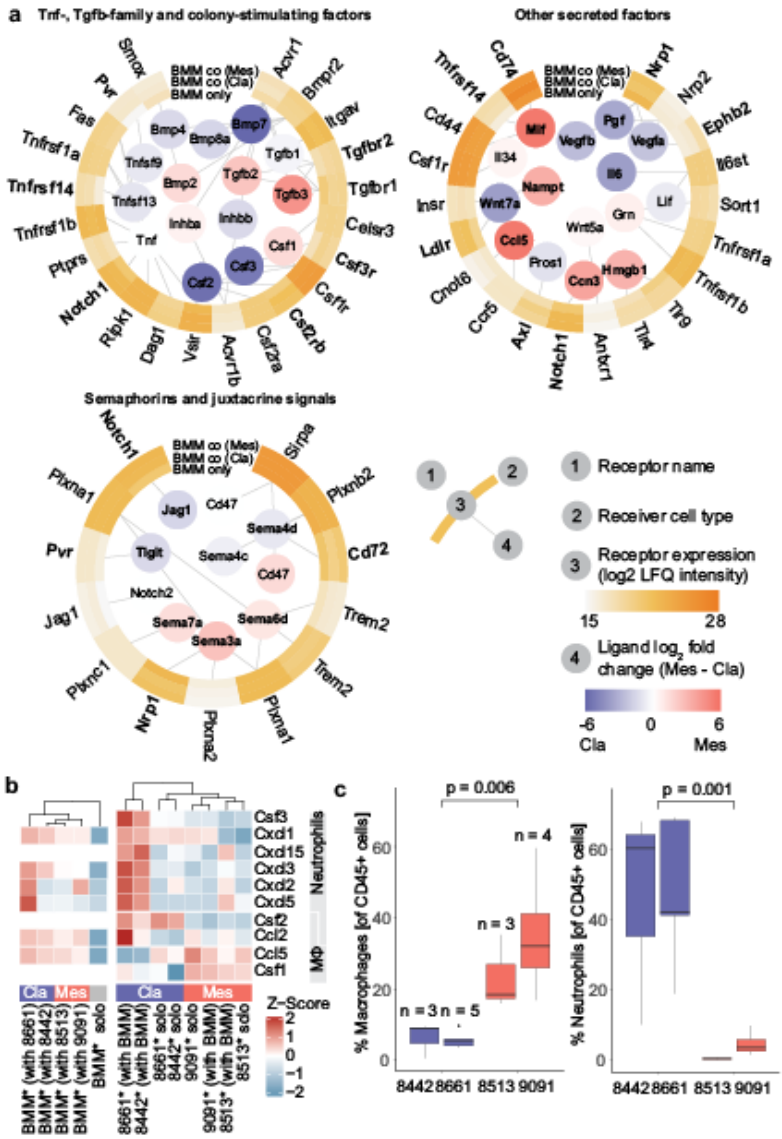

Fig. 4 | Intercellular signals and signal receptors involved in BMM adaptions to PDAC co-culture. a Macrophage polarization-associated intercellular signaling protein expressed by mesenchymal or classical PDAC cells in co-culture with corresponding receptors detected in BMM proteomes. Ligands with significantly different secretion among PDAC subtypes (two-sided Student's *t*-test, permutation-based FDR = 0.05, S0 = 0.1) and BMM receptors with significantly different levels of abundance between culture conditions (ANOVA, permutation-based FDR = 0.05, S0 = 1) are indicated in bold. **b** Heatmaps of primarily macrophage and neutrophil chemoattractants secreted by PDAC cells and BMMs. **c** Macrophage and neutrophil count as a percentage of CD45-positive cells in tumors from orthotopically transplanted classical and mesenchymal cancer cells analyzed by flow cytometry. Numbers of biological replicates and two-sided Welch's *t*-test *p*-values between cell ratios in classical or mesenchymal tumors are indicated. Source data are provided as a Source Data file.

Supplementary Fig. 7). For example, co-culture induced increased Il6 release by both subtypes but with much higher levels in classical PDAC cells, whereas specifically mesenchymal PDAC cells strongly increased secretion of CCL8 and 9. Moreover, significant enrichment of surface-exposed plasma membrane proteins in secretomes, including MHCI proteins, suggested increased shedding activity in cancer cells (Fig. 3d).

Upon interaction with classical PDAC cells, BMMs expressed higher levels of proteins associated with exogenous antigen presentation, T cell regulation, and regulation of key cytokines involved in the coordination of pro- and antitumoral response reactions[48,49] (Fig. 3c). Although trends could also be observed upon co-culture with mesenchymal PDAC cells, effects were less pronounced and did not reach statistical significance. However, BMM secretomes showed strong enrichment of immunomodulatory proteins, hormones, and growth factors, and extracellular matrix (ECM)-modifying proteins after co-culture with both PDAC subtypes (Fig. 3e). In addition to many cytokines, interaction with cancer cells broadly induced ECM regulators such as matrix metalloproteinases (MMPs), a disintegrin and metalloproteinases (ADAMs), and ADAMs with thrombospondin motifs (ADAMTSs), with crucial functions in cancer[50,51] (Supplementary Fig. 7).

https://doi.org/10.1038/s41467-023-38171-8

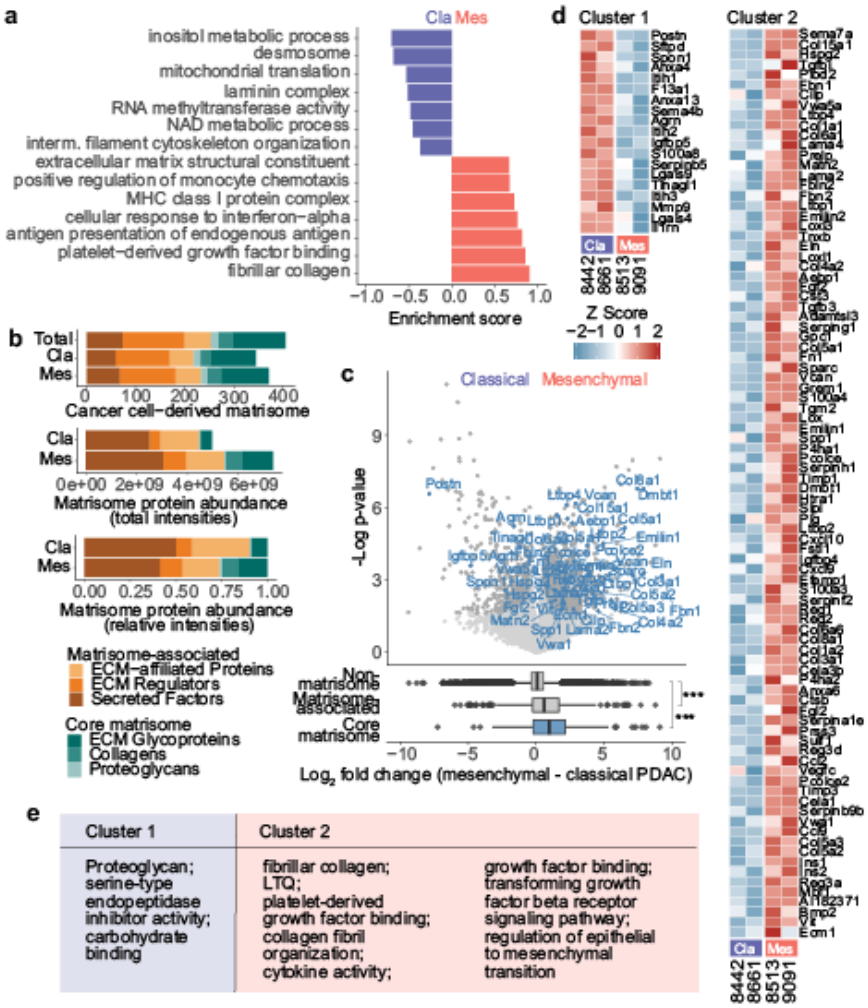

Fig. 5 | PDAC subtype-specific expression of cancer cell-derived matrisome proteins in primary tumors. a Significantly enriched gene ontology terms (1D annotation enrichment, Benjamini–Hochberg FDR = 0.05) in classical and mesenchymal cancer cell proteomes after orthotopic transplantation into fully immunocompetent syngeneic mice (8442, 8513, 8661: $n = 3$, 9091: $n = 2$, biological replicates) (full list in Supplementary Data 4). **b** Left: Cancer cell-derived matrisome proteins annotated according to Naba et al.[75] Right: Summed total and relative LFQ intensities per matrisome category. **c** Volcano plot of cancer cell-derived proteins in mesenchymal and classical PDAC tumors. Significantly regulated core matrisome proteins are highlighted in blue (two-sided Student's *t*-test, permutation-based FDR = 0.05, S0 = 0.1). Boxplots show quantitative distributions of core matrisome, matrisome-associated and all identified non-matrisome proteins between the PDAC subtypes. *P*-values were determined by two-sided Welch's *t*-test: ***$p \leq 0.001$ (1: $p = 1.7 \times 10^{-5}$, 2: $p = 5.9 \times 10^{-6}$). **d** Heatmap of matrisome proteins with significant expression differences between classical and mesenchymal PDAC cells in vivo (two-sided Student's *t*-test, permutation-based FDR = 0.05, S0 = 0.1). **e** Gene ontology terms and UniProtKB keywords found overrepresented by Fisher's exact test within each cluster are indicated (Benjamini–Hochberg FDR = 0.05, full list in Supplementary Data 4). Source data are provided as a Source Data file.

Co-cultured macrophages acquire TAM-like features driven by a complex mix of cancer cell-secreted and -displayed signaling proteins

To further evaluate the cancer-cell-induced macrophage states in co-culture, we annotated proteins from BMM-selective secretome and cellular proteome datasets using a panel of markers commonly associated with macrophage polarization[52]. M1 and M2 states exemplify broadly clustered extremes on a spectrum of macrophage states—with M1 being associated with interferon and Toll-like receptor signals and efficient production of effector molecules and inflammatory cytokines, and M2 macrophages with the resolution of inflammation or T_H2 response-driven physiological reponses[52,53]. As an experimental reference, we stimulated MetRS*-expressing BMMs with lipopolysaccharide (LPS), a Toll-like receptor 4 (TLR4) agonist, and acquired their proteome and secretome profiles. As expected, LPS-stimulated BMMs showed exclusive expression and strong upregulation of M1-associated marker proteins compared to unstimulated cells (Fig. 3f). PDAC co-cultured macrophage M1-associated marker expression was detected only sporadically and mostly at basal levels, except for increased secretion of the pro-inflammatory cytokines Il6 and Tnf upon interaction with 8661 classical PDAC cells. Instead, co-culture primarily induced upregulation of M2-associated markers such as Arg1 and Chil3, again often with stronger responses to classical PDAC cells. Together, cancer cell co-culture therefore induced fast and profound adaptions in BMMs reminiscent of tumor-associated macrophage (TAM) features, which often show M2-like differentiation, contribute to immune cell recruitment and regulation, and remodeling of the tumor ECM[54–56].

Cell-selective proteomes and secretomes also allowed us to investigate potentially active intercellular signaling circuits that shaped macrophage polarization. We mapped PDAC-released proteins with corresponding macrophage receptors using ligand-receptor interactions curated in CellPhoneDB[39]. While PDAC cells did not release hallmark M2 polarizing factors IL-4 and IL-13, we found a complex mix of other proteins that have been associated with macrophage polarization (Fig. 4a): Some proteins were secreted without significant differences between subtypes, such as Tgfb1, a known M2 promoter[57], or Tnf (at much lower abundance, see also Supplementary Data 1), an important M2-suppressing factor in cancer[58]. Other Tgfb- and Tnf-family members, macrophage survival essential colony-stimulating factors (Csfs), and many other signaling proteins, however, showed strong and consistent differential expression between PDAC subtypes. Classical PDAC cells secreted, for example, more Il6, a pleiotropic cytokine that has been described to enhance both M1- or M2-like states[59], and Tnfsf15 (Supplementary Fig. 7), which has recently been shown to promote macrophage differentiation toward an M1 phenotype and increased cancer cell phagocytosis[60]. Mesenchymal PDAC cells secreted higher levels of Tgfb2 and Tgfb3 as well as Mif, Ccl5, and the alarmin Hmgb1, which have been found to skew macrophage polarization toward M1- and M2-like states in a context-dependent manner[61–64]. Furthermore, both PDAC subtypes expressed similar levels of Cd47, a contact-dependent anti-phagocytotic signal often upregulated by cancer cells to escape elimination by phagocytes[65,66]. Also, there is increasing evidence for the contribution of semaphorins to macrophage recruitment and differentiation, a family of exclusively secreted (class 3) or membrane-bound proteins (that can act as contact-dependent signals) with important roles in cancer[67]. For example, increased Sema3a has been associated with poor outcomes in PDAC[68] and attraction of tumor-associated macrophages[69], while Sema7a was shown to recruit and polarize macrophages toward the M2 state in the context of sepsis[70].

The majority of detected PDAC signal corresponding receptors on BMMs showed stable expression, but some were regulated upon co-culture with cancer cells (Fig. 4a). Notably, BMMs upregulated Pvr (Poliovirus receptor) expression after interaction with both PDAC subtypes. Pvr activation on macrophages has been linked to an anti-inflammatory phenotype[71], and targeting the Pvr-Tigit axis is being explored as a potential cancer immunotherapy strategy[72].

PDAC cancer cell subtype-specific chemokine secretion patterns correlate with immune cell recruitment in vivo

Overall, both macrophages and PDAC cells responded to co-culture with increased production and release of immunomodulatory signaling proteins. Looking specifically at expression differences of immune cell recruiting factors, we noticed clear trends between PDAC subtypes: Mesenchymal PDAC cells secreted high levels of key monocyte recruitment and macrophage survival signals such as Ccl5 and Csf1 (Fig. 4b). In isolation, all four PDAC cell lines secreted many primarily neutrophil attracting proteins at similar levels. Interestingly, interaction with BMMs, however, strongly induced neutrophil recruiting chemokines like Cxcl2, Cxcl3, Cxcl5, and Cxcl15 in classical PDAC cells, whereas release remained unchanged (9091) or increased much less (8513) in mesenchymal cancer cells. BMM chemokine secretion patterns followed similar trends. Intrigued, we investigated the TME composition of tumors formed by the four PDAC subtype lines after orthotopic transplantation into mice. Immunophenotyping by flow cytometry revealed subtype-specific differences in immune cell populations. Among the analyzed cell types, differences between macrophage and neutrophil recruitment were the most significant and reflected the recruitment factor expression patterns from our secretomics experiments (Fig. 4c and Supplementary Fig. 8).

PDAC tumors show systematic differences in matrisome protein production between mesenchymal and classical cancer subtypes

To further investigate subtype differences between classical and mesenchymal PDAC, we transplanted all four MetRS*-expressing cancer lines orthotopically into syngeneic mice and compared cancer cell protein expression in the complex TME in vivo. In total, we identified 9415 specifically enriched cancer cell-derived proteins, which makes this one of the deepest cell type-specific PDAC in vivo proteomics datasets to date. Gene ontology enrichment analysis indicated pronounced differences in hallmark processes of epithelial–mesenchymal transition (EMT), such as cytoskeleton organization, ECM modulation, and cell–cell junctions (Fig. 5a). Moreover, mesenchymal PDAC cells showed an enriched interferon response signature and elevated antigen presentation-related protein expression, reminiscent of the adaptions that we observed in co-culture with macrophages in vitro and coinciding with the higher macrophage infiltration in these tumors (Fig. 3b and Fig. 4c).

Notably, many of the most prominent differences between mesenchymal and classical PDAC cell protein expression in vivo were ECM-related. Among diverse functions in cancer progression, dysregulated ECM in tumors strongly contributes to drug resistance, immune suppression, and metastasis[51]. Recent research has shown that, in particular, pancreatic cancer cell- rather than stromal cell-derived matrix proteins correlate with poor patient survival, although contributing only a minor fraction of the total ECM mass[73,74]. This introduced cell type-resolved profiling of ECM in tumors as a promising resource for therapeutic target and biomarker discovery. In contrast to the previous studies that characterized the cancer cell-derived matrix using xenotransplants[73,74], Anl-labeling allows cell type-resolved analysis in syngeneic immunocompetent mice. Therefore, our PDAC model integrates interactions with infiltrating immune cells, which directly modulate the tumor ECM and change the ECM-associated protein expression of other cell types such as cancer cells[50,51] (see also Supplementary Fig. 7). Motivated by this and the previously demonstrated advantages of Anl-enrichment for extracellular protein characterization (Fig. 2e), we further investigated ECM-related proteins in our data.

We annotated proteins that constitute the ECM using an in silico defined matrisome atlas by Naba et al.[75], which specifies "core matrisome" proteins such as collagens and proteoglycans, or proteins that are "matrisome-associated" such as ECM remodeling enzymes or secreted growth factors and cytokines that are known to bind to the ECM. Cancer cells expressed a diverse representation of each category, covering 405 matrisome proteins with only minor differences in overall identification numbers and very similar class distribution between classical and mesenchymal subtypes (Fig. 5b). Mesenchymal PDAC cancer cells have been shown to suppress cancer-associated fibroblasts (CAFs), the most prominent producers of ECM proteins in PDAC tumor stroma, leading to tumors with lower overall stromal and collagen content than classical PDAC[76]. However, quantitative analysis of cancer cell-derived proteins showed a higher abundance of mesenchymal-derived matrisome proteins and over-proportional expression of core matrisome and ECM regulators (Fig. 5b), indicating an increased relative contribution to the tumor ECM. Rather than being driven by a few highly abundant outliers, increased abundance of core matrisome expression in mesenchymal cells was a broad and statistically significant motif (Fig. 5c).

At the individual protein level, more than a hundred matrisome protein groups had significant expression differences between the two PDAC subtypes (Fig. 5d). This included proteins recently identified as promising therapeutic targets, such as the predominantly cancer cell- rather than stromal cell-expressed PDAC metastasis promoters Agrn, Serpinb5, and Cstb[74]. All three proteins were detected in our experiment, and classical PDAC cancer cells produced significantly more

https://doi.org/10.1038/s41467-023-38171-8

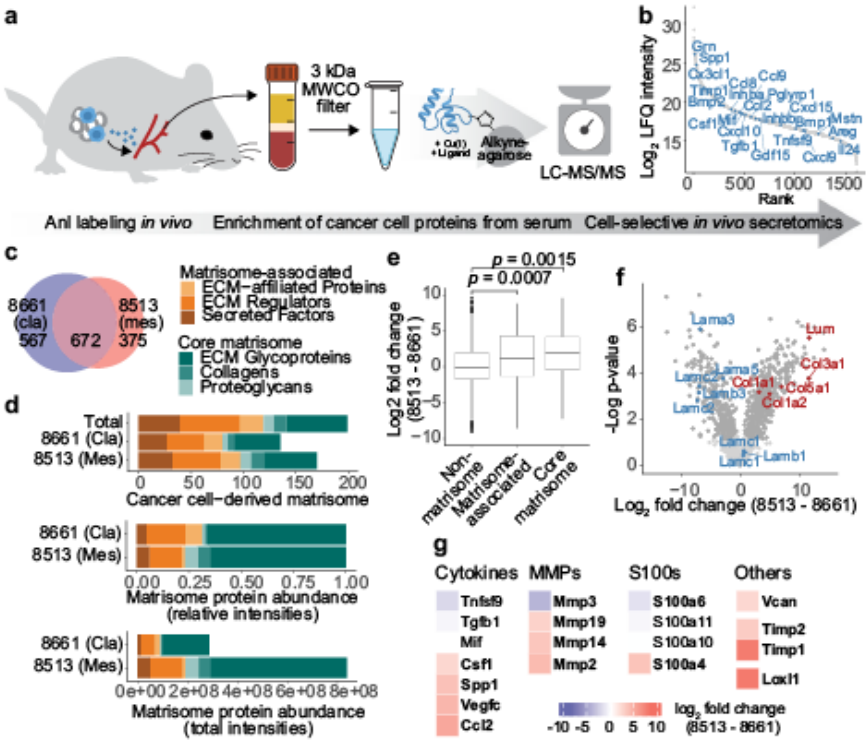

Fig. 6 | PDAC subtype-specific detection of cancer cell-derived proteins in circulation. **a** Scheme of cancer cell-derived protein capture from serum: After orthotopic transplantation of MetRS*-expressing or WT (Ctrl) PDAC cells and ANL labeling, tumor-bearing mouse sera were collected, and tumor-derived proteins were enriched and analyzed. **b** Specifically enriched cancer cell-derived serum protein groups ranked by intensity. Proteins with cytokine function are indicated. **c** Exclusively identified and overlap of specifically enriched 8513 and 8661 cancer cell-derived proteins (8661: $n = 4$, 8513: $n = 3$, biological replicates). **d** Cancer cell-derived matrisome proteins counts, summed total and relative LFQ intensities per matrisome category. **e** Fold change distribution of non-matrisome, and matrisome class proteins between PDAC subtypes. *P*-values were determined by a two-sided Welch's *t*-test. **f** Volcano plot of 8661 and 8513 cancer cell-derived proteins in serum. GOCC annotated Laminin complex proteins (blue), fibrillar collagens (red), and proteins with significant fold changes (dark gray) are highlighted (two-sided Student's *t*-test, permutation-based FDR = 0.05, S0 = 0.1). **g** Fold changes of pre-metastatic niche formation-associated proteins. Proteins with significant fold changes (two-sided Student's *t*-test, permutation-based FDR = 0.05, S0 = 0.1) are indicated in bold. Source data are provided as a Source Data file.

Agrn and SerpinB5, suggesting potential subtype-specific responses to inhibition. Mesenchymal cancer cells, however, consistently produced higher amounts of EMT-promoting matrisome components, for example, fibrillar collagen types I and V, fibronectin, Fgf2, Tgfb family proteins such as Tgfb3 and Bmp2 as well as proteins involved in Tgfb signaling modulation, indicating a feed-forward loop with sustained local EMT signals (Fig. 5d, e). Moreover, we detected a much higher expression of lysyl oxidases Lox, Loxl1, and Loxl3 in mesenchymal cancer cells. Lysyl oxidase-family members mediate crosslinking of collagens and elastin and regulate cellular processes like adhesion, motility, and invasion[77]. They correlate with unfavorable patient prognosis in many cancers, including PDAC, and have been shown to promote chemoresistance, EMT, and metastasis[78].

In vivo, secretomics reflects tumor subtype and pathogenesis based on more than 1000 cancer cell-derived proteins in circulation

In addition to local effects, tumor cell-derived proteins can act in distant tissues after entering circulation through the lymph or leaky blood vessels. Contrary to inference from cell expression data, profiling of such proteins in the bloodstream would give spatially-specific insights into many crucial aspects of tumor progression that involve long-distance signals and effectors and would also be invaluable for biomarker discovery. However, the lack of cell type-selectivity and the high dynamic range, with extremely abundant functional blood proteins and comparatively low abundance of tissue leakage proteins[79], make this challenging with conventional methods.

To evaluate whether Anl-labeling could be used to enrich cancer cell-derived proteins directly from body fluids, we collected mouse serum after orthotopic PDAC transplantation and Anl labeling of MetRS*-expressing cancer cells (Fig. 6a). Particularly, serum samples from mice bearing the 8661 (classical) and 8513 (mesenchymal) PDAC subtype tumors showed a good signal-to-noise ratio, with all replicates distinctly clustering from negative controls and each other in a principal component analysis (Supplementary Fig. 9). In these samples, 1614 proteins passed filtering criteria for specific enrichment, including 64 CellPhoneDB-annotated intercellular signaling protein ligands such as 23 cytokines (Fig. 6b), with around 42% identification overlap between the subtypes (Fig. 6c).

After discovering significant differences in matrisome protein expression between both PDAC subtypes in primary tumors, we were interested if these would be reflected in circulation. In total, we detected 199 core matrix or matrix-associated cancer cell-derived proteins in serum. While identified proteins had a very similar qualitative matrisome class distribution as primary tumors, quantitative distribution in serum was distinct, with the top two highest summed intensity classes shifting from secreted factors and ECM-affiliated proteins to ECM glycoproteins and ECM regulators (Figs. 6d and 5b). However, differences between subtypes followed the trends observed in primary tumors: Mesenchymal-derived matrisome proteins were

more abundant and had an over-proportional share of core matrix proteins, specifically collagens and proteoglycans (Fig. 6d, e). At the individual protein level, we again found a higher abundance of laminin complex proteins in classical and fibrillar collagens in mesenchymal PDAC samples (Fig. 6f). Also, key subtype differences in immunomodulatory and matrix-modifying protein release identified in our previous experiments could be captured in serum, such as high Loxl1 and Csf1 secretion by mesenchymal cancer cells, providing direct evidence for potential long-range effects (Fig. 6g). Both proteins have indeed been described to pre-condition future places of metastases and, strikingly, we identified many other previously described pre-metastatic niche conditioning factors[80–83] (Fig. 6g). A supportive pre-metastatic niche is vital for metastatic colonialization, which is considered a rate-limiting step of the invasion-metastatic cascade[84,85]. The premetastatic-niche-promoting signature of cancer cell-derived proteins in circulation likely contributes to the previous observation that increased $Kras^{G12D}$ gene dosage *(Kras mut-iGD)* promotes EMT and metastasis in the mesenchymal PDAC subtype[45].

Discussion

Increasing insight into intercellular communication in the tumor microenvironment has helped to identify cancer vulnerabilities, for example, crucial immunosuppressive intercellular signaling circuits[40,86]. The combination of MS-based proteomics and cell-selective labeling is emerging as a powerful strategy to further accelerate the knowledge gained about heterocellular processes driving the disease. Direct analyses of labeled peptides offer straightforward solutions for multiplexed cell type-resolved proteomics and the evaluation of enrichment specificity[87]. However, with thorough background interference controls, analyses of all peptides from labeled proteins yield increased sensitivity and protein quantification accuracy.

Nonetheless, previous studies were limited by low proteome coverage and/ or used extensive offline fractionation and less stringent filtering criteria to increase identifications[19,23,26,88,89]. The latter comes at the cost of sample throughput and specificity of enriched proteins, which are both key for the discovery of specific pathophysiological mechanisms. Here, we strongly increased the achievable proteomics depth with Anl labeling-based cell-selective proteomics by improving the biochemical enrichment of azide-modified proteins from complex biomolecule backgrounds. Beyond that, the increased recovery and enrichment specificity enabled additional applications for this concept, where low signal-to-noise was previously prohibitive. Combined with high-end mass spectrometry, data-independent acquisition, and recently developed software[90], our workflow provides comprehensive and MS time-efficient cell-selective proteomes and secretomes in vitro and in vivo.

In this study, we applied our improved workflows for the in-depth exploration of TME features between classical and mesenchymal PDAC subtypes in model systems with different degrees of complexity. In vitro, co-culture experiments offer a very controlled environment for focused and detailed mechanistic investigation of heterocellular interaction. Frequently used indirect co-culture systems such as supernatant transfer experiments or transwell assays facilitate cell-selective analysis by keeping cell types physically separated. However, they cannot cover all communication channels and reciprocal signaling dynamics[91,92]. In contrast, cell-selective labeling enables analysis of cells in direct co-culture, which fully integrates reciprocal communication means, including cell contact formation. Cell-selective labeling using amino acid precursors (CTAP)[93], for example, granted invaluable insight into reciprocal signaling between pancreatic cancer cells and fibroblasts[18]. Specific enrichment of cell-selectively Anl-labeled proteins allowed us to extend this concept to in-depth profiling of heterocellular secretomes. Our findings not only recapitulated the pro-inflammatory secretory programs of macrophages as determined previously by distinct proteomics methods independent of MetRS*[12,38] but identified, for example, 68 cancer cell-derived proteins with cytokine function in serum-containing culture media. Co-culture of PDAC cells and macrophages underlined the advantage of experiments that allow bidirectional intercellular communication, revealing broad reciprocal adaptions and strong regulation of intercellular signals upon co-culture, with an overall trend toward increased secretion of cytokines and chemokines in both cell types. While macrophages will be exposed to many more stimuli in tumors in vivo, including signals from other stromal cell types, both PDAC subtypes secreted a complex mix of macrophage polarization-associated proteins. Direct interaction with PDAC cells for less than two days was sufficient for macrophages to acquire many TAM-associated features. Moreover, in vitro secretomics allowed in-depth analysis of cancer cell-released chemokines and showed systematic differences between PDAC subtypes that reflected significant differences in TME cell composition, with higher macrophage infiltration in mesenchymal and higher neutrophil infiltration in classical PDAC tumors. This suggests that pancreatic cancer cell-derived signals directly contribute to the recruitment of these cell types. Specifically, large parts of the classical PDAC cell neutrophil recruiting signature became only apparent in co-culture, exemplifying how heterocellular systems expand the intercellular signaling capacity of a single cell type.

For cell type-specific proteomics analysis in vivo, cells are typically extracted from tissue and sorted by FACS or MACS. We have shown that MetRS*-based cell-selective protein labeling and enrichment can have a fundamental cell-type-of-interest protein recovery advantage in pancreatic tumors compared to cell sorting. The high specific yields promise more effective analysis of less abundant or less robust cell types and even provide enough peptides to reach the higher input material demands of extended proteomics techniques such as offline fractionation for the construction of large peptide libraries or post-translational modification-specific enrichment. Importantly, Anl-enrichment also allows freezing of the cell states in tissues directly after harvesting, which provides an additional major benefit for PTM analysis since PTM-states such as protein phosphorylation are often highly dynamic and can be enzymatically modified within minutes in response to environmental changes[94,95]. The combination of Anl-enrichment and PTM analysis, therefore, outlines highly promising avenues for future research.

Here, we focused on another advantage of the technique—the accessibility of extracellular proteins for click chemistry enrichment. Anl labeling facilitates the cell-selective analysis of secreted proteins in tissue or body fluids, which is of great interest and difficult to achieve with conventional techniques. For example, recent pioneering work has demonstrated the high value of cancer cell-selective matrisome analyses in primary tumors and metastases[73,96] but relied on xenotransplants and immunocompromised mice to achieve cell-selectivity. In comparison, MetRS*-based cell-selective proteomics can provide additional value by overcoming the need for species-distinguishing peptides and avoiding potential dynamic range issues caused by the co-analysis of abundant host proteins, which can both reduce the cell-selective matrisome coverage. Moreover, in principle, any cell type can be studied without the need for immunosuppression.

Our MS-based proteomics approach revealed pancreatic cancer cell and subtype-specific matrisome proteins in fully immunocompetent mice and provided proof-of-concept for in-depth analysis of cancer cell-derived proteins in tumor-bearing mouse serum. Previous research has shown a higher cellularity, less activated CAFs, and a less pronounced desmoplastic reaction in mesenchymal PDAC tumors[97]. Our cell-selective tumor analysis revealed that, among the lines we tested, mesenchymal cancer cells themselves produce significantly higher levels of matrisome proteins, particularly core matrix proteins, compared to classical PDAC cells. Furthermore, mesenchymal cancer cells exhibited a distinct matrisome signature

that promotes epithelial-to-mesenchymal transition (EMT). Studies of human PDAC patient cohorts have demonstrated a high ECM content for the mesenchymal subtype, and mesenchymal/ECM-high PDAC correlated with a poor prognosis in comparison to classical/immune-rich PDAC[98]. Matrisome protein release could clearly segregate PDAC subtypes in our experiments, even when analyzing cancer cell-derived proteins in circulation. Remodeled ECM in cancer has been appreciated as critical for tumor progression[51,99]. Early trials directed towards broad depletion of aberrant stroma, however, revealed a dichotomous nature of the ECM and underlined the need for a more precise understanding of stromal components and their role in pathogenesis[100–102]. Using cell type-specific MetRS* mouse models, stromal cell types and their contribution to the tumor ECM can be studied systematically in the future. This combined knowledge will help to evaluate the sources and functions of individual tumor stromal components and identify tumor-promoting candidates for targeted inhibition without simultaneous interference with protective functions. Specifically, we detected elevated expression levels of Lox, Loxl1, and Loxl3 in mesenchymal cancer cells. Loxl2 has been identified as an independent prognostic factor in pancreatic cancer patients associated with poor survival[103,104]. However, anti-Loxl2 mAb treatment in a PDAC transplantation mouse model has caused a significant reduction in matrix content and accelerated tumor growth[105]. Other studies have shown a significant reduction of metastasis, chemosensitization, and prolonged survival after lysyl oxidase inhibition in PDAC[78] or other cancers[106,107]. Future studies should evaluate how cell-type specific lysyl oxidases shape the composition of the tumor microenvironment and contribute to cancer progression.

Cell type-selective profiling of tumor-derived proteins in body fluids opens exciting opportunities for a more precise understanding of long-range intercellular processes such as tumor cell recruitment and the metastatic cascade. In this study, we detected more than 1600 cancer cell-derived proteins in serum, including more than 20 cytokines, strongly improving the coverage achieved in previously published in vivo secretomics approaches, which range from a few dozen to a few hundred cells selectively identified proteins[108–111]. Our data revealed a strong release of pre-metastatic niche formation-associated factors by a mesenchymal compared to a classical PDAC line. Because the abundance of tumor-derived proteins in serum was very low even after enrichment, we expect current developments towards high sensitivity proteomics[112,113] to be highly complementary for even more comprehensive cell-selective in vivo secretomics.

Our study has identified differentiating features among PDAC subtypes with high consistency in our selected models. However, the limited sample size, with only two cell lines per subtype and one line per subtype in the serum secretomics experiment, and the small number of replicates in in vivo mouse experiments do pose limitations to our findings. Despite this, our results demonstrate the unique strengths of cell-selective proteomics analyses in uncovering disease mechanisms and provide a foundation for further research with larger sample sizes to statistically validate and expand upon these findings.

Although our cell type-specific metabolic labeling approach cannot be directly applied to human cancer patients, it offers several possibilities for clinical translation. MetRS* transduced human premalignant cells (e.g., from pancreatic intraepithelial neoplasia (PanIN) or intraductal papillary mucinous neoplasm (IPMNs)), as well as PDAC cells and organoids (e.g., from invasive tumors representing various stages of PDAC progression, differences in metastatic capacity or molecular subtypes), can be transplanted into immunodeficient mice or mice with a humanized immune system[114]. Subsequent MetRS*-based proteomic profiling of tumors and body fluids, such as the blood, enables not only a deeper understanding of PDAC development, progression, and subtype specification but has also the potential for biomarker identification. So far, biomarkers for PanIN/IPMN and early PDAC detection, subtype classification, prognostic and therapeutic stratification, and the monitoring of targeted interventions are widely lacking[115–117]. Together, MetRS* based proteomic profiling holds the promise of biomarker discovery in tumors and circulation, which can be subsequently tested and validated in prospective studies in cancer patients.

Methods

LysMCre-MetRS* mice

LysM$^{Cre/Cre}$[118] and *LSL-R26*$^{CAG\text{-}GFP;Mats^{*}L274G/CAG\text{-}GFP;Mats^{*}L274G}$ (MetRS*)[23] mice have been described previously. Strains were on a C57Bl/6J background and interbred to obtain homozygous LysMCre-MetRS* mice for bone marrow isolation.

Cell culture

293 T cells were obtained from ATCC (CRL-3216) and maintained at 37 °C, 5% CO_2 in Dulbecco's Modified Eagle Medium (DMEM) supplemented with 10% (v/v) heat-inactivated FCS (FCS HI) (complete DMEM).

Primary mouse PDAC cells were obtained from autochthonous PDAC tumors as described before[119] and maintained in complete DMEM for less than 30 passages.

The preparation of bone marrow-derived macrophages (BMMs) followed the procedure described in Weischenfeldt and Porse (2008)[120]. In brief, bone marrow was harvested from femurs and tibiae of C57BL/6J wild-type (WT) or LysM-Cre-MetRS* mice. Bone marrow cells were passed through 70 μm nylon mesh filters and then plated on sterile, non-tissue culture-treated Petri dishes (5×10^6 cells/dish). After culture for 7 days in macrophage differentiation medium (DMEM supplemented with 10% (v/v) FCS HI and 20% (v/v) Csf1-containing L929 cell-conditioned media (replenished on day 3), BMMs were harvested in cold PBS and used for experiments.

Cell lines were authenticated by genotyping and regularly tested for mycoplasma contamination by PCR.

Transfection, lentivirus production, and transduction

For Met-substitute incorporation comparison experiments, 293 T cells were transfected with an eGFP-MetRS* expression vector based on the pEGFP-C1 (Clontech) plasmid. Transient transfections were done with Lipofectamine 3000 (Invitrogen) according to the manufacturer's instructions.

For stable MetRS* expression, PDAC cells were lentivirally transduced using a modified Precision LentiORF Collection (pLOC) library (GE Healthcare) plasmid (pLOC-CMV > MetRS*:IRES:TurboGFP:P2A:BlastR; enrichment method comparison experiment), generated as described previously[121], or a pLV-EF1A > MetRS*:P2A:EGFP:T2A:Puro plasmid, constructed by VectorBuilder.

For virus production, 293 T cells were transfected with helper plasmids pMD2.G (Addgene), and psPAX (Addgene), and a MetRS* plasmid at a ratio of 1:1.5:2 (3 μg of plasmid DNA in total) in six-well plates using Lipofectamine 3000 and following the manufacturer's instructions for lentiviral production, but using a total of 2 ml complete DMEM for virus collection 48 h post-transfection. After harvesting, polybrene was added to virus-containing supernatants at 10 μg/ml final concentration. 1 ml of virus and polybrene-containing supernatant was added to 2.5×10^5 PDAC cells seeded in 6-well plates and mixed with 1 ml complete DMEM. After 16 h, media were exchanged with 2 ml complete DMEM. Forty-eight hours post-transduction, successfully transduced cells were selected with antibiotics (Blasticidin for pLOC-MetRS* and Puromycin for pLV-MetRS*) at a final concentration of 10 μg/ml.

Pulse labeling with azidonorleucine or other Met-substitutes in vitro

Cells were washed twice with PBS and then pre-incubated in methionine (Met)-free DMEM supplemented with 10% FCS HI for 30 min. Afterward, the medium was replaced by Met-free DMEM, 10% FCS HI containing 4 mM azidonorleucine (Iris Biotech) or other Met-substitutes (azidohomoalanine, L-methionine-methyl-$^{13}C,d_3$ (Met+4)). Cells were incubated for 8 h, washed twice with PBS, and harvested by scraping. For Anl enrichment-based secretome experiments, serum concentration during labeling was reduced to 5% to avoid protein precipitation in the supernatant concentration steps of the enrichment workflow.

BMM–PDAC co-culture and LPS stimulation of BMMs

2×10^7 primary WT or MetRS* BMMs and 5×10^6 primary WT or MetRS* PDAC cells were seeded in mono- or co-culture on 15 cm dishes, incubated for 28 h in complete DMEM, and subsequently labeled for 8 h in 4 mM Anl (see above for details). BMMs seeded and cultured in parallel to co-culture experiment samples were treated with 500 ng/ml LPS or vehicle simultaneously with the Anl-labeling. Cells and supernatants were harvested for cell-selective in vitro global proteomics and secretomics analyses (see below for details).

Orthotopic transplantation and Anl administration in vivo

In vivo transplantation experiments were performed as described in *Nature Cancer volume 3, pages 318–336 (2022)*[40]. In brief, 1×10^4 MetRS*/WT mouse PDAC cells were orthotopically transplanted into the pancreas of syngeneic immunocompetent C57Bl/6J mice. PDAC cell lines isolated from female endogenous mice were transplanted in female recipients and vice versa for male mice. Two to three weeks after transplantation, mice were treated with Anl (200 µl 300 mM Anl, twice a day for 5 days, intraperitoneal injections). Animals were sacrificed when individual mice reached the human endpoint or after Anl treatment.

All mice experiments were performed in compliance with the European and the ARRIVE guidelines for the care and use of laboratory animals and were approved by the Institutional Animal Care and Use Committees (IACUC) of the local authorities of Technische Universität München and the Regierung von Oberbayern. A tumor diameter of 1.5 cm and a specific burden score, defined by a cumulative burden score, allowed by the IACUC and Regierung von Oberbayern were not surpassed in this study. All mice were kept in dedicated facilities, with a light–dark cycle of 12:12 h, housing temperature between 20 and 24 °C, and relative air humidity of 55%.

Serum collection

Blood from orthotopically transplanted mice was collected from the submandibular vein in serum collection tubes and further processed for downstream analysis (see below).

Flow cytometry analysis and FACS

Acquisition of eGFP-positive PDAC cell cultures by flow cytometry. Cultured MetRS* and WT 8661 PDAC cell lines were detached using trypsin, then washed three times with ice-cold PBS, filtered through a 30 µm mesh, and resuspended in an adjusted volume of ice-cold PBS. Cell acquisition was performed using the BD FACS Aria Fusion. Flow cytometry data were analyzed using FlowJo software (v10.6.2).

Acquisition and sorting of eGFP-positive cells from in vivo tumors by flow cytometry. Dissociation of fresh tumor samples was performed as described previously[40]. Next, the debris removal solution (Miltenyi #130-109-398) was used to discard cell debris from the cell suspension, and the removal of dead cells was performed using the dead cell removal kit (Miltenyi #130-090-101). The enriched fraction of live cells were collected in ice-cold 2% FCS/PBS buffer and filtered through a 30 µm mesh before acquisition. Cell sorting was performed using the BD FACS Aria Fusion. EGFP-positive cells were sorted in low-bind tubes in PBS, washed two times with PBS, and the resulting cell pellet was shortly dried and snap-frozen. Flow cytometry data were analyzed using FlowJo software (v10.6.2).

Immunophenotyping by flow cytometry. Dissociation of fresh tumor samples and antibody staining was performed as described previously[40]. Cells were blocked with anti-mouse CD16/CD32 FC block (Biolegend, 1:100) for 10 min on ice and stained with Zombie Aqua Fixable Viability Kit (Biolegend, 1:500) to discriminate live and dead cells. The following antibody cocktails were used: CD4 BUV805 (BD, 1:100), CD3εBUV395 (BD, 1:20), CD8a BV785 (Biolegend, 1:100), CD25 BV650 (Biolegend, 1:50), TCRγ/δ BV421 (Biolegend, 1:100), CD62L PE (Biolegend, 1:500), CD44 APC-Fire (Biolegend, 1:30), CD45 PerCP Cy5.5 (Biolegend, 1:100), CD19 FITC (Biolegend, 1:100), EpCAM APC/AF647 (Biolegend, 1:200) for acquisition of adaptive immune cells; CD11c BUV737 (BD, 1:30), NK1.1 BUV395 (BD, 1:25), Ly6C BV785 (Biolegend, 1:200), CD11b BV650 (Biolegend, 1:100), F4/80 BV421/PB (Biolegend, 1:30), CD45 PerCP Cy5.5 (Biolegend, 1:100), Ly6G PE (Biolegend, 1:200), CD68 APC-CY7 (Biolegend, 1:20), EpCAM APC/AF647 (Biolegend, 1:200) for acquisition of innate immune cells. 1×10^6 events were acquired per antibody panel on the BD LSRFortessa. Flow cytometry data were analyzed using FlowJo software (v10.6.2).

Enrichment of Anl-containing proteins

DST-based enrichment. DST-based enrichment was done as described in *Methods in Molecular Biology volume 1266 pages 199–215 (2015)*[122] with slight modifications. In brief, samples were lysed in 1% (w/v) SDS, 2% Triton X-100, PBS pH 7.8 supplemented with EDTA-free protease inhibitors (PI) (Roche), diluted with PBS PI 1:1 for DNA digestion by benzonase (added 1:1000 (v/v)), heated for 10 min at 95 °C, diluted further with PBS PI to a final concentration of 0.1% SDS and 0.2% Triton X-100, and cleared by centrifugation for 5 min at 3000×*g*, 4 °C. Lysates were reduced and alkylated with immobilized TCEP and iodoacetamide (IAA), and subsequently desalted with PD-10 columns (GE Healthcare) to remove excess of reduction and alkylation agents. Click reactions were started by sequential addition of 200 µM tris((1-benzyl-4-triazolyl)methyl)amine, 25 µM disulfide biotin alkyne-tag (DST) (Click Chemistry Tools), and 100 µg/ml Cu(I)Br suspension and samples were incubated in an end-over-end mixer overnight at 4 °C. Following a second desalting step with PD-10 columns, elution in 10.5 ml 0.05% SDS, PBS pH 7.5, and the addition of 1% (v/v) NP40, tagged proteins were bound to 300 µl washed NeutrAvidin agarose (Thermo Scientific, 29202) in an end-over-end mixer overnight at 4 °C. Afterwards, the resins were sequentially washed with a total of 36 ml 0.2% SDS, 1% Triton X-100, PBS pH 7.4, then 18 ml PBS pH 7.4, and finally 18 ml 50 mM ammonium bicarbonate. Tagged proteins were eluted in a two-step procedure with a 5% (v/v) 2-mercaptoethanol/ammonium bicarbonate solution and subsequently lyophilized. After drying, proteins were resolubilized in 8 M Urea, 50 mM Tris-HCl pH 8 with 1 µg trypsin and lysC, predigested for 4 h at room temperature, and then diluted with 50 mM Tris-HCl pH 8 to a final concentration of 2 M urea for overnight digestion. Digests were desalted with C18 SepPak cartridges and in-house-made styroldivinylbenzol reversed phase sulfonate (SDB-RPS) (3 M Empore, 2241) StageTips.

DBCO-agarose SPAAC enrichment. DBCO-agarose enrichment was done as described in Mahdavi et al.[19] with slight modifications. In brief, samples were lysed in 1% SDS, 100 mM chloroacetamide, PBS PI pH 7.4, heated at 95 °C for 10 min, sonicated to shear DNA, and centrifuged at 14.000 × g for 30 min. Cleared lysates were incubated for 3 h at room temperature with 100 µl washed dibenzocyclooctyne (DBCO)-agarose in an end-over-end mixer, and unreacted DBCO groups were subsequently quenched for 30 min by addition of 4 mM Anl. Afterward,

bound proteins were reduced with 10 mM DTT for 15 min at 70 °C and alkylated with 40 mM IAA for 30 min at room temperature. The resins were sequentially washed with a total of 40 ml 0.8% SDS in PBS, 40 ml 8 M urea in 100 mM Tris-HCl (pH 8.0), and 40 ml 20% acetonitrile. Washed resins were resuspended in 100 µl 10% acetonitrile, 50 mM ammonium bicarbonate, and bound proteins were on-bead digested at 37 °C overnight with 1 µg of trypsin and lysC. Digests were collected, resins were washed with 500 µl 50 mM ammonium bicarbonate, washes were combined with digests and desalted with C18 SepPak cartridges.

Alkyne-agarose CuAAC enrichment. Samples were lysed in gua-lysis buffer (6 M guanidinium chloride, 4% (w/v) CHAPS, 0.5 M NaCl, 200 mM Hepes (pH 8) PI), heated at 95 °C for 5 min, sonicated to shear DNA and centrifuged at 10,000×*g* for 30 min. Cleared lysates were mixed with 100 µl (enrichment method comparison) or 50 µl (all other experiments) washed alkyne-agarose and diluted with ddH_2O and a premixed catalyst solution to a final concentration of 1.5 M guanidinium chloride, 1 mM $CuSO_4$, 6.25 mM BTTAA (Click Chemistry Tools), and 10 mM sodium ascorbate. Samples were incubated at room temperature overnight in an end-over-end mixer. Afterward, resins were washed twice with ddH_2O and once with SDS wash buffer (1% (w/v) SDS, 250 mM NaCl, 5 mM EDTA, 100 mM Tris pH 8). After protein reduction with 10 mM DTT for 15 min at 70 °C and alkylation with 40 mM IAA for 30 min at room temperature in SDS wash buffer, resins were sequentially washed with a total of 20 ml SDS wash buffer, 20 ml 20% isopropanol, 20 ml 6 M guanidinium chloride, 100 mM Tris-HCl (pH 8), and 20 ml 20% acetonitrile. Washed resins were resuspended in 100 µl 10% acetonitrile, 2 mM $CaCl_2$, 50 mM Tris-HCl pH 8, and bound proteins were on-bead digested at 37 °C overnight with 1 µg of trypsin and lysC. Digests were collected, resins were washed with 500 µl ddH_2O, washes were combined with digests and desalted with C18 SepPak cartridges (enrichment method comparison and in vitro experiments) or Pierce Peptide Desalting Spin Columns (Thermo Scientific) (in vivo experiments).

For Anl-enrichment-based in vitro or in vivo secretomes experiments, 15 ml cell-conditioned media or 400 µl tumor-bearing mouse serum were collected after Anl labeling (if yields from individual animals were lower, serum from multiple mice was pooled to reach the total volume). Conditioned media were centrifuged for 5 min at 1000×*g* to remove cell debris and supplemented with protease inhibitors. Conditioned media or mouse sera were washed twice with 15 ml 50 mM Tris-HCl pH 8 and concentrated to a volume of 250 µl using Ultracel-3 regenerated cellulose centrifugation filter units with a 3 kDa molecular weight cutoff (Millipore). Samples were mixed 1:1 with gua-lysis buffer, heated for 5 min at 95 °C, 1200 rpm, and then further processed using the alkyne-agarose CuAAC enrichment workflow (see above).

Before lysis and CuAAC Anl-protein enrichment, tissue samples were homogenized to a fine powder with a mortar and pestle in liquid nitrogen.

Sample preparation for mass spectrometry

For proteomics analysis without Anl-enrichment, cells were lysed in SDC buffer (1% sodium deoxycholate (SDC), 10 mM tris(2-carboxy(ethyl)phosphine) (TCEP), 40 mM 2-chloroacetamide (CAA), 100 mM Tris-HCl pH 8.5) heated at 95 °C for 10 min and sonicated to shear DNA. Proteins were digested with trypsin and lysC (1:100 enzyme/protein ratio, w/w) at 37 °C, 1000 rpm overnight. Digests were desalted using in-house-made SDB-RPS StageTips.

Desalted peptides from workflows with or without Anl-enrichment were dried in a vacuum concentrator and resolubilized in 0.1% formic acid. Concentrations were determined using a NanoDrop spectrophotometer and normalized between samples for equal peptide injection. Negative control (WT) samples for evaluating Anl-enrichment specificity were adjusted with corresponding volumes to their corresponding MetRS* samples for injections of equal total yield proportions.

For offline high pH reversed-phase fractionation of peptide samples into 16 fractions (Fig. 1e), a spider fractionator was used as described previously[123].

LC–MS/MS

Peptide mixtures were analyzed with an EASY-nLC 1000 or 1200 ultrahigh-pressure system (Thermo Fisher Scientific) coupled to a Q Exactive HF (293 T Met-substitution), Q Exactive HF-X (enrichment and acquisition method comparisons) or Orbitrap Exploris 480 (all other experiments) instrument (Thermo Fisher Scientific). Peptides (500 ng injections for Q Exactives or 300 ng for Exploris machines) were separated on 50 cm in-house-made 75 µm inner diameter columns, packed with 1.9-µm ReproSil C18 beads (Dr. Maisch GmbH) at a flow rate of 300 nl min^{-1} and 60 °C maintained by an in-house-made column oven. Offline pre-fractionated samples used for acquisition method comparison (see Fig. 1) were eluted with a binary buffer system (buffer A: 0.1% formic acid; buffer B: 80% acetonitrile, 0.1% formic acid) and a nonlinear gradient starting at 3% buffer B followed by a stepwise increase to 23% in 82 min, 40% in 8 min and a wash-out step for 10 min with an increase to 98% buffer B. Spectra were acquired with a data-dependent Top15 MS/MS method: Full scans (300–1650 m/z, automatic gain control (AGC) target = 3e6, maximum injection time = 25 ms, resolution = 60,000 at 200 m/z) were followed by up to 15 MS/MS scans with higher-energy collisional dissociation (HCD) (AGC target = 1e5, maximum injection time = 25 ms, isolation window = 1.5 m/z, normalized collision energy (nce) = 27%, resolution = 15,000 at 200 m/z). All other samples were analyzed without prefractionation in single shot measurements with a nonlinear gradient starting at 5% buffer B followed by a stepwise increase to 30% in 95 min, 60% in 5 min and a wash-out step for 20 min with an increase to 95% buffer B and subsequent decrease to 5% buffer B. Spectra were acquired with a data-dependent Top15 MS/MS method (as described above, but full scans with maximum injection time = 20 ms and MS/MS scans with maximum injection time = 28 ms, isolation window = 1.4 m/z) or data-independent acquisition (used for acquisition method comparison (Fig. 1e) and all following experiments) using full scans with a range of 300–1650 m/z (AGC target = 3e6, maximum injection time = 60 ms, resolution = 120,000 at 200 m/z) followed by MS/MS scans with 32 windows (nce = 27%, AGC target = 1e6, maximum injection time = 54 ms, resolution = 30,000 at 200 m/z). Data acquisition was controlled by Xcalibur (version 4.4.16.14, Thermo Fisher Scientific).

LC–MS/MS data analysis

DDA MS raw files were processed by MaxQuant[124] (version 2.0.1.0.) using default parameters for orbitrap instruments with 1% FDR at the peptide and protein level, enabling MaxLFQ for label-free quantification. For analysis of Met-substitute incorporation in 293 T cells, Met-Anl, Met-Aha, and Met-Met+4 substitutions were added as variable modifications.

DIA MS raw files were processed by DIA-NN[90] (version 1.8) with FASTA digest for library-free search and deep learning-based spectra, RTs, and IMs prediction enabled. Precursor FDR was set to 1%, and default parameters were used with the following changes: The precursor range was restricted to 300–1650 m/z, and the fragment ion range to 200 – 1650 m/z. The "--relaxed-prot-inf" option was enabled via the command line. Mass accuracies and scan windows were optimized for individual experiments as recommended by the developers. MBR was enabled, neural network classifier was set to "double-pass mode," and the quantification strategy to "robust LC (high accuracy)."

Spectra were matched against the human (June 2022, 79,276 entries) or mouse (January 2022, 55,105 entries) UniProt FASTA database.

Raw files were processed in two separate analyses for optimal independence of FACS- and AnI enrichment-based cancer cell-selective proteomics results (Fig. 2). MetRS*/ WT 8661 tumor rawfiles were reprocessed together with samples from other PDAC subtypes for in vivo PDAC cell subtype comparison (Fig. 5). 8661 PDAC (solo) secretome results (Fig. 3) were also used for secretome benchmarking (Fig. 1).

Evaluation of AnI-enrichment specificity. Except for enrichment method benchmarking (Fig. 1c, d), data from all AnI-enrichment-based experiments were filtered for specifically enriched proteins before further analysis. To evaluate enrichment specificity, samples were compared to corresponding negative control samples (WT equivalents of MetRS*-expressing cells that were treated equally and processed in parallel) and only proteins that were not identified in controls or had an at least 3fold higher median intensity than in controls were retained. For technical experiments (Figs. 1 and 2), PDAC MetRS* tumor comparison experiments (Fig. 5), and serum secretomics experiments with the PDAC lines 8661 and 8513 (Fig. 6), corresponding WT controls were used in triplicates for each PDAC line. We used aggregated control sample groups for multiple experimental groups in the co-culture experiments (Figs. 3 and 4): Three BMM WT samples were used to control BMM MetRS* samples cultured in isolation. A group of four co-cultured BMM WT + PDAC WT samples (one with each of the four PDAC lines) was used as controls for all BMM MetRS* + PDAC WT co-culture samples. Both solo and co-cultured PDAC MetRS* samples were controlled with the more conservative corresponding co-culture control samples (PDAC WT + BMM WT in triplicates for each of the PDAC lines).

Statistical analysis. Bioinformatic analyses were performed with Perseus[125] (version 1.6.10.43) and R (version 4.1.2). Before statistical analysis, quantified proteins were filtered for at least two valid values in at least one group of replicates. The remaining missing values were imputed by random draw from a normal distribution with a width of 0.3 and a downshift of 1.8 relatives to the standard deviation of measured values. Statistical tests and parameters used to evaluate annotation enrichment and significant abundance differences of quantified proteins are specified in the figure legends. For box-and-whisker plots, standard boxplot features (lower quartile, median, upper quartile) were used as defined by ggplot2 version 3.4.0.

Intercellular communication analysis. Interactions between PDAC cells and macrophages in co-culture were inferred based on annotated ligand–receptor interactions from CellPhoneDB[39] (v.2.0) extended by proteins with secretomes-derived experimental evidence[126]. BMM receptor expression levels were sourced from global proteomes, PDAC cell ligand expression levels from secretomes for secreted ligands, and global proteomes for membrane-bound ligands after filtering and imputation of missing values (see above).

Reporting summary

Further information on research design is available in the Nature Portfolio Reporting Summary linked to this article.

Data availability

The mass spectrometry proteomics data have been deposited to the ProteomeXchange Consortium (http://proteomecentral.proteomexchange.org) via the PRIDE partner repository[127] with the dataset identifier PXD040084, which is publicly available. Source data are provided in this paper.

References

1. Siegel, R. L., Miller, K. D., Fuchs, H. E. & Jemal, A. Cancer statistics, 2022. *CA Cancer J. Clin.* **72**, 7–33 (2022).
2. Neesse, A., Algul, H., Tuveson, D. A. & Gress, T. M. Stromal biology and therapy in pancreatic cancer: a changing paradigm. *Gut* **64**, 1476–1484 (2015).
3. Hosein, A. N., Brekken, R. A. & Maitra, A. Pancreatic cancer stroma: an update on therapeutic targeting strategies. *Nat. Rev. Gastroenterol. Hepatol.* **17**, 487–505 (2020).
4. Collisson, E. A., Bailey, P., Chang, D. K. & Biankin, A. V. Molecular subtypes of pancreatic cancer. *Nat. Rev. Gastroenterol. Hepatol.* **16**, 207–220 (2019).
5. Collisson, E. A. et al. Subtypes of pancreatic ductal adenocarcinoma and their differing responses to therapy. *Nat. Med.* **17**, 500–503 (2011).
6. Moffitt, R. A. et al. Virtual microdissection identifies distinct tumor- and stroma-specific subtypes of pancreatic ductal adenocarcinoma. *Nat. Genet.* **47**, 1168–1178 (2015).
7. Bailey, P. et al. Genomic analyses identify molecular subtypes of pancreatic cancer. *Nature* **531**, 47–52 (2016).
8. S, N. K. et al. Morphological classification of pancreatic ductal adenocarcinoma that predicts molecular subtypes and correlates with clinical outcome. *Gut* **69**, 317–328 (2020).
9. Aung, K. L. et al. Genomics-driven precision medicine for advanced pancreatic cancer: early results from the COMPASS trial. *Clin. Cancer Res.* **24**, 1344–1354 (2018).
10. Schwanhausser, B. et al. Global quantification of mammalian gene expression control. *Nature* **473**, 337–342 (2011).
11. Jovanovic, M. et al. Immunogenetics. Dynamic profiling of the protein life cycle in response to pathogens. *Science* **347**, 1259038 (2015).
12. Meissner, F., Scheltema, R. A., Mollenkopf, H. J. & Mann, M. Direct proteomic quantification of the secretome of activated immune cells. *Science* **340**, 475–478 (2013).
13. Rieckmann, J. C. et al. Social network architecture of human immune cells unveiled by quantitative proteomics. *Nat. Immunol.* **18**, 583–593 (2017).
14. Swietlik, J. J., Sinha, A. & Meissner, F. Dissecting intercellular signaling with mass spectrometry-based proteomics. *Curr. Opin. Cell Biol.* **63**, 20–30 (2020).
15. Mertins, P. et al. Proteogenomics connects somatic mutations to signalling in breast cancer. *Nature* **534**, 55–62 (2016).
16. Jayavelu, A. K. et al. Splicing factor YBX1 mediates persistence of JAK2-mutated neoplasms. *Nature* **588**, 157–163 (2020).
17. Mund, A. et al. Deep Visual Proteomics defines single-cell identity and heterogeneity. *Nat. Biotechnol.* https://doi.org/10.1038/s41587-022-01302-5 (2022).
18. Tape, C. J. et al. Oncogenic KRAS regulates tumor cell signaling via stromal reciprocation. *Cell* **165**, 910–920 (2016).
19. Mahdavi, A. et al. Engineered aminoacyl-tRNA synthetase for cell-selective analysis of mammalian protein synthesis. *J. Am. Chem. Soc.* **138**, 4278–4281 (2016).
20. Ngo, J. T. et al. Cell-selective metabolic labeling of proteins. *Nat. Chem. Biol.* **5**, 715–717 (2009).
21. Tanrikulu, I. C., Schmitt, E., Mechulam, Y., Goddard, W. A. 3rd & Tirrell, D. A. Discovery of Escherichia coli methionyl-tRNA synthetase mutants for efficient labeling of proteins with azidonorleucine in vivo. *Proc. Natl Acad. Sci. USA* **106**, 15285–15290 (2009).
22. Liu, Y. et al. Application of bio-orthogonal proteome labeling to cell transplantation and heterochronic parabiosis. *Nat. Commun.* **8**, 643 (2017).
23. Alvarez-Castelao, B. et al. Cell-type-specific metabolic labeling of nascent proteomes in vivo. *Nat. Biotechnol.* **35**, 1196–1201 (2017).
24. Hines, W. C., Su, Y., Kuhn, I., Polyak, K. & Bissell, M. J. Sorting out the FACS: a devil in the details. *Cell Rep.* **6**, 779–781 (2014).
25. Elkord, E., Williams, P. E., Kynaston, H. & Rowbottom, A. W. Human monocyte isolation methods influence cytokine production from

in vitro generated dendritic cells. *Immunology* **114**, 204–212 (2005).
26. Andra, I. et al. An evaluation of T-cell functionality after flow cytometry sorting revealed p38 MAPK activation. *Cytometry A* **97**, 171–183 (2020).
27. Llufrio, E. M., Wang, L., Naser, F. J. & Patti, G. J. Sorting cells alters their redox state and cellular metabolome. *Redox Biol.* **16**, 381–387 (2018).
28. Azizian, N. G. et al. Selective labeling and identification of the tumor cell proteome of pancreatic cancer in vivo. *J. Proteome Res.* **20**, 858–866 (2021).
29. Bekker-Jensen, D. B. et al. A compact quadrupole-orbitrap mass spectrometer with FAIMS interface improves proteome coverage in short LC gradients. *Mol. Cell Proteom.* **19**, 716–729 (2020).
30. Erdmann, I. et al. Cell-selective labelling of proteomes in *Drosophila melanogaster*. *Nat. Commun.* **6**, 7521 (2015).
31. Muller, A., Stellmacher, A., Freitag, C. E., Landgraf, P. & Dieterich, D. C. Monitoring astrocytic proteome dynamics by cell type-specific protein labeling. *PLoS ONE* **10**, e0145451 (2015).
32. McKay, C. S. & Finn, M. G. Click chemistry in complex mixtures: bioorthogonal bioconjugation. *Chem. Biol.* **21**, 1075–1101 (2014).
33. Presolski, S. I., Hong, V. P. & Finn, M. G. Copper-catalyzed azide-alkyne click chemistry for bioconjugation. *Curr. Protoc. Chem. Biol.* **3**, 153–162 (2011).
34. Yang, Y., Yang, X. & Verhelst, S. H. Comparative analysis of click chemistry mediated activity-based protein profiling in cell lysates. *Molecules* **18**, 12599–12608 (2013).
35. Besanceney-Webler, C. et al. Increasing the efficacy of bioorthogonal click reactions for bioconjugation: a comparative study. *Angew. Chem. Int. Ed. Engl.* **50**, 8051–8056 (2011).
36. van Geel, R., Pruijn, G. J., van Delft, F. L. & Boelens, W. C. Preventing thiol-yne addition improves the specificity of strain-promoted azide-alkyne cycloaddition. *Bioconjug. Chem.* **23**, 392–398 (2012).
37. Alvarez-Castelao, B., Schanzenbacher, C. T., Langer, J. D. & Schuman, E. M. Cell-type-specific metabolic labeling, detection and identification of nascent proteomes in vivo. *Nat. Protoc.* **14**, 556–575 (2019).
38. Eichelbaum, K., Winter, M., Berriel Diaz, M., Herzig, S. & Krijgsveld, J. Selective enrichment of newly synthesized proteins for quantitative secretome analysis. *Nat. Biotechnol.* **30**, 984–990 (2012).
39. Efremova, M., Vento-Tormo, M., Teichmann, S. A. & Vento-Tormo, R. CellPhoneDB: inferring cell-cell communication from combined expression of multi-subunit ligand-receptor complexes. *Nat. Protoc.* **15**, 1484–1506 (2020).
40. Falcomata, C. et al. Selective multi-kinase inhibition sensitizes mesenchymal pancreatic cancer to immune checkpoint blockade by remodeling the tumor microenvironment. *Nat. Cancer* **3**, 318–336 (2022).
41. Varnavides, G. et al. In search of a universal method: a comparative survey of bottom-up proteomics sample preparation methods. *J. Proteome Res.* **21**, 2397–2411 (2022).
42. Alfonso-Garrido, J., Garcia-Calvo, E. & Luque-Garcia, J. L. Sample preparation strategies for improving the identification of membrane proteins by mass spectrometry. *Anal. Bioanal. Chem.* **407**, 4893–4905 (2015).
43. Clark, C. E. et al. Dynamics of the immune reaction to pancreatic cancer from inception to invasion. *Cancer Res.* **67**, 9518–9527 (2007).
44. Ruffell, B. & Coussens, L. M. Macrophages and therapeutic resistance in cancer. *Cancer Cell* **27**, 462–472 (2015).
45. Mueller, S. et al. Evolutionary routes and KRAS dosage define pancreatic cancer phenotypes. *Nature* **554**, 62–68 (2018).
46. Ashburner, M. et al. Gene ontology: tool for the unification of biology. The Gene Ontology Consortium. *Nat. Genet.* **25**, 25–29 (2000).
47. Hollmen, M., Roudnicky, F., Karaman, S. & Detmar, M. Characterization of macrophage–cancer cell crosstalk in estrogen receptor positive and triple-negative breast cancer. *Sci. Rep.* **5**, 9188 (2015).
48. Castro, F., Cardoso, A. P., Goncalves, R. M., Serre, K. & Oliveira, M. J. Interferon-gamma at the crossroads of tumor immune surveillance or evasion. *Front. Immunol.* **9**, 847 (2018).
49. Setrerrahmane, S. & Xu, H. Tumor-related interleukins: old validated targets for new anti-cancer drug development. *Mol. Cancer* **16**, 153 (2017).
50. Winkler, J., Abisoye-Ogunniyan, A., Metcalf, K. J. & Werb, Z. Concepts of extracellular matrix remodelling in tumour progression and metastasis. *Nat. Commun.* **11**, 5120 (2020).
51. Cox, T. R. The matrix in cancer. *Nat. Rev. Cancer* **21**, 217–238 (2021).
52. Murray, P. J. Macrophage polarization. *Annu Rev. Physiol.* **79**, 541–566 (2017).
53. Mantovani, A., Sica, A. & Locati, M. Macrophage polarization comes of age. *Immunity* **23**, 344–346 (2005).
54. Candido, J. B. et al. CSF1R(+) macrophages sustain pancreatic tumor growth through T cell suppression and maintenance of key gene programs that define the squamous subtype. *Cell Rep.* **23**, 1448–1460 (2018).
55. Kemp, S. B. et al. Pancreatic cancer is marked by complement-high blood monocytes and tumor-associated macrophages. *Life Sci. Alliance* https://doi.org/10.26508/lsa.202000935 (2021).
56. Zhu, Y. et al. Tissue-resident macrophages in pancreatic ductal adenocarcinoma originate from embryonic hematopoiesis and promote tumor progression. *Immunity* **47**, 323–338.e326 (2017).
57. Zhang, F. et al. TGF-beta induces M2-like macrophage polarization via SNAIL-mediated suppression of a pro-inflammatory phenotype. *Oncotarget* **7**, 52294–52306 (2016).
58. Kratochvill, F. et al. TNF counterbalances the emergence of M2 tumor macrophages. *Cell Rep.* **12**, 1902–1914 (2015).
59. Fernando, M. R., Reyes, J. L., Iannuzzi, J., Leung, G. & McKay, D. M. The pro-inflammatory cytokine, interleukin-6, enhances the polarization of alternatively activated macrophages. *PLoS ONE* **9**, e94188 (2014).
60. Zhao, C. C. et al. TNFSF15 facilitates differentiation and polarization of macrophages toward M1 phenotype to inhibit tumor growth. *Oncoimmunology* **11**, 2032918 (2022).
61. Li, M. et al. CCL5 deficiency promotes liver repair by improving inflammation resolution and liver regeneration through M2 macrophage polarization. *Cell Mol. Immunol.* **17**, 753–764 (2020).
62. Castro, B. A. et al. Macrophage migration inhibitory factor down-regulation: a novel mechanism of resistance to anti-angiogenic therapy. *Oncogene* **36**, 3749–3759 (2017).
63. Yaddanapudi, K. et al. Control of tumor-associated macrophage alternative activation by macrophage migration inhibitory factor. *J. Immunol.* **190**, 2984–2993 (2013).
64. Schaper, F. et al. High mobility group box 1 skews macrophage polarization and negatively influences phagocytosis of apoptotic cells. *Rheumatology* **55**, 2260–2270 (2016).
65. Willingham, S. B. et al. The CD47-signal regulatory protein alpha (SIRPa) interaction is a therapeutic target for human solid tumors. *Proc. Natl Acad. Sci. USA* **109**, 6662–6667 (2012).
66. Zhang, M. et al. Anti-CD47 treatment stimulates phagocytosis of glioblastoma by M1 and M2 polarized macrophages and promotes M1 polarized macrophages in vivo. *PLoS ONE* **11**, e0153550 (2016).
67. Tamagnone, L. Emerging role of semaphorins as major regulatory signals and potential therapeutic targets in cancer. *Cancer Cell* **22**, 145–152 (2012).

68. Muller, M. W. et al. Association of axon guidance factor semaphorin 3A with poor outcome in pancreatic cancer. *Int. J. Cancer* **121**, 2421–2433 (2007).
69. Casazza, A. et al. Impeding macrophage entry into hypoxic tumor areas by Sema3A/Nrp1 signaling blockade inhibits angiogenesis and restores antitumor immunity. *Cancer Cell* **24**, 695–709 (2013).
70. Korner, A. et al. Sema7A is crucial for resolution of severe inflammation. *Proc. Natl Acad. Sci. USA* https://doi.org/10.1073/pnas.2017527118 (2021).
71. Chen, X. et al. TIGIT negatively regulates inflammation by altering macrophage phenotype. *Immunobiology* **221**, 48–55 (2016).
72. Gorvel, L. & Olive, D. Targeting the "PVR-TIGIT axis" with immune checkpoint therapies. *F1000Res* https://doi.org/10.12688/f1000research.22877.1 (2020).
73. Tian, C. et al. Proteomic analyses of ECM during pancreatic ductal adenocarcinoma progression reveal different contributions by tumor and stromal cells. *Proc. Natl Acad. Sci. USA* **116**, 19609–19618 (2019).
74. Tian, C. et al. Cancer cell-derived matrisome proteins promote metastasis in pancreatic ductal adenocarcinoma. *Cancer Res.* **80**, 1461–1474 (2020).
75. Naba, A. et al. The matrisome: in silico definition and in vivo characterization by proteomics of normal and tumor extracellular matrices. *Mol. Cell Proteom.* **11**, M111 014647 (2012).
76. Puleo, F. et al. Stratification of pancreatic ductal adenocarcinomas based on tumor and microenvironment features. *Gastroenterology* **155**, 1999–2013.e1993 (2018).
77. Kagan, H. M. & Li, W. Lysyl oxidase: properties, specificity, and biological roles inside and outside of the cell. *J. Cell Biochem.* **88**, 660–672 (2003).
78. Miller, B. W. et al. Targeting the LOX/hypoxia axis reverses many of the features that make pancreatic cancer deadly: inhibition of LOX abrogates metastasis and enhances drug efficacy. *EMBO Mol. Med.* **7**, 1063–1076 (2015).
79. Geyer, P. E., Holdt, L. M., Teupser, D. & Mann, M. Revisiting biomarker discovery by plasma proteomics. *Mol. Syst. Biol.* **13**, 942 (2017).
80. Liu, Y. & Cao, X. Characteristics and significance of the pre-metastatic niche. *Cancer Cell* **30**, 668–681 (2016).
81. Peinado, H. et al. Pre-metastatic niches: organ-specific homes for metastases. *Nat. Rev. Cancer* **17**, 302–317 (2017).
82. Hoye, A. M. & Erler, J. T. Structural ECM components in the pre-metastatic and metastatic niche. *Am. J. Physiol. Cell Physiol.* **310**, C955–C967 (2016).
83. Gillot, L., Baudin, L., Rouaud, L., Kridelka, F. & Noel, A. The pre-metastatic niche in lymph nodes: formation and characteristics. *Cell Mol. Life Sci.* **78**, 5987–6002 (2021).
84. Valastyan, S. & Weinberg, R. A. Tumor metastasis: molecular insights and evolving paradigms. *Cell* **147**, 275–292 (2011).
85. Vanharanta, S. & Massague, J. Origins of metastatic traits. *Cancer Cell* **24**, 410–421 (2013).
86. Ribas, A. & Wolchok, J. D. Cancer immunotherapy using checkpoint blockade. *Science* **359**, 1350–1355 (2018).
87. Schiapparelli, L. M. et al. Activity-induced cortical glutamatergic neuron nascent proteins. *J. Neurosci.* **42**, 7900–7920 (2022).
88. Rayaprolu, S. et al. Cell type-specific biotin labeling in vivo resolves regional neuronal and astrocyte proteomic differences in mouse brain. *Nat. Commun.* **13**, 2927 (2022).
89. Sun, X. et al. Deep single-cell-type proteome profiling of mouse brain by nonsurgical AAV-mediated proximity labeling. *Anal. Chem.* **94**, 5325–5334 (2022).
90. Demichev, V., Messner, C. B., Vernardis, S. I., Lilley, K. S. & Ralser, M. DIA-NN: neural networks and interference correction enable deep proteome coverage in high throughput. *Nat. Methods* **17**, 41–44 (2020).
91. Bogdanowicz, D. R. & Lu, H. H. Studying cell-cell communication in co-culture. *Biotechnol. J.* **8**, 395–396 (2013).
92. Vis, M. A. M., Ito, K. & Hofmann, S. Impact of culture medium on cellular interactions in in vitro co-culture systems. *Front. Bioeng. Biotechnol.* **8**, 911 (2020).
93. Gauthier, N. P. et al. Cell-selective labeling using amino acid precursors for proteomic studies of multicellular environments. *Nat. Methods* **10**, 768–773 (2013).
94. Mertins, P. et al. Ischemia in tumors induces early and sustained phosphorylation changes in stress kinase pathways but does not affect global protein levels. *Mol. Cell Proteom.* **13**, 1690–1704 (2014).
95. Tanzer, M. C., Bludau, I., Stafford, C. A., Hornung, V. & Mann, M. Phosphoproteome profiling uncovers a key role for CDKs in TNF signaling. *Nat. Commun.* **12**, 6053 (2021).
96. Di Martino, J. S. et al. A tumor-derived type III collagen-rich ECM niche regulates tumor cell dormancy. *Nat. Cancer* **3**, 90–107 (2022).
97. Steins, A. et al. High-grade mesenchymal pancreatic ductal adenocarcinoma drives stromal deactivation through CSF-1. *EMBO Rep.* **21**, e48780 (2020).
98. Maurer, C. et al. Experimental microdissection enables functional harmonisation of pancreatic cancer subtypes. *Gut* **68**, 1034–1043 (2019).
99. Pickup, M. W., Mouw, J. K. & Weaver, V. M. The extracellular matrix modulates the hallmarks of cancer. *EMBO Rep.* **15**, 1243–1253 (2014).
100. Cox, T. R. & Erler, J. T. Fibrosis and cancer: partners in crime or opposing forces. *Trends Cancer* **2**, 279–282 (2016).
101. Ozdemir, B. C. et al. Depletion of carcinoma-associated fibroblasts and fibrosis induces immunosuppression and accelerates pancreas cancer with reduced survival. *Cancer Cell* **25**, 719–734 (2014).
102. Rhim, A. D. et al. Stromal elements act to restrain, rather than support, pancreatic ductal adenocarcinoma. *Cancer Cell* **25**, 735–747 (2014).
103. Tanaka, N. et al. Clinical implications of lysyl oxidase-like protein 2 expression in pancreatic cancer. *Sci. Rep.* **8**, 9846 (2018).
104. Alonso-Nocelo, M. et al. Macrophages direct cancer cells through a LOXL2-mediated metastatic cascade in pancreatic ductal adenocarcinoma. *Gut* https://doi.org/10.1136/gutjnl-2021-325564 (2022).
105. Jiang, H. L. et al. Pancreatic ductal adenocarcinoma progression is restrained by stromal matrix. *J. Clin. Invest.* **130**, 4704–4709 (2020).
106. Saatci, O. et al. Targeting lysyl oxidase (LOX) overcomes chemotherapy resistance in triple negative breast cancer. *Nat. Commun.* **11**, 2416 (2020).
107. Rachman-Tzemah, C. et al. Blocking surgically induced lysyl oxidase activity reduces the risk of lung metastases. *Cell Rep.* **19**, 774–784 (2017).
108. Kim, K. E. et al. Dynamic tracking and identification of tissue-specific secretory proteins in the circulation of live mice. *Nat. Commun.* **12**, 5204 (2021).
109. Droujinine, I. A. et al. Proteomics of protein trafficking by in vivo tissue-specific labeling. *Nat. Commun.* **12**, 2382 (2021).
110. Wei, W. et al. Cell type-selective secretome profiling in vivo. *Nat. Chem. Biol.* **17**, 326–334 (2021).
111. Liu, J., Jang, J. Y., Pirooznia, M., Liu, S. & Finkel, T. The secretome mouse provides a genetic platform to delineate tissue-specific in vivo secretion. *Proc Natl Acad Sci USA* https://doi.org/10.1073/pnas.2005134118 (2021).
112. Brunner, A. D. et al. Ultra-high sensitivity mass spectrometry quantifies single-cell proteome changes upon perturbation. *Mol. Syst. Biol.* **18**, e10798 (2022).

113. Demichev, V. et al. dia-PASEF data analysis using FragPipe and DIA-NN for deep proteomics of low sample amounts. *Nat. Commun.* **13**, 3944 (2022).
114. Allen, T. M. et al. Humanized immune system mouse models: progress, challenges and opportunities. *Nat. Immunol.* **20**, 770–774 (2019).
115. Guler, G. D. et al. Detection of early stage pancreatic cancer using 5-hydroxymethylcytosine signatures in circulating cell free DNA. *Nat. Commun.* **11**, 5270 (2020).
116. Hosein, A. N., Dougan, S. K., Aguirre, A. J. & Maitra, A. Translational advances in pancreatic ductal adenocarcinoma therapy. *Nat. Cancer* **3**, 272–286 (2022).
117. Hyeon, D. Y. et al. Proteogenomic landscape of human pancreatic ductal adenocarcinoma in an Asian population reveals tumor cell-enriched and immune-rich subtypes. *Nat. Cancer* https://doi.org/10.1038/s43018-022-00479-7 (2022).
118. Clausen, B. E., Burkhardt, C., Reith, W., Renkawitz, R. & Forster, I. Conditional gene targeting in macrophages and granulocytes using LysMcre mice. *Transgenic Res.* **8**, 265–277 (1999).
119. von Burstin, J. et al. E-cadherin regulates metastasis of pancreatic cancer in vivo and is suppressed by a SNAIL/HDAC1/HDAC2 repressor complex. *Gastroenterology* **137**, 371.e361–365 (2009). 361-371.
120. Weischenfeldt, J. & Porse, B. Bone marrow-derived macrophages (BMM): isolation and applications. *CSH Protoc.* **2008**, pdb prot5080 (2008).
121. Frauenstein, A. et al. Identification of covalent modifications regulating immune signaling complex composition and phenotype. *Mol. Syst. Biol.* **17**, e10125 (2021).
122. Landgraf, P., Antileo, E. R., Schuman, E. M. & Dieterich, D. C. BONCAT: metabolic labeling, click chemistry, and affinity purification of newly synthesized proteomes. *Methods Mol. Biol.* **1266**, 199–215 (2015).
123. Kulak, N. A., Geyer, P. E. & Mann, M. Loss-less nano-fractionator for high sensitivity, high coverage proteomics. *Mol. Cell Proteom.* **16**, 694–705 (2017).
124. Cox, J. & Mann, M. MaxQuant enables high peptide identification rates, individualized p.p.b.-range mass accuracies and proteome-wide protein quantification. *Nat. Biotechnol.* **26**, 1367–1372 (2008).
125. Tyanova, S. et al. The Perseus computational platform for comprehensive analysis of (prote)omics data. *Nat. Methods* **13**, 731–740 (2016).
126. Phulphagar, K. et al. Proteomics reveals distinct mechanisms regulating the release of cytokines and alarmins during pyroptosis. *Cell Rep.* **34**, 108826 (2021).
127. Perez-Riverol, Y. et al. The PRIDE database and related tools and resources in 2019: improving support for quantification data. *Nucleic Acids Res.* **47**, D442–D450 (2019).
128. Cox, J. & Mann, M. 1D and 2D annotation enrichment: a statistical method integrating quantitative proteomics with complementary high-throughput data. *BMC Bioinforma.* **13**, S12 (2012).

Acknowledgements

We thank I. Paron, C. Deiml, A. Strasser, J. B. Mueller-Reif, L. Schweizer, S. Steigerwald and P. Skowronek for MS assistance; V. Boeck, S. Ettl, M. Zukowska, A. Kudaliyanage, Y. P. Alvarez Valdivia, and A. Ullrich for technical assistance; T. Viturawong for intercellular communication analysis framework; M. Oroshi for computer and database support; and M. Mann and Marc Schmidt-Supprian for helpful discussions. This work was funded by the Max Planck Society for the Advancement of Science, the German Cancer Consortium (DKTK), the Wilhelm Sander-Stiftung (2020.174.1 and 2017.091.2) and the Deutsche Forschungsgemeinschaft (DFG, German Research Foundation), Cluster of Excellence EXC 2151 ImmunoSensation2, Project-ID 360372040 (SFB 1335), Project-ID 408885537 (TRR 274), Project-ID 432325352 (SFB 1454), Project-ID 450149205 (TRR 333), Project-ID 329628492 (SFB 1321), Project-ID 515991405 (ME 4766/2-1 and SA 1374/8-1), Project-ID 515571394 (SA 1374/7-1), Project-ID 360394750 (SCHO 1732/2-1), Project ID 458890590 (SA 1374/6-1), Project ID 219542602 (SA 1374/4-3), Project-ID 97850925 (SFB854), and Project-ID 362321501 (GRK2413) and the Bundesministerium für Bildung und Forschung (BMBF) Kmu-innovativ 031B0686B.

Author contributions

J.J.S. performed experiments. J.J.S. developed and implemented bioinformatics methods. J.J.S. and F.M. conceived the data analysis and interpreted the data. SB and CF bred MetRS*-LysMCre mice, performed PDAC cell culture, characterization, and quality control, in vivo mouse experiments, flow cytometry analyses, and FACS. DS analyzed and interpreted data with S.B. and C.F. A.S. contributed to initial mouse experiments, testing of in vivo labeling schemes, and consultation on data analysis methods. D.F. contributed to co-culture experiments and figure design. J.C. prepared communication plot visualizations. S.E. helped with bone marrow-derived macrophage generation and experiments. P.L. and D.D. supplied reagents, initial training, and consultation on Anl-enrichment procedures. H.D. provided advice and supervision of initial experiments. F.M. conceived the study. F.M. and D.S. provided funding and supervised the experiments. J.S.S. and F.M. wrote the paper.

Funding

Open Access funding enabled and organized by Projekt DEAL.

Competing interests

The authors declare no competing interests.

Additional information

Supplementary information The online version contains supplementary material available at https://doi.org/10.1038/s41467-023-38171-8.

Correspondence and requests for materials should be addressed to Dieter Saur or Felix Meissner.

Peer review information *Nature Communications* thanks Arnaud Droit and the other, anonymous, reviewer(s) for their contribution to the peer review of this work. A peer review file is available.

Article 3: MetRS*-based deep cell-selective tissue proteomics and secretomics in vivo

Methods in Cell Biology 202, in press

Jonathan J. Swietlik[1], Felix Meissner[2]

[1] Experimental Systems Immunology, Max Planck Institute of Biochemistry, Martinsried, Germany

[2] Institute of Innate Immunity, Department of Systems Immunology and Proteomics, Medical Faculty, University of Bonn, Bonn, Germany

Developing a highly efficient click chemistry enrichment proteomics workflow was essential in enabling our successful cell-selective analysis of pancreatic ductal adenocarcinoma mouse models (see Article 2). This method's high yields and specificity allowed for unprecedented depth in MetRS*-based tissue analyses and introduced a new standard for the sensitive detection of cell type-specific secretomes *in vivo*. Encouraged by these results, we expanded the application of this technique to a broader range of contexts, launching diverse collaborative projects across various fields of biology, aiming to address questions that were previously difficult to explore due to the limitations of conventional cell isolation methods.

To make our protocols easily accessible to the broader scientific community, we accepted an invitation to contribute a comprehensive description of our workflow to an issue of *Methods in Cell Biology*. In this book chapter, we provide a detailed protocol for sample preparation, discuss best practices for experimental design, control strategies, and data analysis, and share advice for troubleshooting.

Contribution

I developed the workflows and guidelines detailed in this publication. Felix Meissner and I co-wrote the manuscript.

MetRS*-based deep cell-selective tissue proteomics and secretomics *in vivo*

Jonathan J. Swietlik[a] **and Felix Meissner**[a,b,*]

[a]Experimental Systems Immunology, Max Planck Institute of Biochemistry, Martinsried, Germany
[b]Department of Systems Immunology and Proteomics, Medical Faculty, Institute of Innate Immunity, University of Bonn, Bonn, Germany
[*]Corresponding author: e-mail address: felix.meissner'at'uni-bonn.de

Contents

Abstract

Combining MetRS*-based cell-selective protein labeling with mass spectrometry-based proteomics is a powerful approach for investigating intercellular communication within tissues. Cell-selective labeling overcomes limitations of cell sorting techniques and facilitates cell type-specific proteome and secretome analyses *in vivo*. Our recent work has showcased the application of this method for the comprehensive proteomic characterization of cellular proteins in tissues, as well as released proteins in the bloodstream. Here, we present experimental guidelines for MetRS*-based cell-selective proteomics experiments *in vivo* and a detailed sample preparation protocol for tissues and body fluids.

Methods in Cell Biology
ISSN 0091-679X
https://doi.org/10.1016/bs.mcb.2024.08.002

1. Introduction

Mass spectrometry (MS)-based proteomics enables in-depth analyses of cellular proteomes, providing a key foundation for discovery-driven biomedical research and systems biology. Unlike transcriptomics methods, it offers insights on post-translationally modified proteoforms and protein localization, including extracellular proteins, making it uniquely suited for mechanistic investigations of intercellular signaling (Meissner, Scheltema, Mollenkopf, & Mann, 2013; Phulphagar et al., 2021; Rieckmann et al., 2017; Swietlik, Sinha, & Meissner, 2020).

To delineate cell type-specific proteome dynamics in complex heterocellular systems like tissues, MS is frequently combined with cell dissociation and sorting methods like fluorescence-activated cell sorting (FACS). Yet, some research questions remain challenging to address due to technical constraints inherent in cell sorting. For example, isolating intact cells without significant disturbance of their native state can be aggravated by morphological features, such as the delicate cell extensions of neurons, or tight association with other cells and extracellular matrix. Moreover, extracellular proteins are lost in the process of cell sorting, which has constrained cell-specific secretomics studies primarily to experiments with cultured cells *in vitro*. However, a direct and cell type-resolved analysis of protein secretion within native tissue contexts could significantly advance our understanding of intercellular signaling networks, underscoring a need for innovative techniques that circumvent these limitations.

Cell-selective protein labeling is emerging as a complementary strategy for cell type-resolved MS-based proteomics. Recently, techniques such as BioID, TurboID, and related proximity labeling methods have been successfully adapted to profile cell-selective proteomes and secretomes in model organisms (Droujinine et al., 2021; Kim et al., 2021; Liu, Jang, Pirooznia, Liu, & Finkel, 2021; Spence et al., 2019; Wei et al., 2021; Yang et al., 2022). In addition, metabolic protein labeling methods have shown to be particularly effective in resolving intercellular communication mechanisms within heterocellular model systems and tissues. While techniques like cell-selective labelling with amino acid precursors (CTAP) (Gauthier et al., 2013) have enabled the dissection of cellular crosstalk *in vitro* (Tape et al., 2016), labeling with non-canonical amino acids that facilitate specific protein enrichment are well suited for applications with high background protein levels, especially *in vivo*. One of the most widely adapted approaches

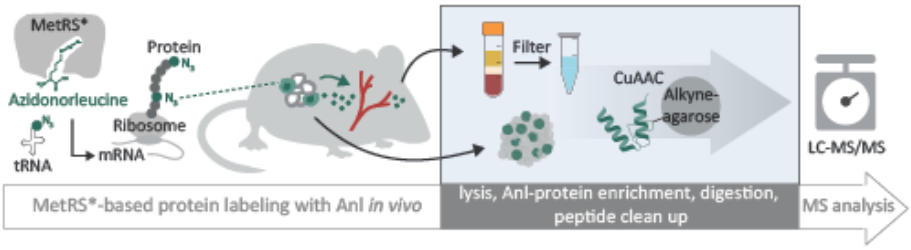

Fig. 1 Scheme of MetRS*-based cell selective proteomics and secretomics experiments: MetRS*-expressing cells incorporate Anl into proteins. Anl-modified proteins are enriched from tissue or body fluid samples by copper(I)-catalyzed azide-alkyne cycloaddition (*CuAAC*). Enriched proteins are digested, resulting peptides are cleaned by solid phase extraction, and analyzed by mass spectrometry.

is metabolic protein labeling with azidonorleucine (Anl) (Mahdavi et al., 2016; Ngo et al., 2009; Tanrikulu, Schmitt, Mechulam, Goddard, & Tirrell, 2009) (see Fig. 1). Anl incorporation relies on the expression of the engineered enzyme methionyl-tRNA synthetase L274G (MetRS*), which carries a point mutation that expands its amino acid binding pocket. MetRS*-expressing cells activate Anl, and incorporate it into proteins as a methionine substitute, whereas cells missing the enzyme are not labeled. Multiple studies in model organisms have confirmed very high incorporation specificity and broad tissue compatibility (Alvarez-Castelao et al., 2017; Azizian et al., 2021; Erdmann et al., 2015; Liu et al., 2017). Although the incorporation of non-canonical amino acids may affect the structure and function of modified proteins, previous research has shown ranges of Anl treatment doses and durations that are well tolerated, with minimal or no apparent adverse effects (Alvarez-Castelao, Schanzenbacher, Langer, & Schuman, 2019; Burgess et al., 2023; Erdmann et al., 2015; Muller, Stellmacher, Freitag, Landgraf, & Dieterich, 2015). A commercially available transgenic STOPflox R26-MetRS* mouse line enables cross-breeding with Cre-recombinase expressing strains for selective MetRS* expression in various cell types and tissues (Alvarez-Castelao et al., 2017).

Applying MetRS*-based cell-selective proteomics to pancreatic cancer models, we have recently demonstrated that target cell protein recovery can strongly exceed FACS yields, providing deep cell-selective proteome coverage with a particularly good representation of extracellular proteins such as cytokines and extracellular matrix components (Swietlik et al., 2023). Profiling of cell supernatants and mouse serum allowed the dissection of intercellular crosstalk *in vitro* and *in vivo*, and revealed context dependent

cancer subtype-specific signaling networks. Here, we provide a detailed protocol for highly efficient Anl-protein enrichment from tissues and body fluids.

2. General considerations for the experimental design

MetRS*-based Anl labeling facilitates in depth cell-selective *in vivo* global proteomics and secretomics analyses. Crucial to the success of these experiments are sufficient labeling of proteins, and thorough enrichment specificity controls.

2.1 Anl labeling and evaluation of labeling efficiency

In MetRS*-expressing cells, Anl competes with methionine for protein incorporation. The labeling efficiency is influenced by multiple factors, such as the expression level of MetRS*, the protein synthesis rate of target cells, and the concentrations of Anl and methionine. Notably, the significantly slower amino acid activation kinetics of Anl compared to methionine (Mahdavi et al., 2016) generally result in a low frequency of Met-Anl substitutions, thereby labeling only a small fraction of protein copies within the target cell proteome (Muller et al., 2015; Swietlik et al., 2023). Our protocol facilitates highly efficient enrichment of target cell-derived proteins from predominantly unlabeled proteins within tissues or body fluids. Nonetheless, to obtain deep cell-selective proteome coverage, we recommend a thorough pre-assessment of labeling conditions, particularly when targeting low frequency cell populations. Since MetRS* copy numbers in cells affect labeling, we recommend choosing models with high expression levels. For example, when MetRS* levels are controlled by Cre expression using a cell type-specific promotor, evaluation of efficient recombination and opting for homozygous expression may be considered. For transplantation models, we recommend the selection of MetRS* expression in cells under a strong and stable promoter.

Anl can be administered in various ways, including through injections, food, or drinking water. Required dose and length of treatment should be tested and adapted to the specific research question. As a starting point for mouse model experiments, we suggest administering Anl in drinking water at a concentration of 1% (w/v). The supplementation of sweeteners such as maltose or sucrose to the drinking water may be considered to increase water intake. If water consumption varies during the experiment,

we recommend administration by daily intraperitoneal injections, e.g., of a 300 mM Anl solution, adjusted to physiological pH, at a dosage of 10 mL/kg. In our experience, 5 days of ANL administration is often sufficient, however, optimal labeling time frames need a case-by-case evaluation. Chow with reduced methionine content may be used to improve the labeling efficiency.

A suite of complementary analysis techniques can help to evaluate and optimize labeling efficiency, without the need for Anl-protein enrichment and MS analysis. MetRS* expression can be conveniently quantified by co-expression of a reporter protein. Fluorescent non-canonical amino acid tagging (FUNCAT) (Tom Dieck et al., 2012), click reaction with biotin probes combined with western blots (Carlisle, Gotz, & Bodea, 2023; Hibbert, Jorgenson, Zhu, Steinert, & Hornberger, 2023) or fluorescent probes and in-gel detection (Hatzenpichler et al., 2014) can provide fast quantification of Anl incorporation in target cells.

3. Enrichment specificity controls

Although rigorous washing steps in the enrichment protocol strongly reduce unspecific binding to alkyne-resin and other surfaces, it cannot be completely eliminated. It is therefore crucial to include enrichment specificity controls in the experimental design to assess background interference at the individual protein level and exclude unspecifically bound proteins from cell-selective analyses.

To effectively distinguish proteins derived from MetRS*-expressing target cell types from those enriched unspecifically, each experimental group should include matching control samples from cells that do not express MetRS* but were otherwise treated equally. For instance, in mouse models where MetRS* expression depends on Cre-induction, using mice where Cre was not induced can provide appropriate negative controls. Negative controls should ideally match the number of replicates used in corresponding MetRS* samples (a minimum of triplicate samples is recommended). Further considerations for the MS acquisition and post-MS data processing are detailed in Sections 4.5 and 4.6.

3.1 Materials

- Amicon Ultra-15 Centrifugal filter units (3 kDa MWCO) (Millipore, UFC9003)
- Bio-Spin chromatography columns and end caps (Bio-Rad, 7326008)

- Nitrogen-cooled mortar (e.g., Bel-Art, H372600000)
- Pierce BCA Protein Assay Kit (Thermo Scientific, 23227)
- Pierce peptide desalting spin columns (Thermo Scientific, 89852)
- 2 mL protein LoBind reaction tubes (Eppendorf, 022431102)

3.2 Reagents

- Acetonitrile, LC-MS grade (Fisher Scientific, A955-500)
- Alkyne agarose (Vector Laboratories, CCT-1032)
- Azidonorleucine (Anl) (Iris Biotech, HAA9210)
- 2-(4-((Bis((1-(tert-butyl)-1H-1,2,3-triazol-4-yl)methyl)amino)methyl)-1H-1,2,3-triazol-1-yl)acetic acid (BTTAA) (Vector Laboratories, CCT-1236)
- 1 M Calcium chloride (CaCl2) (Sigma-Aldrich, 21115)
- 2-Chloroacetamide (CAA) (Sigma-Aldrich, 22790)
- 3-[(3-Cholamidopropyl)dimethylammonio]-1-propanesulfonate (CHAPS) (Millipore, 220201)
- Copper(II) sulfate pentahydrate ($CuSO_4$) (Sigma-Aldrich, C8027)
- EDTA-free protease inhibitor cocktail (Roche, 4693124001)
- Ethylenediaminetetraacetic acid (EDTA) (Sigma-Aldrich, E9884)
- Formic acid, LC-MS grade (Thermo Scientific, 28905)
- Guanidinium chloride (Sigma-Aldrich, G3272)
- 1 M HEPES (Gibco, 15630080), adjust to pH 8
- Isopropanol (Sigma-Aldrich, 190764)
- 0.5 M neutralized TCEP (Thermo Scientific, 77720)
- Sodium ascorbate (Sigma-Aldrich, 11140)
- Sodium chloride (NaCl) (Sigma-Aldrich, S9888)
- Sodium dodecyl sulfate (SDS) (Sigma-Aldrich, 75746)
- Trifluoroacetic Acid (TFA), LC-MS Grade (Thermo Scientific, 85183)
- 1 M Tris buffer, pH 8 (e.g., Millipore, 648314)
- Trypsin/Lys-C mix, MS grade (Promega, V5073)
- Water, LC-MS grade (Fisher Scientific, 10505904)

3.3 Preparation of buffers

- Click lysis buffer: 6 M guanidinium chloride, 4% (w/v) CHAPS, 0.5 M NaCl, 200 mM HEPES (pH 8), store at 4 °C. Add EDTA-free protease inhibitor cocktail fresh before use at 2× concentration.
- 100 mM $CuSO_4$ in ddH_2O, store at room temperature.

- 100 mM BTTAA in ddH_2O, prepare fresh.
- 1 M sodium ascorbate, prepare directly before use.
- SDS wash buffer: 1% (w/v) SDS, 250 mM NaCl, 5 mM EDTA, 100 mM Tris pH 8, store at 4 °C. Bring to room temperature to redissolve SDS before use.
- Guanidine wash buffer: 6 M guanidinium chloride, 100 mM Tris-HCl (pH 8), store at room temperature.
- 20% isopropanol in ddH_2O, store at room temperature.
- 20% acetonitrile in ddH_2O, store at room temperature.
- Digestion buffer: 10% acetonitrile, 2 mM $CaCl_2$, 50 mM Tris-HCl pH 8, store at 4 °C. Use to reconstitute Trypsin/Lys-C mix at a concentration of 20 μg/mL just before use.
- 0.1% LC-MS grade TFA in LC-MS grade water, store at room temperature.
- MS sample buffer: 0.1% LC-MS grade formic acid in LC-MS grade water, store at room temperature.

4. Methods

4.1 Tissue preparation for cell-selective global proteomics

1. Grind frozen tissue samples in liquid nitrogen using a pestle and mortar.
2. Transfer frozen, pulverized tissue samples into a polypropylene centrifuge tube and add click lysis buffer. For each specific tissue type, lysis volumes should be optimized to ensure efficient protein extraction while keeping the azide protein concentration high and the click reaction volume minimal. As an initial guideline, we recommend 5 mL of lysis buffer per gram of tissue wet weight.
3. Heat samples for 5 min at 95 °C while shaking at 800 rpm.
4. Using a probe sonicator, thoroughly homogenize the lysates until they reach water-like consistency.
5. Centrifuge lysates at 10,000 × *g* for 30 min to clarify them. Carefully transfer the clear lysates to new tubes without disturbing any insoluble material either settled at the bottom as a pellet or floating at the top of the solution (see **Note 1**).
6. Quantify lysate protein concentrations by BCA and normalize the protein concentration across samples with lysis buffer. Thorough input normalization is critical for reliable enrichment specificity evaluation with negative controls.

4.2 Body fluid preparation for cell-selective secretomics

1. Pre-wash Amicon Ultra-15 Centrifugal filter units (3 kDa MWCO) by adding 15 mL ddH2O and centrifuging at 4000 × *g* for 30 min.
2. Decant remaining water and then transfer body fluid samples into the pre-washed filter units. Maintain samples on ice. For enrichment of Anl-labeled proteins from mouse blood, we recommend using 400 µL serum per sample. Avoid reagents that interfere with the CuAAC reaction, such as EDTA, when collecting body fluid samples.
3. To minimize residual free azidonorleucine in the samples, add 15 mL of pre chilled 50 mM HEPES (pH 8) and centrifuge at 4000 × *g*, 4 °C until the sample volumes reduce to below 500 µL. Repeat these steps for a second wash, concentrate samples to a final volume of 250 µL and transfer to a 1.5 mL reaction tube.
4. To denature proteins, mix concentrated samples 1:1 with click lysis buffer and heat for 5 min at 95 °C while shaking at 800 rpm.

4.3 CuAAC click-chemistry enrichment

1. Wash 50% alkyne-agarose bead slurry twice with ddH2O and dispense 100 µL washed 50% slurry into individual 2 mL reaction tubes for each sample (**see Note 2**). Use wide-bore pipetting tips for all bead transfer steps.
2. Add 500 µL of either tissue lysate or body fluid lysis buffer mix (see Section 3.1 a and b) (**see Note 3**).
3. Freshly prepare a 2× catalyst solution master mix:
   - **3.1.** For each sample, combine 835 µL ddH2O with 125 µL of 100 mM BTTAA and 20 µL of 100 mM CuSO4 and thoroughly mix.
   - **3.2.** Add 20 µL of freshly prepared 1 M sodium ascorbate per sample just prior to use and briefly mix (**see Note 4**). Upon sodium ascorbate addition, the catalyst master mix transitions from blue to colorless.
4. Add 1 mL of the 2× catalyst master mix to each sample. Incubate for 3 h to overnight at room temperature with slow rotation on an end-over-end mixer.
5. After the click reaction, centrifuge samples for 5 min at 1000 × *g*, discard the supernatants, add 1.9 mL ddH2O to the beads and mix. Repeat these steps for a second wash, and subsequently centrifuge and remove supernatants.

6. Resuspend beads in 1 mL SDS wash buffer, supplemented with 10 mM neutralized TCEP and 30 mM CAA.
7. Incubate for 10 min at 70 °C, 800 rpm.
8. Transfer the beads into disposable Bio-Spin chromatography columns (**see Note 5**) and perform sequential washes using 20 mL each of SDS wash buffer, 20% isopropanol, guanidine wash buffer, and 20% acetonitrile.
9. Seal the bottom openings of the chromatography columns, then add 500 µL ddH2O to the beads. Afterwards, transfer the beads into 2 mL protein LoBind reaction tubes. To ensure thorough collection, wash the filter columns with an additional 500 µL of ddH2O, and combine the wash with the previously transferred beads.
10. Centrifuge beads for 5 min at 1000 × *g* and remove the supernatant.
11. Add 1 µg Trypsin/Lys-C mix in 50 µL digestion buffer and incubate samples at 37 °C, 800 rpm overnight.
12. After digestion, centrifuge samples for 5 min at 1000 × *g* and transfer the supernatants to new LoBind reaction tubes. To ensure thorough collection and dilution of acetonitrile to a final concentration of <2%, add 300 µL ddH2O to the beads, mix thoroughly, centrifuge for 5 min at 1000 × *g* and combine the supernatants with the previously transferred digests.
13. Acidify diluted digests to pH ~3 by adding TFA (start at 0.1% final TFA concentration, check with pH paper and increase if needed).

4.4 Peptide desalting by solid phase extraction

1. Condition Pierce Peptide Desalting Spin Columns (Thermo Scientific, 89852) (**see Note 6**), following the manufacturer's instructions:
   - **1.1.** Remove the white protection tips covering the bottom of the columns, place columns into 2 mL reaction tubes, and then centrifuge for 1 min at 5000 × *g* to remove the storage solution.
   - **1.2.** Discard the storage solution from the reaction tubes, add 300 µL acetonitrile into the columns and centrifuge for 1 min at 5000 × *g*. Discard the acetonitrile and repeat the wash.
   - **1.3.** Wash the resins twice with 0.1% TFA, as described above.
2. Add diluted and acidified samples from step Section 3.2 to conditioned columns. Centrifuge for 1 min at 3000 × *g*. Remove and store or discard flow-through.

3. Add 300 µL 0.1% TFA in water, centrifuge for 1 min at 3000 × *g*, and discard the wash eluate. Repeat this step once more for a total of two washes.
4. To elute bound peptides, place columns into new LoBind 2 mL reaction tubes, add 300 µL 50% Acetonitrile, 0.1% TFA, and centrifuge for 1 min at 3000 × *g*. Repeat this step and combine both eluates.
5. Dry desalted peptides by vacuum centrifugation.

4.5 Peptide reconstitution for LC-MS analysis

In vivo applications of MetRS*-based Anl labeling often yield peptides in the low microgram range post-enrichment. Therefore, we advise initial reconstitution in small volumes, such as 10 µL of MS sample buffer. To ensure optimal LC-MS loading, peptide concentrations should be measured, for example, with a microvolume spectrophotometer, and adjusted if required (**see Note 7**). However, loading input amounts of MetRS*-samples and corresponding negative controls should *not* be equalized but maintained at their original ratios to accurately assess enrichment specificity.

4.6 Considerations for post-MS data processing

Following MS-analysis, MetRS*-samples and their corresponding negative controls should be compared to exclude proteins that are unspecifically enriched or show strong background interference from further analysis. We recommend excluding proteins from MetRS* samples that overlap with negative controls and show less than a threefold higher intensity in MetRS* samples compared to control samples. To define biologically relevant differences of cell-type specific protein abundance, an appropriate statistical test across conditions dependent on the hypothesis and experimental design is required in addition to the removal of non-cell type-specific proteins.

5. Notes

Note 1: To ensure efficient protein extraction and minimize non-specific protein retention during pulldowns, thorough lysate homogenization and clarification is crucial. If homogenization appears to be incomplete after the lysis process, with visibly large tissue fragments remaining, consider increasing the lysis buffer to tissue ratio and intensifying sonication.

Note 2: The bead amount per pulldown can be adjusted to optimize capture efficiency and signal-to-noise for specific applications. We recommend 2 mL reaction tubes for reliable bead resuspension at moderate shaking speeds.

Note 3: If available, increasing the sample input may improve results by increasing signal-to-background ratios and cell-selective protein coverage. Yet, instead of simply scaling up reaction volumes, we recommend performing multiple click reactions in sequence following the protocol described in Section 3.2. Larger sample volumes can be processed in 500 µL batches while reusing the same beads for successive reactions. The incubation time per reaction can be shortened to 1.5 h.

Note 4: 2× catalyst mix, excluding sodium ascorbate, can be prepared in advance, and stored short-term at 4 °C. However, it's important to prepare sodium ascorbate freshly and add it to the mix immediately before each use to ensure optimal reactivity.

Note 5: Secure columns in a raised rack and allow wash buffers to rinse beads by gravity flow; for processing large numbers of samples, fritted multi-well plates (e.g., Porvair Sciences, 240002) can be used to facilitate bead washing *via* low-speed centrifugation. Take care to prevent the beads from drying out completely during the wash steps.

Note 6: For processing large numbers of samples, alternative SPE materials such as Sep-Pak tC18 plates (Waters, 186002320) can be used.

Note 7: Final peptide yields can serve as quality control measures before MS acquisition and may guide troubleshooting. A systematically higher peptide yield in MetRS* samples compared to controls implies successful specific Anl-enrichment. Low or no difference at peptide yields in the low µg range may indicate a low enrichment efficiency or low overall Anl-protein amounts in the original MetRS* samples. Nonetheless, in secretomics studies, experiments with limited cell numbers, or low expected labeling efficiency, a modest MetRS*-to-control peptide yield ratio may not necessarily be reason for concern and samples might still yield valuable insights. High peptide yields in negative controls (more than a few µg) or contaminant signal in absorption spectra suggest suboptimal clean up.

References

Alvarez-Castelao, B., Schanzenbacher, C. T., Langer, J. D., & Schuman, E. M. (2019). Cell-type-specific metabolic labeling, detection and identification of nascent proteomes in vivo. *Nature Protocols*, *14*, 556–575. https://doi.org/10.1038/s41596-018-0106-6.

Alvarez-Castelao, B., et al. (2017). Cell-type-specific metabolic labeling of nascent proteomes in vivo. *Nature Biotechnology*, *35*, 1196–1201. https://doi.org/10.1038/nbt.4016.

Azizian, N. G., et al. (2021). Selective labeling and identification of the tumor cell proteome of pancreatic Cancer in vivo. *Journal of Proteome Research*, *20*, 858–866. https://doi.org/10.1021/acs.jproteome.0c00666.

Burgess, J. D., et al. (2023). A mutant methionyl-tRNA synthetase-based toolkit to assess induced-mesenchymal stromal cell secretome in mixed-culture disease models. *Stem Cell Research & Therapy*, *14*, 289. https://doi.org/10.1186/s13287-023-03515-0.

Carlisle, A. K., Gotz, J., & Bodea, L. G. (2023). Three methods for examining the de novo proteome of microglia using BONCAT bioorthogonal labeling and FUNCAT click chemistry. *STAR Protocols*, *4*, 102418. https://doi.org/10.1016/j.xpro.2023.102418.

Droujinine, I. A., et al. (2021). Proteomics of protein trafficking by in vivo tissue-specific labeling. *Nature Communications*, *12*, 2382. https://doi.org/10.1038/s41467-021-22599-x.

Erdmann, I., et al. (2015). Cell-selective labelling of proteomes in Drosophila melanogaster. *Nature Communications*, *6*, 7521. https://doi.org/10.1038/ncomms8521.

Gauthier, N. P., et al. (2013). Cell-selective labeling using amino acid precursors for proteomic studies of multicellular environments. *Nature Methods*, *10*, 768–773. https://doi.org/10.1038/nmeth.2529.

Hatzenpichler, R., et al. (2014). In situ visualization of newly synthesized proteins in environmental microbes using amino acid tagging and click chemistry. *Environmental Microbiology*, *16*, 2568–2590. https://doi.org/10.1111/1462-2920.12436.

Hibbert, J. E., Jorgenson, K. W., Zhu, W. G., Steinert, N. D., & Hornberger, T. A. (2023). Protocol for quantifying the in vivo rate of protein degradation in mice using a pulse-chase technique. *STAR Protocols*, *4*, 102574. https://doi.org/10.1016/j.xpro.2023.102574.

Kim, K. E., et al. (2021). Dynamic tracking and identification of tissue-specific secretory proteins in the circulation of live mice. *Nature Communications*, *12*, 5204. https://doi.org/10.1038/s41467-021-25546-y.

Liu, J., Jang, J. Y., Pirooznia, M., Liu, S., & Finkel, T. (2021). The secretome mouse provides a genetic platform to delineate tissue-specific in vivo secretion. *Proceedings of the National Academy of Sciences of the United States of America*, *118*. https://doi.org/10.1073/pnas.2005134118.

Liu, Y., et al. (2017). Application of bio-orthogonal proteome labeling to cell transplantation and heterochronic parabiosis. *Nature Communications*, *8*, 643. https://doi.org/10.1038/s41467-017-00698-y.

Mahdavi, A., et al. (2016). Engineered aminoacyl-tRNA Synthetase for cell-selective analysis of mammalian protein synthesis. *Journal of the American Chemical Society*, *138*, 4278–4281. https://doi.org/10.1021/jacs.5b08980.

Meissner, F., Scheltema, R. A., Mollenkopf, H. J., & Mann, M. (2013). Direct proteomic quantification of the secretome of activated immune cells. *Science*, *340*, 475–478. https://doi.org/10.1126/science.1232578.

Muller, A., Stellmacher, A., Freitag, C. E., Landgraf, P., & Dieterich, D. C. (2015). Monitoring astrocytic proteome dynamics by cell type-specific protein labeling. *PLoS One*, *10*, e0145451. https://doi.org/10.1371/journal.pone.0145451.

Ngo, J. T., et al. (2009). Cell-selective metabolic labeling of proteins. *Nature Chemical Biology*, *5*, 715–717. https://doi.org/10.1038/nchembio.200.

Phulphagar, K., et al. (2021). Proteomics reveals distinct mechanisms regulating the release of cytokines and alarmins during pyroptosis. *Cell Reports*, *34*, 108826. https://doi.org/10.1016/j.celrep.2021.108826.

Rieckmann, J. C., et al. (2017). Social network architecture of human immune cells unveiled by quantitative proteomics. *Nature Immunology*, *18*, 583–593. https://doi.org/10.1038/ni.3693.

Spence, E. F., et al. (2019). In vivo proximity proteomics of nascent synapses reveals a novel regulator of cytoskeleton-mediated synaptic maturation. *Nature Communications*, *10*, 386. https://doi.org/10.1038/s41467-019-08288-w.

Swietlik, J. J., Sinha, A., & Meissner, F. (2020). Dissecting intercellular signaling with mass spectrometry-based proteomics. *Current Opinion in Cell Biology*, *63*, 20–30. https://doi.org/10.1016/j.ceb.2019.12.002.

Swietlik, J. J., et al. (2023). Cell-selective proteomics segregates pancreatic cancer subtypes by extracellular proteins in tumors and circulation. *Nature Communications*, *14*, 2642. https://doi.org/10.1038/s41467-023-38171-8.

Tanrikulu, I. C., Schmitt, E., Mechulam, Y., Goddard, W. A., 3rd, & Tirrell, D. A. (2009). Discovery of Escherichia coli methionyl-tRNA synthetase mutants for efficient labeling of proteins with azidonorleucine in vivo. *Proceedings of the National Academy of Sciences of the United States of America*, *106*, 15285–15290. https://doi.org/10.1073/pnas.0905735106.

Tape, C. J., et al. (2016). Oncogenic KRAS regulates tumor cell signaling via stromal reciprocation. *Cell*, *165*, 910–920. https://doi.org/10.1016/j.cell.2016.03.029.

Tom Dieck, S., et al. (2012). Metabolic labeling with noncanonical amino acids and visualization by chemoselective fluorescent tagging. *Current Protocols in Cell Biology*. https://doi.org/10.1002/0471143030.cb0711s56. Chapter 7, 7.11 1–17 11.29.

Wei, W., et al. (2021). Cell type-selective secretome profiling in vivo. *Nature Chemical Biology*, *17*, 326–334. https://doi.org/10.1038/s41589-020-00698-y.

Yang, R., et al. (2022). A genetic model for in vivo proximity labelling of the mammalian secretome. *Open Biology*, *12*, 220149. https://doi.org/10.1098/rsob.220149.

Article 4: Selective multi-kinase inhibition sensitises mesenchymal pancreatic cancer to immune checkpoint blockade by remodelling the tumor microenvironment

Nat Cancer 3, 318-336 (2022)

Chiara Falcomatà[1,2,3,17], Stefanie Bärthel[1,2,3,17], Sebastian A. Widholz[3,4,5], Christian Schneeweis[5,6], Juan José Montero[3,4,5], Albulena Toska[7], Jonas Mir[7], Thorsten Kaltenbacher[3,4,5], Jeannine Heetmeyer[1,2,3], **Jonathan J. Swietlik**[8], Jing-Yuan Cheng[8], Bianca Teodorescu[1,2,3], Oliver Reichert[1,2,3], Constantin Schmitt[1,2,3], Kathrin Grabichler[1,2,3], Andrea Coluccio[1,2,3,6], Fabio Boniolo[1,2,3], Christian Veltkamp[1,2,3], Magdalena Zukowska[1,2,3], Angelica Arenas Vargas[1,2,3], Woo Hyun Paik[1,2,3], Moritz Jesinghaus[1,2,3,9,10], Katja Steiger[9], Roman Maresch[3,4,5], Rupert Öllinger[3,4,5], Tim Ammon[3,5,11], Olga Baranov[3,4,5], Maria S. Robles[12], Julia Rechenberger[13], Bernhard Kuster[5,13], Felix Meissner[8,14], Maximilian Reichert[5,6,15], Michael Flossdorf[7], Roland Rad[3,4,5,6], Marc Schmidt-Supprian[3,5,11], Günter Schneider[5,6,16] & Dieter Saur[1,2,3,6]

[1] Division of Translational Cancer Research, German Cancer Research Center and German Cancer Consortium, Heidelberg, Germany

2 Chair of Translational Cancer Research and Institute of Experimental Cancer Therapy, Klinikum rechts der Isar, School of Medicine, Technische Universität München, Munich, Germany

3 Center for Translational Cancer Research (TranslaTUM), School of Medicine, Technical University of Munich, Munich, Germany

4 Institute of Molecular Oncology and Functional Genomics, School of Medicine, Technische Universität München, Munich, Germany

5 German Cancer Consortium, Heidelberg, Germany

6 Department of Internal Medicine II, Klinikum rechts der Isar, Technische Universität München, Munich, Germany

7 Institute for Medical Microbiology, Immunology and Hygiene, Technische Universität München, Munich, Germany

8 Experimental Systems Immunology Laboratory, Max Planck Institute of Biochemistry, Martinsried, Germany

9 Institute of Pathology, Technische Universität München, Munich, Germany

10 Institute of Pathology, University Hospital Marburg, Marburg, Germany

11 Institute of Experimental Hematology, School of Medicine, Technical University of Munich, Munich, Germany

12 Institute of Medical Psychology, Faculty of Medicine, LMU Munich, Munich, Germany

13 Chair of Proteomics and Bioanalytics, Technical University of Munich, Freising, Germany

14 Institute of Innate Immunity, Department of Systems Immunology and Proteomics, Medical Faculty, University of Bonn, Bonn, Germany

15 Center for Protein Assemblies, Technische Universität München, Garching, Germany

16 University Medical Center Göttingen, Department of General, Visceral and Pediatric Surgery, Göttingen, Germany
# These authors contributed equally to the work.

Although pancreatic ductal adenocarcinoma (PDAC) has a low incidence of around 13 per 100.000 people per year, it is currently the third leading cancer-related cause of death in the United States and is projected to become the second within the next decade[252-254]. In contrast to many other cancers, cure rates have only marginally improved over the last decades, and the 5-year survival rate has remained below 10 %. PDAC often grows aggressively, metastasizes early, and is strongly resistant to chemo- and radiotherapy[255]. Moreover, the typically dense, desmoplastic stroma, often rich in myeloid cells and with low effector T cell infiltration, along with a comparably low mutational burden, contribute to a highly immunosuppressive tumor microenvironment (TME) and poor response to immunotherapy[256]. An increased gene dose of mutant KRAS has recently been identified as an important driver of mesenchymal PDAC, the most aggressive and resistant subtype of PDAC.

While trametinib-mediated MEK inhibition alone did not succeed in unstratified clinical trials for the treatment of PDAC, here, a systematic co-treatment screen of 418 drugs demonstrated striking synergy with nintedanib, an FDA-approved inhibitor of nonreceptor tyrosine kinases and receptor tyrosine kinases. The drug combination showed selective efficacy for mesenchymal PDAC cells, translating to strongly prolonged survival in mouse models. Further investigation of drug treatment-induced effects uncovered systematic remodeling of the TME, with strongly increased cytotoxic T cell infiltration. In tumors, T cell infiltration rather than tumor cell intrinsic effects alone was a major driver of efficacy. Moreover, co-treatment with trametinib and nintedanib sensitized mesenchymal tumors for checkpoint inhibition, leading to further increasing survival with additional PD-L1 inhibition. To investigate mechanisms of TME remodeling, we explored treatment effects on intercellular communication. Secretomics analyses of PDAC lines showed significant changes in releasing immunomodulatory signals in response to treatment. Among those, critical chemokines linked to tumor-infiltrating lymphocyte recruitment and associated with a favorable prognosis, such as CXCL16, were selectively induced in mesenchymal but not classical PDAC cells. Collectively, the findings from this study suggest a promising path for urgently needed advancements in PDAC therapy.

Contribution:

This highly collaborative study was led by the Saur group at the translaTUM in Munich. I contributed by developing an optimized serum-free secretomics workflow to improve cytokine coverage in PDAC supernatants and performed secretomics sample preparation, MS acquisition, and secretomics data analyses. Together with Jingyuan Cheng, I conducted integrative analyses of RNAseq and secretomics data to infer cell communication channels between cancer cells and tumor stromal cell types. Specifically, I contributed to Figure 8d, Supplementary Figures 10 a-b, and proteomics method sections.

ARTICLES
https://doi.org/10.1038/s43018-021-00326-1

nature cancer

Selective multi-kinase inhibition sensitizes mesenchymal pancreatic cancer to immune checkpoint blockade by remodeling the tumor microenvironment

Chiara Falcomatà[1,2,3,17], Stefanie Bärthel[1,2,3,17], Sebastian A. Widholz[3,4,5], Christian Schneeweis[5,6], Juan José Montero[3,4,5], Albulena Toska[7], Jonas Mir[7], Thorsten Kaltenbacher[3,4,5], Jeannine Heetmeyer[1,2,3], Jonathan J. Swietlik[8], Jing-Yuan Cheng[8], Bianca Teodorescu[1,2,3], Oliver Reichert[1,2,3], Constantin Schmitt[1,2,3], Kathrin Grabichler[1,2,3], Andrea Coluccio[1,2,3,6], Fabio Boniolo[1,2,3], Christian Veltkamp[1,2,3], Magdalena Zukowska[1,2,3], Angelica Arenas Vargas[1,2,3], Woo Hyun Paik[1,2,3], Moritz Jesinghaus[1,2,3,9,10], Katja Steiger[9], Roman Maresch[3,4,5], Rupert Öllinger[3,4,5], Tim Ammon[3,5,11], Olga Baranov[3,4,5], Maria S. Robles[12], Julia Rechenberger[13], Bernhard Kuster[5,13], Felix Meissner[8,14], Maximilian Reichert[5,6,15], Michael Flossdorf[7], Roland Rad[3,4,5,6], Marc Schmidt-Supprian[3,5,11], Günter Schneider[5,6,16] and Dieter Saur[1,2,3,6] ✉

***KRAS*-mutant pancreatic ductal adenocarcinoma (PDAC) is highly immunosuppressive and resistant to targeted and immunotherapies. Among the different PDAC subtypes, basal-like mesenchymal PDAC, which is driven by allelic imbalance, increased gene dosage and subsequent high expression levels of oncogenic *KRAS*, shows the most aggressive phenotype and strongest therapy resistance. In the present study, we performed a systematic high-throughput combination drug screen and identified a synergistic interaction between the MEK inhibitor trametinib and the multi-kinase inhibitor nintedanib, which targets *KRAS*-directed oncogenic signaling in mesenchymal PDAC. This combination treatment induces cell-cycle arrest and cell death, and initiates a context-dependent remodeling of the immunosuppressive cancer cell secretome. Using a combination of single-cell RNA-sequencing, CRISPR screens and immunophenotyping, we show that this combination therapy promotes intratumor infiltration of cytotoxic and effector T cells, which sensitizes mesenchymal PDAC to PD-L1 immune checkpoint inhibition. Overall, our results open new avenues to target this aggressive and therapy-refractory mesenchymal PDAC subtype.**

With a 10-year survival rate of approximately 1%, PDAC is almost universally fatal[1]. Recently, it surpassed breast cancer in becoming the third leading cause of cancer-related deaths in the western world[2]. PDAC is highly refractory to all available treatment options, including chemo- and immunotherapies. Meaningful treatment responses are limited almost exclusively to the classical glandular subtype of the disease, characterized by an epithelial morphology and gene-expression program[3–5]. Undifferentiated nonglandular PDACs display a mesenchymal morphology and a basal-like transcriptional program[3–5]. These tumors are characterized by a particularly poor prognosis, often not responding to standard-of-care chemotherapy, and therefore representing an unmet clinical need[3–5,7].

New therapeutic approaches, such as immune checkpoint blockade (ICB), have demonstrated no effect in trials of PDAC patients[9]. This lack of response probably results from the relatively low mutational burden, leading to a low number of immunogenic neoantigens. Combined with multiple immunosuppressive features of the

[1]Division of Translational Cancer Research, German Cancer Research Center and German Cancer Consortium, Heidelberg, Germany. [2]Chair of Translational Cancer Research and Institute of Experimental Cancer Therapy, Klinikum rechts der Isar, School of Medicine, Technische Universität München, Munich, Germany. [3]Center for Translational Cancer Research (TranslaTUM), School of Medicine, Technical University of Munich, Munich, Germany. [4]Institute of Molecular Oncology and Functional Genomics, School of Medicine, Technische Universität München, Munich, Germany. [5]German Cancer Consortium, Heidelberg, Germany. [6]Department of Internal Medicine II, Klinikum rechts der Isar, Technische Universität München, Munich, Germany. [7]Institute for Medical Microbiology, Immunology and Hygiene, Technische Universität München, Munich, Germany. [8]Experimental Systems Immunology Laboratory, Max Planck Institute of Biochemistry, Martinsried, Germany. [9]Institute of Pathology, Technische Universität München, Munich, Germany. [10]Institute of Pathology, University Hospital Marburg, Marburg, Germany. [11]Institute of Experimental Hematology, School of Medicine, Technical University of Munich, Munich, Germany. [12]Institute of Medical Psychology, Faculty of Medicine, LMU Munich, Munich, Germany. [13]Chair of Proteomics and Bioanalytics, Technical University of Munich, Freising, Germany. [14]Institute of Innate Immunity, Department of Systems Immunology and Proteomics, Medical Faculty, University of Bonn, Bonn, Germany. [15]Center for Protein Assemblies, Technische Universität München, Garching, Germany. [16]University Medical Center Göttingen, Department of General, Visceral and Pediatric Surgery, Göttingen, Germany. [17]These authors contributed equally: Chiara Falcomatà, Stefanie Bärthel. ✉e-mail: dieter.saur@tum.de

PDAC tumor microenvironment (TME), this leads to scarcity of tumor-infiltrating lymphocytes (TILs)[9]. Recent studies reported rare cases of PDAC patients presenting tumors with high T-cell infiltration, a feature associated with prolonged overall survival[10–12]. These reports highlighted the potential to treat PDAC more effectively by targeting the immunosuppressive TME and recruiting TILs via rational combination therapies.

KRAS is mutationally activated in >90% of PDAC patients. However, to date no clinically applicable strategy has been developed to effectively treat *KRAS*-mutant PDAC. Downstream of oncogenic *KRAS*, the RAF–MEK–ERK pathway plays a central role in tumor initiation[13]. Although MEK inhibitors yielded therapeutic value in *RAS*-mutant melanoma and lung cancer[14,15], unstratified trials failed in PDAC patients. Recently, we and others showed that an increased gene dosage (iGD) and expression of mutant *KRAS* (*KRAS-mut*) drives the disease, with the mesenchymal, nonglandular, basal-like subtype displaying the highest *KRAS-mut* gene-expression levels[5,16,17]. Based on the strong effects of *KRAS-mut* expression on PDAC phenotypes, we set out to develop a combination therapy for mesenchymal tumors that targets KRAS-driven tumor-cell intrinsic signaling and, in parallel, reprograms the TME. By high-throughput drug screening combining the MEK inhibitor (MEKi) trametinib with 418 drugs, we identified a synergistic combination with the multi-kinase inhibitor nintedanib, inducing cell death and widespread reprogramming of the immunosuppressive microenvironment. The combination therapy activates an anti-tumor immune response, resulting in the recruitment of cytotoxic T cells, sensitizing mesenchymal tumors to ICB.

Results

Mesenchymal PDAC is resistant to MEK pathway inhibition. Recent data show that *KRAS-mut* expression levels have a strong impact on PDAC differentiation and phenotype, including the response to standard-of-care polychemotherapy[5,16,17]. In addition, the mesenchymal basal-like phenotype is linked to poor prognosis (Fig. 1a)[3,5–8]. Based on the hypothesis that oncogenic *KRAS* overexpression provides a unique vulnerability in mesenchymal tumors, we systematically explored canonical RAF–MEK–ERK pathway inhibition. To this end, a panel of primary patient-derived cell cultures and conventional human PDAC (hPDAC) cell lines was screened with the MEKi trametinib. Unexpectedly, mainly cell lines with a classical epithelial morphology and gene expression signature[18,19] showed high sensitivity toward MEKi (Fig. 1b and Extended Data Fig. 1a). The hPDAC cells of complete mesenchymal morphology, representing the most undifferentiated and aggressive subtype, are underrepresented and commonly not observed in surgically resectable cancers. Therefore, we extended our screen to mouse primary cell cultures (mPDAC cells) isolated from tumors of mice expressing $Kras^{G12D}$ in the pancreas[16]. Mesenchymal mPDAC cells expressed $Kras^{G12D}$ to the highest levels (Fig. 1c)[16]. In line with hPDAC, mainly classical mPDAC cells were sensitive to MEKi, whereas almost all mesenchymal cells showed remarkable resistance (Fig. 1d and Extended Data Fig. 1a). These differences were not due to different dependence on the driving oncogene *KRAS*, or direct *KRAS*-downstream targets, as indicated by similar dependence scores of CRISPR (clustered regularly interspaced short palindromic repeats)–Cas9-based negative selection screens (Extended Data Fig. 1b–d). In contrast, we observed fundamental differences in signaling output. Site-specific protein-phosphorylation profiling revealed enrichment of platelet-derived growth factor (PDGF), ERBB2 (Erb-B2 receptor tyrosine kinase 2), mammalian target of rapamycin complex 1 (mTORC1), receptor tyrosine kinase (RTK), neurotrophic tyrosine receptor kinase (NTRK) signaling and the vascular endothelial growth factor A (VEGFA)/VEGF receptor (VEGFR) pathway in mesenchymal tumor cells, whereas classical profiling showed, for example, higher levels of the insulin receptor and AKT (protein kinase B) signaling cascade (Extended Data Fig. 1e,f and Supplementary Table 1).

To exclude insufficient MEK1/2 inhibition and/or feedback/crossactivation of the pathway in primary resistant cells, we developed a dual-recombinase-based PDAC mouse model[20] allowing the inducible permanent genetic inactivation of the MEK pathway in established tumors (Fig. 1e and Extended Data Fig. 2a): we crossed *Pdx1-Flp;FSF-Kras*$^{G12D/+}$*;FSF-R26*$^{CAG\text{-}CreERT2/+}$ mice with animals harboring *loxP*-flanked *Mek1* and *Mek2* alleles, and subsequently ablated MEK1/2 in PDAC cells by tamoxifen administration in vitro and in vivo after orthotopic transplantation (Fig. 1e,f and Extended Data Fig. 2a–h). Loss of MEK1/2 reduced cell proliferation in vitro, without triggering cell death. In-line ablation of MEK1/2 in vivo did not induce tumor regression or a complete growth arrest as assessed by Ki67 staining, but delayed tumor progression of the respective animals (Fig. 1f and Extended Data Fig. 2b–h). In parallel, we found that pharmacological MEKi delayed disease progression in classical epithelial PDAC significantly ($P=0.0002$ versus controls), but only moderately in the mesenchymal subtype ($P=0.0506$ versus controls). Of note, trametinib did not induce tumor regression as observed in other cancer types, such as nonsmall-cell lung cancer (NSCLC; Fig. 1g–i)[14,21]. Therefore, neither MEKi nor complete sustained genetic disruption of canonical *KRAS*-downstream signaling is sufficient to induce PDAC regression, demonstrating the need to develop combination treatment strategies.

Drug screening identifies new therapies for mesenchymal PDAC. We performed a systematic, high-throughput, combination compound screen to identify drugs synergizing with MEKi. We screened two hPDAC and two mPDAC cultures, representing both classical and mesenchymal *KRAS* subtypes, with trametinib in combination with 418 drugs in preclinical and clinical investigations (Fig. 2a and Supplementary Table 2). One of the top hits in mesenchymal PDAC was the clinically approved RTK inhibitor nintedanib (Fig. 2b). We validated our findings in long-term clonogenic assays in a larger cohort and observed synergistic interactions of trametinib and nintedanib in 11 of 15 hPDAC cultures, with the strongest effect in the 5 mesenchymal cultures (Fig. 2c–e; $P=0.009$). We extended the combination screen to 30 additional mPDAC cultures[16]. A high synergism was achieved in most of the models, with the mesenchymal *Kras-mut*-overexpressing cells predominantly benefitting from the treatment (Fig. 2f–h). Antagonism was observed in 3 of 15 human and 6 of 30 mouse cell cultures, respectively, which were characterized almost exclusively by a classical epithelial morphology. In line with the heterogeneity of responses observed in the clinical setting, even within molecularly stratified cohorts, we detected synergism in some classical PDAC cultures, demonstrating heterogeneity within subtypes (Fig. 2c–h and Extended Data Fig. 3a,b). Trametinib and nintedanib (T/N)-treated epithelial and mesenchymal PDAC cells revealed similar changes in ERK phosphorylation, indicating that primary sensitivity and resistance to T/N is not due to differences in canonical pathway blockade (Extended Data Fig. 3c). Increasing the dosage of both inhibitors did not alter the antagonistic action of the drug combination substantially, arguing for fundamental biological differences between the tumors (Extended Data Fig. 3d). Strikingly, we observed cell death on T/N treatment, with the strongest effects in mesenchymal PDAC (Fig. 2i).

We assessed the consequences of oncogenic *KRAS-mut* expression on cell morphology and treatment response using classical mPDAC cells transduced with a doxycycline-inducible $KRAS^{G12D}$ vector or *GFP* as control. $KRAS^{G12D}$ overexpression led to increased ERK1/2 phosphorylation, decreased E-cadherin expression (*Cdh1*) and morphological changes of the epithelial PDAC cells toward a mesenchymal spindle-shaped morphology, which increased from day 1 to day 14 (Extended Data Fig. 3e–h). T/N treatment revealed a remarkable change in drug sensitivity. Although the controls

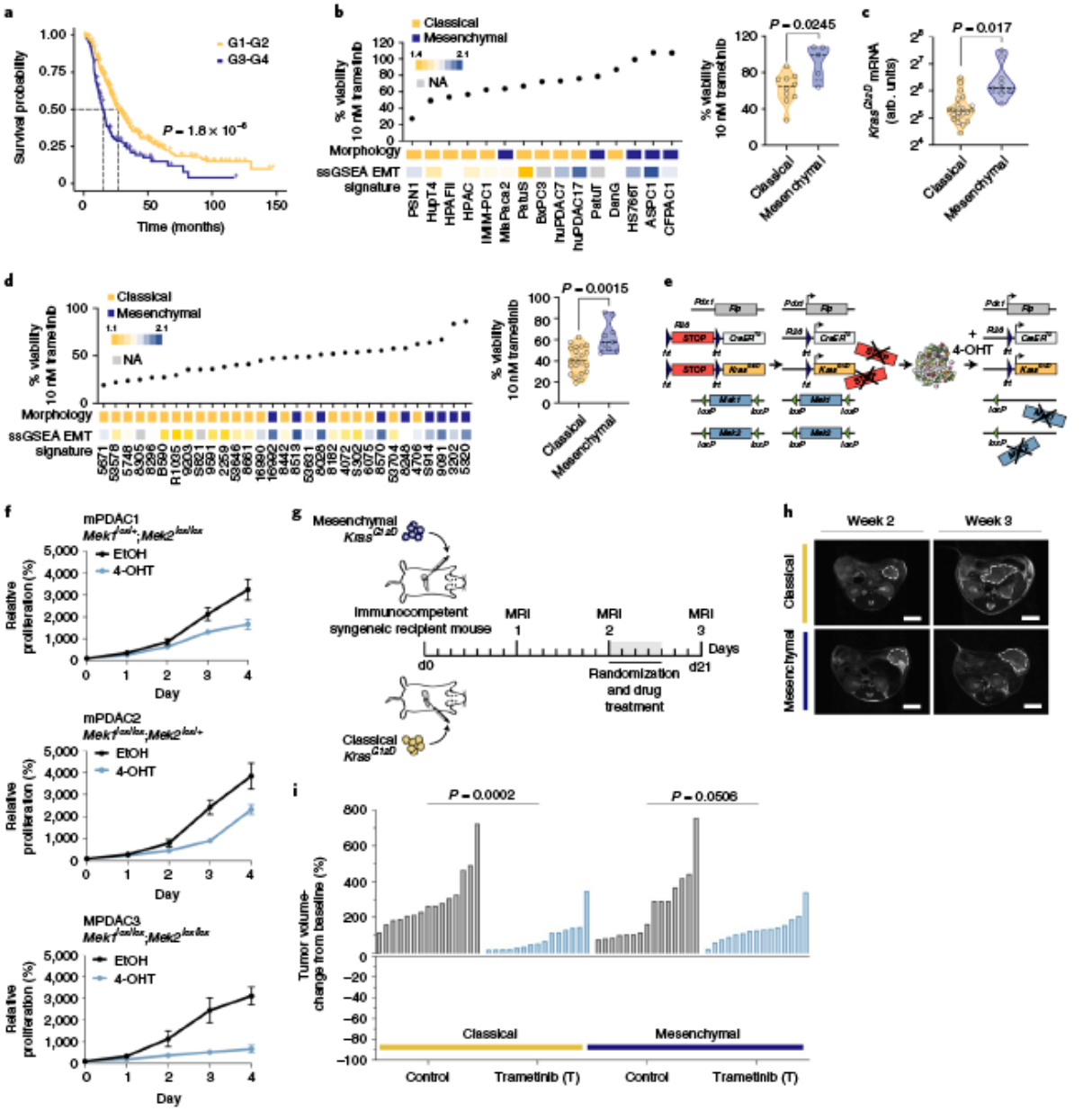

Fig. 1 | Resistance to MEK inhibition in vitro and in vivo. a, Kaplan–Meier analysis comparing survival of surgically resected patients having either G1–G2 or G3–G4 tumor grading. We combined data from refs. [6–8]. **b**, Left: percentage of cell viability at 10 nM trametinib in hPDAC cell lines. Cell morphology and ssGSEA EMT signature are integrated below. Cells showing a classical phenotype are marked in yellow, and those presenting a mesenchymal phenotype in blue. The hPDAC17 and hPDAC7 are primary human patient-derived PDAC cell cultures generated from PDX models in our laboratory[22]. Right: violin plots comparing the percentage of cell viability at 10 nM trametinib between classical and mesenchymal hPDAC cell cultures. **c**, Allele-specific *Kras*^{G12D} mRNA expression in classical (n = 21 mice) and mesenchymal (n = 9 mice) tumors by combining amplicon-based RNA-seq and reverse transcription-quantitative PCR. AU, arbitrary units. **d**, Left: percentage of cell viability at 10 nM trametinib in mPDAC cell cultures. Cell morphology and ssGSEA EMT signature are integrated below. Right: comparison of the percentage of cell viability at 10 nM trametinib between classical and mesenchymal mPDAC cell cultures. **e**, Schematic representation of the dual-recombinase system to inducibly delete floxed *Mek1* and *Mek2* in established tumors using a tamoxifen-activatable *CreER*^{T2} allele. **f**, Viability assay of 4-hydroxytamoxifen (4-OHT)-treated *Mek1*$^{lox/+}$;*Mek2*$^{lox/lox}$ (mPDAC1), *Mek1*$^{lox/lox}$;*Mek2*$^{lox/+}$ (mPDAC2) and *Mek1*$^{lox/lox}$;*Mek2*$^{lox/lox}$ (mPDAC3) cell cultures compared with vehicle (ethanol, EtOH). Data are shown as mean ± s.d. (n = 3 independent experiments). **g**, Schematic representation of the experimental set-up to test treatment efficacy of trametinib in vivo using subtype-specific models. Mesenchymal (9091) and classical (8661) mPDAC cells were used for the orthotopic transplantation experiments. **h**, Representative MRI of trametinib-treated mice before (week 2) and after 1 week of treatment (week 3). Scale bars, 5 mm. **i**, Waterfall plot of the fold-change in tumor volume compared with baseline (determined by MRI-based volumetric measurements) of orthotopically transplanted classical and mesenchymal tumors after 1 week of trametinib treatment. *P* values in **b** (right), **c**, **d** (right) and **i** were calculated using a two-tailed, unpaired Student's *t*-test. The *P* value in **a** was calculated using the log(rank) (Mantel–Cox) test.

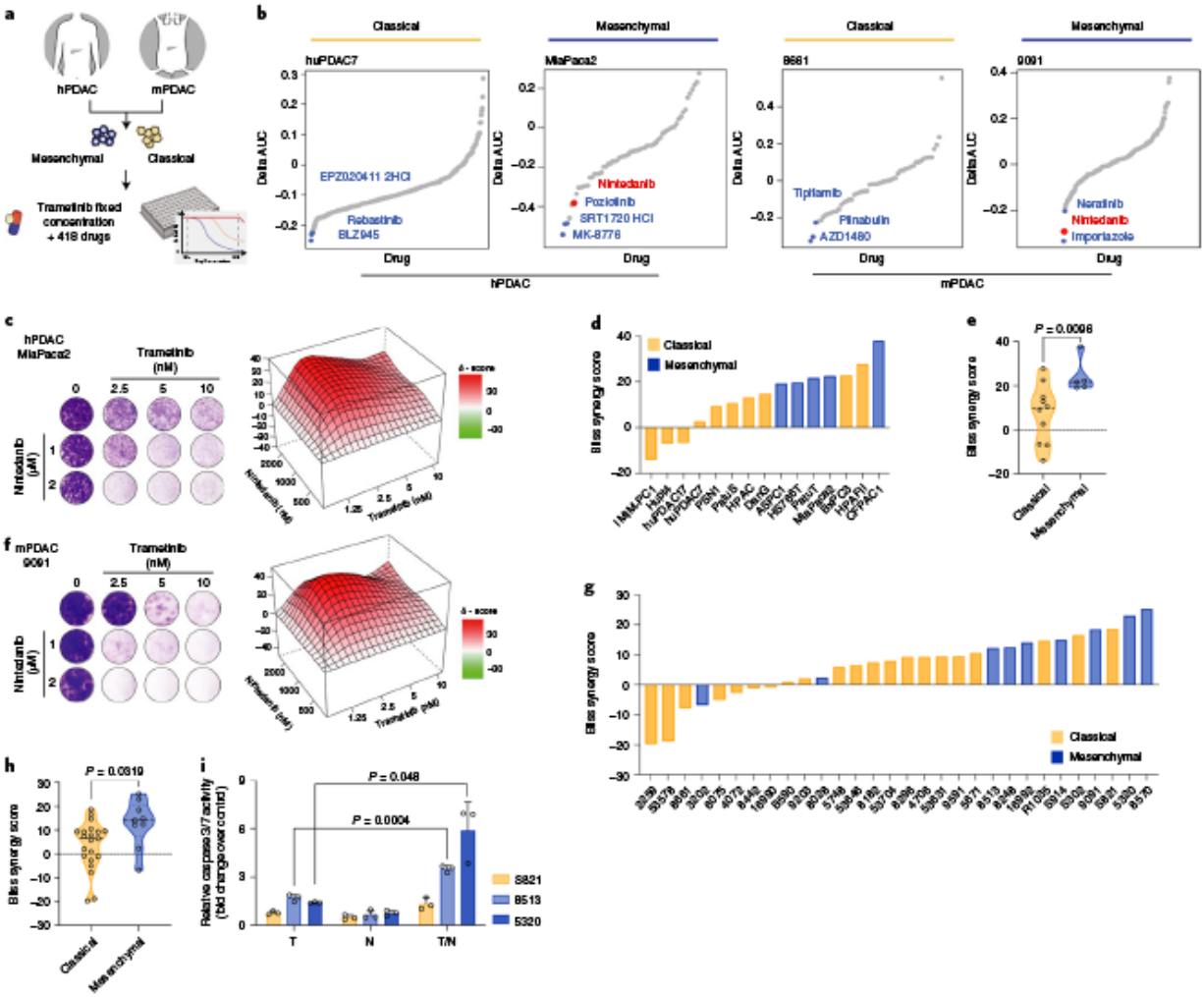

Fig. 2 | Systematic combination drug screens identify new therapies for nonglandular mesenchymal PDAC. a, Experimental set-up of the high-throughput drug screen. **b**, Combination drug screen on two mPDAC (9091, 8661) and two hPDAC (MiaPaca2, huPDAC7) cell cultures. **c**,**f**, Clonogenic assay and synergy map of representative hPDAC (**c**) and mPDAC (**f**) cultures treated with the indicated concentrations of trametinib and nintedanib. **d**,**g**, Bliss synergy scores integrated with cell morphology for hPDAC (**d**) and mPDAC (**g**) cell cultures (classical subtype in yellow, mesenchymal in blue). **e**,**h**, Comparison of the Bliss synergy scores, from **d** and **g**, between classical and mesenchymal hPDAC (**e**) and mPDAC (**h**) cells. **i**, Induction of caspase-3/7 activity on treatment with trametinib (10 nM), nintedanib (2 μM) or the combination of both for 24 h relative to the vehicle-treated control. Data are shown as mean ± s.d. (n = 3 independent experiments). P values in **e**,**h** and **i** were calculated using a two-tailed, unpaired Student's t-test.

showed antagonism, this was reverted to synergism in the *KRAS*^{G12D} overexpression system (Extended Data Fig. 3i,j), supporting the notion that *KRAS* levels impact on cellular differentiation states[16], are the main drivers of mesenchymal PDAC and provide therapeutic vulnerabilities.

To uncover the direct targets of trametinib and nintedanib, and to elucidate the drivers of treatment response and resistance, we performed kinobead pulldown assays on six mPDAC cultures of both subtypes. Although trametinib showed selectivity for binding MEK1/2, nintedanib displayed a broad range of targets, enriched in RTKs and cell-surface receptors (Extended Data Fig. 4a–c). Importantly, expression of the nintedanib targets was subtype dependent. Four were selective for mesenchymal PDAC, including PDGF receptor B (PDGFRB), fibroblast growth factor receptor 1 (FGFR1) and discoidin domain tyrosine kinase receptor 2 (DDR2), and 24 were shared by both subtypes. Furthermore, expression of these targets remained largely unchanged after drug perturbation (Extended Data Fig. 4d,e). Therefore, differences in the basal gene expression program underlie synergistic drug action in PDAC subtypes.

To identify the functional relevant pathways mediating response to T/N, we analyzed changes in the phosphoproteome. In mesenchymal PDAC, we observed a decreased activity of a broad range of important cancer-relevant pathways, such as the cell-cycle regulators cyclin-dependent kinase 2 (CDK2), cyclin D and cyclin E, PP2A and immediate early response 3 (IER3) that regulate phosphoinositide 3-kinase/AKT signaling, and ERBB2, mTOR and KIT downstream signaling, as well as RAF-dependent and -independent ERK1/2 activation (Extended Data Fig. 4f and Supplementary Table 3). These findings support the view that mesenchymal PDAC cells depend on broad RTK-driven signaling input. In contrast, we found

a more limited spectrum of altered pathways in classical tumors, including distinct downregulation of the VEGFA/VEGFR pathway and Rho GTPases, as well as decreased mitogen-activated protein kinase activation (Extended Data Fig. 4g and Supplementary Table 3). This confirmed and extended our initial observation of fundamental differences in signaling between classical and mesenchymal tumors under basal conditions (Extended Data Fig. 1), reinforcing the notion that multiple kinases need to be targeted to achieve meaningful responses in the mesenchymal subtype.

Next, we assessed other drugs sharing targets with nintedanib. Strikingly, in mesenchymal PDAC several top hits of our combination drug screen are multi-kinase inhibitors that display an overlapping target spectrum with nintedanib (Extended Data Fig. 5a,b and Supplementary Tables 2 and 4). In addition, we tested new compounds with overlapping targets (Extended Data Fig. 5c; https://www.proteomicsdb.org). AZD4547, which shares with nintedanib, among others, the targets PDGFRB, FGFR1, DDR1 and DDR2, mimics the synergistic responses observed with T/N and could potentially be used in combination with trametinib. In contrast, other drugs that share targets with nintedanib, including imatinib, display highly heterogeneous responses, showing cell-type- and context-specific synergisms (Extended Data Fig. 5c–e).

To functionalize the targets of nintedanib and decipher key genes synergizing with MEKi, we employed pooled genome-wide, as well as focused, CRISPR–Cas9-based negative selection (viability) screens in three mesenchymal mPDAC cell cultures. We performed a genome-scale screen in 9091 cells and an in-house-developed, nintedanib-target-focused screen in 8248 and 8570 cells, with and without trametinib (Fig. 3a–e, Extended Data Fig. 6a–f and Supplementary Tables 5 and 6). To identify genes altering trametinib sensitivity, we calculated differential sensitivity scores, as the difference in β-score between the trametinib- and dimethylsulfoxide (DMSO)-treated arms. We focused on genes displaying a negative differential sensitivity score, indicating enhanced depletion in the presence of trametinib (Fig. 3b and Extended Data Fig. 6f).

In the genome-scale CRISPR screen we identified 8 nintedanib targets out of a total of 758 hits with statistically significant β-scores, the inactivation of which resulted in the specific depletion of trametinib-treated cells (Fig. 3b–d). In the focused screens in 8248 and 8570 cells, nine and four nintedanib targets cooperated with trametinib, respectively (Fig. 3d). Altogether, of 53 nintedanib targets identified in kinobead pulldown experiments, 15 showed functional relevance in the presence of trametinib in mesenchymal PDAC cells (Fig. 3d). Importantly, the three different mesenchymal cell cultures showed some degree of heterogeneity across relevant nintedanib targets, indicating potential differences in underlying genetic, epigenetic and phenotypic characteristics of this subtype. Further analysis of the targets and their interaction using the STRING database (http://string-db.org) revealed a high degree of interconnectivity and convergence on FGFR, MEK/ERK family members and PDGFR-regulated networks, with different members of these pathways observed in the three screens (Fig. 3d). Unexpectedly, gene expression profiling revealed no clear correlation between messenger RNA abundance of nintedanib targets and trametinib sensitization on depletion (Extended Data Fig. 6g). Taken together, these data indicate that no single kinase, but rather a specific spectrum of targets, such as PDGFR, FGFR and MEK/ERK family members, act in concert to mediate therapeutic efficacy in a context-specific manner.

Analysis of the 758 hits of the genome-scale CRISPR screen allowed us to identify pathways in mesenchymal PDAC, which globally cooperated with MEKi, such as ERBB, PDGFRB, KIT and the retinoblastoma gene (*RB1*) (Fig. 3e). These pathways correlated to a high degree with the phosphoproteomic analysis of the T/N-treated mesenchymal PDAC cells, thereby crossvalidating these results functionally (Extended Data Fig. 4).

To extend and validate the top-scoring nintedanib targets of our negative selection screens, we exploited single and combination CRISPR–Cas9 single-guide (sg)RNA-based approaches. First, we individually depleted Acvr1, Grb2, Map2k5, Map3k3, Prkaa1 and Fgfr1, and assessed cell growth using clonogenic assays with and without trametinib. In line with our negative selection screens, we observed heterogeneity in the cooperation of these nintedanib targets with MEKi across the different models (Fig. 3f,g and Extended Data Fig. 6h–j). To probe the cooperation among the identified targets in mediating trametinib sensitization, we next depleted Acvr1, Grb2, Map2k5, Map3k3, Prkaa1 and Fgfr1 in triple combinations with and without trametinib, using a transfection-based Cas9–sgRNA RNP approach (Fig. 3h–k and Extended Data Fig. 6k,l). In addition, we correlated the relative indel frequency of each combination with the loss of viability in the presence of trametinib (Fig. 3h,k). Consistently, we observed a heterogeneous response across the three cellular models, with the combination depletion of Prkaa1, Fgfr1 and Map2k5 being most efficient in two out of three mesenchymal cell cultures in the presence of trametinib. This confirmed our hypothesis that the depletion not of one, but of a combination of, multiple targets is important to sensitize mesenchymal PDAC toward MEKi. Thus, broad targeting is needed to efficiently and comprehensively treat mesenchymal PDAC.

T/N triggers a T cell-dependent anti-tumor immune response. Our in vitro findings prompted us to explore the combination treatment in vivo in syngeneic orthotopic transplantation models of

Fig. 3 | Genetic screens uncover nintedanib targets that sensitize mesenchymal PDAC toward trametinib. a, Schematic representation of genome-scale and nintedanib-target-focused CRISPR–Cas9 screens. **b**, Genome-scale screen in mesenchymal mPDAC 9091 cells. Trametinib sensitivity (*x* axis) represents β-scores calculated as sgRNA representation difference between trametinib-treated cells and their initial representation. Differential sensitivity (*y* axis) indicates β-score differences between trametinib- and DMSO-treated arms. In red are genes presenting differential sensitivity ≤−0.25. **c**, Venn diagram of overlap of genome-wide screening hits (**b**) (differential sensitivity ≤−0.25 and FDR ≤ 0.05) and the nintedanib targets. **d**, Network of nintedanib targets of CRISPR–Cas9 screens in 9091 (genome-wide), 8248 and 8570 (focused) cells built on the string database and visualized using Cytoscape. Nintedanib targets are color coded according to the differential sensitivity between trametinib- and DMSO-treated arms. **e**, Pathway enrichment within the MSigDB canonical pathway database of genome-wide screening hits of **b** showing a differential sensitivity ≤−0.25. **f**, Lentiviral CRISPR–Cas9-mediated deletion of selected top-scoring nintedanib targets in 9091 cells. Knockout cells were treated with trametinib (5 nM) or DMSO and viability was assessed through clonogenic assays. **g**, Quantification of **f**. Data are normalized to DMSO-treated nontargeting controls (mean ± s.d.; $n = 3$ biological replicates). The dashed line represents the mean of trametinib-treated nontargeting controls. **h**, Combinatorial deletion of nintedanib targets via RNP electroporation. Mesenchymal mPDAC cells 9091, 8248 and 8570 were electroporated to deliver the Cas9–sgRNA complex. The resulting cells were treated for 7–9 d with DMSO or trametinib (5 nM). Cell viability was assessed via clonogenic assays (**i** and **j** and Extended Data Fig. 6) and indel frequencies via sequencing (**k**). The indels were used to determine the $\log_2$(fold-change) (LFC) of the indel frequency in **k**. **i**, Clonogenic assays of 9091 cells electroporated with RNPs targeting the indicated nintedanib targets. Knockout cells were treated with trametinib (5 nM) or DMSO. **j**, Quantification of **i**. Data are normalized to DMSO-treated nontargeting controls (mean ± s.d.; $n = 3$ biological replicates). The dashed line represents the mean of trametinib-treated nontargeting controls. **k**, Left: heatmap of the indel frequencies LFC (trametinib/DMSO) as described in **h**. Comb., combination. Right: heatmap of relative viability (trametinib/DMSO) of the clonogenic experiments described in **i** and **j**.

classical and mesenchymal PDAC (Fig. 1g). These models resemble the clinical course of PDAC patients, with the mesenchymal subtype model being more aggressive, displaying rapid and uniform tumor progression to death (Fig. 4a).

We randomized tumor-bearing mice and observed that the T/N combination led to a remarkable response of mesenchymal PDAC with a significant reduction in tumor volume of up to ~40% and doubled survival (Fig. 4b–d). Moreover, we observed not only a decrease in tumor-cell proliferation, but also vascular remodeling as evidenced by an increased amount of CD31+ vessels (Fig. 4e–h), as well as markers of angiogenesis and endothelial cell activation (Extended Data Fig. 7a–c).

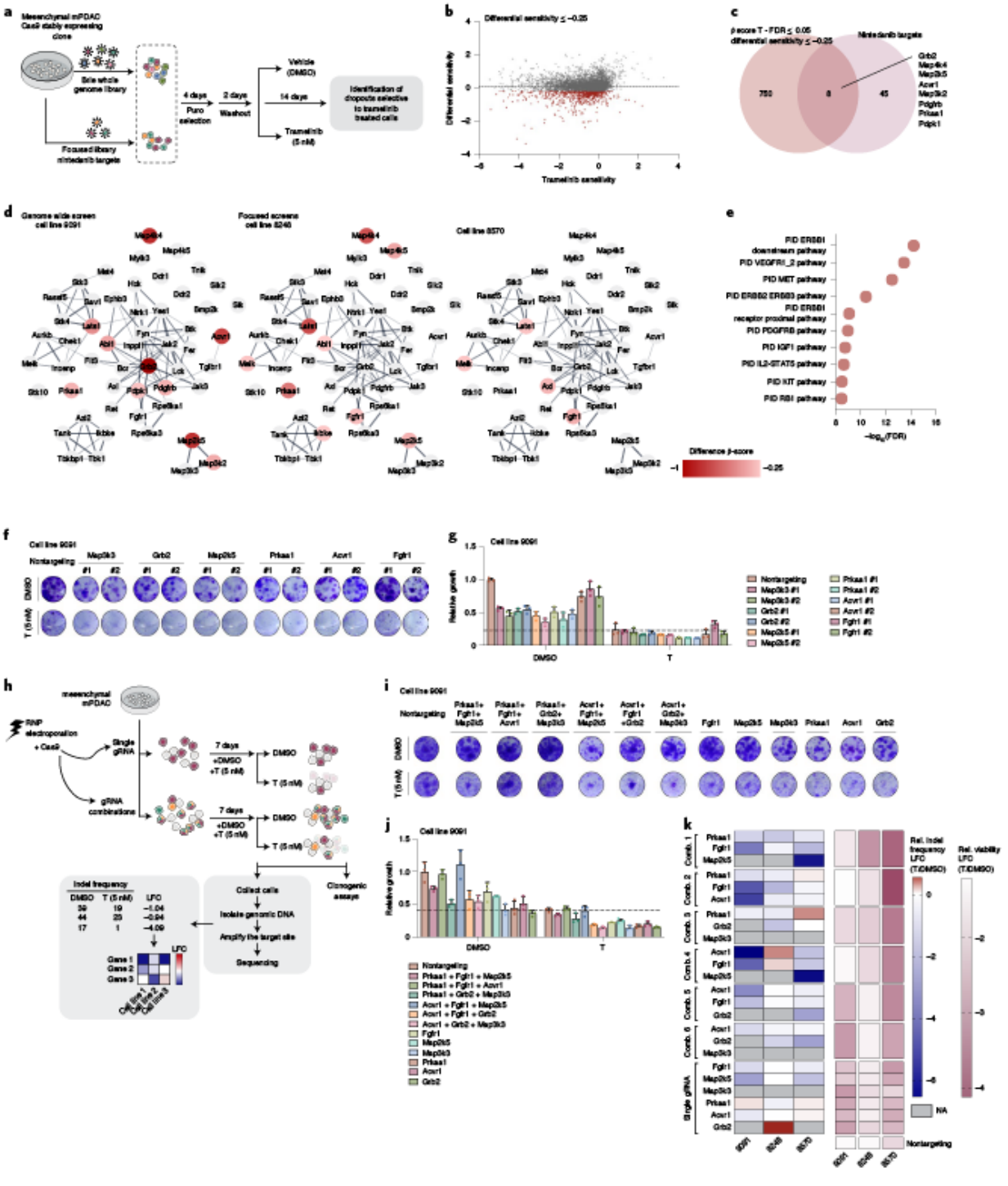

Unexpectedly, also the classical subtype responded to the combination therapy; however, this effect was mainly mediated by trametinib as evidenced by similar tumor volumes of trametinib- and T/N-treated cancers (P=0.786; Fig. 4b). In addition, mesenchymal tumors showed a superior overall response with two partial remissions and stable disease in 12 of 21 mice treated with T/N, according to the response evaluation criteria in solid tumors (RECIST) (Fig. 4b,c). In contrast, classical tumors showed no partial remission and only 3 of 18 mice displayed stable disease. Accordingly, the difference in T/N-induced tumor regression between both subtypes is statistically significant (P= 0.0162; Fig. 4b). This translated into improved overall survival, which was doubled in the mesenchymal subtype (36 d for T/N versus 16 d for controls), whereas classical tumors displayed only a 50% increase (27 d for T/N versus 20 d for controls; Fig. 4d). This difference in survival benefit is statistically significant (P= 0.0007; Fig. 4d, right panel). Thus, the new combination is, to our knowledge, the first preclinical therapy that induces tumor regression and an increase in overall survival in *Kras-mut* iGD-driven mesenchymal PDAC. In line with the differential response, we observed a subtype-specific decrease in PDGFRB–Tyr1021 and AMPKα–Thr172 (PRKAA1) phosphorylation of T/N-treated mesenchymal tumors in vivo (Fig. 4i). Both kinases are important nintedanib targets identified in the proteomic kinobead-based pulldown approach (Extended Data Fig. 4).

PDAC is considered to be immunologically 'cold': its microenvironment is characterized by a lack of cytotoxic T cells and infiltration of immunosuppressive immune cells[9,21]. T/N treatment substantially increased T-cell infiltration into mesenchymal tumors. In contrast, classical tumors displayed features of immune exclusion—showing only a moderate enrichment of T cells at the tumor margins (Fig. 5a–d and Extended Data Fig. 7d–f). Immunophenotyping of mesenchymal tumors revealed increased infiltration of CD8$^+$ T cells, localized preferentially around vessels, arguing that vascular remodeling on drug perturbation contributes to cytotoxic T-cell infiltration (Extended Data Fig. 7a–c).

To investigate the role of T cells in therapy response, we employed CD3ε-knockout mice on a C57BL/6 background, lacking all T cells[22] (Fig. 5e–h and Extended Data Fig. 7g,h). T-cell deficiency blunted the T/N response and diminished the survival benefits of mesenchymal tumors (Fig. 5f–h and Extended Data Fig. 7h). The tumor volume decreased significantly in wild-type (WT) versus CD3ε-knockout mice (P=0.0124; Fig. 5f). In addition, T/N treatment prolonged survival compared with controls by 20 d in WT mice, but only marginally by 5 d in mice lacking T cells (P=4.9×10^{-5}; Fig. 5g,h). These data support the notion that T cells contribute significantly to the in vivo efficacy of the T/N combination in the mesenchymal subtype. However, treatment response is not mediated by T cells alone, but depends on TME reprogramming and tumor-cell intrinsic drug action.

In contrast to mesenchymal PDAC, the classical subtype showed a mixed response in T-cell-deficient animals. There was no difference in tumor volume (P=0.563, WT versus CD3ε-knockout mice; Fig. 5e), but a slight effect of T-cell deficiency on survival, which was reduced by 5 d in T/N-treated CD3ε-knockout mice (P= 0.028; Fig. 5g,h), indicating immune surveillance also in this model on therapy, but to a significantly smaller extent (P= 0.0014; Fig. 5h).

Cancer therapies can affect macrophage functions and alter their recruitment or polarization states[23]. The combination treatment did not change the overall number of macrophages substantially (Extended Data Fig. 8a,b). However, their polarization changed from the pro-tumorigenic M2- to an anti-tumorigenic M1-like state (Extended Data Fig. 8c–e), suggesting that they might contribute to anti-tumor responses. However, this effect was present in both subtypes. Therefore, these changes do not explain the observed subtype-specific differences.

Distinctively, epithelial tumors displayed an increase of neutrophils on treatment (Extended Data Fig. 8a,f). The role of tumor-associated neutrophils is controversial; some studies have shown their ability to block anti-tumor immune responses and mediate CD8$^+$ T-cell suppression, and others have highlighted their various anti-tumor properties, including direct cytotoxicity and inhibition of metastasis[24–26]. Therefore, distinct immune cell types and mechanisms seem to contribute to the anti-tumor effects of the drug combination in both subtypes, with T cells being the key contributor to the strong effects observed in mesenchymal PDAC.

The T/N combination sensitizes mesenchymal PDAC toward ICB. Our in vivo findings prompted us to investigate whether the combination therapy could sensitize the highly aggressive mesenchymal subtype toward ICB. Compared with controls, anti-programmed death-ligand 1 (PD-L1)- and T/N-treated groups, T/N+anti-PD-L1 therapy-induced tumor regression up to ~80% and increased survival selectively in mesenchymal PDAC (P=0.016, T/N+anti-PD-L1 versus T/N; Fig. 6a–c). The median survival benefit by adding anti-PD-L1 to the combination was 10.5 d compared with T/N alone and 30.5 d compared with vehicle, representing an almost threefold increase in survival (Fig. 6c). Six of sixteen mice showed objective tumor regression with a partial response according to RECIST. Of the remaining ten mice, eight displayed stable and only two progressive disease (P= 0.078 T/N+anti-PD-L1 versus T/N; Fig. 6a). In contrast, no tumor regression, survival benefit or increased response rate was observed in classical PDAC, and both subtypes did not respond to ICB with PD-L1 alone (Fig. 6a,c).

In summary, the triple treatment with ICB markedly improves anti-tumor responses, offering a clear survival benefit selectively in mesenchymal PDAC.

Fig. 4 | The combination treatment prolongs survival and reprograms the TME in vivo. a, Kaplan–Meier curve comparing the survival of classic and mesenchymal orthotopic PDAC models. The number of mice per treatment condition is indicated. **b**, Quantification of tumor volume changes of the classical and mesenchymal subtype after 1 week of indicated treatment assessed by MRI. Each column represents one mouse, in comparison with baseline MRI measurements before treatment. Control, T, N and T/N cohorts are shown. **c**, Representative MRI of vehicle (control) and T/N-treated mice before (week 2) and after 1 week of treatment (week 3). Scale bars, 5 mm. **d**, Left and middle panels: Kaplan–Meier survival curve of classical and mesenchymal orthotopic models. The number of mice per treatment condition is indicated. Right: comparison of the ratio between the survival of mice treated with T/N and the median survival of their respective vehicle-treated controls. **e**, Representative H&E and IHC staining for Ki67 and CD31 of tumor sections from orthotopically transplanted classical and mesenchymal PDAC subtype models treated with vehicle (control) or T/N for 1 week. Scale bars, 50 µm. **f**, Quantification of Ki67$^+$ cells (classical: control n=6, T/N n=5; mesenchymal: control n=8, T/N n=7). HPF, high-power field. **g**, Quantification of the number of mitoses per high-power field (classical: control n=6, T/N n=6; mesenchymal: control n=9, T/N n=8). **h**, Quantification of vessels CD31$^+$ (classical: control n=5, T/N n=5; mesenchymal: control n=9, T/N n=8). **i**, Representative IHC staining for pPDGRFb-Tyr1021, pAMPKa-Thr172 and p-p44/42 (Thr202/Tyr204) of tumor sections from orthotopically transplanted classical and mesenchymal PDAC subtype models treated with vehicle (control) or T/N for 1 week. Scale bars, 100 µm. P values in **b**,**d** (right), **f**–**h** were calculated using a two-tailed, unpaired Student's t-test. P values in **a** and **d** (left and middle) were calculated using log(rank) (Mantel–Cox) test. Note that the classical and mesenchymal cohorts in **a** are the same as those shown in **d**. Vehicle- and trametinib-treated cohorts shown in **b** are the same as shown in Fig. 1i.

ScRNA-seq reveals context-specific T/N-driven changes. To investigate therapy-induced TME changes in a global and unbiased fashion, and to mechanistically decipher the drug action on epithelial and mesenchymal tumor cells and their environment in vivo, we performed single-cell RNA sequencing (scRNA-seq) of whole tumors. One to two PDAC per model and treatment condition were dissociated, sorted into mesenchymal/fibroblast and epithelial/immune-enriched cell fractions and sequenced (Fig. 7a). To define cell populations, we combined the data from both subtypes and all treatment groups, representing a total of 30,677 cells (1,677–13,169 cells per model and treatment condition; Fig. 7b). In both subtypes we identified tumor cells, acinar cells, T cells, natural killer cells, B cells, myeloid populations, such as macrophages and neutrophils, and fibroblasts (Extended Data Fig. 9a). In the classical tumors we

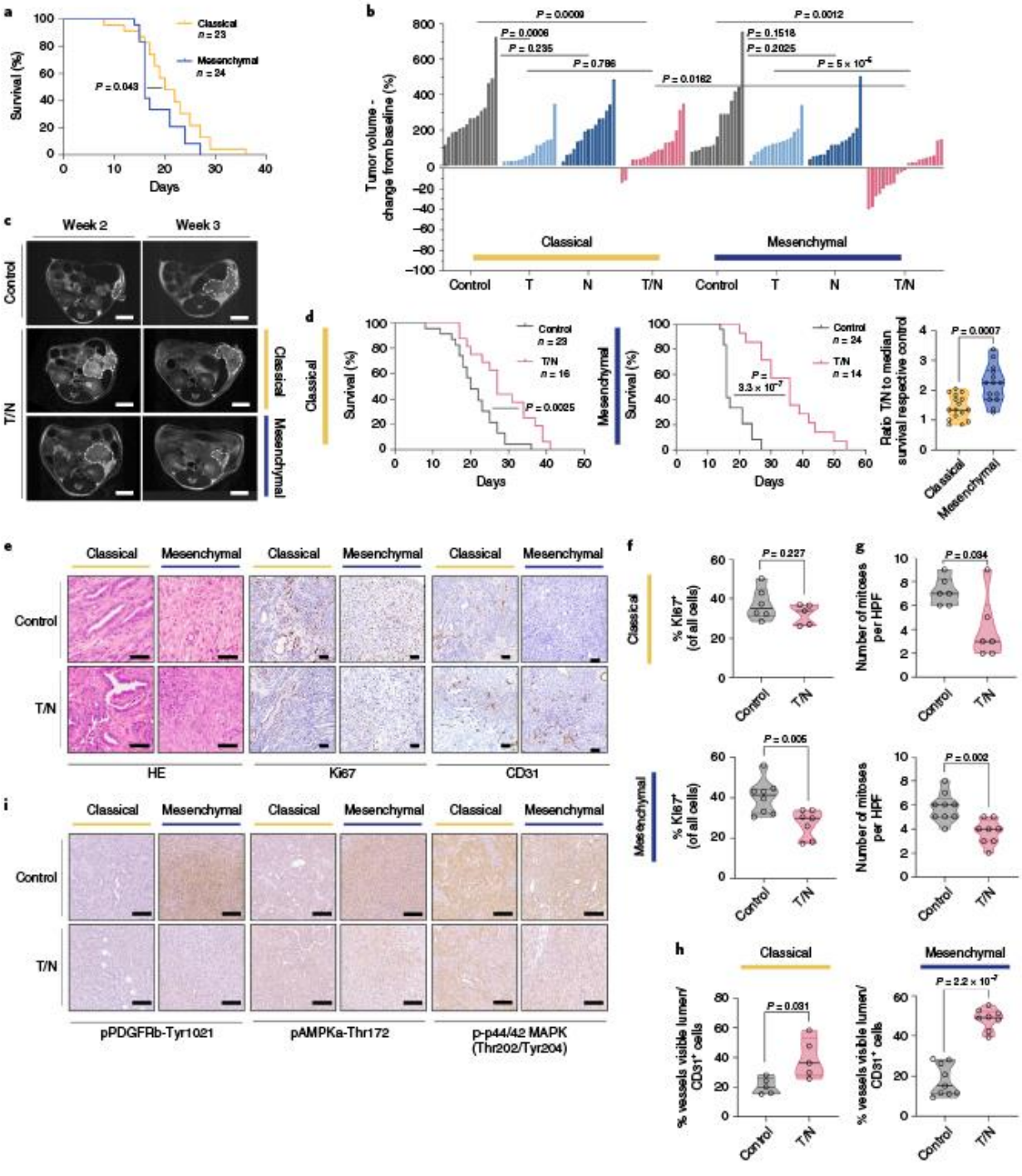

additionally identified a cluster of endothelial cells (Fig. 7b and Extended Data Fig. 9a,b).

Treatment-induced cancer cell transcriptional changes. We assessed the impact of the combination therapies on gene expression of cancer cells and observed no evidence of epithelial-to-mesenchymal transition (EMT) or the reverse process (MET) in T/N-treated tumors with and without ICB (Extended Data Fig. 9c). Gene set enrichment analysis (GSEA) uncovered widespread and, in part, context-specific, treatment-induced alterations of immune-related pathways in tumor cells (Fig. 7c–e). For both subtypes, we observed an induction of antigen processing and crosspresentation (Fig. 7d). In addition, mesenchymal PDAC showed an exclusive and striking enrichment for interferon signaling signatures, including an interferon-γ response as well as interferon regulatory factor 2 (IRF2) induction in the context of triple therapy (Fig. 7d,e and Extended Data Fig. 9d).

A growing body of evidence connects immune responses to errors in DNA replication and genomic instability[27,28]. GSEA revealed treatment-induced DNA damage in both subtypes. We validated this observation by γH2AX IHC, a marker for DNA damage. It is interesting that induction of DNA damage was stronger in the classical subtype, indicating that the remarkable treatment response of mesenchymal PDAC is not mediated by DNA damage alone (Extended Data Fig. 9e–g). Several studies link DNA damage to the senescence-associated secretory phenotype (SASP) as well as anti-tumor immune responses[29]. GSEA showed that SASP was strongly enriched exclusively in classical PDAC and this was maintained across treatments (Fig. 7f). Senescence-associated β-galactosidase (SA-β-Gal) staining confirmed this phenotype (Fig. 7g). This indicates that the therapeutic effects observed in the classical subtype are mediated by a complex combination of mechanisms, which include induction of DNA damage, SASP and a reduction in cell proliferation.

Drug treatment-induced immune responses. Our in vivo immune profiling shows a robust anti-tumor immune program in mesenchymal PDAC centered on T cells on T/N treatment. Analysis of the T cells (3,260 cells) of our scRNA-seq dataset (Fig. 8) revealed 6 subpopulations for both PDAC subtypes (clusters 1–6) (Fig. 8a and Methods).

T/N-treated mesenchymal tumors showed a substantial decrease of CD4+ and CD8+ T cells with a gene expression signature resembling naive T cells, and a dramatic increase in T cells with functional cytotoxic, effector and memory gene expression signatures (Fig. 8b,c). Addition of anti-PD-L1 to T/N resulted in a further increase of cytotoxic and effector T cells up to almost 75% of all T cells (Fig. 8b).

In contrast to recent studies indicating that SASP induces vascular remodeling leading to T-cell infiltration and anti-tumor immunity[21], the T/N combination reprogrammed the TME of classical PDAC toward a decrease of regulatory and effector T cells and an increase in the naive-like CD4+ compartment (Fig. 8b). Furthermore, the functional gene expression signature was much weaker in the cytotoxic and effector clusters in classical compared with mesenchymal tumors (Fig. 8c).

Together, our findings show that, in mesenchymal tumors, the T/N combination alone leads to a considerable increase of effector-like, activated and cytotoxic T cells, indicating an effective anti-tumor immune response, which was further enhanced by anti-PD-L1 treatment. This contrasts with the classical subtype, which showed a reduction of regulatory and effector T cells on treatment despite displaying an SASP phenotype.

To gain insights into changes that could mediate T-cell infiltration on therapy, we analyzed the secretomes of T/N-treated epithelial and mesenchymal tumor cells with mass spectrometry (MS)-based proteomics[30]. We observed profound T/N-induced changes in the secretion of immunomodulatory chemokines and cytokines between both subtypes (Extended Data Fig. 10a). To get a comprehensive overview of the resulting intercellular communication networks, we integrated tumor-cell-secreted proteins across treatment conditions with cell populations expressing the corresponding receptors as identified by scRNA-seq. This revealed key differences in the secretion of factors previously shown to modulate immune cell recruitment, differentiation and expansion, as well as tumor immune responses (Fig. 8d and Extended Data Fig. 10b, inner circle)[31–36]. In mesenchymal PDAC, the T/N combination specifically induced CXCL12, CXCL16 and TNFSF12 secretion, whereas CCL2, CSF1 and LGALS9 were downregulated (Fig. 8d). This contrasts with the classical subtype, which showed reduced levels of secreted CXCL12, CXCL16 and CXCL20, as well as an increase in CCL2 and CSF1 on T/N treatment (Extended Data Fig. 10a,b). CXCL16, which is upregulated in mesenchymal PDAC on T/N treatment, is a key chemoattractant for TILs and high expression levels correlate with a favorable prognosis and increases TILs, for example, in colorectal and breast cancer[31,32,37]. Accordingly, PDAC tumors with high CXCL16 mRNA expression levels display an increased overall survival ($n=176$ samples, log(rank) test, $P=0.042$; https://www.proteinatlas.org/ENSG00000161921-CXCL16/pathology/pancreatic+cancer)[38]. CXCL12 increases cytotoxic T-cell infiltration in osteosarcoma[33] and CCL2 and CSF1 mediate immunosuppression in various cancer types[34,35]. Therefore, T/N treatment induces a tumor-cell-derived favorable reprogramming of the immunosuppressive TME, thereby priming mesenchymal PDAC for ICB.

Cancer-associated fibroblast reprogramming. PDAC subtypes differ in cancer-associated fibroblasts (CAFs), desmoplastic stroma and extracellular matrix content, most abundant in classical, although

Fig. 5 | The combination treatment enhances tumor immune infiltration specifically in the mesenchymal subtype. a, Fraction of adaptive immune cell populations in tumors from vehicle- (control) and T/N-treated mice. Classical and mesenchymal orthotopic transplanted tumors, originating from 8661 and 9091 mPDAC cells, respectively, were analyzed by flow cytometry. The number of tumors per condition analyzed is depicted in the corresponding panel. **b**, FACS staining for CD4+ and CD8+ T cells of tumors treated with vehicle or the T/N combination for 1 week. Individual tumors are shown as single points in the graph (classical: control $n=5$, T/N $n=5$; mesenchymal: control $n=6$, T/N $n=6$). **c**, Representative images of IHC staining for CD3+ and CD8+ T cells of tumor sections from orthotopically transplanted mesenchymal models treated with vehicle or T/N for 1 week. Scale bars, 50 µm. **d**, Representative images of tissue sections stained for CD3+ cells (green). Keratin 18 detects epithelial PDAC cells in classical tumors whereas vimentin detects undifferentiated tumor cells in mesenchymal tumors (white). DAPI was used for nuclear staining (blue). Tumor borders are marked by a white dotted line and tumor localization is indicated. Scale bars, 25 µm. **e**,**f**, Waterfall plot of the response of classical (**e**) and mesenchymal (**f**) tumors orthotopically transplanted in syngeneic immunocompetent C57BL/6 WT and T-cell-deficient CD3*e* C57BL/6-knockout (*CD3e*-KO) mice after 1 week of T/N treatment (fold-change compared with baseline before treatment based on MRI volumetric measurements; *y* axis). KO, knockout. **g**, Kaplan–Meier survival curve of *CD3e*-KO and C57BL/6 WT mice orthotopically transplanted with classical (upper panel) or mesenchymal (lower panel) tumor cells. The number of mice per treatment condition is shown. **h**, Comparison of the ratio between the survival of mice treated with T/N and the median survival of their respective vehicle-treated controls. *P* values in **b**,**e**,**f** and **h** were calculated using a two-tailed, unpaired Student's *t*-test. *P* values in **g** were calculated using the log(rank) (Mantel–Cox) test. Note that the immunocompetent cohorts shown in **e** (left), **f** (left), **g** (left) and **h** are the same as shown in Fig. 3a,b,d (left and middle panels).

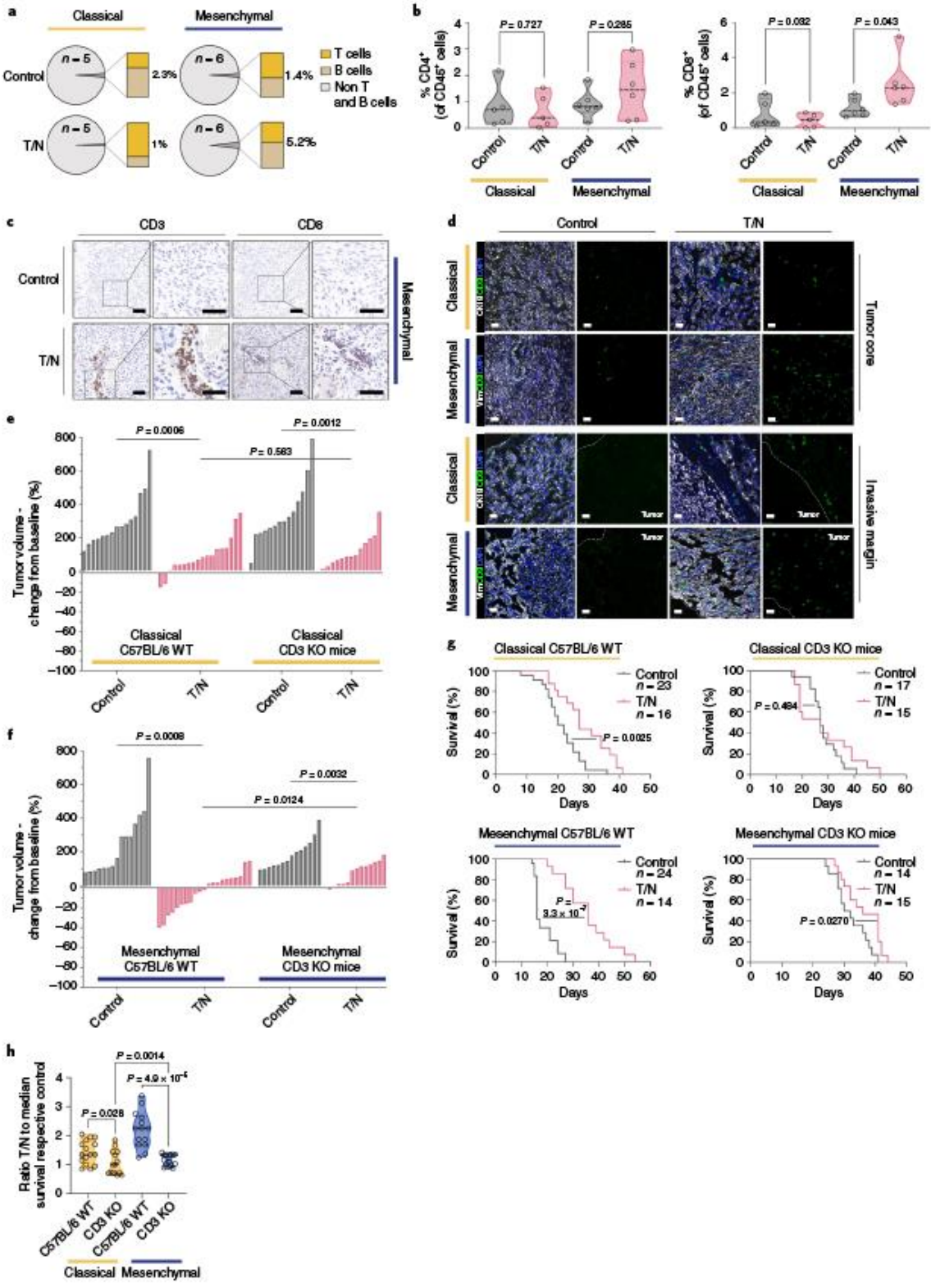
a
Classical
Mesenchymal
Control
T/N
n = 5
n = 6
2.3%
1.4%
1%
5.2%
T cells
B cells
Non T and B cells
b
P = 0.727
P = 0.285
P = 0.032
P = 0.043
% CD4+ (of CD45+ cells)
% CD8+ (of CD45+ cells)
Control
T/N
Classical
Mesenchymal
c
CD3
CD8
Control
T/N
Mesenchymal
d
Control
T/N
Classical
Mesenchymal
Tumor core
Invasive margin
Tumor
e
P = 0.0006
P = 0.583
P = 0.0012
Tumor volume - change from baseline (%)
Classical C57BL/6 WT
Classical CD3 KO mice
f
P = 0.0008
P = 0.0124
P = 0.0032
Mesenchymal C57BL/6 WT
Mesenchymal CD3 KO mice
g
Classical C57BL/6 WT
Classical CD3 KO mice
Mesenchymal C57BL/6 WT
Mesenchymal CD3 KO mice
Survival (%)
Days
Control n = 23
T/N n = 16
P = 0.0025
Control n = 17
T/N n = 15
P = 0.484
Control n = 24
T/N n = 14
P = 9.3 x 10-7
Control n = 14
T/N n = 15
P = 0.0270
h
P = 0.0014
P = 4.9 x 10-5
P = 0.028
Ratio T/N to median survival respective control
C57BL/6 WT
CD3 KO
C57BL/6 WT
CD3 KO
Classical
Mesenchymal

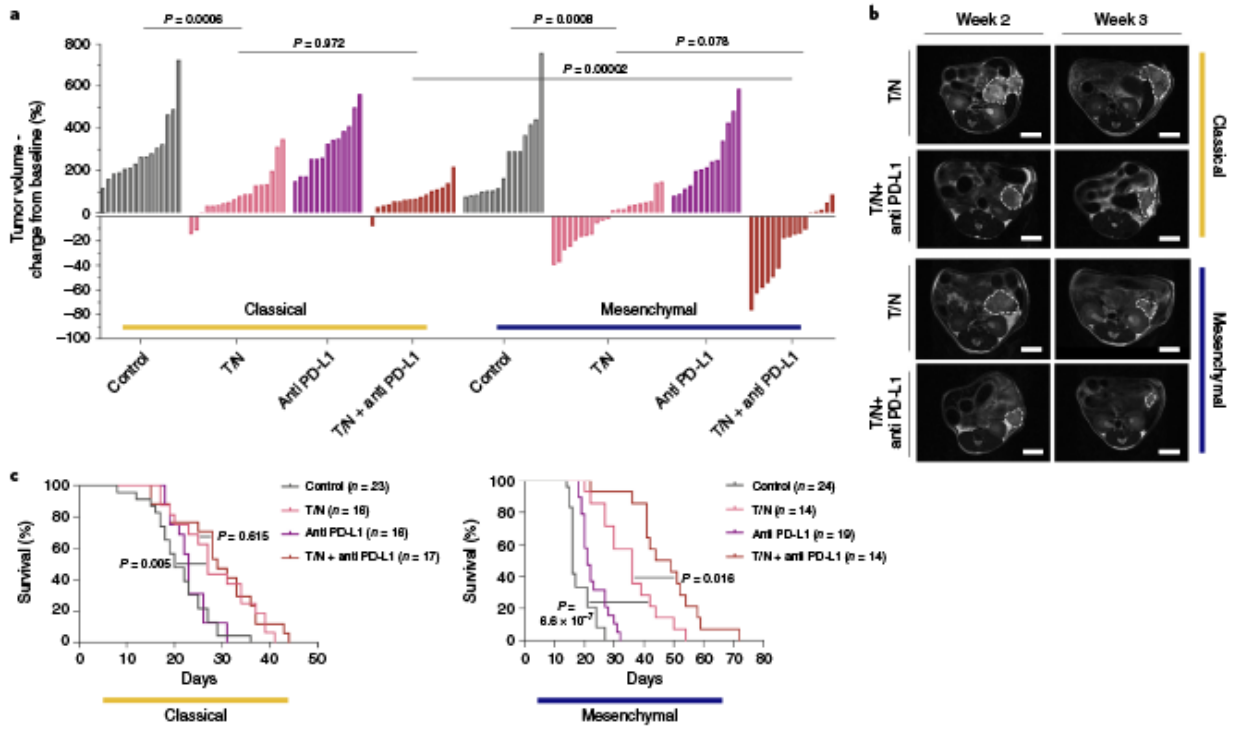

Fig. 6 | The T/N combination sensitizes mesenchymal PDAC toward anti-PD-L1 ICB. a, Waterfall plot showing tumor response of classical and mesenchymal PDAC to T/N + anti-PD-L1 versus vehicle control, T/N and baseline anti-PD-L1 therapy after 1 week of treatment (values represent fold-change compared with baseline before treatment based on MRI volumetric measurements; *y* axis). *P* values were calculated using a two-tailed, unpaired Student's *t*-test. **b**, Representative MRI of vehicle- and T/N + anti-PD-L1-treated mice before (week 2) and after 1 week of treatment (week 3). Scale bars, 5 mm. **c**, Kaplan–Meier survival curves of classical and mesenchymal, orthotopically transplanted models of the indicated treatment arms. The number of mice is indicated in the corresponding panels. The *P* value was calculated using the log(rank) (Mantel–Cox) test. Note that the classical and mesenchymal cohorts, control and T/N, in **a** and **c**, are the same as shown in Fig. 3a,b,d (left and middle panels).

almost absent in mesenchymal, tumors[39]. CAFs are highly heterogeneous, displaying diverse effects on tumor progression and therapeutic response[40,41]. Recently, at least three different CAF subpopulations, myofibroblast-like (termed myoCAFs), inflammatory (iCAFs) and antigen-presenting CAFs (apCAFs), were characterized in PDAC[40,42].

To investigate the dynamics of CAF subtypes in the PDAC TME, we analyzed their number and polarization making use of our scRNA-seq dataset (Extended Data Fig. 10c–h). Fibroblasts comprised only 9% of sorted classical tumors, in line with recent human PDAC datasets, which contain only <2% CAFs out of all cells in scRNA-seq experiments[42]. Mesenchymal tumors consist of densely packed tumor cells that lack the classical desmoplastic stroma[43,44]. Accordingly, only very few CAFs were detected in vivo, preventing the analysis of this population.

In classical PDAC, T/N-treated tumors displayed a substantially reduced number of myoCAFs and a remarkable increase in iCAFs. In addition, myoCAFs presented reduced *Tgfb1* expression on dual and triple treatment (Extended Data Fig. 10c–h). In line with its well-known role in blocking immune responses within the TME[45], transforming growth factor (TGF)-β1 downregulation was paralleled by decreased regulatory T cells (Fig. 8b).

Collectively, our data highlight distinct treatment- and context-specific reprogramming of the TME between subtypes. Exploiting these changes for additional rational therapeutic intervention could lead to improved treatment efficacy also in classical PDAC.

Discussion

PDAC is a complex disease with diverse molecular and morphological subtypes showing TME heterogeneity. Classical PDAC is characterized by a dense desmoplastic stroma, which fosters an immunosuppressive hypovascularized TME, believed to play a major role in primary therapy resistance[21,46,47]. Conversely, the mesenchymal *KRAS-mut* iGD PDAC subtype shows high tumor cellularity and sparse stroma, and is commonly more aggressive and unresponsive to all, to date, attempted polychemotherapies, targeted therapies and ICB[3–5,7,17,48].

In the present study, we identified a new targeted therapy for mesenchymal PDAC by high-throughput combination drug screening. We showed how this therapy remodels the immune landscape in vivo and creates new vulnerabilities toward ICB in mesenchymal tumors. The T/N combination reprogrammed the immunosuppressive mesenchymal cancer cell secretome and downregulated cytokines and chemokines, including CCL2 and CSF1, capable of attracting and inducing expansion of macrophages and myeloid-derived suppressor cells. In parallel, it induced secretion of T-cell modulators, such as CXCL16 and CXCL12, important for TIL recruitment[32–35,37], and provoked upregulation of antigen-processing and presentation pathways in mesenchymal PDAC cells in vivo. Finally, the combination strongly impacts on the TME by increasing blood vessel density, inducing endothelial cell activation and vascular remodeling, and facilitating cytotoxic and effector T-cell infiltration. Thus, we show that reprogramming of the immunologically 'cold' to a 'hot' tumor stroma of the highly aggressive mesenchymal

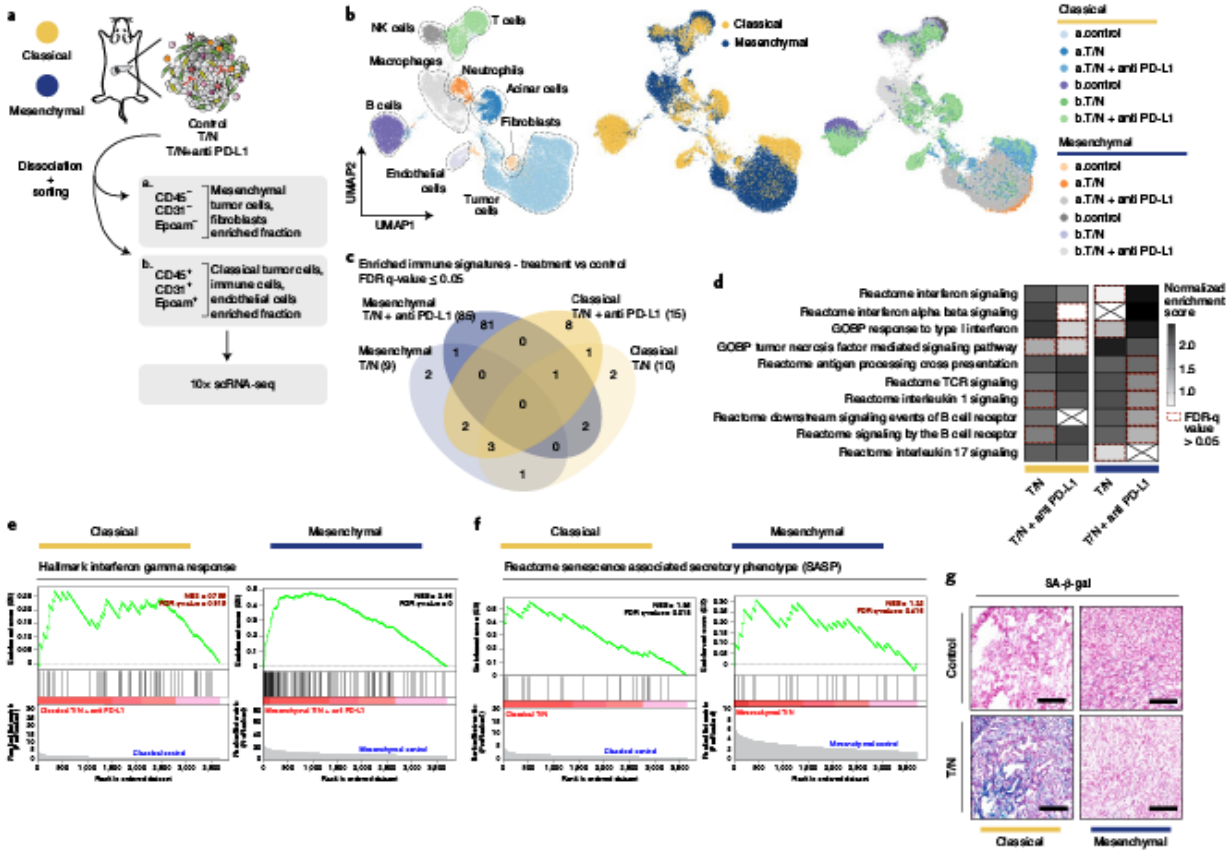

Fig. 7 | ScRNA-seq analysis reveals context-specific responses of tumor cells and their microenvironment on combination drug treatment. a, Scheme of the experimental strategy of the scRNA-seq experiment. One or two tumors per model and treatment condition were dissociated and sorted into mesenchymal/fibroblast (a.) and epithelial/immune-enriched (b.) fractions and subjected to scRNA-seq analysis (10x Chromium). **b**, Left: UMAP plot showing all identified cell populations within the scRNA-seq experiment. Middle: UMAP plot showing classic (yellow) and mesenchymal (blue) tumors from all groups. Right: UMAP plot showing the treatment-induced changes in cell-type composition among the identified cell populations across subtypes. Sorted cell fractions depicted in panel **a** are indicated with (a.) or (b.). **c**, Venn diagram showing the overlap of immune-related signatures obtained from GSEA of the tumor-cell cluster across treatment conditions for both subtypes. Only those presenting an FDR *q* value ≤0.05 are shown. **d**, GSEA signatures presenting at least one overlap in **c**. The normalized enrichment scores (NESs) are plotted in the heatmap. The red dotted line marks the signatures showing an FDR *q* value >0.05. **e**, GSEA of the differentially expressed genes induced by T/N+anti-PD-L1 in classical and mesenchymal tumor cells in vivo. For the mesenchymal subtype, the top immune-related, positively regulated 'hallmark' signature is 'interferon-γ response' and is shown for both classical and mesenchymal tumors. The NES and FDR *q* values are indicated. **f**, GSEA of the differentially expressed genes induced by T/N in classical and mesenchymal tumor cells in vivo. The 'reactome' signature SASP is shown. NES and FDR *q* values are indicated. **g**, Representative images of three independent experiments of SA-β-Gal staining of tissue sections of classical and mesenchymal control and T/N-treated tumors. Scale bars, 70 µm.

subtype is possible and can be exploited therapeutically by adding anti-PD-L1 ICB to the T/N combination.

The context-specific impact of the T/N combination on the immune system was not expected. Although a link across the DNA-damage response, induction of antigen processing and presentation, and activation of strong immune responses is well established[49–52], the lack of these effects in classical PDAC was surprising. Although the combination induces DNA damage, it also induces immunosuppression by increasing the secretion of CCL2 and CSF1. Differences in oncogenic *KRAS* signaling outputs might drive immune signaling divergence between subtypes. High levels of *KRAS* expression, as observed in mesenchymal tumors, were shown to repress interferon-γ signaling in vivo as evidenced by reduction in IRF2 (ref. [53]). Blockade of *KRAS* signaling by MEKi in combination with broad RTK and PD-L1 inhibition might release this important pathway and—in combination with therapy-induced DNA damage—boost neoantigen presentation while inducing anti-tumor immunity in mesenchymal tumors[53]. In line with this, we observed selective upregulation of IRF2 in PDAC cells on T/N+anti-PD-L1 therapy in this subtype in vivo.

Although highly antagonistic in vitro, the combination also showed substantial anti-tumor effects in classical PDAC in vivo, indicating an impact on the TME[54]. The failure of the in vitro drug screen to predict in vivo responses of this subtype is remarkable. Therefore, treatment-mediated TME remodeling should be considered for the transition of in vitro screening hits to the (pre) clinical setting.

We observed an antiproliferative effect of the combination in classical PDAC, as well as the selective induction of SASP. SASP is characterized by the secretion of chemokines, cytokines, matrix metalloproteinases and other paracrine factors[21,29,55]. In classical *KRAS*-driven PDAC, it has been shown that the combination of MEKi

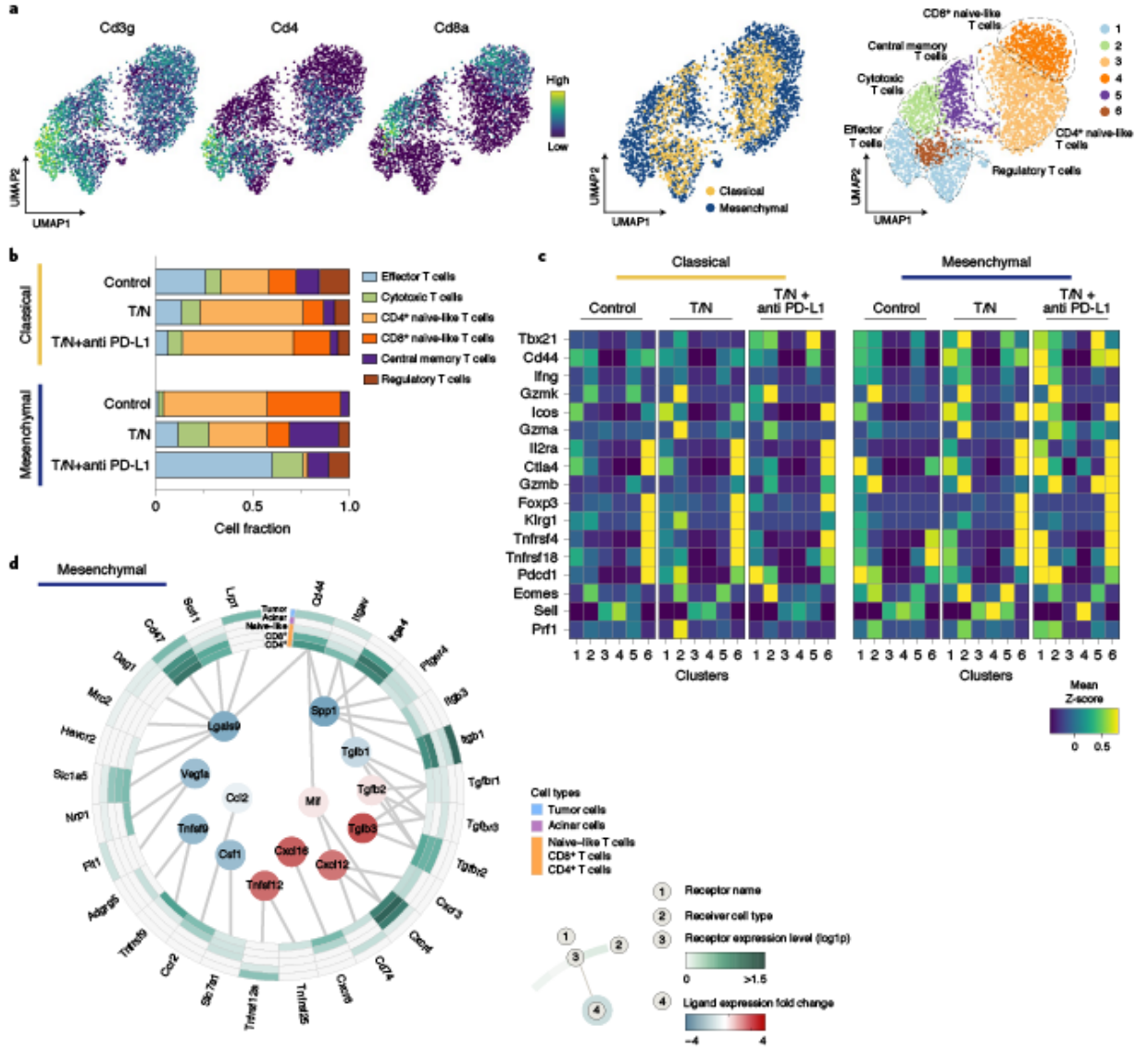

Fig. 8 | The combination therapy induces a T-cell-mediated anti-tumor immune response in mesenchymal PDAC. a, Left: UMAP plots displaying Cd3g, Cd4 and Cd8a marker gene expression across the whole population of T cells identified by scRNA-seq in classical and mesenchymal tumors. Center: UMAP plots of classical (yellow) and mesenchymal (blue) T cells from all treatment and vehicle groups. Right: UMAP plots showing the six T-cell subpopulations identified by scRNA-seq. **b**, Proportion of cells divided by treatment condition and PDAC subtype as identified by scRNA-seq analysis of the T-cell clusters annotated in **a**. **c**, Heatmap displaying expression of selected genes across the identified T-cell clusters (1–6) for both classical and mesenchymal tumors. The different treatment conditions are shown separately. **d**, Circos plot showing the key communication signals from tumor cells to T-cell subpopulations, tumor cells and acinar cells in mesenchymal mPDAC. The ligand protein expression fold-change, identified from secretome experiments, between T/N and control is shown in the middle. Normalized receptor expression levels obtained from scRNA-seq data are shown in the outer concentric circles.

and CDK4/6 inhibitors induces a strong SASP response, with the release of proangiogenic factors that promote tumor vascularization, endothelial cell activation and vascular cell adhesion protein 1 expression. This, in turn, promotes T-cell extravasation into tumors and sensitizes this subtype to ICB[21]. In contrast, we found no evidence for SASP-induced vascular remodeling in classical PDAC on T/N therapy. In line with this, classical T/N-treated tumors did not show T-cell infiltration into the tumor core. This might be due to insufficient levels of SASP induction or other treatment-induced, context-specific effects on the cancer cells and their environment, counteracting vascular remodeling, T-cell extravasation and reactivity. Of note, our study supports the notion that SASP induction is context specific[29] because we were unable to detect therapy-induced senescence in vivo in mesenchymal *KRAS-mut*-driven PDAC. This demonstrates that the biology, stromal composition and treatment response of PDAC are highly context dependent and differ substantially between PDAC subtypes.

Trametinib and nintedanib are both clinically approved by the US Food and Drug Administration/European Medicines Agency.

Trametinib is used for treatment of patients with unresectable or metastatic *BRAF*-mutant melanoma, NSCLC and anaplastic thyroid cancer. Nintedanib, in combination with docetaxel, has been approved for the second-line treatment of advanced NSCLC and first-line therapy for idiopathic pulmonary fibrosis (IPF) (www.accessdata.fda.gov/scripts/cder/daf/index.cfm?event=BasicSearch.process). IPF is characterized by the activation of fibroblasts toward a myofibroblast differentiation[56,57]. Accordingly, blocking myofibroblast activation by nintedanib, or pirfenidone, which targets the TGF-β pathway, slows down pulmonary disease progression[56]. Classical PDAC harbors a dense stroma, which is composed in large parts of activated myoCAFs and TGF-β expression (Extended Data Fig. 10)[42,43]. We therefore hypothesized that adding nintedanib to trametinib might reprogram myoCAFs, thereby contributing to stromal normalization in classical PDAC. Using scRNA-seq, we observed that the number of myoCAFs decreased on T/N therapy, and TGF-β1 expression, which can contribute to immunosuppression via regulatory T cells, is downregulated. This demonstrates that reprogramming of the fibrotic microenvironment of the classical subtype is feasible and could be exploited for further improved therapeutic responses.

To identify the therapeutically relevant targets of the multi-kinase inhibitor nintedanib, we performed multiscale analyses, ranging from kinobead-based proteomic identification of the nintedanib-bound kinases to phosphoproteomic analyses of drug action, and genome-scale and focused CRISPR–Cas9-based negative selection screens. This revealed a key set of nintedanib targets, including FGFR, kinases belonging to the MEK/ERK family and PDGFR-regulated networks that cooperate with trametinib in mesenchymal PDAC. However, it also revealed heterogeneity of the functionally relevant targets within this subtype. This is remarkable and indicates that, indeed, broad multi-kinase inhibition is needed to target this highly aggressive and therapy-resistant subtype efficiently across the whole spectrum of its phenotypes. In addition, it supports the notion that no single target gene is responsible for the synergistic effect of the T/N combination and challenges the one biomarker per drug paradigm in oncology. Indeed, mesenchymal cancer cell morphology and the underlying genetic program are the strongest predictor of therapeutic response to T/N.

In summary, our work sets the basis for the combination of T/N with immunotherapy in the treatment of mesenchymal PDAC and provides a step toward molecularly stratified combination therapies in the clinic. Considering the widespread occurrence of *RAS*-driven tumor entities with an increased *RAS* gene dosage and a mesenchymal differentiation state, our data suggest that combining T/N with ICB or other forms of immunotherapy might trigger anti-tumor immunity and improve therapeutic outcomes across entities.

Methods

Our study complies with all relevant ethical regulations. Animal experiments were approved by the institutional animal care and use committees (IACUCs) of the local authorities of Technische Universität München and Regierung von Oberbayern.

Primary PDAC cell culture, clonogenics and inhibitors. Primary mPDAC cell cultures were isolated from autochthonous PDAC and cultured as described previously[58]. All cells were cultivated for <30 passages, authenticated by genotyping and tested for *Mycoplasma* contamination by PCR. Conventional hPDAC cell lines and primary patient-derived, low-passaged PDAC cell cultures were established and cultured as previously reported[26].

For long-term clonogenic cell proliferation assays, cells were seeded into 24-well plates (density $1–2\times10^3$ cells per well, depending on growth rate). The following day, plates were treated with different concentrations of drugs as indicated. Every 7 d, medium and drug were refreshed. Cells were fixed and stained with 0.2% Crystal Violet in an ethanol:water solution 7–13 d after the start of treatment, according to the confluence reached by the untreated control. Crystal Violet was solubilized with 10% acetic acid and absorbance was quantified at 595 nm. The resulting values were used to calculate the Bliss synergy score with the online software Synergy Finder (v.1.0)[60]. All assays were performed independently at least three times. Trametinib, nintedanib, AZD4547, imatinib and PF-3758309 were obtained from Selleckchem, 4-hydroxytamoxifen (4-OHT) from Sigma-Aldrich, murine anti-PD-L1 monoclonal antibody (Anti-PD-L1-mIgG1e3 InvivoFit) was purchased from InvivoGen and tamoxifen for in vivo treatment from Sigma-Aldrich.

Caspase-3/7 assay. To assess apoptosis, 1,000 cells per well were seeded in 96-well plates and treated after 24 h with trametinib (10 nM) or nintedanib (2 μM) alone or in combination as indicated. After 24 h from the start of treatment, caspase-3/7 activity was determined measuring luminescence using caspase-3/7 assay (Promega), according to the kit instruction. All assays were performed independently at least three times.

Kinobead pulldowns. Kinobead pulldown assays were performed as previously described[61]. In-gel digestion was performed according to standard procedures[62]. Peptide/protein identification and quantification were performed with MaxQuant (v.1.5.7.4) by utilizing the Swissprot database (murine, 16,996 entries, downloaded 23 November 2018) using the search engine Andromeda. Data analysis was performed as previously described[63].

Automated combination drug screen. The screened compounds were purchased from SelleckChem either in DMSO or in water. A total of 1,000–2,000 cells were seeded in 96-well plates using a Multidrop Combi (Thermo Fisher Scientific) dispenser. The optimal cell number for each cell culture was determined to ensure that each cell line had undergone at least two cell doublings by the end of the assay, 96 h after seeding (~85% confluence). After overnight incubation, cells were treated with a seven-point dilution series (seven concentrations of each compound, threefold dilutions, highest concentration 10 μM) and DMSO as control, using liquid handling robotics (CyBio Felix), and assayed 72 h later. Each cell culture was treated with a library of 418 compounds either in monotherapy or in combination with a fixed concentration of trametinib (final concentration: 5 nM). Viability was measured using a CellTiter-Glo Luminescent Assay (Promega). CellTiter-Glo reagent was added using the Multidrop Combi dispenser, and cells were shaken and incubated for 10 min in the dark. Luminescence was measured using an Infinite Pro 2000 Lumi (Tecan) Luminometer.

Dose–response curves were generated for both monotherapy and combination using the R package GRmetrics (v.3.14)[64,65] to derive both growth-rate-adjusted and traditional measures of drug sensitivity (half-maximal inhibitory concentration (IC_{50}), area under the curve (AUC), efficacy (E_{max}) and half-maximal effective concentration (EC_{50})). Only drugs for which a sigmoid curve could be fitted (coefficient of determination, $r^2 > 0.9$) were considered for further analysis. For each drug, we calculated an expected effect of the combination with trametinib using the Bliss independence model. We used the delta of the AUC between the expected and the measured response to the combination as a proxy for synergy. Drug sensitivity parameters for each cell culture are summarized in Supplementary Table 2.

Phosphoprotein array sample preparation and analysis. The mPDAC cells 9091 and 8661 were plated in 10-cm dishes. The next day, they were treated for 6 h with DMSO (vehicle) or T/N (10 nM trametinib and 2 μM nintedanib) and analyzed using the Phospho Explorer antibody microarray, which contains 1,318 antibodies (Full Moon Biosystems), according to the protocol of the manufacturer.

Pathway enrichment analysis was based on the Reactome gene set and performed through Cytoscape (v.3.8.2) with ClueGO (v.2.5.8)[66], a Cytoscape plug-in to decipher functionally grouped pathway annotation networks. The functionally grouped networks used for visualization present terms as nodes and are linked based on their κ score level (≥0.4). The node size represents the term-enrichment significance and functionally related groups are depicted by similar colors.

Cloning of focused Cas9 sgRNA library. For the customized sgRNA Cas9 library, four sgRNAs (from the Brie library (Addgene, catalog no. 73633)) per target, nontargeting controls, common essential genes and trametinib-sensitizing/resistance genes were included to a total of 350 sgRNA sequences, which were embedded into an oligo sequence with flanking PCR handles and BsmBI restriction sites[67]. The oligo pool (Twist Bioscience) was then amplified at 5 nM input with NEBNext Ultra II polymerase and primers binding the PCR handles, followed by purification with AmpureXP beads (Beckman Coulter). For Golden Gate cloning, BsmBI-v2 (New England Biolabs)-digested pLenti-guide puro (Addgene, catalog no. 52963) was mixed with T4 DNA ligase (New England Biolabs), 10× T4 buffer, BsmBI-v2, linearized backbone and amplified insert (1:3 molar ratio; 30 cycles, Golden Gate). The assembled product was purified with AmpureXP beads and electroporated into Endura Competent cells (Lucigen) using a BioRad MicroPulser (1.8 kV in 0.1-cm gap cuvettes (Sigma-Aldrich)). Bacteria were grown at 33 °C overnight (LB Medium (Sigma) with 100 μg ml^{-1} of ampicillin). DNA was extracted using the NucleoBond Xtra Midi EF Kit (Macherey-Nagel). Libraries for next-generation sequencing (NGS) were constructed according to the protocol given below to determine sgRNA abundance. Sequences of oligonucleotides for all described methods from the present study are provided in Supplementary Table 7.

Lentivirus production and titration. For virus production of sgRNA libraries, HEK293FT cells were seeded into 15-cm dishes to reach confluence of 60% the following day. Cells were transfected with 14.3 µg of library plasmid, 10.9 µg of psPAX2 (Addgene, catalog no. 12260) and 7.1 µg of pMD2.G (Addgene, catalog no. 12259) per plate using 119 µl of TransIT-LT1 (Mirus Bioscience) in 850 µl of OptiMEM (Gibco). Then, 48 h and 72 h post-transfection, the supernatant was collected and filtered (0.45 µm). For other constructs, HEK293FT cells were seeded in 10-cm plates and transfected with 2 µg of viral plasmid, 1.25 µg of psPAX2 and 0.75 µg of pMD2.G per plate using 18 µl of TransIT-LT1 in 270 µl of OptiMEM (Gibco) the next day.

Lentiviral sgRNA libraries were functionally titrated by spinfection (2 h, 1,000*g*, 33 °C) of target cells with varying amounts of lentiviral supernatant in 12-well plates and 3×10^6 cells per well as described previously[68]. The amount of lentivirus needed per 12-well for a target multiplicity of infection of 0.3 was calculated as survival of 0.25 relative to unselected control.

Whole-genome and focused CRISPR–Cas9 screens. CRISPR–Cas9 screens were performed in clonal Cas9-expressing cells, with the focused Cas9 library at 1,000× coverage and with the genome-wide Brie library (pLenti-guide puro) at 500× coverage. Parental cell lines were infected with pLenti Cas9-2A-BSD (Addgene, catalog no. 52962) and selected with BlasticidinS (Invivogen; 10 µg ml^{-1}). Single clones were obtained by limited dilution in 96-well plates, tested for Cas9 expression by western blotting and validated by resistance to 6-thioguanine (Sigma-Aldrich) treatment in cells edited at the *Hprt* locus (mediated by an sgRNA cloned into pLenti-guide puro).

The final dose of trametinib for the screens was determined by culturing the cells with different concentrations of trametinib (1.25 nM, 2.5 nM, 5 nM, 10 nM and 20 nM) and assessing cell proliferation and ERK1/2 phosphorylation; 500,000 cells were seeded in 10-cm dishes and trametinib at the indicated concentrations was added. Cells were passaged every 3–4 d and counted at each passage. Protein samples were harvested at each count and phospho-ERK levels were assessed by western blot analysis.

The CRISPR–Cas9 screens were performed in side-by-side duplicates (genome wide) or triplicates (focused Cas9). Cas9-expressing cells were transduced with the lentiviral libraries and selected in medium containing puromycin (Sigma-Aldrich; final concentration: for 9091 and 8248, 4 µg ml^{-1}; for 8570, 12 µg ml^{-1}). Then, 4 d after infection, puromycin was washed out and the cells were allowed to recover for 2 d. Cells were assigned to control (vehicle, DMSO) and experimental arms (5 nM trametinib), and passaged every 3–4 d for 2 weeks, thereby refreshing the drug treatment and maintaining representation. At the final timepoint, cells were harvested and genomic DNA (gDNA) was extracted using the DNeasy Blood & Tissue kit (focused libraries) or the Blood & Cell Culture DNA Maxi Kit (both QIAGEN) according to the manufacturer's instructions.

SgRNA library construction, NGS and MaGECK analysis. Approximately 230 µg (genome-wide screen) and 9 µg (focused screen) of gDNA was used for library preparation. One PCR reaction (50 µl) contained 6 µg of gDNA, 25 µl of 2× KAPA HiFi HotStart ReadyMix (Roche) and 2 µl each of forward/reverse primer (10 µM) with unique sequencing-barcode indices. PCRs were purified using NEB Monarch PCR-cleanup kit, pooled and quantified using the KAPA library quantification kit for Illumina. Pooled libraries were sequenced on Illumina NextSeq 500 (customized read and indexing primers spiked in). Read depth was intended to maintain library coverage (35 Mio reads for genome wide, 350,000 reads for customized library).

Downstream processing was conducted with MAGeCK v.0.5.9.4 (ref. [69]). Reads were aligned to the reference of sgRNA sequences and counted. b-scores were calculated using the maximum likelihood estimation method utilizing the information from nontargeting control guides, resulting in a single score for each gene (β-score). The final score represents enrichment (+) or depletion (−) of the sgRNAs with respect to their initial abundance.

To investigate significantly depleted nintedanib targets in the presence of trametinib, the score difference between both arms of the experiment was calculated (DMSO and trametinib). Values falling in the left and right tails of this distribution (<5th and >95th percentiles) were considered to confer resistance or synergize with drug treatment.

Lentiviral CRISPR–Cas9-induced deletion of individual genes. The sgRNAs were designed using CRISPick[70] (https://portals.broadinstitute.org/gppx/crispick/public) and synthesized as complementary forward and reverse oligos (Eurofins Genomics GmbH; Supplementary Table 7). Oligos were annealed in T4 DNA-ligase buffer (New England Biolabs), cloned into CRISPR expression vectors (either pLenti CRISPR V2, Addgene, catalog no. 52961, or pLenti-guide puro) using BsmBI-v2 and T4 DNA ligase (both New England Biolabs), transformed into chemically competent bacteria (Stbl3 strain) using 5× KCM buffer (500 mM KCl, 150 mM $CaCl_2$, 250 mM $MgCl_2$) and grown on ampicillin-containing (100 µg ml^{-1}) Luria–Bertani plates overnight. Plasmid DNA was isolated using the Monarch Plasmid MiniPrep Kit (New England Biolabs) and used for lentivirus production.

For lentiviral transduction of target cell lines, 1×10^6 cells were seeded into 6-well plates. The following day, medium was replaced with 1 ml of lentiviral supernatant, 1 ml of fresh medium and polybrene (final concentration of 8 µg ml^{-1}). Then, 48 h post-transduction, selection with puromycin was initiated. Indel analysis was performed by gDNA extraction using the DNeasy Blood & Tissue kit (QIAGEN). PCR amplification was done with primers flanking the genomic sgRNA-binding site using 2× KAPA HiFi HotStart ReadyMix (Roche). The PCR product was purified (Monarch PCR-cleanup kit, New England Biolabs), submitted to Sanger sequencing (Eurofins) and analyzed for CRISPR edits using the web-based application Inference of CRISPR editing (ICE; Synthego, v.2.0: https://ice.synthego.com/). Edited cells were seeded and clonogenic assays performed in 24-well plates (1,000 cells per well) in the presence and absence of trametinib as described above.

Electroporation of CRISPR–Cas9 RNPs and indel depletion assay. For multiplexed validation of targets conferring sensitivity to trametinib, sgRNAs were synthesized as CRISPR (cr)RNAs (Integrated DNA Technologies (IDT); Supplementary Table 7) and complexed with a *trans*-activating crRNA (tracrRNA; IDT) according to the manufacturer's instructions. The resulting crRNA:tracrRNA duplex was complexed at 22 pmol with Alt-R Cas9 enzyme (Alt-R S.p. Cas9 Nuclease V3, IDT) at 18 pmol and room temperature (RT) for 20 min, thus forming RNPs.

Cells were detached trypsin free by using phosphate-buffered saline (PBS)–EDTA (0.046%) and the cell number was adjusted to obtain 400,000 cells per transfection (10-µl volume). Complexed RNPs were added to the cell solution and electroporated using the Neon Transfection system (Thermo Fisher Scientific) according to the manufacturer's instructions. Next, cells were seeded for clonogenic growth as described above. To determine the indel shift due to drug exposure, 20,000 cells were seeded in 6-well plates and subjected to trametinib (5 nM) or vehicle (DMSO) treatment the next day. Cells were passaged if necessary and drug was renewed after 4 d. After 7–9 d, gDNA was extracted and PCR amplified as described above. Indel frequency was determined by Sanger sequencing and ICE analysis (Synthego, v.2.0) for DMSO- and trametinib-treated samples.

Mouse strains, tumor models and in vivo treatment. *LSL-Kras*$^{G12D/+}$ (ref. [71]), *Pdx1-Cre*[72], *Ptf1a*$^{Cre/+}$ (ref. [73]), *Pdx1-Flp*, *FSF-R26*$^{CAG\text{-}CreERT2/+}$, *FSF-Kras*$^{G12D/+}$ ref. [20]) and *Map2k1*$^{tm/tm}$ (ref. [74]) mice have been described previously. *Map2k2*$^{tm/tm}$ (Map2k2tm1e(EUCOMM)Wtsi) mice were obtained from EUCOMM. The strains were on a mixed C57Bl/6;129S6/SvEv genetic background and interbred to obtain compound mutant mice that develop autochthonous tumors in the pancreas.

For transplantation experiments, cancer cells (2,500–10,000) were orthotopically grafted into the pancreas of syngeneic immunocompetent C57Bl/6J wild-type, or T cell deficient C57BL/6 CD3e-knockout mice[22]. When tumors grew to a size ~100 mm^3, mice were randomized into the different treatment arms. The following drugs were used: trametinib (3 mg kg^{-1}, 5 d a week, oral gavage), nintedanib (50 mg kg^{-1}, 5 d a week, oral gavage), anti-PD-L1 antibody (200 µg per mouse, every third day, intraperitoneal injections) and tamoxifen (4 mg per mouse, every third day, intraperitoneal injections). One week after implantation, mice were scanned by magnetic resonance imaging (MRI) for the presence of tumors. Animals were sacrificed when individual mice reached the human endpoint or at the completion of treatment.

All animal studies were conducted in compliance with the ARRIVE and the European guidelines for the care and use of laboratory animals, and were approved by the IACUCs of the local authorities of Technische Universität München and Regierung von Oberbayern. A maximal tumor size of 1.5 cm and a specific burden score (determined by a cumulative burden score) permitted by the IACUCs and Regierung von Oberbayern were not exceeded in the present study.

Animals were kept in a dedicated facility, with a light:dark cycle of 12 h:12 h, a housing temperature between 20 and 24 °C and a relative air humidity of 55%.

MRI and quantification. Animals were anesthetized with isoflurane to perform MRI of the pancreas using a Bruker Biospec 7T MRI scanner to scan 35 consecutive sections. Tumor volume was quantified using the Horos medical image viewer software to reconstruct MRI volumetric measurements (v.3.3.6). Horos is an open-source code software (FOSS) program that is distributed free of charge under the LGPL license at Horosproject.org and sponsored by Nimble Co LLC d/b/a Purview. Acquisition of the MRI signal was adapted according to cardiac and respiratory cycles to minimize motion effects during imaging.

Histology and IHC. Mouse pancreatic tumors were fixed in 4% paraformaldehyde (PFA; Carl Roth), embedded in paraffin and cut into 1-µm sections. Hematoxylin and eosin (H&E) staining of tissue sections was performed according to standard protocols. The following primary antibodies were used for immunohistochemistry (IHC): rat anti-CK19 (DHSB, 1:250), rabbit anti-KI67 (Thermo Fisher Scientific, 1:50), rat anti-CD31 (Optistain, 1:50), rabbit anti-CD3 (Zytomed Systems, 1:100), rat anti-CD8 (Dianova, 1:100), rabbit anti-phospho-histone H2A.X (Ser139) (Cell Signaling Technology, 1:500), rabbit anti-MEK1 (30C8) (Cell Signaling Technology, 1:50), rabbit anti-MEK2 (13E3) (Cell Signaling Technology, 1:50), rabbit anti-pERK (p-p44/42 MAPK Thr202/Tyr204) (Cell Signaling Technology, 1:50), rabbit anti-pPDGF Receptorβ (Tyr1021) (Cell Signaling Technology, 1:50) and rabbit anti-pAMPKα (Thr172) (Cell Signaling Technology, 1:50). Antibody detection

was performed using the Bond Polymer Refine Detection Kit (Leica) or rabbit anti-rat immunoglobulin (Ig)G (Vector Laboratories, 1:200) secondary antibody or followed by a secondary antibody conjugated to biotin (Vector Laboratories). Detailed protocols of individual staining are available on request. Images were acquired using Leica AT2 Scanner (Leica) and processed by Aperio Image Scope (Leica, v.12.3.3) and FIJI (National Institutes of Health (NIH), v.2.1.0). For quantification of Ki67, CD31 and γH2AX staining, five fields of view of individual tumors per treatment condition were analyzed in a blinded fashion. In at least six individual tumors per treatment condition, mitoses were counted per high-power field in areas showing increased mitotic activity on scanning magnification. M. Jesinghaus, a board-certified pathologist, performed all quantifications.

SA-β-Gal staining. PFA-fixed, OCT-embedded tumor tissues were cut into 5-µm sections and mounted on slides. SA-β-Gal staining was performed using a Senescence β-Galactosidase Staining Kit (Cell Signaling Technology) at pH 6.0. Images were acquired using Aperio Versa Scanner (Leica) and were processed by FIJI (NIH, v.2.1.0).

Immunofluorescence staining and imaging. PFA-fixed, OCT-embedded tumor tissues were cut into 5- or 10-µm sections and mounted on slides. The slides were incubated with acetone (Sigma-Aldrich) for 6 min at 4 °C. After rehydration with PBS for 10 min, the tissues were blocked for 1 h at RT with 10% goat serum and 10% donkey serum in PBS. The following primary antibodies were used for immunofluorescence staining of T cells, endothelial cells, and epithelial and mesenchymal tumor cells: rat anti-CD3 (BioLegend, 1:50), Armenian hamster anti-CD31 (Abcam, 1:400), rabbit anti-aSMA (Abcam, 1:100), rabbit anti-P-selectin (LSbio, 1:200), rabbit anti-CK18 (Sigma, 1:800) and chicken anti-vimentin (Invitrogen, 1:100). Primary antibodies were each incubated for 3 h at RT and diluted in 3% bovine serum albumin (BSA; Sigma-Aldrich) in PBS. Goat anti-rat AF680 (Invitrogen, 1:200), donkey anti-rat AF488 (Invitrogen, 1:200), goat anti-Armenian hamster IgG Cy3 (Jackson Immuno, 1:200), goat anti-rabbit AF488 (1:200) and goat anti-chicken AF680 (1:200) were used as secondary antibodies (staining for 1 h at RT diluted in in 3% BSA in PBS). Nuclear staining was performed for 10 min at RT with DAPI (Biotium, 1:500) in 3% BSA in PBS.

The following primary antibodies were used for immunofluorescence staining of macrophage subpopulations: rat anti-CD68 (BioRad, 1:150), rabbit anti-ARG1 (Thermo Fisher Scientific, 1:300) and rabbit anti-CD80 (Abcam, 1:300). Donkey anti-rat AF594 (Invitrogen, 1:200) and goat anti-rabbit AF488 (Invitrogen, 1:200) were used as secondary antibodies (staining for 1 h at RT diluted in in 3% BSA + 6% Triton X-100 in PBS). Nuclear staining was performed with DAPI (Biotium, 1:1,000) in 0.25% BSA in PBS.

After three washes in PBS, slides were mounted using Vectashield Mounting Medium (Vector Laboratories). Images were acquired using a TCS SP8 Confocal Laser Scanning Microscope (Leica) and were processed by FIJI (NIH, v.2.1.0). For quantification of T cells, ten fields of view of four individual tumors per treatment condition were analyzed. For quantification of macrophage subpopulations, five fields of view of five individual tumors per treatment condition were analyzed.

Immunophenotyping by flow cytometry. Fresh tumor samples were minced and enzymatically digested with the tumor dissociation kit (Miltenyi, catalog no. 130-096-730) for 40 min at 37 °C with agitation. The cell suspension was strained through a 100-µm strainer, spun down and resuspended in 2% fetal calf serum (FCS)/PBS. Cells were blocked for 10 min on ice with anti-mouse CD16/CD32 FC block (BioLegend, 1:100) and stained with Zombie Aqua Fixable Viability Kit (BioLegend, 1:500) and the following antibody cocktails: CD4 BUV805 (BD, 1:100), CD3eBUV395 (BD, 1:20), CD8a BV785 (BioLegend, 1:100), CD45 PerCP Cy5.5 (BioLegend, 1:100), CD19 FITC (BioLegend, 1:100), EpCAM APC/AF647 (BioLegend, 1:200) for acquisition of adaptive immune cells; CD11c BUV737 (BD, 1:30), NK1.1 BUV395 (BD, 1:25), Ly6C BV785 (BioLegend, 1:200), CD11b BV650 (BioLegend, 1:100), F4/80 BV421/PB (BioLegend, 1:30), CD45 PerCP Cy5.5 (BioLegend, 1:100), Ly6G PE (BioLegend, 1:200), CD68 APC-CY7 (BioLegend, 1:20), EpCAM APC/AF647 (BioLegend, 1:200) for acquisition of innate immune cells. Per panel, 1,000,000 events were acquired on the BD LSRFortessa. Flow cytometry data were analyzed using FlowJo software (v.10.6.2).

Whole-cell lysates and western blotting. Protein extraction from cells and tissues, western blotting and subsequent detection of proteins were performed as described[58,59]. The following primary antibodies were used: HSP90 (1:1,000, catalog no. sc-13119, Santa Cruz Biotechnology), MEK1 rabbit monoclonal antibody (1:1,000, catalog no. 9146, Cell Signaling Technology), MEK2 rabbit monoclonal antibody (1:1,000, catalog no. 9147, Cell Signaling Technology), p-ERK (1:1,000, catalog no. 4377, Cell Signaling Technology), ERK (1:1,000, catalog no. 610123, BD), CAS9 (1:1,000, catalog no. 14697, Cell Signaling Technology) and β-actin (1:1,000, catalog no. 4970, Cell Signaling Technology).

***KRAS*^{G12D} induction after lentiviral transduction of mPDAC cells.** The pINDUCER20 vector system comprising a puromycin resistance gene was used for doxycycline-inducible *KRAS*^{G12D} overexpression as previously described[16].

Gene expression profiling and amplicon-based deep sequencing at the *Kras* locus or of *Kras* mRNA expression. Drug-perturbed cells were seeded in a 10-cm dish and treated the following day with 10 nM trametinib or vehicle. RNA was isolated with the RNeasy kit (QIAGEN) from 80% confluent primary cells and immediately transferred into RLT buffer (QIAGEN) containing 2-mercaptoethanol.

RNA-seq library preparation, amplicon-based deep sequencing at the *Kras* locus or of *Kras* mRNA was performed as previously described[16].

Analyses were carried out using R v.3.6.2 (R Core Team, 201) and Bioconductor v.3.1. Differential gene expression analysis was performed using DESeq2 v.1.26.0. A gene was considered to be differentially expressed with a Benjamini–Hochberg-adjusted *P* value of 0.05 and an absolute fold-change >1.

We used the single-sample gene set enrichment analysis (ssGSEA) function from the gene set variation analysis (GSVA v.3.14)[18] and the Hallmark gene set EMT[19] to estimate the classical or mesenchymal gene expression programs in our collection of hPDAC and mPDAC cell cultures.

Sample preparation for scRNA-seq. Tumor specimens were dissociated and enzymatically digested with the tumor dissociation kit as described above. The cell suspension was strained through a 100-µm strainer, spun down and resuspended in 2% FCS/PBS including RNase inhibitor (New England Biolabs, catalog no. M0314L, 1:100). Debris removal solution (Miltenyi, catalog no. 130-109-398) was used to remove cell debris from the dissociated tissue. Then the dead cell removal kit (Miltenyi, catalog no. 130-090-101) was used to enrich live cells. The cell suspension was spun down and then resuspended in PBS and blocked for nonantigen-specific binding for 10 min on ice with anti-mouse CD16/CD32 FC block (BioLegend, 1:100). Cells were stained with the following antibodies for FACS sorting: TER-119 BV421 (BioLegend, 1:100), CD45-AF647 (BioLegend, 1:20), CD31-AF647 (BioLegend, 1:20) and EPCAM-AF647 (BioLegend, 1:20) for 30 min on ice. Cell sorting was performed using the BD FACS Aria Fusion. The sorted cells from the TER-119-negative/CD45-/CD31-/EPCAM-positive fraction (for enrichment of immune, endothelial and epithelial tumor cells, and exclusion of erythrocytes), as well as the TER-119-/CD45-/CD31-/EPCAM-negative fraction (for enrichment of fibroblasts/mesenchymal tumor cells and exclusion of erythrocytes), were collected in 2% FCS/PBS.

ScRNA-seq library preparation and sequencing. The sorted cells were counted, diluted in 2% FCS/PBS and up to 20,000 cells were loaded per lane on a 10× Chromium chip to generate gel beads in emulsion (GEMs). Single-cell GEM generation, barcoding and library construction were performed by using 10× Chromium Single Cell 3′ v.3 chemistry according to the manufacturer's instructions. Complementary DNA and generated libraries were checked for sample size and quality on an Agilent Bioanalyzer 2100 using HS DNA Kit (Agilent). Libraries were sequenced on Illumina NovaSeq 6000 S2 (Paired ends (PE), 28+94 bp).

Data preprocessing and quality control. Alignment of the scRNA-seq data to the mouse reference genome (mm10, release 108.20200622), filtering, barcode and unique molecular identifier counting was performed using the 10× Genomics Cell Ranger software (v.3.1.0). Python (v.3.8.3) and the Python software package SCANPY were used for all further analyses (v.1.6.0)[75]. Cells that expressed <200 genes or had >10% mitochondrial gene counts were excluded from the analysis. We also filtered out genes with <20 counts. Counts were per-cell normalized and (log+1) transformed. Highly variable genes were computed using the first $n = 4{,}000$ most variable genes for the analyses across cell types, tumor cells, T cells, fibroblasts, macrophages and treatment conditions. Batch-effect correction was performed using BBKNN (batch balanced *k* nearest neighbors, v.1.5.1).

Dimensionality reduction and clustering. The Leiden algorithm (v.0.8.1) was used for cell clustering and Uniform Manifold Approximation and Projection (UMAP v.0.4.6) for dimensionality reduction. The clusters were further annotated by assessment of known cell-type-specific markers. Principal component analysis was performed with default parameters. Neighborhood graphs were computed based on $n = 10$ principal components and $k = 30$ neighbors. The calculation of all UMAP projections was based on default parameters. The number of Leiden clusters was adjusted according to the sample of consideration.

GSEA. Differential gene expression analysis was performed using the tool rank_genes_groups, which is part of the SCANPY package (v.1.6.0, https://github.com/theislab/scanpy). The Benjamini–Hochberg method was used to correct for multiple testing. Subsequent GSEA was performed using GSEA v.4.1.0 jar package and MSigDB v.7.1 gene sets provided by Broad Institute, Massachusetts Institute of Technology and Harvard University. GSEA was conducted on a preranked gene list output of the differential gene expression analysis, and genes were ranked based on the Student's *t*-test metric. Parameters were set as follows: the number of permutations was set to 1,000 and the enrichment statistic for scoring was set as 'weighted'; other parameters were set as default. The cut-off for a significant false discovery rate (FDR) *q* value was set at 0.05 and nominal *P* value at 0.05.

Cell-type-specific analysis. *CAFs identification.* In classical and mesenchymal tumors, scRNA-seq uncovered six different T-cell clusters. The identified CD4

naive-like populations expressed *Cd4* and the naive T-cell marker *Sell*; in addition, they lacked the expression of *Cd44* and T-cell activation genes, such as *Icos*, *Lag3*, *Havcr2* (*Tim-3*), *Pdcd1*, *Tnfrsf4* and *Ctla4*. The identified activated/effector T cells showed the highest levels of activated markers such as *Icos*, *Tim-3*, *Ctla4* and *Pdcd1*, and intermediate levels of *Sell* and *Cd44*. Regulatory T cells expressed high levels of *Cd4* and *Foxp3*, and intermediate levels of the T-cell activation genes *Icos*, *Ctla4* and *Pdcd1*. Central memory T cells were positive for *Cd4*, *Cd27*, *Cd28*, *Cd44* and *Il7r*, and displayed a unique central memory marker signature including *Sell* and *Ccr7*. CD8 naive-like T cells expressed high levels of *Cd8a* and *Sell*. Cytotoxic T cells showed the highest levels of T-cell activation genes *Lag3*, *Tim-3*, *Pdcd1*, *Tnfrsf18* and *Ifng*, and cytotoxic markers *Gzma*, *Gzmb* and *Prf1*.

CAF identification. ScRNA-seq uncovered a sufficient number of CAFs for downstream analysis only in classical tumors. We defined CAFs based on the expression of the following genes: *Vim*, *S100a4*, *Acta2*, *Col6a1*, *Col1a2*, *Fap*, *Pdgfra* and *Cspg4*. MyoCAFs expressed *Tagln*, *Acta2*, *Postn*, *Thy1*, *Col12a1*, *Thbs2*, apCAFs *H2-Ab1*, *Cd74*, *Saa3* and *Slpi*, and iCAFs *Clec3b*, *Col14a1*, *Il6*, *Pdgfra*, *Cxcl12*, *Dpt*, *Lmna*, *Cxcl1*, *Cxcl2* and *Ccl2*.

Conditioned medium collection. The mPDAC cells 9091 and 8661 were plated in 10-cm dishes, and subsequently treated after 24 h for 3 d in the presence of DMSO (vehicle) or T/N (10 nM trametinib and 2 µM nintedanib). At day 3 of drug treatment, the medium was removed, cells were washed once with PBS, twice with serum/phenol-red-free medium, and incubated for 6 h in 5 ml of serum/phenol-red free medium with DMSO or T/N. The resulting conditioned medium was then collected, filtered with 0.2-µm pores and used for downstream secretome analysis.

MS-based secretomics. Cell supernatants were concentrated to ~250 µl and washed with 50 mM Tris, pH 8, using Amicon Ultra 3-kDa cutoff filter units (Merck) at 4 °C and 4,000*g*. Then, 50 µl of concentrated supernatants was supplemented with 10 mM tris(2-carboxyethyl)phosphine and 40 mM 2-chloroacetamide, and heated in a thermoshaker for 10 min at 95 °C and 1,000 r.p.m. Afterwards, samples were digested with 1.5 µg of trypsin/LysC mix for 16 h at 37 °C and 1,000 r.p.m. Samples were acidified by adding 100 µl of isopropanol and 1% trifluoroacetic acid, and desalted using in-house-made SDB–RPS StageTips.

Desalted peptide mixtures were reconstituted in buffer A (0.1% formic acid) and analyzed with an EASY-nLC 1200 ultrahigh-pressure system (Thermo Fisher Scientific) coupled to an Orbitrap Exploris 480 instrument (Thermo Fisher Scientific). Peptide, 300 ng, was loaded on to a 50-cm in-house-made column with 75-µm inner diameter, packed with C18 1.9-µm ReproSil beads (Dr. Maisch GmbH). Peptides were eluted with a linear gradient from 5% to 30% buffer B (0.1% formic acid and 80% acetonitrile) in 95 min at a flow rate of 300 nl min^{-1}. An in-house-made column oven maintained the temperature at 60 °C.

Data were acquired with a data-dependent tandem MS (MS/MS) method. Full scans (300–1,650 m/z, R = 60,000 at 200 m/z) at a normalized AGC target of 300% were followed by 15 MS/MS scans with higher-energy collisional dissociation (HCD; normalized AGC target = 100%, maximum injection time = 28 ms, isolation window = 1.4 m/z, HCD collision energy = 30% and R = 15,000 at 200 m/z). A dynamic exclusion of 30 s was enabled.

Data analysis. MS raw files were processed with the Andromeda search engine built into MaxQuant3 (v.1.6.2.10) and MS/MS spectra were matched against the mouse UniProt FASTA database (June 2019) with an FDR of 0.01 at the protein and peptide level, and a minimum peptide length of seven amino acids. A match between runs was enabled and the minimal ratio count for label-free quantification was set to 1. Proteins were filtered for extracellular annotation (Gene Ontology Cellular Component terms 'extracellular space' and 'extracellular matrix', UniProt keywords 'secreted'). Missing values were replaced from a Gaussian distribution (30% width and downshift by 1.8 s.d. of measured values) and Student's t-tests were performed with a permutation-based FDR of 0.05.

Intercellular communication analysis. Cell-to-cell interactions were inferred based on the expression of known ligand–receptor pairs in different cell types. Specifically, we used the ligand–receptor interactions from CellPhoneDB (v.2.0)[76] complemented by proteins with secretomics-derived experimental evidence[77]. Communication networks were devised by integrating quantitative MS secretome data of 'sending' tumor cells with scRNA-seq data of 'receiving' cell populations.

Statistics and reproducibility. No statistical method was used to predetermine sample size. No data were excluded from the analyses. If possible, the experiments were randomized and the Investigators blinded to allocation during the experiments and outcome assessment. Graphical depiction, data correlation and statistical analysis were performed with GraphPad Prism (v.8). Unless otherwise indicated, all data were determined from at least three independent experiments. For comparisons between datasets, a log(rank) test or two-tailed Student's t-test with Welch's correction was employed and the resulting P values are indicated in the respective figures. The significance level was set to 0.05. If more than one statistical test was performed simultaneously on a single dataset, and Bonferroni's adjusted significance level was calculated to account for the increased possibility of false-positive results. Survival analysis was carried out using the log(rank) test.

Reporting Summary. Further information on research design is available in the Nature Research Reporting Summary linked to this article.

Data availability

The RNA-seq dataset has been deposited in the EBIArrayExpress repository with accession no. E-MTAB-11187. The MS kinobead pulldown and the MS secretomics data have been deposited in the ProteomeXchange Consortium (http://proteomecentral.proteomexchange.org) via the PRIDE partner repository with accession nos. PXD023267 and PXD027877, respectively. The scRNA-seq data have been deposited in the EBIArrayExpress repository with accession no. E-MTAB-9954. The human pancreatic cancer data were derived from previous studies and are available in the supplementary information of the respective publications[6–8]. All other data have been provided as supplementary tables or source data files. Mice and cell lines are available from the corresponding author on reasonable request. Key resources are listed in Supplementary Table 8. Source data are provided with this paper.

Code availability

Analyses were performed using open-source software, and in-house scripts in R v.3.6.2 and Python v.3.8.3, which are available from the corresponding author on reasonable request. Codes are provided via the GitHub repository at the following link: https://github.com/stefanie-baerthel/combinatorial_treatment_analysis.

Received: 5 December 2020; Accepted: 13 December 2021;
Published online: 31 January 2022

References

1. Quaresma, M., Coleman, M. P. & Rachet, B. 40-year trends in an index of survival for all cancers combined and survival adjusted for age and sex for each cancer in England and Wales, 1971–2011: a population-based study. *Lancet* 385, 1206–1218 (2015).
2. Siegel, R. L., Miller, K. D. & Jemal, A. Cancer statistics, 2020. *CA Cancer J. Clin.* 70, 7–30 (2020).
3. Aung, K. L. et al. Genomics-driven precision medicine for advanced pancreatic cancer: early results from the COMPASS trial. *Clin. Cancer Res.* 24, 1344–1354 (2018).
4. Kalimuthu, S. N. et al. Morphological classification of pancreatic ductal adenocarcinoma that predicts molecular subtypes and correlates with clinical outcome. *Gut* 69, 317–328 (2020).
5. Chan-Seng-Yue, M. et al. Transcription phenotypes of pancreatic cancer are driven by genomic events during tumor evolution. *Nat. Genet.* 52, 231–240 (2020).
6. Bailey, P. et al. Genomic analyses identify molecular subtypes of pancreatic cancer. *Nature* 531, 47–52 (2016).
7. Dijk, F. et al. Unsupervised class discovery in pancreatic ductal adenocarcinoma reveals cell-intrinsic mesenchymal features and high concordance between existing classification systems. *Sci. Rep.* 10, 337 (2020).
8. Puleo, F. et al. Stratification of pancreatic ductal adenocarcinomas based on tumor and microenvironment features. *Gastroenterology* 155, 1999–2013.e1993 (2018).
9. Morrison, A. H., Byrne, K. T. & Vonderheide, R. H. Immunotherapy and prevention of pancreatic cancer. *Trends Cancer* 4, 418–428 (2018).
10. Balachandran, V. P. et al. Identification of unique neoantigen qualities in long-term survivors of pancreatic cancer. *Nature* 551, 512–516 (2017).
11. Chen, D. S. & Mellman, I. Elements of cancer immunity and the cancer-immune set point. *Nature* 541, 321–330 (2017).
12. Ino, Y. et al. Immune cell infiltration as an indicator of the immune microenvironment of pancreatic cancer. *Br. J. Cancer* 108, 914–923 (2013).
13. Collisson, E. A. et al. A central role for RAF–>MEK–>ERK signaling in the genesis of pancreatic ductal adenocarcinoma. *Cancer Discov.* 2, 685–693 (2012).
14. Blumenschein, G. R. Jr et al. A randomized phase II study of the MEK1/MEK2 inhibitor trametinib (GSK1120212) compared with docetaxel in KRAS-mutant advanced non-small-cell lung cancer (NSCLC). *Ann. Oncol.* 26, 894–901 (2015).
15. Caunt, C. J., Sale, M. J., Smith, P. D. & Cook, S. J. MEK1 and MEK2 inhibitors and cancer therapy: the long and winding road. *Nat. Rev. Cancer* 15, 577–592 (2015).
16. Mueller, S. et al. Evolutionary routes and KRAS dosage define pancreatic cancer phenotypes. *Nature* 554, 62–68 (2018).
17. Miyabayashi, K. et al. Intraductal transplantation models of human pancreatic ductal adenocarcinoma reveal progressive transition of molecular subtypes. *Cancer Discov.*10, 1566–1589 (2020).

18. Hänzelmann, S., Castelo, R. & Guinney, J. GSVA: gene set variation analysis for microarray and RNA-Seq data. *BMC Bioinformatics* 14, 7 (2013).
19. Liberzon, A. et al. The molecular signatures database Hallmark gene set collection. *Cell Systems* 1, 417–425 (2015).
20. Schönhuber, N. et al. A next-generation dual-recombinase system for time- and host-specific targeting of pancreatic cancer. *Nat. Med.* 20, 1340–1347 (2014).
21. Ruscetti, M. et al. Senescence-induced vascular remodeling creates therapeutic vulnerabilities in pancreas cancer. *Cell* 181, 424–441.e421 (2020).
22. DeJarnette, J. B. et al. Specific requirement for CD3epsilon in T cell development. *Proc. Natl Acad. Sci. USA* 95, 14909–14914 (1998).
23. Pathria, P., Louis, T. L. & Varner, J. A. Targeting tumor-associated macrophages in cancer. *Trends Immunol.* 40, 310–327 (2019).
24. Nywening, T. M. et al. Targeting both tumour-associated CXCR2$^+$ neutrophils and CCR2$^+$ macrophages disrupts myeloid recruitment and improves chemotherapeutic responses in pancreatic ductal adenocarcinoma. *Gut* 67, 1112–1123 (2018).
25. Steele, C. W. et al. CXCR2 inhibition profoundly suppresses metastases and augments immunotherapy in pancreatic ductal adenocarcinoma. *Cancer Cell* 29, 832–845 (2016).
26. Gerrard, T. L., Cohen, D. J. & Kaplan, A. M. Human neutrophil-mediated cytotoxicity to tumor cells. *J. Natl Cancer Instit.* 66, 483–488 (1981).
27. Bakhoum, S. F. & Cantley, L. C. The multifaceted role of chromosomal instability in cancer and its microenvironment. *Cell* 174, 1347–1360 (2018).
28. Mackenzie, K. J. et al. cGAS surveillance of micronuclei links genome instability to innate immunity. *Nature* 548, 461–465 (2017).
29. Faget, D. V., Ren, Q. & Stewart, S. A. Unmasking senescence: context-dependent effects of SASP in cancer. *Nat. Rev. Cancer* 19, 439–453 (2019).
30. Meissner, F., Scheltema, R. A., Mollenkopf, H.-J. & Mann, M. Direct proteomic quantification of the secretome of activated immune cells. *Science* 340, 475–478 (2013).
31. Matsumura, S. et al. Radiation-induced CXCL16 release by breast cancer cells attracts effector T cells. *J. Immunol.* 181, 3099–3107 (2008).
32. Hojo, S. et al. High-level expression of chemokine CXCL16 by tumor cells correlates with a good prognosis and increased tumor-infiltrating lymphocytes in colorectal cancer. *Cancer Res.* 67, 4725–4731 (2007).
33. Li, B. et al. Epigenetic regulation of CXCL12 plays a critical role in mediating tumor progression and the immune response in osteosarcoma. *Cancer Res.* 78, 3938–3953 (2018).
34. Nagarsheth, N., Wicha, M. S. & Zou, W. Chemokines in the cancer microenvironment and their relevance in cancer immunotherapy. *Nat. Rev. Immunol.* 17, 559–572 (2017).
35. Mehta, A. K. et al. Targeting immunosuppressive macrophages overcomes PARP inhibitor resistance in *BRCA1*-associated triple-negative breast cancer. *Nat. Cancer* 2, 66–82 (2021).
36. Peng, D. H. et al. Th17 cells contribute to combination MEK inhibitor and anti-PD-L1 therapy resistance in KRAS/p53 mutant lung cancers. *Nat. Commun.* 12, 2606 (2021).
37. Di Pilato, M. et al. CXCR6 positions cytotoxic T cells to receive critical survival signals in the tumor microenvironment. *Cell* 184, 4512–4530.e4522 (2021).
38. Uhlén, M. et al. Proteomics. Tissue-based map of the human proteome. *Science* 347, 1260419 (2015).
39. Steins, A. et al. High-grade mesenchymal pancreatic ductal adenocarcinoma drives stromal deactivation through CSF-1. *EMBO Rep.* 21, e48780 (2020).
40. Sahai, E. et al. A framework for advancing our understanding of cancer-associated fibroblasts. *Nat. Rev. Cancer* 20, 174–186 (2020).
41. Schneider, G., Schmidt-Supprian, M., Rad, R. & Saur, D. Tissue-specific tumorigenesis: context matters. *Nat. Rev. Cancer* 17, 239–253 (2017).
42. Elyada, E. et al. Cross-species single-cell analysis of pancreatic ductal adenocarcinoma reveals antigen-presenting cancer-associated fibroblasts. *Cancer Discov.* 9, 1102–1123 (2019).
43. Hosein, A. N., Brekken, R. A. & Maitra, A. Pancreatic cancer stroma: an update on therapeutic targeting strategies. *Nat. Rev. Gastroenterol. Hepatol.* 17, 487–505 (2020).
44. Ligorio, M. et al. Stromal microenvironment shapes the intratumoral architecture of pancreatic cancer. *Cell* 178, 160–175.e127 (2019).
45. Batlle, E. & Massagué, J. Transforming growth factor-β signaling in immunity and cancer. *Immunity* 50, 924–940 (2019).
46. Olive, K. P. et al. Inhibition of Hedgehog signaling enhances delivery of chemotherapy in a mouse model of pancreatic cancer. *Science* 324, 1457–1461 (2009).
47. Sherman, M. H. et al. Vitamin D receptor-mediated stromal reprogramming suppresses pancreatitis and enhances pancreatic cancer therapy. *Cell* 159, 80–93 (2014).
48. Hayashi, A. et al. A unifying paradigm for transcriptional heterogeneity and squamous features in pancreatic ductal adenocarcinoma. *Nat. Cancer* 1, 59–74 (2020).
49. Brzostek-Racine, S., Gordon, C., Van Scoy, S. & Reich, N. C. The DNA damage response induces IFN. *J. Immunol.* 187, 5336–5345 (2011).
50. Zhou, F. Molecular mechanisms of IFN-γ to up-regulate MHC class I antigen processing and presentation. *Int. Rev. Immunol.* 28, 239–260 (2009).
51. Respa, A. et al. Association of IFN-γ signal transduction defects with impaired HLA class I antigen processing in melanoma cell lines. *Clin. Cancer Res.* 17, 2668–2678 (2011).
52. Kearney, C. J. et al. Tumor immune evasion arises through loss of TNF sensitivity. *Sci. Immunol.* 3, eaar3451 (2018).
53. Liao, W. et al. KRAS-IRF2 axis drives immune suppression and immune therapy resistance in colorectal cancer. *Cancer Cell* 35, 559–572.e557 (2019).
54. Tape, C. J. et al. Oncogenic KRAS regulates tumor cell signaling via stromal reciprocation. *Cell* 165, 910–920 (2016).
55. Kuilman, T. & Peeper, D. S. Senescence-messaging secretome: SMS-ing cellular stress. *Nat. Rev. Cancer* 9, 81–94 (2009).
56. Lederer, D. J. & Martinez, F. J. Idiopathic pulmonary fibrosis. *N. Engl. J. Med.* 378, 1811–1823 (2018).
57. Richeldi, L. et al. Efficacy and safety of nintedanib in idiopathic pulmonary fibrosis. *N. Engl. J. Med.* 370, 2071–2082 (2014).
58. von Burstin, J. et al. E-cadherin regulates metastasis of pancreatic cancer in vivo and is suppressed by a SNAIL/HDAC1/HDAC2 repressor complex. *Gastroenterology* 137, 361–371.e361-365 (2009).
59. Eser, S. et al. Selective requirement of PI3K/PDK1 signaling for Kras oncogene-driven pancreatic cell plasticity and cancer. *Cancer Cell* 23, 406–420 (2013).
60. Ianevski, A., Giri, A. K. & Aittokallio, T. SynergyFinder 2.0: visual analytics of multi-drug combination synergies. *Nucleic Acids Res.* 48, W488–W493 (2020).
61. Klaeger, S. et al. The target landscape of clinical kinase drugs. *Science* https://doi.org/10.1126/science.aan4368 (2017).
62. Shevchenko, A., Tomas, H., Havli, J., Olsen, J. V. & Mann, M. In-gel digestion for mass spectrometric characterization of proteins and proteomes. *Nat. Protoc.* 1, 2856–2860 (2006).
63. Vizcaíno, J. A. et al. The PRoteomics IDEntifications (PRIDE) database and associated tools: status in 2013. *Nucleic Acids Res.* 41, D1063–D1069 (2013).
64. Hafner, M., Niepel, M., Chung, M. & Sorger, P. K. Growth rate inhibition metrics correct for confounders in measuring sensitivity to cancer drugs. *Nat. Methods* 13, 521–527 (2016).
65. Clark, N. A. et al. GRcalculator: an online tool for calculating and mining dose-response data. *BMC Cancer* 17, 698 (2017).
66. Bindea, G. et al. ClueGO: a Cytoscape plug-in to decipher functionally grouped gene ontology and pathway annotation networks. *Bioinformatics* 25, 1091–1093 (2009).
67. DeWeirdt, P. C. et al. Optimization of AsCas12a for combinatorial genetic screens in human cells. *Nat. Biotechnol.* 39, 94–104 (2021).
68. Joung, J. et al. Genome-scale CRISPR–Cas9 knockout and transcriptional activation screening. *Nat. Protoc.* 12, 828–863 (2017).
69. Li, W. et al. MAGeCK enables robust identification of essential genes from genome-scale CRISPR/Cas9 knockout screens. *Genome Biol.* 15, 554 (2014).
70. Doench, J. G. et al. Optimized sgRNA design to maximize activity and minimize off-target effects of CRISPR–Cas9. *Nat. Biotechnol.* 34, 184–191 (2016).
71. Jackson, E. L. et al. Analysis of lung tumor initiation and progression using conditional expression of oncogenic *K-ras*. *Genes Dev.* 15, 3243–3248 (2001).
72. Hingorani, S. R. et al. Preinvasive and invasive ductal pancreatic cancer and its early detection in the mouse. *Cancer Cell* 4, 437–450 (2003).
73. Nakhai, H. et al. Ptf1a is essential for the differentiation of GABAergic and glycinergic amacrine cells and horizontal cells in the mouse retina. *Development* 134, 1151–1160 (2007).
74. Catalanotti, F. et al. A Mek1–Mek2 heterodimer determines the strength and duration of the Erk signal. *Nat. Struct. Mol. Biol.* 16, 294–303 (2009).
75. Wolf, F. A., Angerer, P. & Theis, F. J. SCANPY: large-scale single-cell gene expression data analysis. *Genome Biol.* 19, 15 (2018).
76. Efremova, M., Vento-Tormo, M., Teichmann, S. A. & Vento-Tormo, R. CellPhoneDB: inferring cell–cell communication from combined expression of multi-subunit ligand–receptor complexes. *Nat. Protoc.* 15, 1484–1506 (2020).
77. Phulphagar, K. et al. Proteomics reveals distinct mechanisms regulating the release of cytokines and alarmins during pyroptosis. *Cell Rep.* 34, 108826 (2021).

Acknowledgements

We thank H. Nakhei, T. Jacks, D. Tuveson, M. Baccarini, R. Schmid and A. Bradley for providing transgenic animals, and the TUM animal facility and imaging core facility of the Department of Nuclear Medicine, Klinikum rechts der Isar, for excellent technical support. The present study was supported by the German Cancer Consortium (DKTK), Deutsche Forschungsgemeinschaft (DFG SA 1374/4-2, SFB 824 C09 to G.S. and D.S., SFB 1321 Project-ID 329628492 P06 to D.S. and M.S.S, P11 to M.S.R. and D.S., and S01 to D.S., M.R., R.R. and G.S., and SFB 1371 Project-ID 395357507 P12 to D.S.), the

Wilhelm Sander-Stiftung (2020.174.1), and the European Research Council (ERC CoG No. 648521, to D.S.).

Author contributions

C.F., S.B., S.A.W., C.S., J.J.M., A.T., J.M., T.K., J.H., J.J.S., B.T., O.R., C.S., K.G., A.C., C.V., M.Z., A.A.V., W.H.P., R.M., R.Ö., T.A. and J.R. performed the research. M.S.R., B.K., K.S., F.M., M.R., M.F., R.R., M.S.S. and D.S. contributed new reagents and analytical tools. C.F., S.B., S.A.W., C.S., J.M., J.J.S., J.C., A.C., F.B., M.J., K.S., O.B., J.R, F.M., M.F., R.R., M.S.S., G.S. and D.S. analyzed the data. C.F. and D.S. wrote the paper.

Competing interests

The authors declare that they have no competing interests. Correspondence and requests for materials should be addressed to D.S.

Additional information

Extended data Extended data are available for this paper at https://doi.org/10.1038/s43018-021-00326-1.

Supplementary information The online version contains supplementary material available at https://doi.org/10.1038/s43018-021-00326-1.

Correspondence and requests for materials should be addressed to Dieter Saur.

Peer review information *Nature Cancer* thanks Michael Hemann and the other, anonymous, reviewer(s) for their contribution to the peer review of this work.

Reprints and permissions information is available at www.nature.com/reprints.

Publisher's note Springer Nature remains neutral with regard to jurisdictional claims in published maps and institutional affiliations.

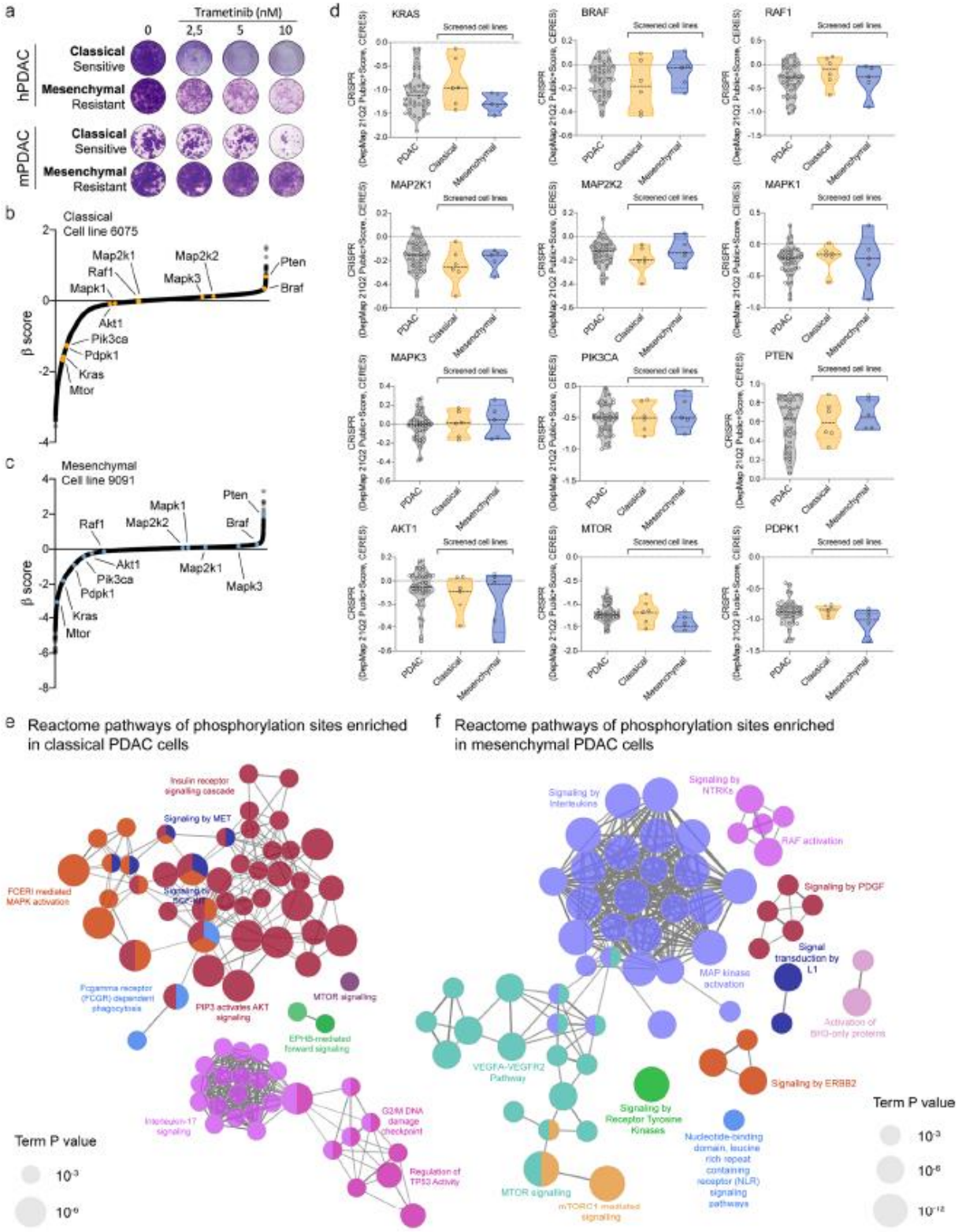

Extended Data Fig. 1 | See next page for caption.

Extended Data Fig. 1 | Assessment of differential pharmacologic and genetic dependencies and signaling pathway activities in PDAC subtypes. **a**, Clonogenic assay of two hPDAC cell lines (top) and two mPDAC cell cultures (bottom) treated with the MEK inhibitor trametinib. The shown cell lines represent the drug-response of the epithelial and mesenchymal subtypes to trametinib treatment. **b**, **c**, β-score distribution of CRISPR/Cas9 genome wide negative-selection (viability) screens performed in one classical (6075, panel (**b**)) and one mesenchymal (9091, panel (**c**)) mPDAC cell line. Highlighted in yellow, for the classical line, and blue, for the mesenchymal line, are the β-scores of KRAS and the core genes involved in direct KRAS downstream signaling. **d**, CRISPR/Cas9 dependency scores of KRAS and core genes involved in direct KRAS downstream signaling. The dependency scores of all hPDAC cell lines were obtained from the DepMap database and are shown in grey. Dependency scores corresponding to classical and mesenchymal cell lines included in the T/N drug screen are represented in the yellow and blue violin plots. Data were obtained from the CRISPR dataset and analyzed through the DepMap release DepMap 21Q2 Public (https://depmap.org/portal/download/). **e**, **f**, Mesenchymal (9091) and classical (8661) PDAC cell cultures were used to generate site-specific phospho-array datasets (Phospho Explorer antibody microarray, Full Moon Biosystems). Phospho-array data (supplementary table 1) were used to test for the enrichment of differentially phosphorylated sites between classical and mesenchymal mPDAC cell lines. Functionally grouped networks with reactome terms as nodes, showing pathways overrepresented in classical (**e**) and mesenchymal (**f**) cells are represented with the ClueGO plugin of Cytoscape. Only the pathways with an adjusted p value (calculated by two-sided hypergeometric test, Bonferroni corrected) ≤ 0.05 are depicted. The node size represents the term enrichment significance.

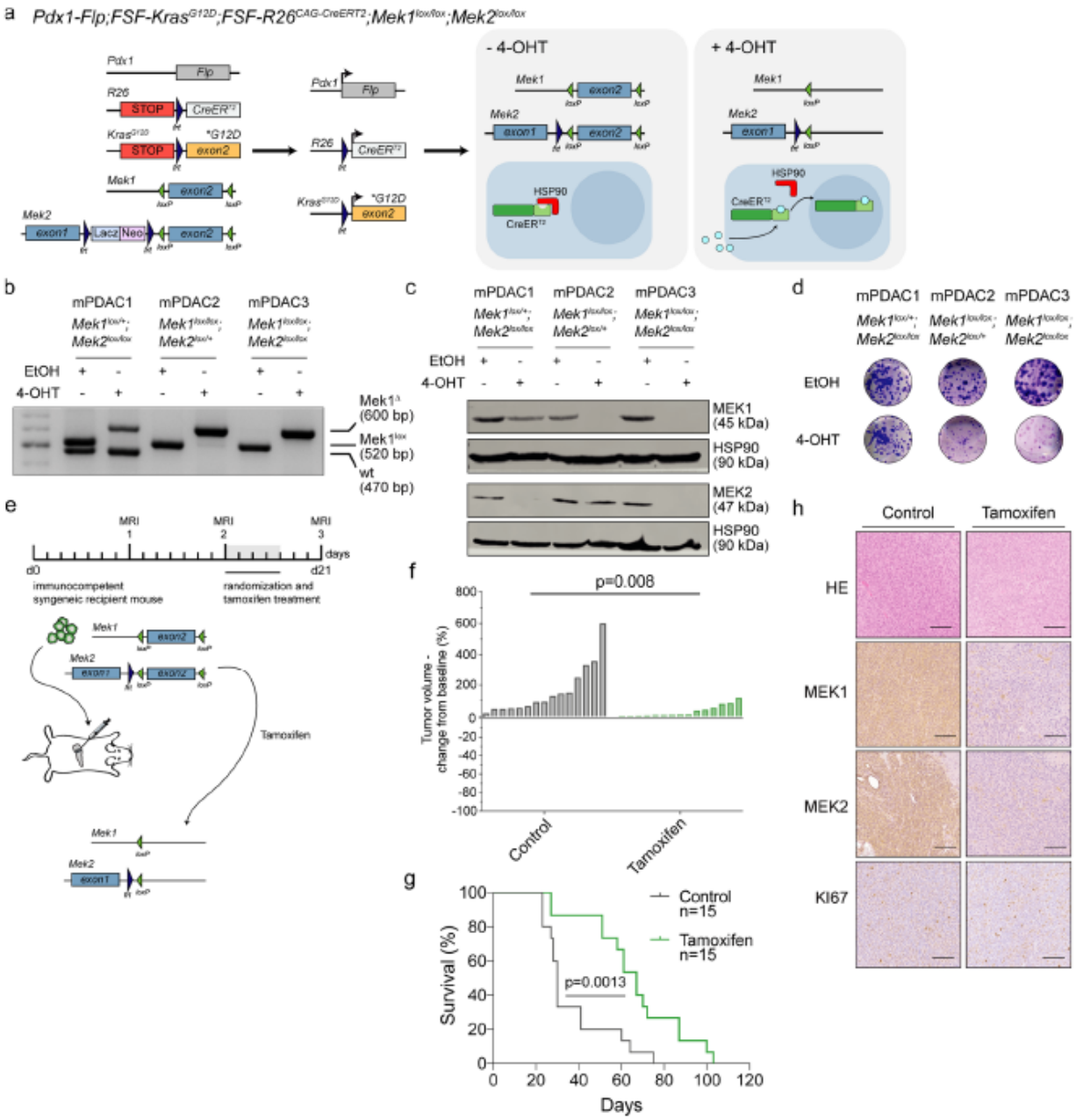

Extended Data Fig. 2 | Genetic depletion of Mek1/2 in established PDAC. a, Genetic strategy to delete *Mek1* and *Mek2* by 4-hydroxytamoxifen (4OHT)-mediated CreER^{T2} activation. *Pdx1-Flp;FSF-Kras$^{G12D/+}$;FSF-R26$^{CAG\text{-}CreERT2/+}$* mice were crossed with mice harboring *loxP*-flanked *Mek1* and *Mek2* alleles. This allowed MEK1/2 deletion in established PDAC by tamoxifen administration *in vitro* and *in vivo* after orthotopic transplantation. **b**, Genotyping PCR of PDAC cells with indicated genotypes to analyze recombination of the floxed *Mek1* allele. Non-recombined mutant, recombined mutant and wild-type PCR products are indicated on the right side. Representative gel of three independent experiments. **c**, Western blot analysis of MEK1 and MEK2 expression in primary PDAC cell cultures with indicated genotypes after 4 days of tamoxifen (4-OHT) and vehicle (ethanol, EtOH) treatment. HSP90 served as loading control. Representative gel of three independent experiments. **d**, Clonogenic assays of mPDAC cells with indicated genotypes. Control cells treated with vehicle (ethanol; EtOH) are shown in the upper row, 4-OHT treated cells in the lower row. **e**, Schematic representation of the experimental set-up to test the effect of *Mek1/2* knockout *in vivo* by tamoxifen administration using syngeneic immunocompetent PDAC models. mPDAC cells with conditional *Mek1$^{lox/lox}$;Mek2$^{lox/lox}$* alleles were used for the orthotopic transplantation experiments. **f**, Waterfall plot showing tumor response of vehicle and tamoxifen treated animals after one week of treatment (fold-change compared to baseline before treatment based on MRI-volumetric measurements, y-axis). Each bar represents one mouse. P values calculated with two-tailed unpaired t test. **g**, Kaplan-Meier survival curve of vehicle and tamoxifen treated PDAC models. Number of mice is indicated in the corresponding panels. P value was calculated with log-rank (Mantel-Cox) test. **h**, Representative images of HE and IHC for MEK1, MEK2 and KI67 of tissue sections of tumors from orthotopically transplanted *Mek1$^{lox/lox}$;Mek2$^{lox/lox}$* models treated with vehicle or tamoxifen. Representative pictures of three independent experiments. Scale bars, 100 µm.

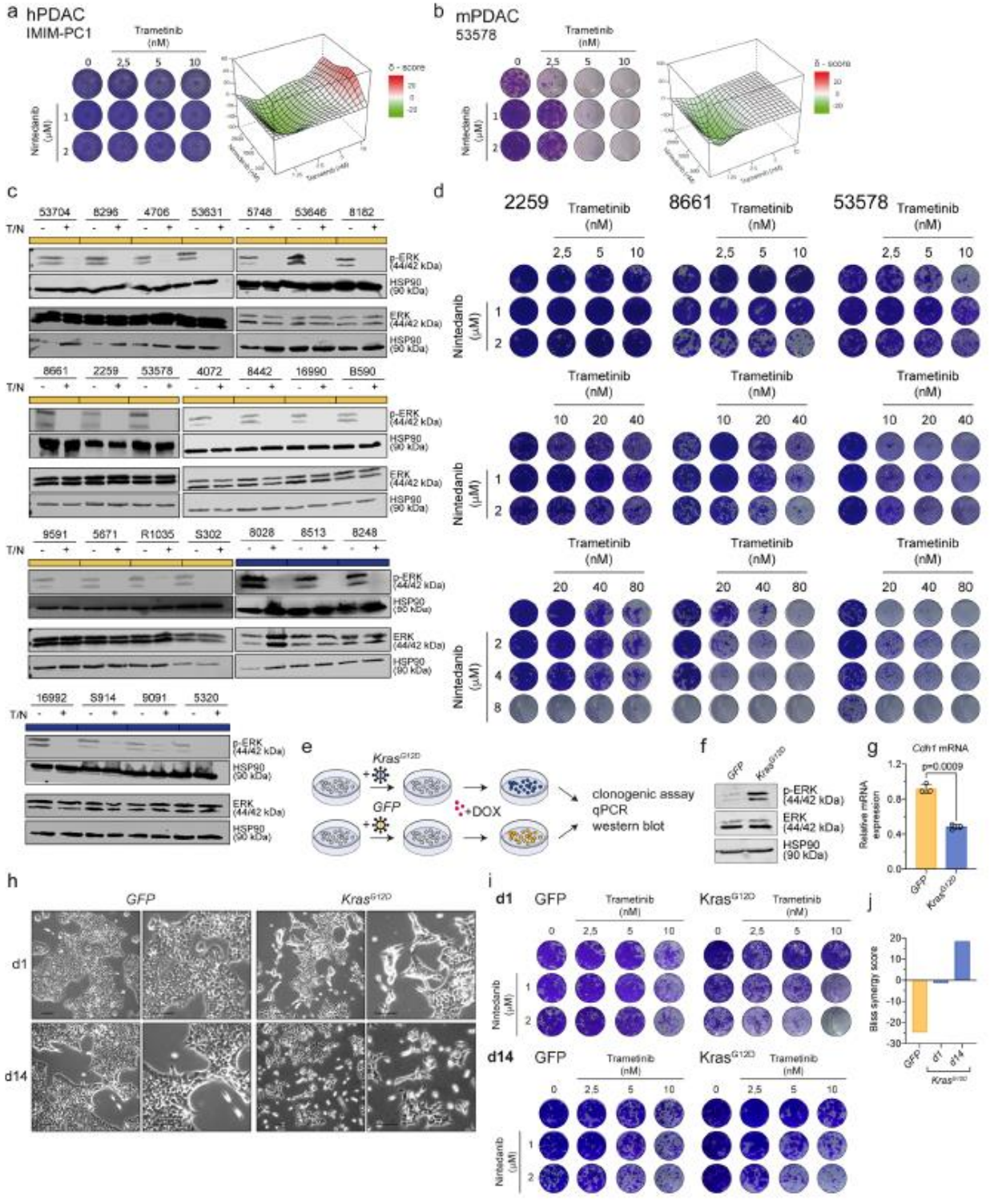

Extended Data Fig. 3 | See next page for caption.

Extended Data Fig. 3 | Pharmacologic and genetic modulation of drug sensitivity in classical and mesenchymal PDAC cell cultures. a, b, Clonogenic assays of a representative human (left) and mouse (right) PDAC cell culture showing antagonism to the trametinib/nintedanib (T/N) combination. Cell cultures were treated with indicated concentrations of T/N. **c**, Western blot of phospho-ERK and ERK in T/N (10 nM trametinib + 2 µM nintedanib) and vehicle treated classical and mesenchymal primary mPDAC cell lines. HSP90 served as loading control. Classical cell lines are marked in yellow, mesenchymal in blue. Representative gels of three independent experiments. **d**, Clonogenic assays using increased drug concentrations of the T/N combination of three of the most antagonistic cell lines, as depicted in Fig. 2, panel (**g**). **e**, Doxycycline-induced overexpression of $KRAS^{G12D}$ in mouse PDAC cells. 2259 mPDAC cells representative of the classical subtype was transduced with lentivirus carrying doxycycline-inducible $KRAS^{G12D}$ or GFP-control expression constructs. $KRAS^{G12D}$ or *GFP* expression were induced by doxycycline (100 ng/ml) for one or 14 days. **f**, Western blot of phospho-ERK and total ERK in cells overexpressing $KRAS^{G12D}$ or *GFP* for one day. HSP90 served as loading control. **g**, Expression of the marker gene *Cdh1* for epithelial cell differentiation was evaluated by qRT-PCR (normalized to *Cyclophilin B*). Data are shown as mean ± SD; n = 3 biological replicates. P value was calculated with two-tailed unpaired t test. **h**, Representative picture of three independent experiments of the morphological changes of PDAC cells upon $KRAS^{G12D}$ induction for one or 14 days of doxycycline treatment. Scale bars, 200 µm. **i**, Representative clonogenic assays of mPDAC cells treated with the indicated concentrations of trametinib and nintedanib upon $KRAS^{G12D}$ (right panel) or *GFP* (left panel) overexpression. **j**, Bliss synergy scores for the mPDAC cell line treated with the combination of trametinib and nintedanib upon $KRAS^{G12D}$ or *GFP* overexpression.

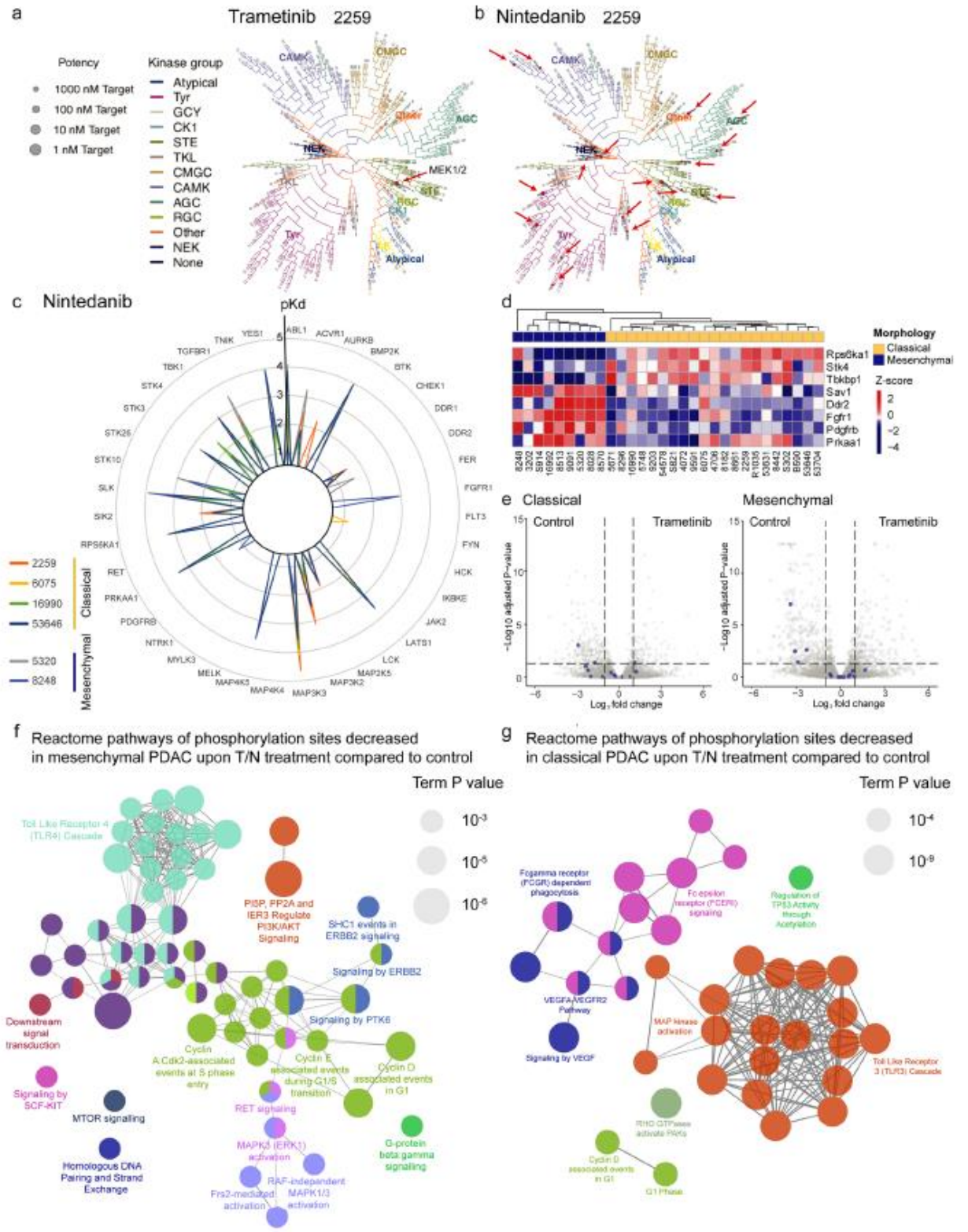

Extended Data Fig. 4 | See next page for caption.

Extended Data Fig. 4 | Kinobead-based proteomic identification of the trametinib and nintedanib targets and treatment-induced changes in the phosphoproteome of classical and mesenchymal PDAC. a, **b**, Representative pictures of the target space of trametinib (**a**) and nintedanib (**b**) for 2259 PDAC cells. A phylogenetic tree of all kinases for the 2259 primary mouse PDAC cell culture is shown. The indicated circle sizes indicate potency (apparent dissociation constants (Kdapp)), the color code specifies protein-drug interaction with the designated or other targets. Arrows highlight the identified targets. **c**, Radar plot showing the overlay of the pKd (−log10Kd) for the targets of nintedanib in the 6 PDAC cell cultures tested. PDAC cells of the classical (n=4) and mesenchymal (n=2) subtype are indicated with the color code. **d**, Heatmap showing the differentially expressed genes between epithelial and mesenchymal cell cultures identified as targets of nintedanib. The color code indicates the Z score. **e**, Volcano plots representing the change in gene expression of the nintedanib targets (in blue) upon trametinib treatment. The x-axis log2 fold change (treated/control), the y-axis shows the per test adjusted p values, which were calculated by differential expression test (using the DESeq2 package). A gene was considered to be differentially expressed with a Benjamini-Hochberg adjusted p-value of 0.05 and an absolute fold change >1. **f**, **g**, Mesenchymal (9091) and classical (8661) PDAC cell cultures were used to generate site-specific phospho-array datasets (Phospho Explorer antibody microarray, Full Moon Biosystems). The cell lines were analyzed at basal condition and in presence of T/N (trametinib 10 nM + nintedanib 2 µM). Phospho-array data (Supplementary Table 3) were used to test for the decrease of differentially phosphorylated sites between T/N and vehicle (DMSO) treated classical and mesenchymal mPDAC cells. Functionally grouped maps, obtained with the ClueGO plugin of Cytoscape, representing pathways overrepresented in mesenchymal (**f**) and classical (**g**) mPDAC upon T/N treatment are shown. Only the pathways with an adjusted p value (calculated by two-sided hypergeometric test, Bonferroni corrected) ≤ 0.05 are represented. The node size represents the term enrichment significance.

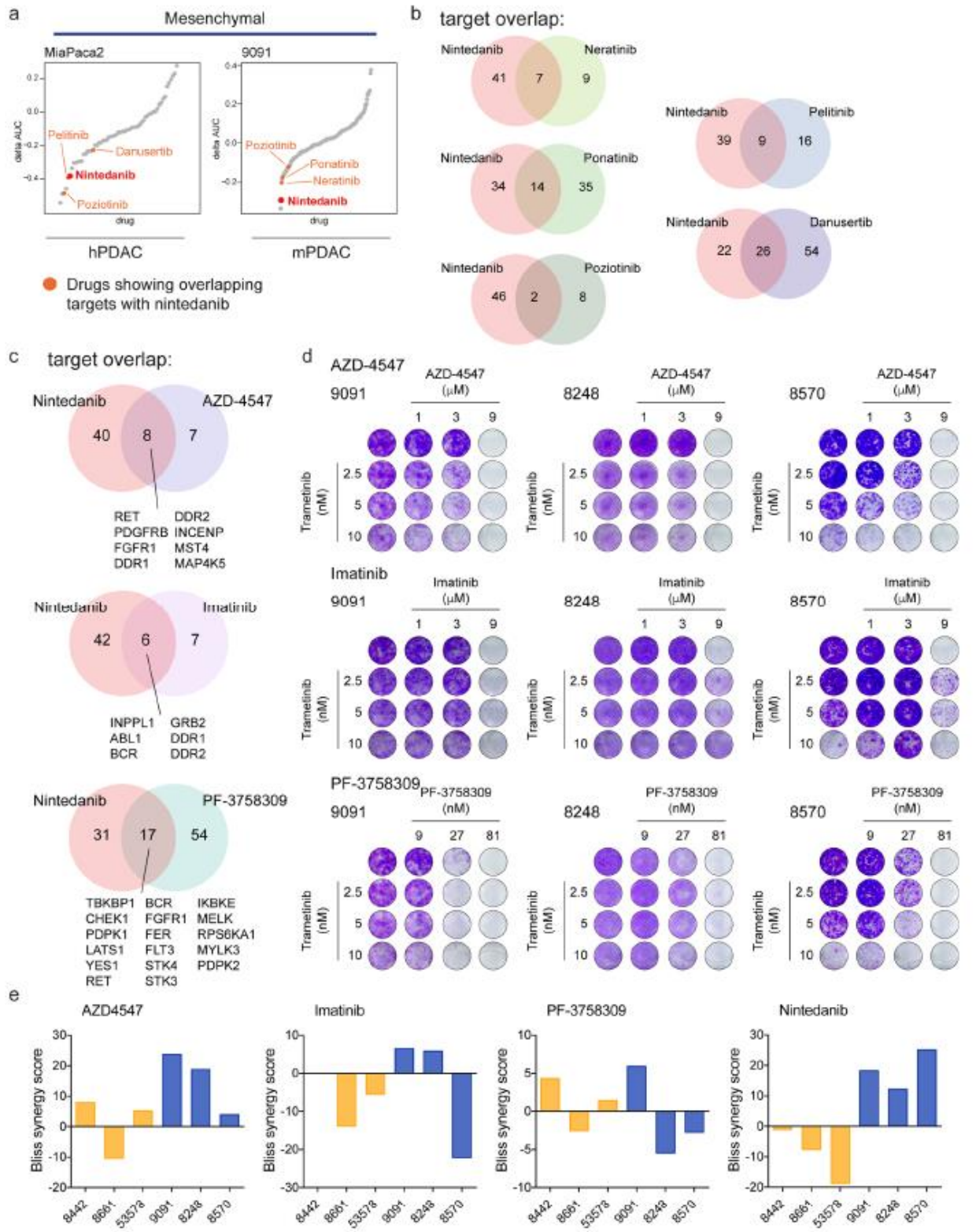

Extended Data Fig. 5 | See next page for caption.

Extended Data Fig. 5 | Pharmacologic assessment of nintedanib targets. a, Combinatorial drug screen on mesenchymal hPDAC cell line MiaPaca2 and mPDAC cell line 9091, as shown in Fig. 2, panel (**b**). The MEK inhibitor trametinib was used in fixed concentration and combined with 418 additional drugs under preclinical and clinical investigation. Highlighted in orange are the drugs in the high-throughput drug screen showing overlapping targets with nintedanib. **b**, Venn diagrams showing the target overlap between the drugs identified in (**a**) and nintedanib (see Supplementary Table 4) as reported from the ProteomicsDB database (https://www.proteomicsdb.org). **c**, Venn diagrams showing the target overlap between nintedanib and additional drugs with an overlapping target profile chosen for further target assessment. The overlapping targets are listed below each figure. The target information was downloaded from the ProteomicsDB database (https://www.proteomicsdb.org). **d**, Representative clonogenic assays of mesenchymal mPDAC cell cultures treated with trametinib in combination with the drugs shown in (**c**) as compared to nintedanib. The cell lines were treated with the indicated concentrations of trametinib and the indicated experimental drug. **e**, Bliss synergy scores of clonogenic assays shown in (**d**) integrated with cell morphology for the treated mPDAC cell cultures (classical subtype depicted in yellow and mesenchymal in blue).

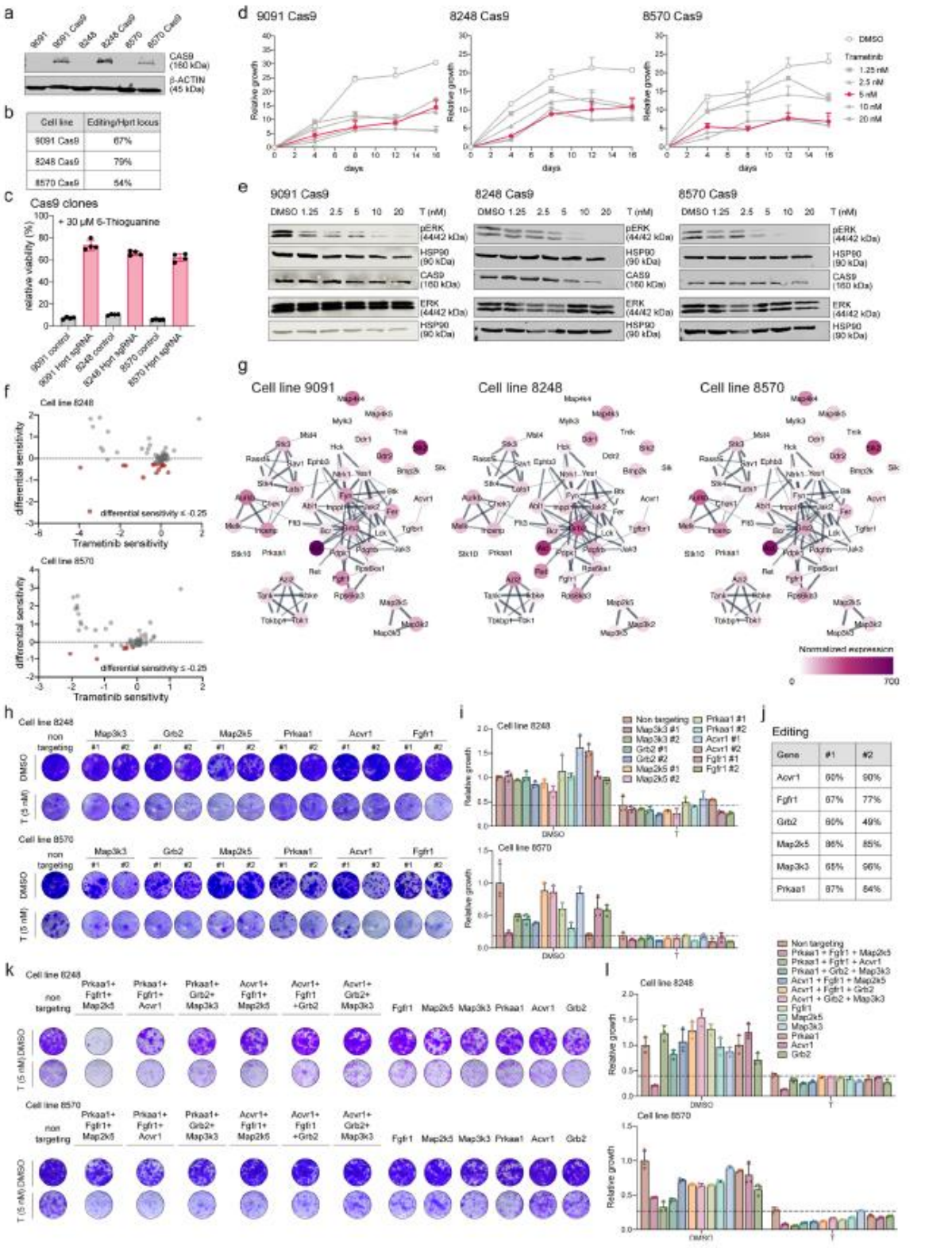

Extended Data Fig. 6 | See next page for caption.

Extended Data Fig. 6 | Genetic screens to identify relevant nintedanib targets sensitizing mesenchymal PDAC towards trametinib. a, Western blot of Cas9 expression in the clonal cell lines used for CRISPR/Cas9 screens. β-Actin served as loading control. **b**, Editing efficiency at the *Hprt* locus. **c**, Relative viability upon 6-Thioguanine treatment to validate Cas9 function in *Hprt* proficient and deficient Cas9 cells (mean ± SD; n = 3 biological replicates). **d**, Relative cell growth (y-axis), assessed by cell counting, in the presence of different concentrations of trametinib (mean ± SD; n = 3 biological replicates). The pink line indicates the trametinib concentration used for the CRISPR/Cas9 screens. **e**, Phospho-ERK, ERK and Cas9 Western blots of clones used for CRISPR/Cas9 screens. Cells were treated with DMSO or trametinib (1.25 nM, 2.5 nM, 5 nM, 10 nM and 20 nM) for 4 days. HSP90 served as loading control. **f**, Focused CRISPR/Cas9-based genetic screening in mesenchymal mPDAC cells 8248 and 8570. Trametinib sensitivity (x-axis) represents β-scores calculated as sgRNA representation difference between trametinib-treated cells and their initial representation. Differential sensitivity (y-axis) indicates β-score differences between trametinib- and DMSO-treated arms. In red, genes presenting differential sensitivity ≤ −0.25. **g**, Network visualization of normalized gene expression (assessed by RNA-seq) of nintedanib targets shown in Fig. 3 (**d**). **h**, Lentiviral CRISPR/Cas9-mediated deletion of selected top-scoring nintedanib targets in 8248 and 8570 cells. Knock-out cells were treated with trametinib (5 nM) or DMSO and viability was assessed through clonogenic assays. **i**, Quantification of panel (**h**). Data are normalized to DMSO-treated non-targeting controls (mean ± SD; n = 3 biological replicates). The dashed line represents the mean of trametinib-treated non-targeting controls. **j**, Editing efficiency of each sgRNA used in Fig. 2 (**f** and **g**) and in panels (**h**) and (**i**) of this figure. **k**, Combinatorial deletion of nintedanib targets via ribonucleoprotein (RNP) electroporation. Mesenchymal 8248 and 8570 knock-out cells were treated with trametinib (5 nM) or DMSO and viability was assessed through clonogenic assays. **l**, Quantification of panel (**k**). Data are normalized to DMSO-treated non-targeting controls (mean ± SD; n = 3 biological replicates). Dashed line represents the mean of trametinib-treated non-targeting controls. The shown gels are representative of three independent experiments.

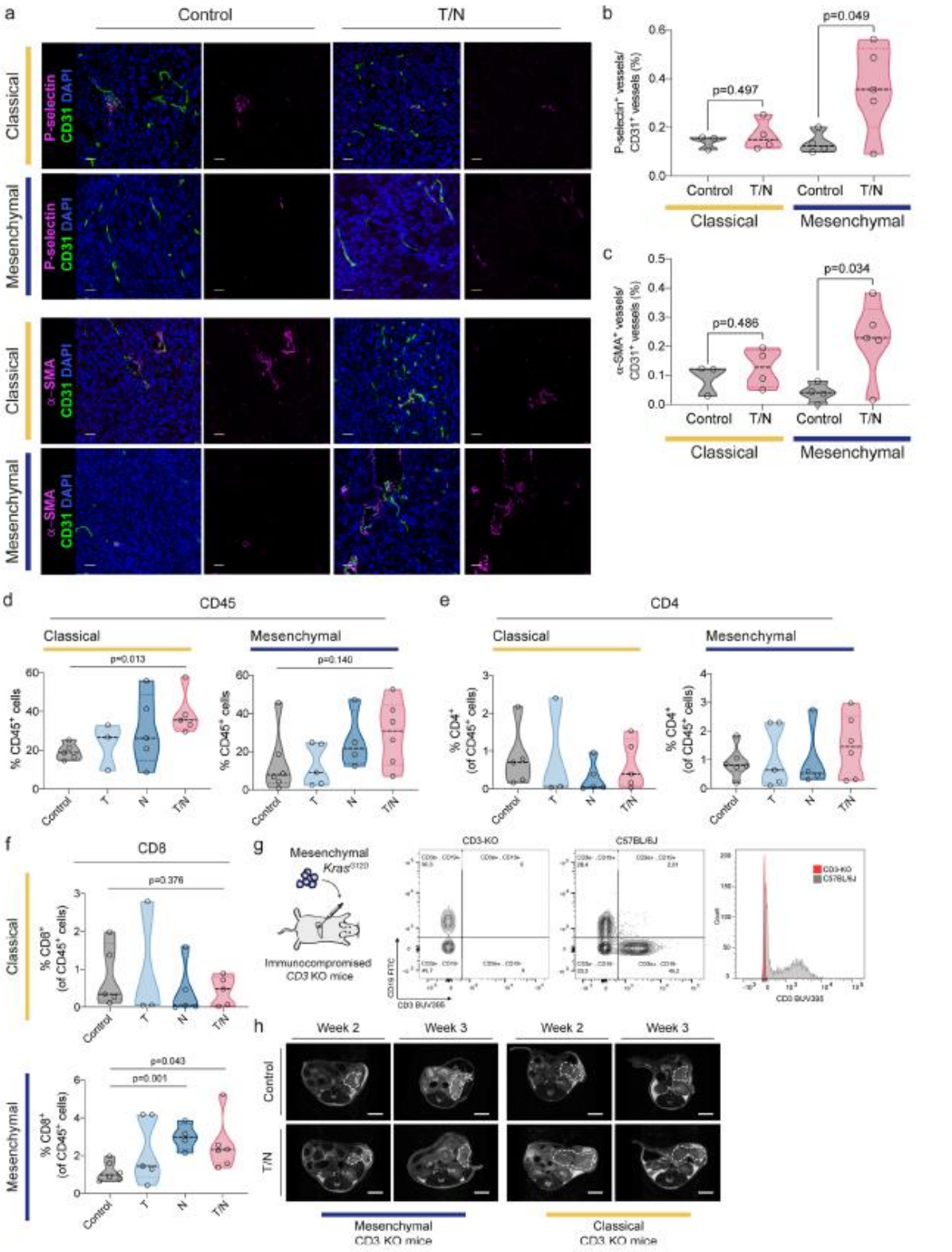

Extended Data Fig. 7 | See next page for caption.

Extended Data Fig. 7 | Characterization of context-specific changes of the tumor vasculature and the adaptive immune system in classical and mesenchymal PDAC subtypes upon therapy. a, Orthotopically transplanted tumors of the indicated subtypes were treated with vehicle (control) and the T/N combination. Representative images of immunofluorescence stainings of tissue sections for P-selectin (upper panel) and α-SMA (lower panel) (magenta). CD31 was used to detect endothelial cells (green). DAPI was used for nuclear staining (blue). Scale bars, 25µm. **b**, **c**, Quantification of the P-selectin+ vessels (**b**) and α-SMA + vessels (**c**) of the immunofluorescence stainings depicted in (**a**). Individual tumors are shown as single dots in the graph (classical: control n = 3, T/N n = 4; mesenchymal: control n = 4, T/N n = 5). **d**, Orthotopically transplanted tumors of the indicated subtypes were treated with vehicle (control) and the indicated drugs and drug combinations, explanted, single cell suspended and analyzed by flow cytometry. Panel (**d**) shows the staining for CD45 + cells. Individual tumors are shown as single points in the graph. **e**, **f**, Graphs representing the percentage of CD4 + (**e**) and CD8 + (**f**) cells in the PDAC control cohort and in the different treatment conditions as analyzed by flow cytometry. Single points represent individual tumors. **g**, Left, scheme of the *in vivo* experimental strategy using orthotopic PDAC cell transplantations into T cell deficient *CD3e* knockout (KO) mice. Right, representative FACS plot of immunodeficient *CD3e-KO* and wild-type C57BL/6 mice, highlighting the lack of T cells in the *CD3e-KO* animals. **h**, Representative MRI picture of vehicle (control) and T/N treated PDAC bearing *CD3e-KO* mice before (week 2) and after 1 week treatment (week 3). P values in (**b**), (**c**), (**d**) and (**f**) were calculated with two-tailed unpaired t test. T: trametinib, N: nintedanib, T/N: trametinib+nintedanib.

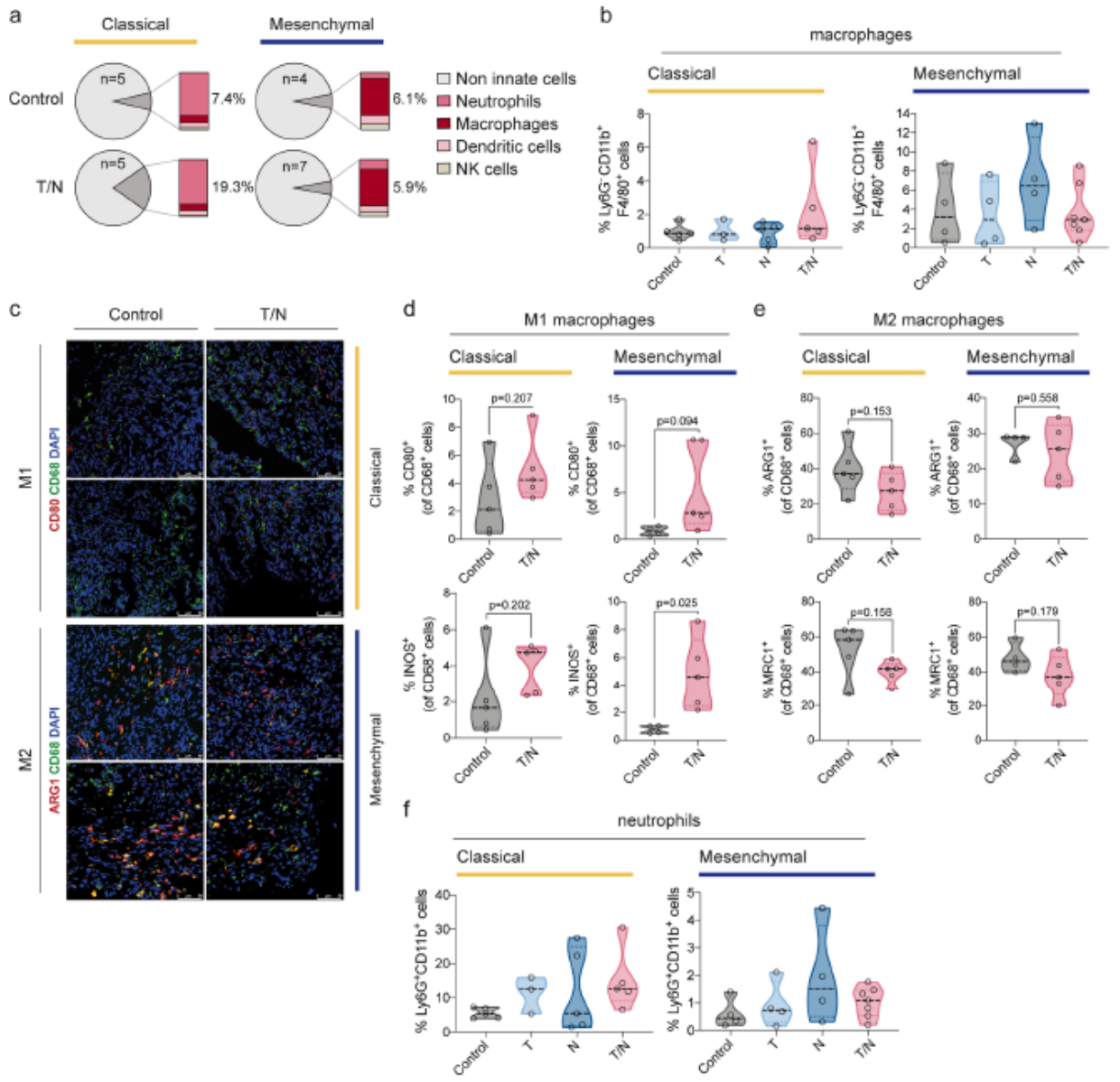

Extended Data Fig. 8 | Characterization of context-specific changes of the innate immune system in classical and mesenchymal PDAC subtypes upon therapy. a, Pie charts representative of the fraction of innate immune cell populations in PDAC from vehicle control and mice that received the combination (T/N) for both classical and mesenchymal orthotopically transplanted tumors as analyzed by flow cytometry. The number of tumors per condition analyzed is depicted in the corresponding panel. **b**, Graphs representing the percentage of Ly6G- CD11b+F4/80+ macrophages in PDAC of the control cohort and in the treatment conditions as analyzed by flow cytometry. Single points represent individual tumors. **c**, Representative immunofluorescence staining for CD80/CD68 and ARG1/CD68 cells in both classical and mesenchymal tumors treated with the T/N combination therapy or vehicle as control. Scale bars, 50 µm. **d**, Quantification of the M1-like polarization macrophage markers CD80/CD68+and INOS/CD68+from the immunofluorescence stainings depicted in (**c**). Individual tumors are shown as single points in the graph (classical: control n=5, T/N n=5; mesenchymal: control n=4, T/N n=5). **e**, Quantification of the M2-like polarization macrophage markers ARG1/CD68+and MRC1/CD68+from the staining depicted in (**c**). Individual tumors are shown as single points in the graph (classical: control n=5, T/N n=5; mesenchymal: control n=4, T/N n=5). **f**, Graphs representing the percentage of Ly6G+CD11b+neutrophils in the control cohort and in the treatment conditions as analyzed by flow cytometry. Single points represent individual tumors. P values in (**d**) and (**e**) were calculated with two-tailed unpaired t test. T: trametinib, N: nintedanib, T/N: trametinib+nintedanib.

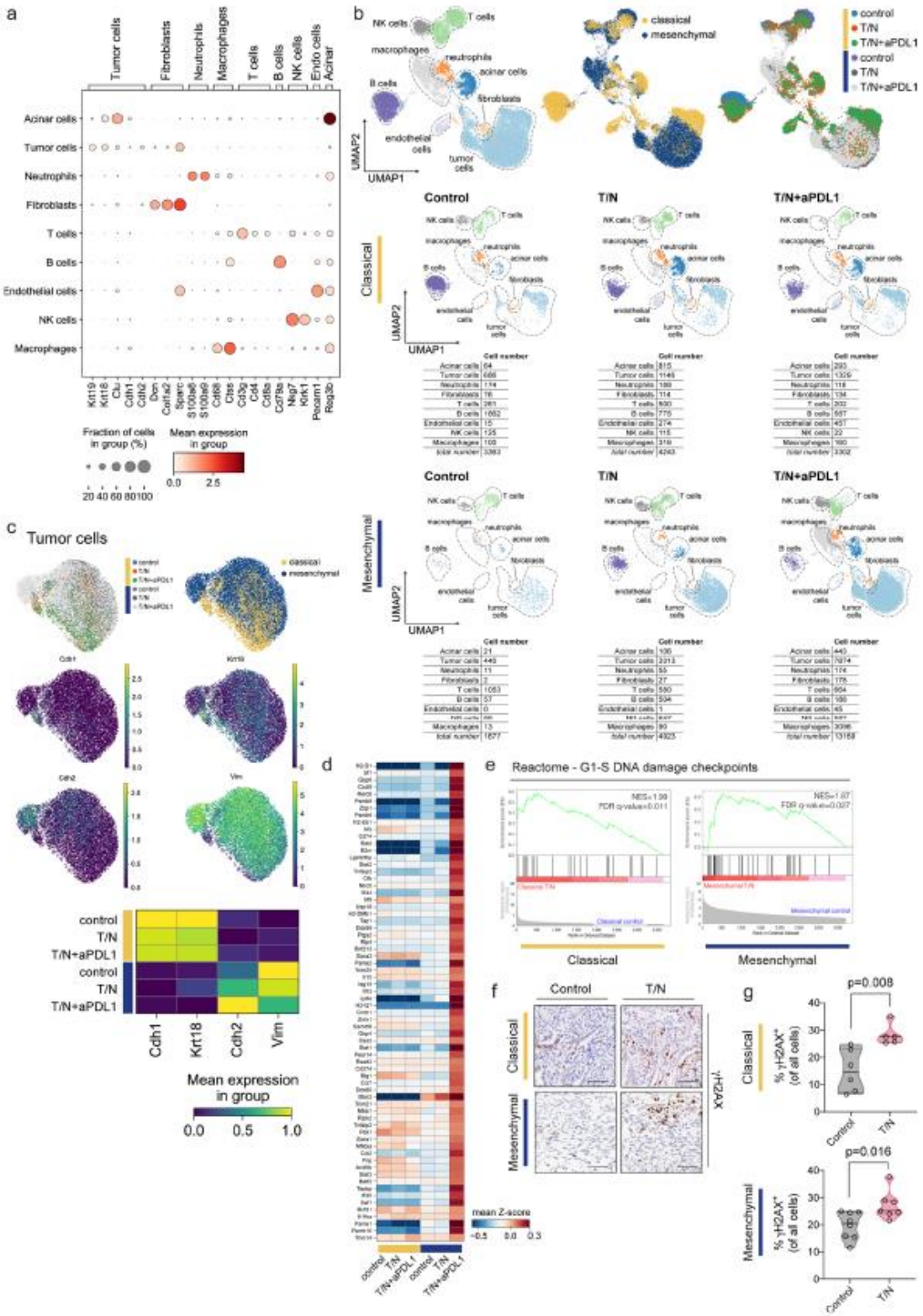

Extended Data Fig. 9 | See next page for caption.

Extended Data Fig. 9 | scRNA-seq reveals treatment-induced changes in TME cell subpopulations and activation of the DNA damage pathway in cancer cells. a, Dotplot displaying marker gene expression across each identified cluster of cancer cells and corresponding tumor microenvironment for both classical and mesenchymal tumors. The clusters are indicated on the y axis and the main markers for each identified population are indicated on the x axis. **b**, Left, UMAP plot showing all identified cell populations within the scRNA-seq experiment. Middle, UMAP plot showing classical (yellow) and mesenchymal (blue) tumors from all treatment and vehicle groups. Right, UMAP plot showing the treatment-induced changes in cell type composition among the identified cell populations across subtypes. Lower part, UMAP density plots showing distribution of annotated clusters upon treatment, cell numbers for each condition are integrated below. **c**, UMAP plot showing the identified tumor cell clusters. The expression of Cdh1 and Krt18, epithelial markers, and of Cdh2 and Vim, mesenchymal markers, across treatment conditions are shown below. **d**, Heatmap of the most differentially expressed genes from the gene expression signature in Fig. 7 across subtypes and treatment conditions. **e**, Gene set enrichment analysis (GSEA) of scRNA-seq data of cancer cells reveals enrichment of DNA damage in both classical and mesenchymal tumors upon treatment with the T/N combination. NES and FDR-q values are indicated. **f**, Representative images of immunohistochemical staining for γH2AX of control and T/N treated tumor sections for both classical and mesenchymal subtypes. Scale bar, 70 µm. **g**, Quantification of γH2AX positive cells in (**f**). Individual tumors are shown as single points in the graph (classical: control n=6, T/N n=5; mesenchymal: control n=8, T/N n=7). P values were calculated with two-tailed unpaired t test. Endo cells: endothelial cells. T/N: trametinib+nintedanib. T/N + aPD-L1: trametinib+nintedanib+anti PD-L1 antibody.

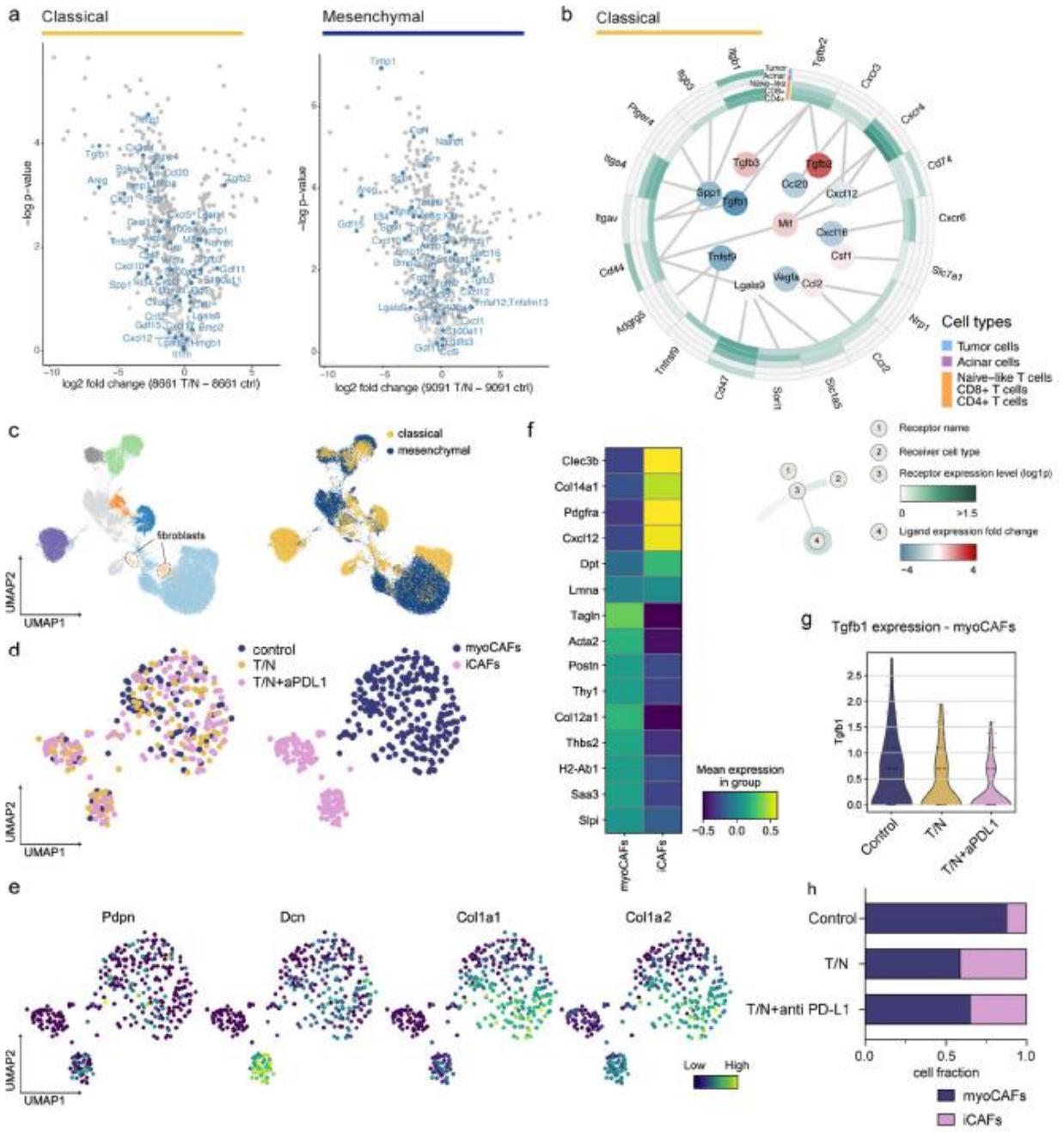

Extended Data Fig. 10 | Context-dependent reprogramming of the cancer cell derived secretome and cancer associated fibroblasts (CAFs) by the T/N combination therapy. a, Volcano plots highlighting the changes in secreted factors upon T/N treatment in classical (left) and mesenchymal (right) PDAC cells. The x-axis shows log2 fold change (treated/control), the y-axis the per test adjusted p values, which were calculated by differential expression test (two-sided t test). **b**, Circos plot showing the key communication signals from tumor cells to T cell subtypes, tumor cells and acinar cells in classical mPDAC. The ligand protein expression fold change, identified from secretome experiments, between T/N and control is shown in the middle. Normalized receptor expression levels obtained from scRNA-seq data are shown in the outer concentric circles. **c**, UMAP plot highlighting the whole population of CAF cells identified in classical and mesenchymal tumors. **d**, Left, UMAP plot showing the CAF population across different treatment conditions in classical tumors. Right, UMAP plots displaying the identified CAF clusters and resulting subpopulations for classical tumors. **e**, UMAP plots of the CAF cluster displaying selected marker gene expression. **f**, Heatmap displaying expression of selected genes in CAFs across the identified clusters. The y axis shows the selected marker genes, the x axis represents each of the identified clusters in (**d**). **g**, Violin plot showing *Tgfb1* expression by myoCAFs across the different treatment conditions. **h**, Proportion of CAF subtypes in the indicated different treatment conditions. CAF subpopulations were identified in the fibroblast cell clusters and annotated with the markers described in (**f**). T/N: trametinib+nintedanib, T/N+ aPD-L1: trametinib+nintedanib+anti PD-L1 antibody.

Article 5: Proteomics reveals distinct mechanisms regulating the release of cytokines and alarmins during pyroptosis

Cell Rep. 34, 108826 (2021)

Kshiti Phulphagar[1,2], Lars I. Kühn[2], Stefan Ebner[2], Annika Frauenstein[2], **Jonathan J. Swietlik**[2], Jan Rieckmann[2], Felix Meissner[1,2]

[1] Experimental Systems Immunology Laboratory, Max Planck Institute of Biochemistry, Martinsried, Germany
[2] Institute of Innate Immunity, Department of Systems Immunology and Proteomics, Medical Faculty, University of Bonn, Bonn, Germany

Pyroptosis is a type of programmed lytic cell death with key roles in immune responses to infection and injury[257]. In contrast to apoptosis, pyroptosis leads to the abundant release of pro-inflammatory signals, alerting the immune system to potential threats. Efficient induction of pyroptosis is mediated by the assembly of inflammasomes, large protein signaling complexes composed of pattern recognition receptors, the adaptor protein apoptosis-associated speck-like protein containing a caspase recruitment domain (ASC), and caspase-1, which triggers critical downstream events including proteolytic maturation of key cytokines and the pore-forming protein gasdermin D[257].

The release of signaling proteins by macrophages during pyroptosis is a complex, multifaceted process involving conventional, unconventional, and cell lysis. Despite its importance, the underlying dynamics and mechanisms remain poorly understood. Using state-of-the-art MS-based secretomics combined with genetic, pharmacological, and biochemical methods, we comprehensively quantify released proteins, including cytokines and alarmins, and systematically deconvolute their cellular exit routes.

Contribution:

I contributed to conceptualizing secretomics analysis strategies and performed secretomics experiments. In particular, I contributed to Figures 3 and S4.

Resource

Cell Reports

Proteomics reveals distinct mechanisms regulating the release of cytokines and alarmins during pyroptosis

Graphical abstract

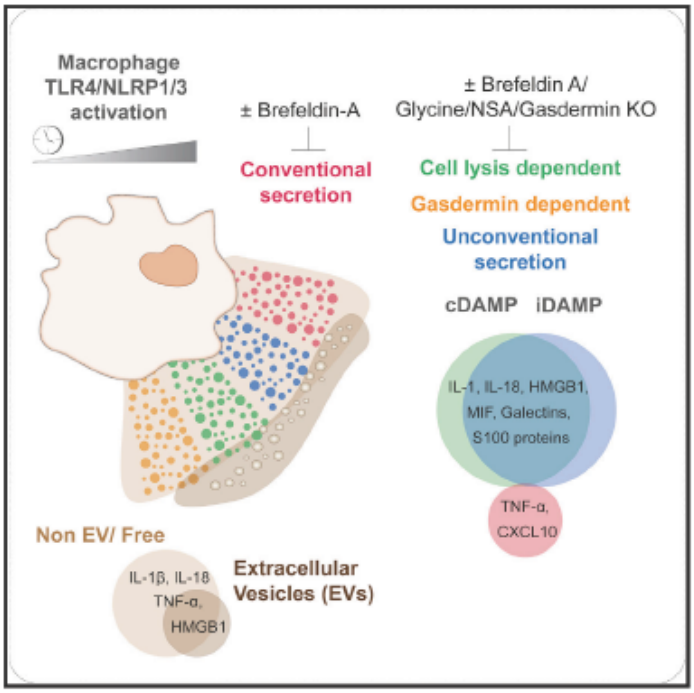

Authors

Kshiti Phulphagar, Lars I. Kühn, Stefan Ebner, Annika Frauenstein, Jonathan J. Swietlik, Jan Rieckmann, Felix Meissner

Correspondence

meissner@biochem.mpg.de

In brief

Using mass-spectrometry-based proteomics in combination with pharmacological and genetic perturbation, Phulphagar et al. dissect protein release during macrophage pyroptosis. The study defines proteins exiting cells through active secretion pathways, extracellular vesicles, organellar damage, and gasdermin pores and identifies the gasdermin-mediated release of multiple alarmins.

Highlights

- Mass spectrometry resource for inflammasome-activated protein release in macrophages
- Inhibition of inflammasome assembly and protein release by ER-Golgi disruption
- Dissection of protein release by gasdermin, organelle damage, and extracellular vesicles
- Identification of released constitutive and induced alarmins

Phulphagar et al., 2021, Cell Reports 34, 108826
March 9, 2021
https://doi.org/10.1016/j.celrep.2021.108826

CellPress

Cell Reports

CellPress
OPEN ACCESS

Resource

Proteomics reveals distinct mechanisms regulating the release of cytokines and alarmins during pyroptosis

Kshiti Phulphagar,[1,2,3] Lars I. Kühn,[1,3] Stefan Ebner,[1] Annika Frauenstein,[1] Jonathan J. Swietlik,[1] Jan Rieckmann,[1] and Felix Meissner[1,2,4,*]

[1]Experimental Systems Immunology Laboratory, Max Planck Institute of Biochemistry, Martinsried, Germany
[2]Institute of Innate Immunity, Department of Systems Immunology and Proteomics, Medical Faculty, University of Bonn, Bonn, Germany
[3]These authors contributed equally
[4]Lead contact
*Correspondence: meissner@biochem.mpg.de
https://doi.org/10.1016/j.celrep.2021.108826

SUMMARY

A major pathway for proinflammatory protein release by macrophages is inflammasome-mediated pyroptotic cell death. As conventional secretion, unconventional secretion, and cell death are executed simultaneously, however, the cellular mechanisms regulating this complex paracrine program remain incompletely understood. Here, we devise a quantitative proteomics strategy to define the cellular exit route for each protein by pharmacological and genetic dissection of cellular checkpoints regulating protein release. We report the release of hundreds of proteins during pyroptosis, predominantly due to cell lysis. They comprise constitutively expressed and transcriptionally induced proteins derived from the cytoplasm and specific intracellular organelles. Many low-molecular-weight proteins including the cytokine interleukin-1β, alarmins, and lysosomal-cargo proteins exit cells in the absence of cell lysis. Cytokines and alarmins are released in an endoplasmic reticulum (ER)-Golgi-dependent manner as free proteins rather than by extracellular vesicles. Our work provides an experimental framework for the dissection of cellular exit pathways and a resource for pyroptotic protein release.

INTRODUCTION

Secreted proteins such as cytokines, chemokines, and growth factors have various functions in the initiation and resolution of inflammation and the regulation of effector cells (Arango Duque and Descoteaux, 2014). A major pathway contributing to protein secretion in macrophages involves a highly pro-inflammatory form of cell death, known as pyroptosis. Pyroptosis plays a central role in the regulation of immune responses during infection and tissue injury (Bergsbaken et al., 2009). Efficient execution of pyroptosis requires the activation of intracellular signaling complexes termed inflammasomes and is regulated tightly in two steps.

Inflammasomes are comprised of activated cytosolic receptors such as certain nucleotide-binding oligomerization domain-like receptors (NLRs), an adaptor protein ASC, and a downstream effector protease known as Caspase-1.

For activation, a first signal induces transcription and expression of some inflammasome proteins such as the NLR family pyrin domain containing protein 3 (NLRP3), whereas some other NLRs such as NLRP1 are expressed constitutively. *In vitro*, this "priming" signal is commonly provided by ligation of innate immune receptors such as Toll-like receptor 4 (TLR4) through the Gram-negative bacterial cell membrane component lipopolysaccharide (LPS) (Broz and Dixit, 2016). LPS also induces numerous cytokines and chemokines including interleukin 1 beta (IL-1β), tumor necrosis factor alpha (TNF-α), and C-X-C motif chemokine ligand 10 (CXCL10), of which most are directly released conventionally through the endoplasmic reticulum (ER)-Golgi secretory pathway (Kaisho and Akira, 2000; Stow et al., 2009).

A second signal triggers inflammasome assembly through the activation of NLRs. Low cytosolic potassium levels activate NLRP3, whereas removal of the N terminus activates NLRP1 (Mitchell et al., 2019; Swanson et al., 2019). NLRs can then recruit the adaptor protein ASC and activate pro-inflammatory caspases such as caspase-1 that cleaves its substrates IL-1β, IL-18, and the gasdermin protein family member Gasdermin-D (GSDMD) into biologically active forms. The N-terminal fragment of GSDMD forms pores in the plasma membrane (PM) and eventually causes cell lysis (Ding et al., 2016; Kayagaki et al., 2015; Liu et al., 2016). GSDMD thereby facilitates the release of proteins lacking a signal peptide such as the cytokines IL-1β and IL-18 and proteins or "alarmins" derived from damaged cellular organelles such as high mobility group box 1 protein HMGB1, which also exhibits paracrine activity (Evavold et al., 2018; Heilig et al., 2018; Lamkanfi et al., 2010). As this protein export pathway does not involve active protein transport through the secretory pathway, it is broadly referred to as "unconventional secretion"

(Lopez-Castejon and Brough, 2011; Ng and Tang, 2016; Nickel and Rabouille, 2009).

Proteins released during inflammasome-activated pyroptosis therefore comprise conventionally (e.g., TNF-α), and unconventionally (e.g., IL-1β) released cytokines as well as alarmins (e.g., HMGB1) and other proteins leaking from the cytosol and damaged intracellular organelles. Unlike conventionally secreted proteins, which can be computationally predicted based on the primary amino acid sequence of their signal peptide, unconventionally released proteins can be identified with high confidence only experimentally by assessment of their release and the accompanied accumulation in cellular supernatants (Nickel and Rabouille, 2009). As IL-1- and IL-18-independent effects of inflammasome-mediated inflammatory programs have been described in different pathologies, the presence of novel immunomodulatory proteins such as alarmins can be hypothesized to be released during pyroptosis (Gong et al., 2020; Lammert et al., 2020).

In addition to translocation through GSDMD pores or cell lysis, various other export mechanisms have also been implicated in unconventional secretion such as secretion by lysosomes, extracellular vesicles (EVs), autophagosomes, and PM-derived microvesicles (Andrei et al., 1999; Baroja-Mazo et al., 2019; Brough et al., 2017; Dupont et al., 2011; Lopez-Castejon and Brough, 2011; Martín-Sánchez et al., 2016; Monteleone et al., 2015; Rubartelli et al., 1990; Tapia et al., 2019; Zhang et al., 2015). The identification of the predominant mechanisms of release for each protein can therefore enable the development of strategies to specifically interfere with distinct export pathways by abrogating the release of defined sets of proteins and thereby altering responses of neighboring cells or the entire organism to pyroptosis.

Mass spectrometry (MS)-based proteomics has matured remarkably over the last years and now provides a powerful set of tools for the systematic and unsupervised examinations of cellular processes (Aebersold and Mann, 2016; Larance and Lamond, 2015). Building on our recently developed MS-based approaches for the comprehensive analysis of intercellular immune signals, we set out to devise an experimental strategy to determine the inflammatory program of pyroptotic macrophages in its entirety and define the exit route for each protein (Meissner et al., 2013; Rieckmann et al., 2017; Tanzer et al., 2020). Our strategy comprises genetic knockouts (KOs) and knockins of inflammasome proteins to specifically inhibit or provide only one of the two signals required for full inflammasome activation. We pharmacologically interfere with ER-Golgi protein transport or passive cell lysis and assess the contribution of membrane-enclosed vesicles and receptor shedding to pyroptotic protein release, with the latter having implications in necroptosis—a distinct form of inflammatory cell death (Cai et al., 2016; Tanzer et al., 2020). Thereby, we determine for each protein whether transcription, caspase activation, active secretion, organellar damage, pore formation, or passive cell lysis is required for its release during pyroptosis.

RESULTS

Quantitative proteomics accurately determines protein release

We activated conventional protein secretion through one signal (TLR4 with LPS) and unconventional secretion through two signals (TLR4 with LPS plus NLRP3 with ATP or Nigericin) in murine bone-marrow-derived and human-monocyte-derived macrophages (BMDMs and HMDMs, respectively) and analyzed the secretory programs by label-free, high-resolution MS in a single-shot liquid chromatography-tandem MS (LC-MS/MS) format by using a Quadrupole-Orbitrap instrument (Figures 1A, S1A, and S1B; Kelstrup et al., 2018; Scheltema et al., 2014). Fold changes of proteins released in mouse and human macrophages upon TLR4 or TLR4 plus NLRP3 activation compared to untreated controls are indicated in Table S1. We identified on average almost 3,000 protein groups in cellular supernatants at a peptide and protein false discovery rate (FDR) of 1% (Figures S2A and 2B). We compared MS- to antibody-based (ELISA) protein quantification using TNF-α and IL-1β as reference proteins for conventional and unconventional secretion pathways (Figures 1B–1G and S2G). Both quantification methods showed similar secretion profiles for the two proteins (Figures 1B–1G), with an average correlation of 0.7 for TNF-α (Figure S2G) and 0.95 for IL-1β (Figure S2G). As expected, TNF-α was secreted after TLR4 activation regardless of the presence of a second activation signal (Figures 1B and 1E). In contrast, IL-1β was only secreted after priming the cells through TLR4, followed by activation of NLRP3 (Figures 1C and 1F). We further determined cell death by lactate dehydrogenase (LDH) release (Figure 1D) as well as by the summed MS signal of all proteins annotated as cytosolic (Figure 1G) and obtained a correlation of 0.85 between the two methods (Figure S2G). Our analysis shows that our method accurately quantifies conventional and unconventional protein secretion as well as cell death in activated macrophages.

Kinetics of conventional and unconventional protein release

To define pyroptotically released proteins, we assigned proteins to either (1) conventionally secreted or (2) unconventionally secreted proteins by comparing kinetics of secretomes from different experimental conditions (Figure 1).

First, we defined conventionally secreted proteins by comparing the secretome of TLR4-activated cells to unstimulated cells (Figure 1H). We identified 36 significantly released proteins, of which 30 exhibit a signal peptide and signal anchor. Among these proteins are known conventionally secreted, inflammatory mediators including cytokines (e.g., TNF-α and IL-6) and chemokines (e.g., CXCL10), confirming results of published work (Meissner et al., 2013). Functional enrichment analysis using annotations from the UniProt Keywords database revealed common terms of conventionally released inflammatory mediators such as "Cytokine," and "Inflammatory response" (Figure S3A).

Second, we defined unconventionally secreted proteins by the combined activation of TLR4 and NLRP3. Under these conditions, cellular supernatants contain conventionally secreted proteins due to the TLR4 priming signal and unconventionally released proteins comprising of proteins released by GSDMD pores or due to cell lysis (Figure 1I). This group of proteins contained prototypic unconventionally secreted proteins such as IL-1β, IL-1α, IL-18, and HMGB1 but excluded prototypic conventionally exported proteins like TNF-α and Cxcl10 (Figure 1I). Enrichment analysis of unconventionally secreted proteins using UniProt Keywords and Pfam protein domains unveiled the presence of diverse protein classes

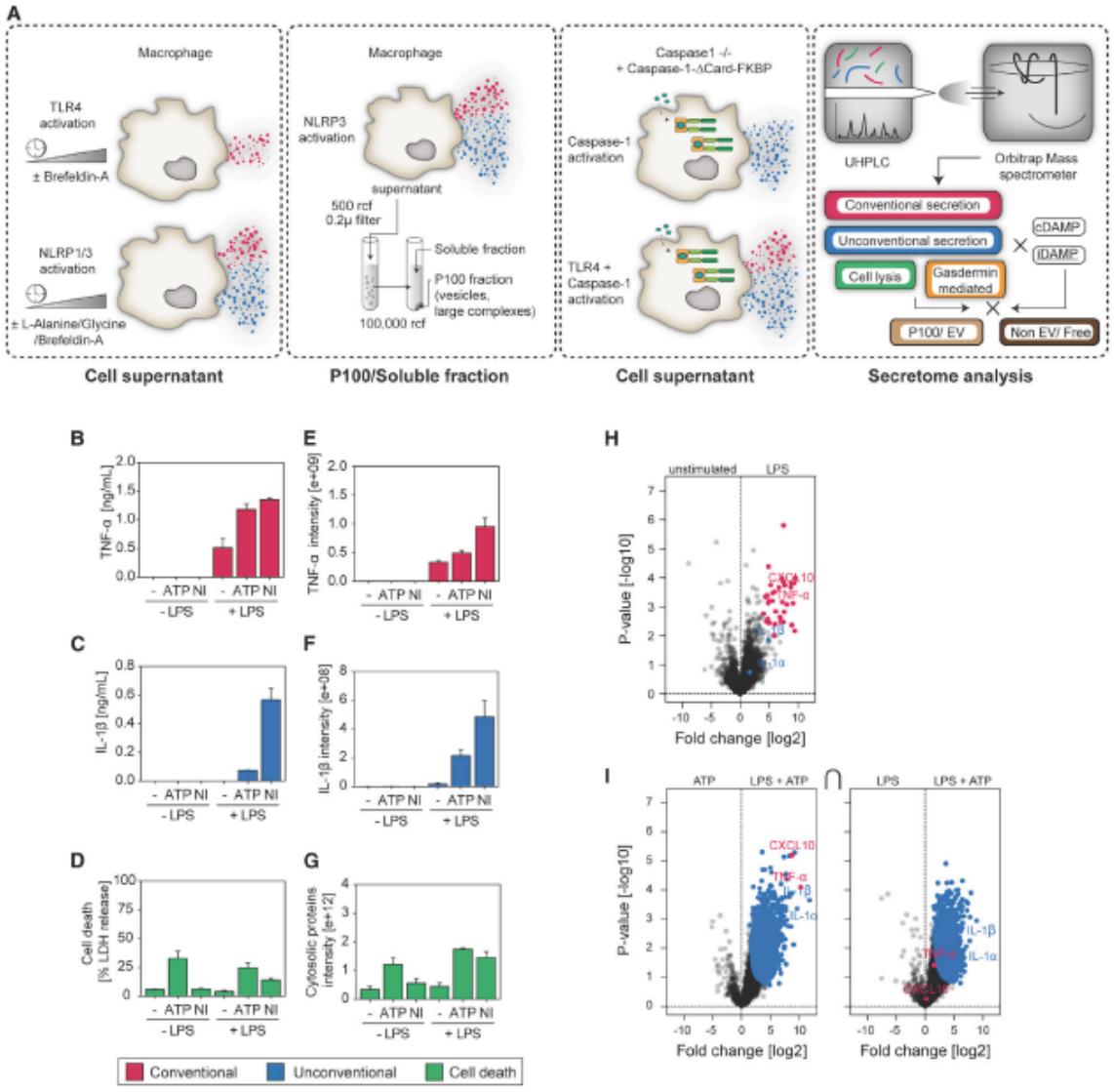

Figure 1. Quantitative proteomics workflow to identify proteins released by macrophage pyroptosis

(A) Schematic illustration of the experimental approach to distinguish between different modalities of protein release from cells, including conventional, unconventional, cell lysis dependent and independent, soluble or extracellular vesicle associated, dissection of released induced or constitutive alarmins, or damage-associated molecular patterns (DAMPs). Workflow consisting of macrophage activation, collection and processing of supernatants, sample preparation, LC-MS/MS analysis, and data processing.

(B–D) Quantification of TNF-α (B) and IL-1β (C) secretion by ELISA or cell death by LDH release (D) after TLR4 and NLRP3 activation in mouse macrophages. Data are represented as mean ± SD of three biological replicates.

(E–G) MS raw intensity-based quantification after TLR4 and NLRP3 activation in mouse macrophages of TNF-α (E) and IL-1β (F) secretion and cell death (G) measured by the summed MS raw intensity of all proteins annotated as "cytoplasm," "cytoplasmic part," "intracellular," or "intracellular part" by GOCC. Data are represented as mean ± SD of three biological replicates.

(H and I) Volcano plots showing secreted proteins from differentially activated BMDMs. Pairwise secretome comparisons to define conventionally (H) and unconventionally (I) released proteins. (H) Conventionally released proteins upon TLR4 activation compared to untreated controls (magenta).

(I) Unconventionally released proteins upon TLR4 plus NLRP3 compared to TLR4 as well as to only NLRP3-activated cells (blue). Significant proteins were determined with a parametric two-tailed Welch's t test (FDR < 0.05, $S_0 = 1$).

See also Figures S1–S4 and Table S1.

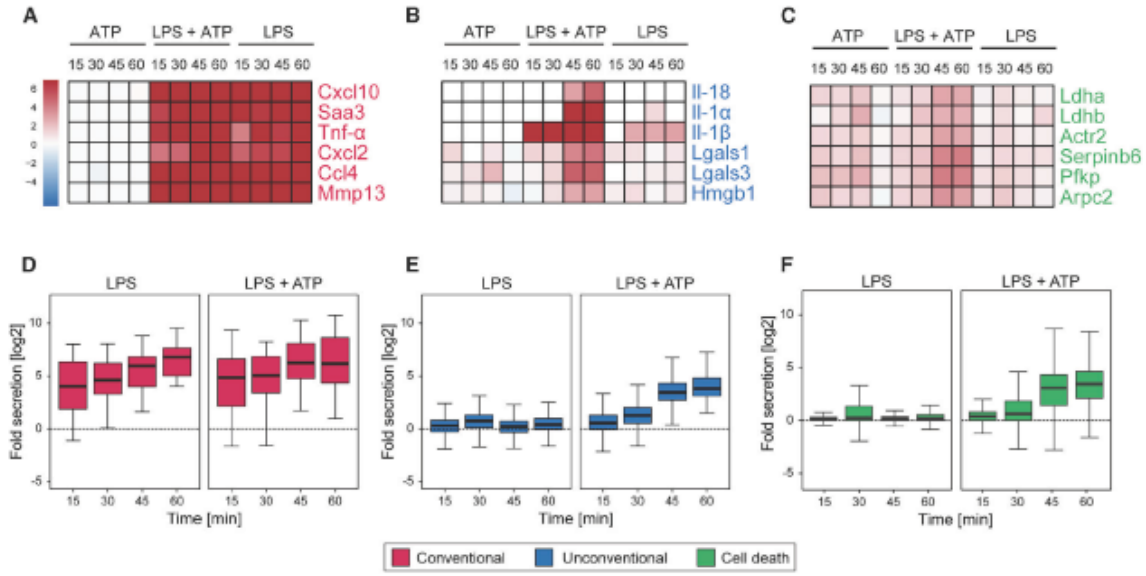

Figure 2. Proteomic analysis of pyroptosis-mediated conventional and unconventional protein secretion

(A–C) Heatmaps with secretion profiles of selected proteins known to be released via conventional unconventional programs.

(A) Cytokines containing a signal peptide and significantly released from cells by conventional secretion upon TLR4 activation with LPS.

(B) Cytokines/alarmins without a signal peptide significantly released from cells by unconventional secretion upon pyroptosis induction by TLR4 and NLRP3 activation with LPS and ATP.

(C) Selected cytoplasmic proteins, including subunits of the LDH complex.

(D–F) Fold secretion over time of conventional (D; magenta), unconventional (E; blue), or proteins annotated as "cytoplasm," "cytoplasmic part," "intracellular," or "intracellular part" by GOCC (F; green) by BMDMs activated for TLR4 with LPS and TLR4 plus ATP for NLRP3.

See also Figures S1, S2, and S4 and Table S1.

and structural domains such as Cofilin-actin de-polymerization factor (Cofilin-ADF) and Lin11, Isl-1 & Mec-3 (LIM), ADP ribosylation factor (ARF), and the caspase activation and recruitment domain (CARD), which is present for example in caspase-1 and ASC, two proteins involved in the formation of the NLRP3 inflammasome (Figure S3B). The abundance of conventionally secreted proteins increased gradually over time in response to TLR4 activation (Figures 2A and 2D), whereas unconventional protein release increased steadily in response only to TLR4 plus NLRP3 and was detectable already at 15 min after activation with a peak at 45–60 min (Figures 2B and 2E). We detected IL-1 release early upon inflammasome activation at 15 min, whereas other pyroptotically released cytokines and damage-associated molecular patterns (DAMPs) like IL-18 and HMGB1, respectively, with a similar size as IL-1β peaked later at 30–45 min (Figures 2B and 2E; Table S1).

Inhibition of NLRP3 with its small-molecule antagonist glyburide or KO of the downstream effector Caspase-1 abrogated the unconventional secretion completely (Figures S3D, S3E, and S4A–S4C; Swanson et al., 2019). Despite multiple comparisons, thousands of proteins were identified to be released with similar kinetics to IL1 and IL-18, impairing the discovery of potential novel alarmins. We therefore set out to define protein release pathways by assessing the role of the ER-Golgi compartment, extracellular vesicles, damaged intracellular organelles, PM pores, or cell lysis during pyroptosis.

The ER-Golgi compartment is required for inflammasome formation and unconventional protein release

Although the role of the ER-Golgi route conventional secretion has been well described, its contribution to unconventionally released cytokines such as IL-1β remains controversial and incompletely understood (Rubartelli et al., 1990; Zhang et al., 2017). We used the fungal metabolite Brefeldin A (BFA) as well as the small molecule Golgicide A (GCA), of which both prevent protein transport from the ER to the Golgi and disrupt the function of ER-Golgi secretory pathway (Chardin and McCormick, 1999; Sáenz et al., 2009). BFA and GCA perturb ER-Golgi trafficking by specifically inhibiting the guanine nucleotide exchange factors (GEFs) that regulate the formation of secretory vesicles. Although BFA targets several GEFs, including Golgi-specific BFA resistance factor 1 (GBF1), BFA-inhibited GEF 1 (BIG1), and BIG2, GCA is highly specific toward GBF1 (Sáenz et al., 2009). As expected, treatment of LPS-stimulated BMDMs with BFA inhibited the secretion of TNF-α and all other proteins we defined as conventionally secreted in a dose-dependent manner (Figures 3A and 3D). BFA also inhibited NLRP3-mediated release of IL-1β and cell death (Figures 3B, 3C, and 3E), in keeping with previous reports with a similar dose dependency (Zhang et al., 2017). However, we also observed a substantial reduction in IL-1β secretion by BFA treatment for inflammasome sensors, including baculoviral inhibitor of apoptosis domain repeat-

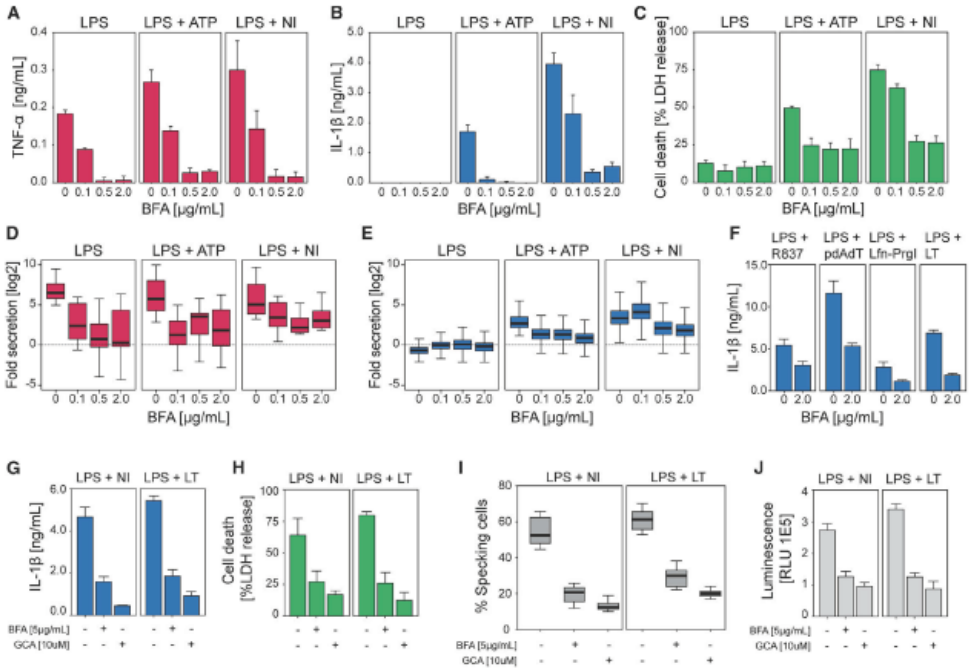

Figure 3. Conventional secretion, inflammasome formation, and unconventional secretion are inhibited by pharmacological ER-Golgi disruption

(A–C) ELISA of TNF-α (A), IL-1β (B), and LDH released (C) in supernatants of TLR4- or NLRP3-activated BMDMs in the presence of the indicated concentrations of BFA. NI, Nigericin

(D and E) Fold secretion of conventionally (D; magenta) and unconventionally (E; blue) released proteins in TLR4- and TLR4 plus NLRP3-activated BMDMs in the presence of the indicated concentrations of BFA.

(F) IL-1β levels as determined by ELISA in supernatants of NLRP3-, AIM2-NLRC4-, and NLRP1-activated BMDMs in the presence of the indicated concentrations of BFA.

(G–H) IL-1β levels as determined by ELISA (G) and LDH release (H) in supernatants of NLRP3- and NLRP1-activated BMDMs in the presence of the indicated concentrations of BFA or GCA.

(I–J) Quantification of NLRP3 or NLRP1 inflammasome assembly in the presence or absence of the indicated concentrations or BFA or GCA by evaluating Asc speck formation by using fluorescent microscopy. Data are compiled from three biological replicates, each with 100–200 quantified cells.

(I) Measurement of Caspase-1 activity by luminescence, in which aminoluciferin generated by cleavage of its substrate Z-WEHD-aminoluciferin results in light production in the presence of the luciferase enzyme. Data are represented as mean ± SD of three biological replicates.

See also Figures S4 and S5 and Table S1.

containing protein 1 (NAIP1) activated with its ligand the bacterial type III secretion system component PrgI and absent in melanoma 2 protein (AIM2) activation with repetitive synthetic double-stranded DNA sequence of poly(dA-dT) (Figure 3F; Broz and Dixit, 2016). GCA induced a similar reduction in IL-1β secretion and cell death in BMDMs activated for both NLRP1 and NLRP3 (Figures 3G and 3H). Notably, we treated cells with BFA or GCA after the first priming signal, suggesting that inhibition occurs at the level of the inflammasome sensor or the execution of pyroptosis but not TLR4. Interestingly, both BFA and GCA substantially reduced Asc speck formation as well as Caspase-1 activation (Figures 3I, 3J, and S5A–S5C). Thus, our data show that ER-Golgi perturbation with BFA and GCA inhibits unconventional protein release by interfering with inflammasome formation, regardless of the tested inflammasome sensor.

Leakage of specific cellular organelles during pyroptosis

We next asked whether pyroptosis leads to the release of subcellular organelles and their contents into the extracellular environment. To assess the leakage of proteins from organelles, we inspected the subcellular origin of all significantly released proteins. We observed an enrichment of cytosolic and lysosomal proteins and, to a lesser degree, endosomal, mitochondrial,

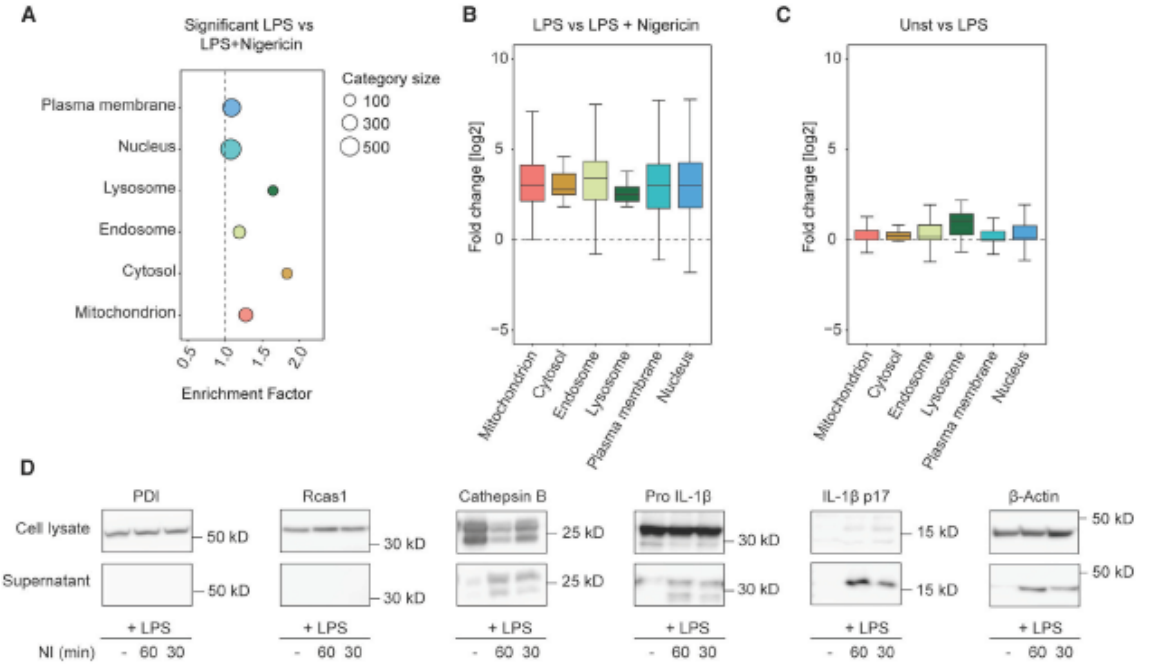

Figure 4. Extracellular leakage of organellar proteins

(A) Balloon plot of organelle marker enrichment analysis on the unconventional secretion signature after TLR4 and NLRP3 activation in mouse macrophages by using GOCC slim terms. Enrichment factors were calculated by Fisher's exact test (annotations with intersection sizes of >15 and $p < 0.002$ are shown). Category sizes are represented by balloon size.

(B and C) Boxplots indicating the fold changes of all detected proteins belonging to indicated organelles in the unconventional (B) and conventional (C) secretomes.

(D) Western blots of cell lysates or supernatants after TLR4 or TLR4 and NLRP3 activation for ER, Golgi, and lysosomal markers PDI, Rcas1, and Cathepsin B, respectively; or pro IL-1β, IL-1β p17 fragment, and the housekeeping protein β-Actin. Immunoblotting data are representative of two biological replicates. See also Figure S3.

nuclear, and PM proteins (Figures 4A and 4B). Interestingly, proteins from the ER and Golgi were not enriched. In agreement with our MS analysis, immunoblotting confirmed the release of the luminal lysosomal marker Cathepsin B and the absence of ER lumen marker protein disulfide isomerase (PDI) and Golgi marker receptor binding cancer antigen expressed on SiSo cells (RCAS1) in pyroptotic supernatants (Figure 4D). Our analysis therefore suggests that pyroptosis induces the release of proteins from specific subcellular localizations into the extracellular environment, whereas other organelles are retained inside the cell corpse.

We and others have described the shedding of receptors during programmed cell death by necroptosis (Tanzer et al., 2020). To determine whether pyroptosis is also accompanied by receptor shedding, we assessed whether cell surface receptors are enriched in pyroptotic cell supernatants. We detected 62 receptors, of which 15 were significantly released. However, examination of the quantified peptides revealed that both cytoplasmic and extracellular domains of these receptors were released to a comparable extent (Figure S5A). These results suggest the absence of an active shedding process involving proteolytic cleavage of receptors, as this would be accompanied by an increase of the extracellular domains of receptors and not the corresponding cytoplasmic domain. We therefore surmise that the presence of receptors and other PM-localized proteins in pyroptotic supernatants can be ascribed primarily to the release of PM fragments or micro-vesicles.

Most cytokines are secreted in a soluble form and not in EVs

EVs have been implicated in programmed cell death and also in NLRP3-mediated release of both pro-form and mature IL-1β and IL-18 (Cypryk et al., 2018). To determine the contribution of this protein release route, we enriched EVs from LPS-activated or pyroptotic supernatants by using differential centrifugation as described previously (Lobb et al., 2015; Table S1). The majority of cytokines including IL-1β and IL-18 were not detected in the EV-enriched P100 fraction, indicating that they are predominantly secreted in a non-EV-bound, soluble form (Figures 5A–5C). Some cytokines like TNF-α and PF4 as well alarmins like HMGB1 were, however, also present in the P100 fraction, suggesting that they might be released in soluble forms as well as in membrane-associated or EV-incorporated forms (Figure 5B). As both, low- and high-abundant cytokines were equally

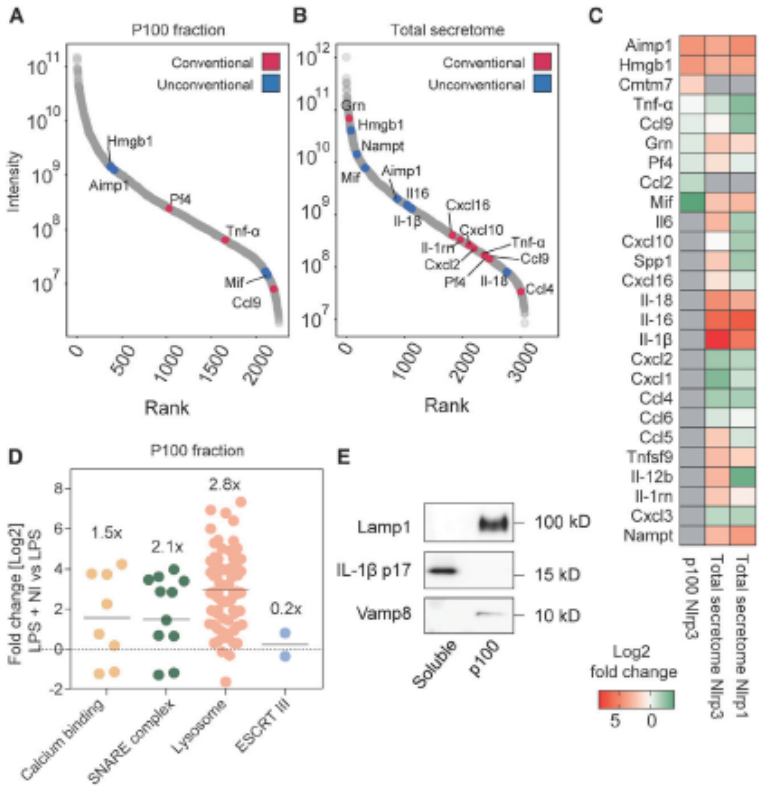

Figure 5. Majority of cytokines are released as free proteins and not in EVs

(A and B) Intensity-based ranking of cytokines identified in either P100 (A) or total secretome (B) of NLRP3-activated murine macrophages.

(C) Heatmap of fold secretion of conventionally and unconventionally released cytokines by murine macrophages in the total secretome after NLRP1/3 activation or P100/EV-associated secretome after NLRP3 activation.

(C) Swarm plots showing log2 fold change of proteins assigned to the annotation "Calcium/phospholipid binding," "SNARE complex," "Lysosome" and "ESCRTIII complex" present in P100/EV fraction of pyroptotic cells compared with TLR4-activated controls.

(D) Presence of lysosomal marker Lamp1, IL-1β p17 fragment, and the SNARE complex member Vamp8 in either the soluble or P100 fraction after NLRP3 activation evaluated by immunoblotting.

See also Figures S1, S3, and S6 and Table S1.

detected in the P100 fraction, our analysis is not biased toward the detection of high-abundant cytokines (Figure 5B). We conclude that secretory processes, in which cytokines and alarmins are packaged into vesicles and released in such a membrane-encapsulated form, contribute only minimally to their release during pyroptosis.

We also observed an enrichment of proteins in the categories "Lysosome," "SNARE complex," and "Calcium/PI binding," which we had also detected previously in vesicles released by cells undergoing necroptosis—another form of lytic cell death (Figure 5D; Tanzer et al., 2020). Both membrane as well as luminal lysosomal proteins were enriched to a comparable degree in the P100 fraction and secretome (Figure S3F). Conversely, cytosolic proteins were largely depleted in this fraction (Figures 5B–5D). Our data therefore suggest that endosomal and lysosomal proteins are released in a vesicular form during pyroptosis. We confirmed the absence of IL-1β or the presence of the lysosomal marker LAMP1 and SNARE complex member VAMP8 in the P100 fraction by immunoblotting (Figure 5E).

Unconventional release of low-MW, lysosomal, and mitochondrial proteins proceeds by a GSDMD-mediated but cell-lysis-independent pathway

Multiple recent studies indicate that during pyroptosis, low-molecular-weight (MW) proteins including IL-1β are released through PM GSDMD pores independently of late-stage cell lysis (DiPeso et al., 2017; Evavold et al., 2018; Heilig et al., 2018). To assess the contribution of GSMDM pores versus cell lysis to protein release, we induced pyroptosis in the presence of osmoprotectants L-alanine or glycine, which have been shown to block cell lysis but not the formation of GSDMD pores (Fink and Cookson, 2006; Loomis et al., 2019). Both L-alanine and glycine inhibited cell lysis that was measured by the release of the LDH complex of approximately 147 kD but not IL-1β (17 kD) or any conventionally secreted cytokine like TNF-α (26 kD), in keeping with previous reports (Figure S4D). We further evaluated protein release in GSDMD KO iBMDMs or wild-type (WT) BMDMs treated with the GSDMD inhibitor necrosulfonamide A (NSA), confirming that cell lysis as well as IL-1β release was inhibited, whereas conventional secretion of TNF-α was not (Figures S4E and S4F; Evavold et al., 2018; Heilig et al., 2018; Rathkey et al., 2018). At the global level, the correlation between all proteins released unconventionally versus the subset released in an osmoprotection-independent manner was mediocre (0.36) (Figures 6A–6C), whereas conventionally versus unconventionally released proteins showed a negative correlation (−0.16), indicating the independence of these two protein export pathways (Figures 6B and 6C).

Our proteomics experiments reveal that sensitivity to osmoprotection depends on the MW of a protein, as the release of low-MW proteins was inhibited far less than high-MW proteins (Figure 6D; Table S1). Osmoprotection barely reduced the release of low-MW proteins. such as IL-1β, the alarmins Galectin 3 (LGALS3) and HMGB1, or cytosolic proteins such as glutaredoxin 5 (GLRX5), whereas GSDMD KO or inhibition completely blocked the release of low- as well as high-MW proteins (Figures 6E and 6F). Surprisingly, a Gene Ontology term cellular component (GOCC) enrichment analysis revealed that proteins derived from lysosomes and, to a lesser extent, from mitochondria

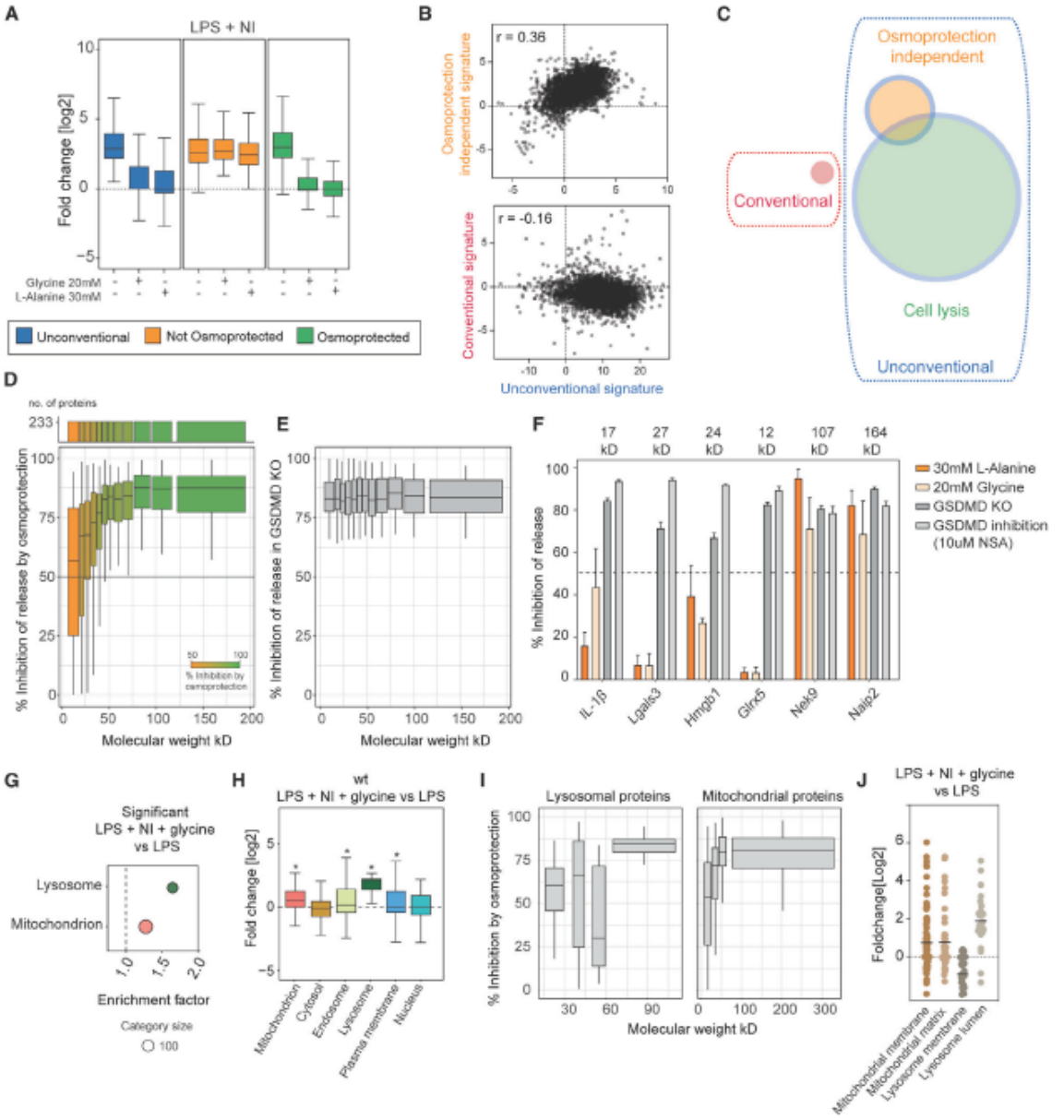

Figure 6. Release of low-MW, mitochondrial, and lysosomal proteins is dependent on GSDMD but proceeds independently of cell lysis

(A) Fold secretion of all unconventional, osmoprotection-independent (orange), and cell-lysis-dependent (green) protein release in TLR4 plus NLRP3-activated BMDMs in the presence of the indicated concentrations of L-Alanine or Glycine.

(B) Correlations of t test differences used to define the conventional, unconventional, osmoprotection, or cell lysis-independent and -dependent signatures. Conventional signature, LPS versus unstimulated; unconventional signature, t test differences LPS + NI versus LPS; and osmoprotection/cell lysis independent, LPS + NI + 30 mM L-alanine/20 mM glycine versus LPS.

(C) Venn diagram of proteins released conventionally, unconventionally, and osmoprotection independently or passively by cell death.

(D–F) Effect of osmoprotection or knockout of GSDMD on unconventionally released proteins with different MWs. Boxplot indicating the extent of inhibition by osmoprotection (D) or GSDMD knockout (E) to unconventionally released proteins binned according to increasing MW. Number of proteins per bin are indicated. Bar plots of selected proteins indicate the degree of inhibition of their release by osmoprotection, GSDMD knockout, or inhibition by NSA (F).

(legend continued on next page)

contribute to the osmoprotection-independent protein release (Figures 6G and 6H). Further analyses revealed that only lysosomal lumen but not membrane proteins are released independent of their MW, presumably as vesicular cargo (Figures 6I and 6J). In contrast, we detected both mitochondrial matrix and mitochondrial membrane proteins, which are sensitive to osmoprotection depending on their MW, arguing against a significant contribution of released mitochondrial vesicles under these conditions (Figure 6J). We therefore conclude that a GSDMD-dependent, cell-lysis-independent pathway facilitates the release of many constitutively expressed small-MW proteins derived from the cytoplasm and other cellular organelles, for which extracellular functions have not been described yet.

The majority of pyroptotically released alarmins do not require induction

As the two-step activation comprising priming and NLR activation executes a convoluted secretory program, we considered experimental systems, in which a single trigger is sufficient for inflammasome activation. Caspase 1/11 double knockout (DKO) iBMDMs reconstituted with Caspase-1 fused to the FK506 binding protein (FKBP) dimerization domain (Casp1ΔCard-FKBP) provides an elegant solution, as Caspase1 can be dimerized and activated by AP20187, leading to pyroptosis (MacCorkle et al., 1998; Rühl et al., 2018). Notably, activation of Caspase-1 is independent of priming and thereby enables the dissection of proteins released with and without priming. As expected, IL-1β is released only upon priming and AP20187 treatment, whereas conventional secretion, for example of TNF-α, requires priming but is unaffected by AP20187 (Figures 7A and 7B). Cell death, however, is executed only upon addition of AP20187, independent of priming (Figure 7C). This experimental setup therefore enables the distinction of two classes of proteins—constitutive and induced damage-associated molecular patterns (c- or iDAMPs) (Yatim et al., 2017). The release of the majority of unconventionally released proteins occurs irrespective of priming (Figure 7D). The alarmin HMGB1 is one such protein and can therefore be classified as a cDAMP. Our proteomic investigations reveal that pyroptotic cell death serves as an exit route also for other cDAMPs, such as macrophage migration inhibitory factor (MIF), mminoacyl TRNA Synthetase Complex Interacting Multifunctional Protein 1 (AIMP1), galectins, and S100 families (Figure 7D; Table S1). We confirmed the release of MIF and AIMP1 by ELISA and immunoblot analysis (Figures 7G and 7H). As most cDAMPs, such as MIF or LGALS 1, 3, and 9, have a low MW, they are released independently of cell lysis, whereas others, such as AIMP1 or nicotinamide phosphoribosyltransferase (NAMPT), are predominantly released due to cell lysis. The cellular mechanisms regulating the exit of major protein classes are shown in Figure 7I and Table S1.

In contrast, IL-1β is released only during pyroptosis after priming and therefore is a paradigm iDAMP (Figure 7E). IL-18 shares some features of both classes, and even though priming boosts its expression and release, a smaller amount is constitutively expressed and therefore released independently of priming (Figures 7E and 7F; Marshall et al., 1999). Our analysis reveals that IL-1β is unique in its regulation and release kinetics, as it is among the top 5 most highly induced proteins upon priming and thereby differs from most other pyroptotically released proteins. (Figure S7A). The majority of strongly induced proteins include conventionally released cytokines that do not require pyroptosis for release (Figure S7B). Only a handful of other proteins not associated with extracellular functions, such as NLRP3, a few Ifit protein family members, and Oasl and Gbp family proteins, require priming for their induction and release by pyroptosis.

According to our global analysis, the cytokines IL-1β and IL-18 are unique in terms of their regulation in multiple steps, such as priming, proteolytic activation, MW, and PM-pore-mediated release. We did not detect any other proteins requiring a comparable complex regulation for release. This underscores the tight regulation of IL-1β and IL-18 activity, as they require hours to unfold their powerful inflammatory potential on neighboring cells or the whole organism. In contrast, a low MW and PM pore formation are sufficient for the release of most alarmins, which can be quickly released into the extracellular space and activate neighboring cells in a matter of minutes.

DISCUSSION

Activated macrophages control immune responses by releasing proteins, such as pro-inflammatory cytokines and alarmins. Variations in the secretory composition results in vastly different physiological responses of neighboring cells and the whole organism (Arango Duque and Descoteaux, 2014). We developed a generic and unbiased secretomics strategy based on pharmacological, genetic, and biochemical dissection of cellular protein release pathways. We applied it to analyze complex proinflammatory programs in macrophages upon activation of the following two major pathways of protein release: TLR4 activation and inflammasome-mediated pyroptotic cell death.

In addition to known cytokines and alarmins, we observed the unconventional release of thousands of proteins with diverse intracellular functions and localization during pyroptotic cell death. Our analytical framework facilitates the discovery of proteins released from sub-cellular organelles, including

(G) Organelle marker enrichment analysis of cell-lysis-independent unconventional release. Proteins significantly released upon NLRP3 activation in the presence of osmoprotection (LPS + Nl + 30 mM L-alanine/20 mM glycine versus LPS) were defined to be cell lysis independent. Significant proteins were determined with a parametric two-tailed Welch's t test (FDR < 0.05, $S_0 = 1$). Enrichment factors were calculated by Fisher's exact test as described previously (annotations with intersection sizes of >15 and $p < 0.002$ are shown). Category sizes are represented by balloon size.
(H) Boxplots indicating the fold changes of all detected proteins belonging to indicated organelles in the unconventional secretomes in the presence of glycine.
(I) Effect of osmoprotection on mitochondrial and lysosomal proteins of different MWs. Boxplots indicating the extent of inhibition by osmoprotection to unconventionally released mitochondrial and lysosomal proteins binned according to increasing MW.
(J) Swarm plots showing log2 fold change of proteins assigned to the indicated annotation released during osmoprotection of pyroptotic cells compared with TLR4 activated controls.
See also Figure S4 and Table S1.

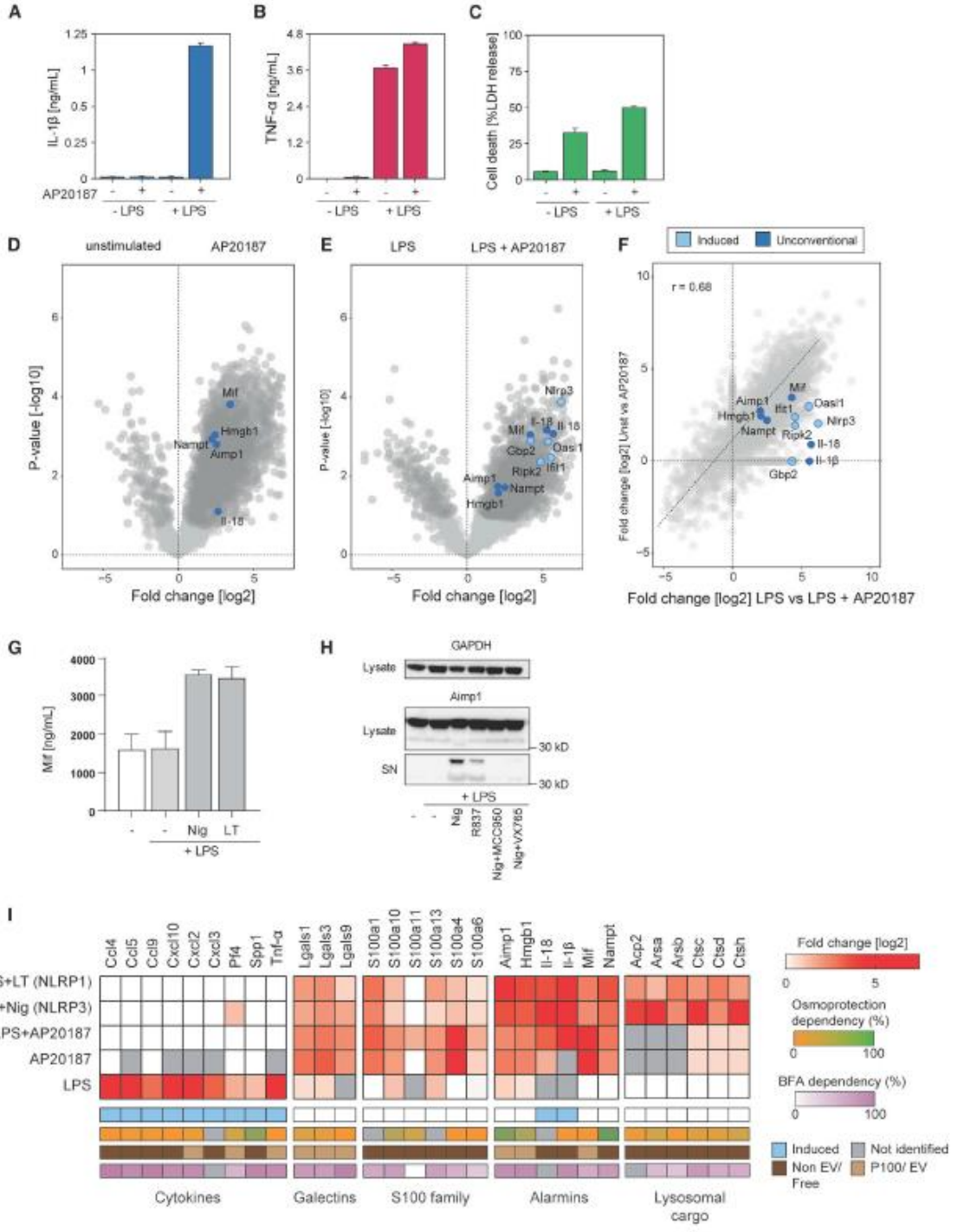

(legend on next page)

intracellular proteins with moonlighting or unexpected extracellular functions (Hernández et al., 2014; Jeffery, 1999). Conventional and unconventional secretory programs appear conserved across species based on the observed high correlation of mouse and human macrophage secretomes (Figure S4F).

We report that ER-Golgi disruption with BFA and GCA inhibits unconventional protein release and pyroptosis by interfering with inflammasome formation. Our data suggest that this effect is not only specific to NLRP3 as reported by Zhang et al. (2017) but also independent of the inflammasome sensor involved, although cell type and duration of BFA treatment affects cellular phenotypes. For example, IL-1β release was reported to be independent from the ER-Golgi compartment in LPS-treated human monocytes (Rubartelli et al., 1990). Moreover, long-term ER stress by BFA presumably activates the unconventional release of IL1β, whereas acute ER stress inhibits it (Bronner et al., 2015; Menu et al., 2012).

We show that EVs do not significantly contribute to cytokine and alarmin release during macrophage pyroptosis. It is interesting to speculate that incorporated or associated proteins might signal over longer durations and distances or upon intracellular release by membrane fusion with recipient cells.

We identified the presence of a large number of lysosomal cargo proteins, including many proteases, in the extracellular space during pyroptosis. Lysosomal proteases have been detected in the extracellular environment during various biological processes, including necroptosis and extensive TLR4 activation (Meissner et al., 2013; Mohamed and Sloane, 2006; Tanzer et al., 2020). Lysosomal exocytosis has been described as a membrane repair mechanism triggered by calcium influx (Bergsbaken et al., 2011; Tanzer et al., 2020). However, it remains unresolved how lysosomal content is released upon TLR4 activation in the absence of pore formation, PM damage, or cell death and whether this involves calcium fluxes. The presence of lysosomal proteases in the extracellular environment has been shown to play a role in tissue regeneration or tumor metastasis by remodeling the extracellular matrix (ECM) (Mohamed and Sloane, 2006; Olson and Joyce, 2015), and further studies should evaluate how these processes are affected by different forms of cell death.

Osmoprotection with the amino acids L-alanine and glycine has been described to delay pyroptotic cell lysis but not GSDMD pore formation in the PM. Under these conditions, protein release takes places through GSDMD pores only. Our data show that although cell lysis facilitates the unconventional release of the majority of proteins, the release of a subset of low-MW proteins, namely, cytokines/DAMPs including IL-1β, occurs independently of cell death by a GSDMD-dependent pathway, confirming previous reports (Evavold et al., 2018; Heilig et al., 2018). Some low-MW proteins, however, are retained in the cell due to osmoprotection. This may be explained by their physiological assembly into higher order structures or large protein complexes.

We show that lysosomal cargo and some mitochondrial proteins are released independently of cell lysis. The osmoprotection-independent extracellular presence of lysosomal lumen proteins with diverse MWs suggests an involvement of a vesicular release route. In contrast, the osmoprotection-sensitive release of both mitochondrial matrix and membrane proteins suggests that mitochondrial proteins enter the cytosol due to organellar damage upon inflammasome activation, followed by their exit along with cytosolic proteins by gasdermin pores. It will be interesting to elucidate the role of vesicular protein release from different cellular compartments during later stages of cell lysis, after pore formation.

PM repair mechanisms activated by membrane damage may further fine-tune paracrine programs by favoring the release of lysosomal cargo and small-MW proteins during sub-lytic inflammasome activation (Rühl et al., 2018).

Different forms of cell death use distinct mechanisms to control their paracrine programs. Pyroptosis is unique in its fast release of cDAMPs and slow release of pro-inflammatory cytokines IL-1β and IL-18. The execution of necroptosis, in contrast, is slower and accompanied by increased receptor shedding, which is not detected in pyroptosis, and decreased cytokine production. Whether distinct sets of proteins exit cells through GSDMD versus the necroptotic terminal effector-mixed lineage kinase domain-like (MLKL)-mediated PM perturbation remains to be determined (Petrie et al., 2017; Tanzer et al., 2020). Furthermore, the cell type specificity of protein exit mechanisms and accompanying paracrine programs are exciting topics for future investigations.

In conclusion, we have devised an MS-based experimental strategy to define the exit routes for each cellular protein. We demonstrated the utility of our approach by identifying multiple alarmins with known extracellular signaling capabilities to be released via cell-lysis-dependent and -independent pathways of pyroptosis. Our work serves as a valuable resource for the identification of proteins with as yet undescribed extracellular functions. Future studies should reveal how the differentially regulated sets of proteins direct paracrine immune responses under inflammatory conditions involving inflammasomes.

Figure 7. Dissection of constitutively expressed versus TLR-activation-induced cytokines and DAMPs

(A–C) Release of TNF-α (A) and IL-1β (B) as measured by ELISA or LDH (C) from supernatants of Caspase 1/11 DKO immortalized murine macrophages expressing an engineered caspase-1 system (Casp1ΔCard-FKBP), allowing its controlled dimerization, activation, and pyroptosis by AP20187 (AP) in the presence or absence of TLR4 and AP20187 activation. Data are represented as mean ± SD of three biological replicates.

(D and E) Volcano plots showing secreted proteins from differentially activated engineered Casp1ΔCard-FKBP-expressing cells. Pairwise secretome comparisons are shown between untreated and AP20187-activated cells to define constitutively released DAMPs and cytokines (D) TLR4 or TLR4 and AP20187-activated cells (E) to define differentially released cytokines and DAMPs that require induction by TLR4 signaling.

(F) Scatterplot of fold changes of released proteins between untreated and AP20187-activated cells versus TLR4 or TLR4 and AP20187-activated cells. Conventionally and unconventionally released cytokines are indicated by red and blue circles, respectively.

(G and H) Quantification of pyroptotic release of MIF (G) and Aimp1 (H) by ELISA and western blot, respectively.

(I) Heatmap of indicated conventionally secreted cytokines and pyroptotically released cDAMPs and iDAMPs or cytokines with mode of release as soluble or vesicle associated; osmoprotection or BFA dependency are indicated with the respective color coding.

See also Figures S1, S4, and S7 and Table S1.

STAR★METHODS

Detailed methods are provided in the online version of this paper and include the following:

- KEY RESOURCES TABLE
- RESOURCE AVAILABILITY
  - Lead contact
  - Materials availability
  - Data and code availability
- EXPERIMENTAL MODEL AND SUBJECT DETAILS
- METHOD DETAILS
  - Isolation and culture of murine bone marrow-derived macrophages
  - Generation of human monocyte-derived macrophages
  - Activation of BMDMs and human macrophages
  - Generation of cell lysates
  - Caspase 1 activity and cytotoxicity (LDH) assays
  - Enzyme-linked immunosorbent assay (ELISA)
  - Western blot
  - Immunostaining and fluorescent microscopy
  - P100 fraction/Extracellular vesicle isolation
  - Sample preparation for mass spectrometry
  - LC-MS/MS
- QUANTIFICATION AND STATISTICAL ANALYSIS
  - LC-MS/MS data analysis
  - Data preparation, quality control, and copy number estimation
  - Bioinformatics analysis of protein secretion signatures and receptor shedding

SUPPLEMENTAL INFORMATION

Supplemental information can be found online at https://doi.org/10.1016/j.celrep.2021.108826.

ACKNOWLEDGMENTS

We thank Matthias Mann for providing LC-MS/MS infrastructure and support. We thank Steven Dewitz, Korbinian Mayr, Mario Oroshi, Igor Paron, Christian Delmi, Bianca Splettstoesser, and Gaby Sowa for excellent technical assistance. Light microscopy was performed in the MPIB Imaging Facility. We thank Petr Broz for the GSDMD KO and Casp1/11 DKO Casp1ΔCard-FKBP iBMDMs. We thank all members of the Meissner, Zychlinsky, and Mann groups for helpful discussions. This work was funded by the Max Planck Society for the Advancement of Science and the Deutsche Forschungsgemeinschaft (DFG, German Research Foundation) project-IDs 165054336 (SFB 914), 360372040 (SFB 1335), and 408885537 (TRR 274). One or more of the authors of this paper self-identifies as a member of the LGBTQ+ community. The author list of this paper includes contributors from the location where the research was conducted who participated in the data collection, design, analysis, and/or interpretation of the work.

AUTHOR CONTRIBUTIONS

F.M. conceived the study. K.P. and F.M. designed experiments. K.P. performed experiments with help from S.E. and J.J.S. L.I.K. contributed experiments and analyses to Figures 1, 3, and S1–S4. K.P. analyzed data with suggestions from F.M. A.F. performed the receptor shedding analysis. K.P. and F.M. interpreted the data and wrote the manuscript.

DECLARATION OF INTERESTS

The authors declare no competing interests.

Received: July 24, 2020
Revised: November 25, 2020
Accepted: February 16, 2021
Published: March 9, 2021

REFERENCES

Aebersold, R., and Mann, M. (2016). Mass-spectrometric exploration of proteome structure and function. Nature *537*, 347–355.

Andrei, C., Dazzi, C., Lotti, L., Torrisi, M.R., Chimini, G., and Rubartelli, A. (1999). The secretory route of the leaderless protein interleukin 1beta involves exocytosis of endolysosome-related vesicles. Mol. Biol. Cell *10*, 1463–1475.

Arango Duque, G., and Descoteaux, A. (2014). Macrophage cytokines: involvement in immunity and infectious diseases. Front. Immunol. *5*, 491.

Baroja-Mazo, A., Compan, V., Martín-Sánchez, F., Tapia-Abellán, A., Couillin, I., and Pelegrín, P. (2019). Early endosome autoantigen 1 regulates IL-1β release upon caspase-1 activation independently of gasdermin D membrane permeabilization. Sci. Rep. *9*, 5788.

Bergsbaken, T., Fink, S.L., and Cookson, B.T. (2009). Pyroptosis: host cell death and inflammation. Nat. Rev. Microbiol. *7*, 99–109.

Bergsbaken, T., Fink, S.L., den Hartigh, A.B., Loomis, W.P., and Cookson, B.T. (2011). Coordinated host responses during pyroptosis: caspase-1-dependent lysosome exocytosis and inflammatory cytokine maturation. J. Immunol. *187*, 2748–2754.

Boucher, D., Monteleone, M., Coll, R.C., Chen, K.W., Ross, C.M., Teo, J.L., Gomez, G.A., Holley, C.L., Bierschenk, D., Stacey, K.J., et al. (2018). Caspase-1 self-cleavage is an intrinsic mechanism to terminate inflammasome activity. J. Exp. Med. *215*, 827–840.

Bronner, D.N., Abuaita, B.H., Chen, X., Fitzgerald, K.A., Nuñez, G., He, Y., Yin, X.M., and O'Riordan, M.X. (2015). Endoplasmic Reticulum Stress Activates the Inflammasome via NLRP3- and Caspase-2-Driven Mitochondrial Damage. Immunity *43*, 451–462.

Brough, D., Pelegrin, P., and Nickel, W. (2017). An emerging case for membrane pore formation as a common mechanism for the unconventional secretion of FGF2 and IL-1β. J. Cell Sci. *130*, 3197–3202.

Broz, P., and Dixit, V.M. (2016). Inflammasomes: mechanism of assembly, regulation and signalling. Nat. Rev. Immunol. *16*, 407–420.

Cai, Z., Zhang, A., Choksi, S., Li, W., Li, T., Zhang, X.M., and Liu, Z.G. (2016). Activation of cell-surface proteases promotes necroptosis, inflammation and cell migration. Cell Res. *26*, 886–900.

Chardin, P., and McCormick, F. (1999). Brefeldin A: the advantage of being uncompetitive. Cell *97*, 153–155.

Cox, J., and Mann, M. (2008). MaxQuant enables high peptide identification rates, individualized p.p.b.-range mass accuracies and proteome-wide protein quantification. Nat. Biotechnol. *26*, 1367–1372.

Cox, J., Neuhauser, N., Michalski, A., Scheltema, R.A., Olsen, J.V., and Mann, M. (2011). Andromeda: a peptide search engine integrated into the MaxQuant environment. J. Proteome Res. *10*, 1794–1805.

Cox, J., Hein, M.Y., Luber, C.A., Paron, I., Nagaraj, N., and Mann, M. (2014). Accurate proteome-wide label-free quantification by delayed normalization and maximal peptide ratio extraction, termed MaxLFQ. Mol. Cell. Proteomics *13*, 2513–2526.

Cypryk, W., Nyman, T.A., and Matikainen, S. (2018). From Inflammasome to Exosome-Does Extracellular Vesicle Secretion Constitute an Inflammasome-Dependent Immune Response? Front. Immunol. *9*, 2188.

Ding, J., Wang, K., Liu, W., She, Y., Sun, Q., Shi, J., Sun, H., Wang, D.C., and Shao, F. (2016). Pore-forming activity and structural autoinhibition of the gasdermin family. Nature *535*, 111–116.

DiPeso, L., Ji, D.X., Vance, R.E., and Price, J.V. (2017). Cell death and cell lysis are separable events during pyroptosis. Cell Death Discov. *3*, 17070.

Dupont, N., Jiang, S., Pilli, M., Ornatowski, W., Bhattacharya, D., and Deretic, V. (2011). Autophagy-based unconventional secretory pathway for extracellular delivery of IL-1β. EMBO J. *30*, 4701–4711.

Evavold, C.L., Ruan, J., Tan, Y., Xia, S., Wu, H., and Kagan, J.C. (2018). The Pore-Forming Protein Gasdermin D Regulates Interleukin-1 Secretion from Living Macrophages. Immunity *48*, 35–44.e6.

Fink, S.L., and Cookson, B.T. (2006). Caspase-1-dependent pore formation during pyroptosis leads to osmotic lysis of infected host macrophages. Cell. Microbiol. *8*, 1812–1825.

Finn, R.D., Coggill, P., Eberhardt, R.Y., Eddy, S.R., Mistry, J., Mitchell, A.L., Potter, S.C., Punta, M., Qureshi, M., Sangrador-Vegas, A., et al. (2016). The Pfam protein families database: towards a more sustainable future. Nucleic Acids Res. *44*, D279–D285.

Gong, T., Liu, L., Jiang, W., and Zhou, R. (2020). DAMP-sensing receptors in sterile inflammation and inflammatory diseases. Nat. Rev. Immunol. *20*, 95–112.

Heilig, R., Dick, M.S., Sborgi, L., Meunier, E., Hiller, S., and Broz, P. (2018). The Gasdermin-D pore acts as a conduit for IL-1β secretion in mice. Eur. J. Immunol. *48*, 584–592.

Hernández, S., Ferragut, G., Amela, I., Perez-Pons, J., Piñol, J., Mozo-Villarias, A., Cedano, J., and Querol, E. (2014). MultitaskProtDB: a database of multitasking proteins. Nucleic Acids Res. *42*, D517–D520.

Jeffery, C.J. (1999). Moonlighting proteins. Trends Biochem. Sci. *24*, 8–11.

Kaisho, T., and Akira, S. (2000). Critical roles of Toll-like receptors in host defense. Crit. Rev. Immunol. *20*, 393–405.

Kayagaki, N., Stowe, I.B., Lee, B.L., O'Rourke, K., Anderson, K., Warming, S., Cuellar, T., Haley, B., Roose-Girma, M., Phung, Q.T., et al. (2015). Caspase-11 cleaves gasdermin D for non-canonical inflammasome signalling. Nature *526*, 666–671.

Kayagaki, N., Warming, S., Lamkanfi, M., Walle, L.V., Louie, S., Dong, J., Newton, K., Qu, Y., Liu, J., Heldens, S., et al. (2011). Non-canonical inflammasome activation targets caspase-11. Nature *479*, 117–121.

Kelstrup, C.D., Bekker-Jensen, D.B., Arrey, T.N., Hogrebe, A., Harder, A., and Olsen, J.V. (2018). Performance Evaluation of the Q Exactive HF-X for Shotgun Proteomics. J. Proteome Res. *17*, 727–738.

Lamkanfi, M., Sarkar, A., Vande Walle, L., Vitari, A.C., Amer, A.O., Wewers, M.D., Tracey, K.J., Kanneganti, T.-D., and Dixit, V.M. (2010). Inflammasome-dependent release of the alarmin HMGB1 in endotoxemia. J. Immunol. *185*, 4385–4392.

Lammert, C.R., Frost, E.L., Bellinger, C.E., Bolte, A.C., McKee, C.A., Hurt, M.E., Paysour, M.J., Ennerfelt, H.E., and Lukens, J.R. (2020). AIM2 inflammasome surveillance of DNA damage shapes neurodevelopment. Nature *580*, 647–652.

Larance, M., and Lamond, A.I. (2015). Multidimensional proteomics for cell biology. Nat. Rev. Mol. Cell Biol. *16*, 269–280.

Liu, X., Zhang, Z., Ruan, J., Pan, Y., Magupalli, V.G., Wu, H., and Lieberman, J. (2016). Inflammasome-activated gasdermin D causes pyroptosis by forming membrane pores. Nature *535*, 153–158.

Lobb, R.J., Becker, M., Wen, S.W., Wong, C.S., Wiegmans, A.P., Leimgruber, A., and Möller, A. (2015). Optimized exosome isolation protocol for cell culture supernatant and human plasma. J. Extracell. Vesicles *4*, 27031.

Loomis, W.P., den Hartigh, A.B., Cookson, B.T., and Fink, S.L. (2019). Diverse small molecules prevent macrophage lysis during pyroptosis. Cell Death Dis. *10*, 326.

Lopez-Castejon, G., and Brough, D. (2011). Understanding the mechanism of IL-1β secretion. Cytokine Growth Factor Rev. *22*, 189–195.

MacCorkle, R.A., Freeman, K.W., and Spencer, D.M. (1998). Synthetic activation of caspases: artificial death switches. Proc. Natl. Acad. Sci. USA *95*, 3655–3660.

Marshall, J.D., Aste-Amézaga, M., Chehimi, S.S., Murphy, M., Olsen, H., and Trinchieri, G. (1999). Regulation of human IL-18 mRNA expression. Clin. Immunol. *90*, 15–21.

Martín-Sánchez, F., Diamond, C., Zeitler, M., Gomez, A.I., Baroja-Mazo, A., Bagnall, J., Spiller, D., White, M., Daniels, M.J.D., Mortellaro, A., et al. (2016). Inflammasome-dependent IL-1β release depends upon membrane permeabilisation. Cell Death Differ. *23*, 1219–1231.

Meissner, F., Scheltema, R.A., Mollenkopf, H.J., and Mann, M. (2013). Direct proteomic quantification of the secretome of activated immune cells. Science *340*, 475–478.

Menu, P., Mayor, A., Zhou, R., Tardivel, A., Ichijo, H., Mori, K., and Tschopp, J. (2012). ER stress activates the NLRP3 inflammasome via an UPR-independent pathway. Cell Death Dis. *3*, e261.

Mitchell, P.S., Sandstrom, A., and Vance, R.E. (2019). The NLRP1 inflammasome: new mechanistic insights and unresolved mysteries. Curr. Opin. Immunol. *60*, 37–45.

Mohamed, M.M., and Sloane, B.F. (2006). Cysteine cathepsins: multifunctional enzymes in cancer. Nat. Rev. Cancer *6*, 764–775.

Monteleone, M., Stow, J.L., and Schroder, K. (2015). Mechanisms of unconventional secretion of IL-1 family cytokines. Cytokine *74*, 213–218.

Nagaraj, N., Kulak, N.A., Cox, J., Neuhauser, N., Mayr, K., Hoerning, O., Vorm, O., and Mann, M. (2012). System-wide perturbation analysis with nearly complete coverage of the yeast proteome by single-shot ultra HPLC runs on a bench top Orbitrap. Mol. Cell Proteomics *11*, M111.013722.

Ng, F., and Tang, B.L. (2016). Unconventional Protein Secretion in Animal Cells. Unconventional Protein Secretion (Springer New York), pp. 31–46.

Nickel, W., and Rabouille, C. (2009). Mechanisms of regulated unconventional protein secretion. Nat. Rev. Mol. Cell Biol. *10*, 148–155.

Olson, O.C., and Joyce, J.A. (2015). Cysteine cathepsin proteases: regulators of cancer progression and therapeutic response. Nat. Rev. Cancer *15*, 712–729.

Petrie, E.J., Hildebrand, J.M., and Murphy, J.M. (2017). Insane in the membrane: a structural perspective of MLKL function in necroptosis. Immunol. Cell Biol. *95*, 152–159.

Rathkey, J.K., Zhao, J., Liu, Z., Chen, Y., Yang, J., Kondolf, H.C., Benson, B.L., Chirieleison, S.M., Huang, A.Y., Dubyak, G.R., et al. (2018). Chemical disruption of the pyroptotic pore-forming protein gasdermin D inhibits inflammatory cell death and sepsis. Sci. Immunol. *3*, eaat2738.

Rieckmann, J.C., Geiger, R., Hornburg, D., Wolf, T., Kveler, K., Jarrossay, D., Sallusto, F., Shen-Orr, S.S., Lanzavecchia, A., Mann, M., and Meissner, F. (2017). Social network architecture of human immune cells unveiled by quantitative proteomics. Nat. Immunol. *18*, 583–593.

Rubartelli, A., Cozzolino, F., Talio, M., and Sitia, R. (1990). A novel secretory pathway for interleukin-1 beta, a protein lacking a signal sequence. EMBO J. *9*, 1503–1510.

Rühl, S., Shkarina, K., Demarco, B., Heilig, R., Santos, J.C., and Broz, P. (2018). ESCRT-dependent membrane repair negatively regulates pyroptosis downstream of GSDMD activation. Science *362*, 956–960.

Sáenz, J.B., Sun, W.J., Chang, J.W., Li, J., Bursulaya, B., Gray, N.S., and Haslam, D.B. (2009). Golgicide A reveals essential roles for GBF1 in Golgi assembly and function. Nat. Chem. Biol. *5*, 157–165.

Scheltema, R.A., and Mann, M. (2012). SprayQc: a real-time LC-MS/MS quality monitoring system to maximize uptime using off the shelf components. J. Proteome Res. *11*, 3458–3466.

Scheltema, R.A., Hauschild, J.-P., Lange, O., Hornburg, D., Denisov, E., Damoc, E., Kuehn, A., Makarov, A., and Mann, M. (2014). The Q Exactive HF, a Benchtop mass spectrometer with a pre-filter, high-performance quadrupole and an ultra-high-field Orbitrap analyzer. Mol. Cell. Proteomics *13*, 3698–3708.

Stow, J.L., Low, P.C., Offenhäuser, C., and Sangermani, D. (2009). Cytokine secretion in macrophages and other cells: pathways and mediators. Immunobiology *214*, 601–612.

Stutz, A., Horvath, G.L., Monks, B.G., and Latz, E. (2013). ASC speck formation as a readout for inflammasome activation. Methods Mol. Biol. *1040*, 91–101.

Swanson, K.V., Deng, M., and Ting, J.P.Y. (2019). The NLRP3 inflammasome: molecular activation and regulation to therapeutics. Nat. Rev. Immunol. *19*, 477–489.

Tanzer, M.C., Frauenstein, A., Stafford, C.A., Phulphagar, K., Mann, M., and Meissner, F. (2020). Quantitative and Dynamic Catalogs of Proteins Released during Apoptotic and Necroptotic Cell Death. Cell Rep. *30*, 1260–1270.e5.

Tapia, V.S., Daniels, M.J.D., Palazón-Riquelme, P., Dewhurst, M., Luheshi, N.M., Rivers-Auty, J., Green, J., Redondo-Castro, E., Kaldis, P., Lopez-Castejon, G., and Brough, D. (2019). The three cytokines IL-1β, IL-18, and IL-1α share related but distinct secretory routes. J. Biol. Chem. *294*, 8325–8335.

Tusher, V.G., Tibshirani, R., and Chu, G. (2001). Significance analysis of microarrays applied to the ionizing radiation response. Proc. Natl. Acad. Sci. USA *98*, 5116–5121.

Tyanova, S., Temu, T., Sinitcyn, P., Carlson, A., Hein, M.Y., Geiger, T., Mann, M., and Cox, J. (2016). The Perseus computational platform for comprehensive analysis of (prote)omics data. Nat. Methods *13*, 731–740.

Weischenfeldt, J., and Porse, B. (2008). Bone Marrow-Derived Macrophages (BMM): Isolation and Applications. CSH Protoc. *2008*, pdb.prot5080-pdb.prot5080.

Yatim, N., Cullen, S., and Albert, M.L. (2017). Dying cells actively regulate adaptive immune responses. Nat. Rev. Immunol. *17*, 262–275.

Zhang, M., Kenny, S.J., Ge, L., Xu, K., and Schekman, R. (2015). Translocation of interleukin-1β into a vesicle intermediate in autophagy-mediated secretion. eLife *4*, e11205.

Zhang, Z., Meszaros, G., He, W.T., Xu, Y., de Fatima Magliarelli, H., Mailly, L., Mihlan, M., Liu, Y., Puig Gámez, M., Goginashvili, A., et al. (2017). Protein kinase D at the Golgi controls NLRP3 inflammasome activation. J. Exp. Med. *214*, 2671–2693.

STAR★METHODS

KEY RESOURCES TABLE

REAGENT or RESOURCE	SOURCE	IDENTIFIER
Antibodies		
Anti-mouse Aimp1	Novus Biologicals	Cat#NBP2-27206SS
Anti-GAPDH	Cell Signaling Technology	Cat#8884s; RRID: AB_11129865
Anti-PDI	Cell Signaling Technology	Cat#3501; RRID: AB_2156433
Anti-Rcas1	Cell Signaling Technology	Cat#12290; RRID: AB_2736985
Anti-Ctsb	Cell Signaling Technology	Cat#31718; RRID: AB_2687580
Anti-β-Actin	Cell Signaling Technology	Cat#8457; RRID: AB_10950489
Anti-Vamp8	Cell Signaling Technology	Cat#13060; RRID: AB_2798103
Anti-Lamp1	Cell Signaling Technology	Cat#3243; RRID: AB_2134478
Anti-Asc	Sigma-Aldrich	04-147; RRID: AB_1977033
F(ab')2-AF647	Thermo Fisher Scientific	A21237; AB_1500743
HRP-linked anti mouse IgG	Cyvita	Cat#NXA931; RRID: AB_772209
HRP-linked anti rabbit IgG	Cyvita	Cat#NA934; RRID: AB_772206
Biological samples		
Buffy Coats	Blood donations to the red cross	"Blutspendedienst des Bayerischen Roten Kreuzes gemeinnützige GmbH"
Chemicals, peptides, and recombinant proteins		
Lipopolysaccharide (LPS) from Salmonella typhimurium S-form	Enzo Life Sciences	ALX-581-013-L002
Nigericin sodium salt from Streptomyces hygroscopicus	Thermo Fisher Scientific	N1495
Adenosine 5′-triphosphate disodium salt hydrate (ATP)	Sigma	Cat#7699
Lethal factor	List Biologicals	Cat#172B
Protective antigen	List Biologicals	Cat#171E
AP20187/B/B homodimerizor	Takara Biotech	Cat#635058
Brefeldin A	Cell Signaling Technology	Cat#9972
Golgicide A	Sigma-Aldrich	G0923
Glybenclamide/Glyburide	Novus Biologicals	Cat#NBP2-30141
Draq5	Thermo Fisher Scientific	Cat#62252
L-Alanine	Sigma-Aldrich	A7469
Glycine	Sigma-Aldrich	G7126
hM-CSF	Cell Signaling Technology	Cat#8929LC
Red blood cell lysis buffer	Sigma-Aldrich	R7757
Histopaque-1077	Sigma-Aldrich	10771
Heat inactivated Fetal Bovine Serum	Invitrogen	10270106
Penicillin/Streptomycin	Invitrogen	15140122
RPMI medium	Invitrogen	61870044
DME medium	Invitrogen	31966047
Phenol red free DMEM	Thermo Fisher Scientific	31053044
Urea	Sigma	45128-500 g
Thiourea	Sigma	T8656-500 g
Trizma	Sigma	T1503-1kg
Dithiothreitol (DTT)	Sigma	D0632-100 g

(Continued on next page)

Continued

REAGENT or RESOURCE	SOURCE	IDENTIFIER
Chloroacetamide (CAA)	Sigma	C0267-100 g
Iodoacetamide (IAA)	Sigma	I6125-100 g
Ammonium bicarbonate	Sigma	A6141
Trypsin	Sigma	T6567-1mg
Lys-C	Wako Chemicals	Cat#129-02541
DMSO	Sigma	D2650-100ml
Acetone	Fisher Chemical	Cat#67-64-1
Acetonitrile	VWR	Cat#20048320
Trifluoroacetic acid	Merck	Cat#8082600100
Formic acid	Merck	Cat#1002641000
PBS	GIBCO	Cat#14190-094
Tween	Acros	Cat#233360010
EDTA	Sigma	03677-500 g
BSA	Serva	Cat#11930.03
Glycerol	Sigma	G5516-1L
Sodium dodecyl sulfate (SDS)	Roth	Cat#CN30.3
Sodium deoxycholate (SDC)	Sigma	30970-100 g
Sodium chloride (NaCl)	VWR	Cat#27810.295
NuPAGE LDS Sample Buffer (4x)	Invitrogen	NP0007
Puromycin	Invivogen	Ant-pr-5
Critical commercial assays		
CytoTox 96 Non-Radioactive Cytotoxicity Assay	Promega	G1780
Human Tnf ELISA kit	R&D Systems	Cat#DY210
Human IL1b ELISA kit	R&D Systems	Cat#DY201
Mouse Tnf ELISA kit	R&D Systems	Cat#DY410
Mouse IL1b ELISA kit	R&D Systems	Cat#DY401
Mouse Mif ELISA kit	R&D Systems	Cat#DY1978
Caspase-Glo® 1 Inflammasome Assay	Promega	G9951
Human Monocyte Isolation Kit II	Miltenyi Biotec	Cat#130-091-153
Deposited data		
Raw Mass Spectrometry Data Files	This paper	ProteomeXchange Consortium via the PRIDE partner repository, with the dataset identifier PXD018659
Experimental models: organisms/strains		
C57BL/6J wild type mice (WT)	The Jackson Laboratory	Cat#000664
Casp1/11 DKO, strain B6.129S2-Casp1tm1SeshCasp11del/J	BASF	N/A
129S4/SvJae	The Jackson Laboratory	Cat#009104
Experimental models: cell lines		
GSDMD –/– iBMDMs	Dr. Petr Broz	Heilig et al., 2018
Casp1/11 DKO iBMDMs reconstituted with Casp1ΔCard-FKBP	Dr. Petr Broz	Boucher et al., 2018
L929 cells	ATCC	ATCC CCL-1
Software and algorithms		
MaxQuant	Cox and Mann, 2008; Version 1.5.0.38	https://www.biochem.mpg.de/5111795/maxquant
Perseus	Tyanova et al., 2016; Version 1.5.3.0	https://www.biochem.mpg.de/5111810/perseus

(*Continued on next page*)

Continued

REAGENT or RESOURCE	SOURCE	IDENTIFIER
XCalibur	Thermo Scientific	https://www.thermofisher.com/order/catalog/product/OPTON-30487
R	N/A	https://www.r-project.org/
ImageJ	N/A	https://imagej.nih.gov/ij/
Adobe Illustrator	N/A	https://www.adobe.com/de/products/illustrator.html
PRIDE	N/A	https://www.ebi.ac.uk/pride/archive/

RESOURCE AVAILABILITY

Lead contact

Further information and requests for resources should be directed to and will be fulfilled by the Lead Contact, Felix Meissner (meissner@biochem.mpg.de).

Materials availability

This study did not generate new unique materials and reagents.

Data and code availability

The datasets generated in this study are available via ProteomeXchange with identifier PXD018659.

EXPERIMENTAL MODEL AND SUBJECT DETAILS

Experiments described in this study are performed with the mouse and human primary macrophages or immortalized mouse macrophages.

C57BL/6J wild-type mice (WT) and 129S4/SvJae mice (WT) were obtained from The Jackson Laboratory. Caspase-1/11 double knockout mice (Casp1/11 DKO, strain B6.129S2-Casp1^{tm1Sesh}Casp11^{del}/J) were kindly provided by BASF. This strain was originally generated as Casp1 deficient mice but is effectively Casp1/11 double deficient due to an additional mutation in the Casp11 gene locus in the 129S2 background used for ES cell generation (Kayagaki et al., 2011). Both mouse strains were housed under specific-pathogen-free (SPF) conditions on a 12-hour light/dark cycle in the animal facility of the Max Planck Institute for Infection Biology OR Biochemistry. 10-12 week old male mice were sacrificed by cervical dislocation and directly used for bone marrow-derived macrophage preparation. Animal experiments were performed according to the German Animal Protection Law.

Human primary macrophages were generated by isolating PBMCs from buffy coats (generated from blood donations to the Red Cross or Blutspendedienst des Bayerischen Roten Kreuzes gemeinnützige GmbH) using Histopaque-1077 (Sigma-Aldrich, 10771). Gender or age of donors is not disclosed by the Red Cross. Monocytes were isolated using a monocyte isolation kit (Miltenyi Biotec, 130-091-153). Immortalized GSDMD KO and Casp1/11 DKO iBMDMs reconstituted with Casp1ΔCard-FKBP were a kind gift from Petr Broz (Boucher et al., 2018; Heilig et al., 2018).

METHOD DETAILS

Isolation and culture of murine bone marrow-derived macrophages

Bone marrow-derived macrophages (BMDMs) were prepared as described elsewhere (Weischenfeldt and Porse, 2008). In brief, bone marrow was collected from the femurs and tibiae of 8-12 weeks old male mice and filtered through a 70 μm nylon mesh filter. 5×10^6 to 1×10^7 bone marrow cells were plated on sterile, non-tissue culture treated Petri plates for a period of 7 days in macrophage differentiation medium DMEM supplemented with 10% (v/v) FCS and 20% (v/v) M-CSF-containing medium. Medium was replenished on day 3 of culture. M-CSF-conditioned medium was collected from L-929 cells. Cells were lifted from plates by incubating in cold PBS and re-plated for experiments.

Immortalized Casp1/11 DKO BMDMs reconstituted with Casp1ΔCard-FKBP were cultured in macrophage differentiation medium supplemented with 10ug/ml Puromycin.

Generation of human monocyte-derived macrophages

Blood was drawn with S-Monovette 9ml K2E-Gel (#02.1333.001, Sarstedt) from healthy volunteers according to the WMA Declaration of Helsinki and the Department of Health and Human Services Belmont Report. Donors provided informed consent and all samples were collected with approval from the ethics committee. Blood was diluted 1:1 with PBS and centrifuged over Histopaque-1077 (#10771, Sigma) at 400 g for 40 min. After centrifugation, the peripheral blood mononuclear cell (PBMC) fraction was

collected and washed three times with PBS followed by centrifugation at 200 g for 15 min to remove platelets. Red blood cells were lysed with RBC lysis buffer (Sigma) for 3 min. PBMCs were washed again with PBS supplemented with 0.5% (w/v) bovine serum albumin (BSA) and 2 mM EDTA. Monocytes were isolated by negative selection using the human Monocyte Isolation Kit II (#130-091-153, Miltenyi Biotec) according to the manufacturer's instructions. For the generation of macrophages, 2×10^7 isolated monocytes were plated on sterile, non-tissue culture treated Petri plates for a period of 7 days in RPMI 1640 supplemented with 10% (v/v) FCS, and 50 ng/mL human M-CSF (#8929LC, Cell Signaling). Medium was refreshed on day 3 of culture. On day 7, cells were lifted from plates by incubating in cold PBS and re-plated for experiments.

Activation of BMDMs and human macrophages

All cells were grown, maintained and activated at 37°C and 5% CO_2 in a water-jacketed incubator. 1×10^6 WT or *Casp1/11* DKO murine macrophages were plated per 12-well in DMEM, 10% (v/v) FCS (DMEM complete medium) one day prior to stimulation. All BMDMs were primed with 200 ng/mL LPS from *Salmonella* Typhimurium for 2 h or left untreated and subsequently washed three times with serum- and phenol red-free DMEM supplemented with 2 mM L-glutamine (DMEM minimal medium). For the time course experiment (Dataset 1), cells were preincubated with 0 or 100 μM glyburide (#NBP2-30141, Novus Biologicals) for 15-30min before 2 mM ATP (#7699, Sigma) or 10 μM nigericin (N1495, Invitrogen) were added for 15, 30, 45, and 60 min. Lethal factor and protective antigen were added at 1ug/ml. To inhibit conventional protein secretion (Dataset 3), 0-2 μg/mL brefeldin A were added for the last 15-30 min of priming. After washing 0-2ug/ml BFA along with 5 mM ATP or 15 μM nigericin were added for 30-45 min. For osmoprotection experiments (Dataset 2), cells were incubated with 20-30mM L-alanine or Glycine in DMEM minimal medium for 1 h after priming and washing, before 5 mM ATP or 15 μM nigericin were added for 30-45 min. AP20187 was added at 100nM for 160min.

Human macrophages (Datasets 5 and 6) were seeded at a density of 1×10^6 cells per 12-well in RPMI 1640 containing 10% (v/v) FCS, 2 mM L-glutamine, MEM NEAA, 100 U/mL penicillin, 100 μg/mL streptomycin (RPMI complete medium) one day before activation. Cells were primed with 200 ng/mL LPS for 2 h in complete medium. 1 μg/mL Brefeldin A was added for the last 30 min of priming before cells were washed three times with serum- and phenol red-free RPMI 1640 supplemented with 2 mM HEPES and 2 mM L-glutamine (RPMI minimal medium). After washing, cells were incubated with 1 μg/mL brefeldin A and 2 mM ATP or 10 μM nigericin for 30-45 min.

All activation experiments were performed in three technical replicates. Cell supernatants were centrifuged at 400 g for 5 min or sterile filtered to remove cell debris and directly used for LDH assay or stored at −80°C until ELISA and sample preparation. After removal of supernatants, untreated and LPS treated samples were used for the generation of total cell lysates (Datasets 4 and 6).

Generation of cell lysates

To generate total lysates for mass spectrometry, cells were washed with PBS and resuspended in 8 M urea in 40 mM HEPES pH 8 and frozen at −80°C until sample preparation.

Caspase 1 activity and cytotoxicity (LDH) assays

Caspase 1 activity was measured using the Caspase-Glo® 1 Inflammasome Assay as per the manufacturer's instructions. Cell death was measured by means of lactate dehydrogenase (LDH) release into the cell supernatant using the CytoTox 96 Non-Radioactive Cytotoxicity Assay (#G1780, Promega). In brief, 50 μL cell supernatant were incubated with 50 μL LDH substrate and incubated in the dark at 37°C for 15 to 30 min. The enzymatic reaction was stopped by adding 50 μL stop solution. Whole cell lysates generated from unstimulated cells incubated with medium supplemented with 1.2% (v/v) Triton X-100 for 30 min served as a reference for maximal cell death. Cell death was calculated as follows: (LDH release/LDH whole cell lysate) × 100.

Enzyme-linked immunosorbent assay (ELISA)

Human and mouse IL-1β, TNF-α and MIF in cell supernatants were measured with ELISA Kits purchased from R and D Systems (#DY201, #DY401, #DY210, #DY410, #DY1978) according to the manufacturer's instructions.

Western blot

Samples were prepared by lysing cells in lysis buffer (1% Triton X-100, 50mM Tris-Hcl pH 7.5, 150mM NaCl. Nuclei were removed by centrifugation (10 min, 1000 × g). Proteins from cell supernatants were precipitated with acetone (final concentration 80%) o/n at −20C. Protein pellets obtained after centrifugation at 3900 x g were solubilized in 2% SDS, 50mM Tris-HCl pH 7.5. Protein concentration was normalized after measurement with a bicinchoninic acid assay (BCA; Thermo Fisher Scientific). Samples were reduced and denatured by adding NuPAGE LDS Sample Buffer (4 ×) and NuPAGE Sample Reducing Agent (10 ×) (both from Thermo Fisher) and heating at 85 °C for 10 min. Proteins were separated by 4%–12% SDS-PAGE in precast gels (Novex; Invitrogen) with MOPS buffer (Novex; Invitrogen). Proteins were transferred onto Immobilon-FL PVDF membranes (Millipore) and nonspecific binding was blocked with 5% non-fat milk in Tris-buffered saline with 0.1% Tween-20 (TBST) for 1 h, followed by overnight incubation with specific primary antibodies in 5% BSA in TBST as per the manufacturer's instructions.

The following primary antibodies were used: PDI (1:1000, CST #3501), Rcas1 (1:1000, CST #12290), Ctsb (1:1000, CST #31718), β-Actin (1:1000, CST #8457), IL-1β (R and D systems, #DY401 ELISA detection antibody 1:50), Aimp1 (NBP2-27206SS), Gapdh (1:1000, CST #8884s), Vamp8 (1:100, CST #13060), Lamp1 (1:100, CST #3243). Membranes were washed 3X and incubated in

HRP linked anti-mouse (Cytiva #NXA931) or rabbit IgG antibodies (Cytiva #NA934) in 5% BSA in TBS-T for 1 h at room temperature (RT) followed by washing 3X in TBS-T

Immunostaining and fluorescent microscopy

BMDMs were fixed with 4% formaldehyde and stained for ASC (Millipore 2EI-7, Thermo Fisher F(ab')2-AF647) as per the manufacturer's instructions. Nuclei were counterstained using Draq5. Microscopy was performed in the MPIB imaging facility. Cells were imaged using a GE Deltavision Elite (Cytiva Life Sciences) epifluorescence microscope. Images were quantified as described previously using ImageJ (Stutz et al., 2013).

P100 fraction/Extracellular vesicle isolation

2e7 bone marrow macrophages were treated for three hours with LPS followed by 45min with Nigericin or ethanol a control. Supernatants were collected and spun for 5 minutes at 500 x g. followed by another spin 30 minutes at 10,000 x g. Supernatants were concentrated 5X using 30kD cellulose filters and the retentates were collected and spun for 60 minutes at 100,000 x g to obtain extracellular vesicle P100 fraction. The pellets were washed with ice cold PBS and again centrifuged for 60 minutes at 100,000 x g. The resulting pellet was lysed in 8 M Urea with 50 mM Tris (pH8), reduced with 10 mM DTT, alkylated with 40 mM CAA and digested for 2 hours with lysC (1 µg/sample) before 1:4 dilution with 50 mM ammonium bicarbonate and the addition of trypsin (1 µg/sample). Trypsin and lysC digestion occurred over night at RT and peptides were cleaned up by C18 stage tipping.

Sample preparation for mass spectrometry

Total lysates were diluted to a final urea concentration of 2 M and sonicated on ice for 15 min (level 5, Bioruptor, Diagenode). Cell supernatants (400 µL each) were denatured with 2 M urea in 10 mM HEPES pH 8. Proteins of both sample types were reduced with 10 mM dithiotreitol for 30 min at RT followed by alkylation with 55 mM iodoacetamide for 20 min at RT in the dark. Remaining iodoacetamide was quenched with 100 mM thiourea. Proteins were digested with 1 µg LysC (#129-02541, Wako Chemicals) at RT for 3 h and 1 µg trypsin (#T6567, Sigma) at RT overnight. Protein digestion was stopped with 0.6% (v/v) trifluoroacetic acid and 2% (v/v) acetonitrile before peptides were loaded onto reversed phase C18 StageTips (#2215, 3M™ Empore™, IVA Analysentechnik). Supernatants and 50 µg of total lysates were loaded onto the C18 StageTips. Peptides were desalted using 0.5% (v/v) acetic acid and subsequently eluted from the C18 StageTips with 50 µL 80% (v/v) acetonitrile in 0.5% (v/v) acetic acid. After concentrating and drying in a SpeedVac (Thermo Scientific), peptides were resuspended in 10 µL 2% (v/v) acetonitrile, 0.1% (v/v) trifluoroacetic acid in 0.5% (v/v) acetic acid and stored at −20°C until mass spectrometric analysis.

LC-MS/MS

Peptide mixtures were analyzed in a single-run liquid chromatography mass spectrometry (LC-MS/MS) format (Nagaraj et al., 2012). Each peptide mixture was loaded onto a C18-reversed phase column (20 cm long for supernatants and 50 cm long for total lysates, 75 µm inner diameter) and separated with a non-linear gradient of 2 - 60% buffer B (80% (v/v) acetonitrile in 0.1% (v/v) formic acid) at a flow rate of 250 nL/min over 107 min for supernatants and 180 min for total lysates using a nanoflow UHPLC instrument (Easy-nLC 1200, Thermo Scientific). Chromatography columns (#TSP075375, Composite Metal Service Ltd.) were packed at the MPI of Biochemistry with ReproSil-Pur 120 C18-AQ 1.9 µm resin (#r119.aq., Dr. Maisch GmbH) in methanol. Chromatography and column oven (Sonation GmbH) temperature were controlled and monitored in real-time with SprayQC (Scheltema and Mann, 2012). Column oven temeprature was set to 40°C for supernatants and 55°C for total lysates. Separated peptides were analyzed on a benchtop quadrupole-Orbitrap instrument (Q Exactive HF/HFx mass spectrometer, Thermo Scientific) with a nanoelectrospray ion source (Thermo Scientific), which was coupled on-line to the liquid chromatography instrument.

The mass spectrometer was operated in a data dependent mode with a survey scan range of 300-1650 m/z and a resolution of 60,000 at m/z 200. Up to the 10 most abundant precursor ions with charge states 2 to 5 were isolated for higher-energy collisional dissociation (HCD) with Thomson (Th) isolation windows of 1.4 m/z for secretomes and 1.8 m/z for total proteomes. Normalized collision energies (NCE) for HCD were 26 (proteomes) and 27 (secretomes), respectively. Fragmentation spectra were acquired with a resolution of 15,000 at m/z 200. Dynamic exclusion duration of sequenced peptides was set to 20 s (secretomes) or 30 s (proteomes) to reduce repeated peptide sequencing. Maximum ion injection times were 20 ms for the full MS scan and 80 ms (secretomes) or 55 ms (proteomes) for the MS/MS scan. Automatic gain control (AGC, ion target values) was set to 3e6 for the survey and 1e5 for the MS/MS scan. MS data were acquired as described previously using the Xcalibur software (Thermo Scientific) (Meissner et al., 2013).

QUANTIFICATION AND STATISTICAL ANALYSIS

LC-MS/MS data analysis

Protein identification and quantification from MS raw files was performed separately for the murine and human datasets using the computational proteomics platform MaxQuant (software version 1.5.5.2 or 1.6.2.1) (Cox and Mann, 2008). Murine and human MS/MS spectra were searched against the respective UniProt FASTA databases and a common contaminant database by the implemented Andromeda search engine (Cox et al., 2011). Secretomes and proteomes of all murine and all human datasets, respectively, were analyzed together. To avoid matching between different sample types, secretomes were set to fraction 1 and parameter

group 0 and total lysates to fraction 3 and parameter group 1. The used digestion mode was Trypsin/P with a minimum peptide length of 7 amino acids and a maximum of two missed cleavages. Cysteine carbamidomethylation was set as fixed and methionine oxidation and N-terminal acetylation as variable modifications. False discovery rates (FDR) were 1% at the peptide and protein level. Peptide identification was performed with an allowed initial precursor mass deviation up to 4.5 ppm and an allowed fragment mass deviation of 20 ppm. Protein identifications required one unique or razor peptide. For nonlinear retention time alignment of all samples, the "Match between runs" option of MaxQuant was used. The time windows for matching peptide identifications across different samples and to search for the best alignment function were set to 0.7 min and 20 min. For label-free quantification (LFQ) via MaxLFQ, a minimum ratio count of 1 was used and Fast LFQ enabled with a minimum of 3 and an average of 6 neighbors (Cox et al., 2014).

Data preparation, quality control, and copy number estimation

Data was analyzed with the Perseus computational platform (version 1.5.5.5) and the statistical software environment R and R Studio, respectively (Tyanova et al., 2016). The integrated graphics device or the package "ggplot2" in R Studio were used to visualize data. Proteins matching to the reversed or contaminants database as well as peptides only identified by side modification were excluded from the analysis. Data were additionally filtered to contain at least two valid values per protein identification in at least one group of replicates. The number of identified protein groups per condition and the Pearson correlation between technical replicates were determined and subsequently missing values were replaced. Missing values were imputed separately for secretomes and proteomes by a Gaussian distribution with a 30% width relative to the standard deviation of the measured values and a downshift of the mean by 1.8 standard deviations of the valid data. To assess the accuracy of the mass spectrometry approach, MS raw intensities and LFQ values were correlated (Pearson) to ELISA values for TNF-α and IL-1β using pairwise complete observations. By analogy, the Pearson correlation of LDH release and the summed MS raw or LFQ intensities of all proteins annotated as "cytoplasm," "cytoplasmic part," "intracellular," or "intracellular part" (cytosolic proteins) by the Gene Ontology (GO) term cellular component (GOCC) was calculated Of note, the label-free quantification technology MaxLFQ that in addition to peptide intensity information involves various normalization steps of the LC MS/MS runs to make protein amounts between different samples more comparable showed overall a much weaker correlation to the alternative (antibody and enzyme-based) quantification methods (Figures S2G–S2J). One reason being that the assumed requirements for MaxLFQ calculation, e.g., that protein compositions do not show major differences across different samples, are not fulfilled in our datasets. Hence, protein amounts were determined by label-free quantification using the summed raw intensities of the MS1 signal of each eluting peptide for all further analyses.

Bioinformatics analysis of protein secretion signatures and receptor shedding

To investigate differences in conventional and unconventional protein secretion from activated macrophages on a global scale we pairwise compared secretomes of differentially treated macrophages by calculating the ratios of individual protein abundances. A parametric two-tailed welch's t test with a permutation-based false discovery rate (FDR) of 5% and a S_0 parameter of 1 was employed to identify proteins that significantly differed in abundance (Tusher et al., 2001). Secretory signatures were functionally characterized by annotation enrichment analysis using annotations from the UniProt Keywords and Pfam protein domain databases (Finn et al., 2016). Enrichment factors were calculated with Fisher's exact test. All annotations with intersection sizes greater than 3 and p values less than 0.00025 were considered.

To analyze pyroptosis dependent receptor shedding, proteins were prefiltered by Uniprot Keywords 'Receptors' and their corresponding peptides were annotated "extracellular" and "intracellular" via Uniprot Keywords, respectively. Peptide intensities were logarithmized and normalized to LPS primed untreated conditions. A two-tailed t test was performed between extracellular and intracellular peptides of all receptors (Figure S6A) and selected receptors (Figures S6B and S6C) and significance was denoted by asterisks (*$p < 0.05$, **$p < 0.01$, ***$p < 0.001$, ****$p < 0.0001$).

Article 6: A Scalable Approach to Capturing Ligand-Receptor Interactions and Mapping Cell Surface Protein Assemblies via Proximity Labeling with Radius Modulation

In preparation

Jonathan J. Swietlik[1], Benedikt O Gansen[1,2], Felix Kühner[1], Alexander Henrici[1], Jonathan J. Scheler[2], Felix Meissner[1,2]

[1] Experimental Systems Immunology, Max Planck Institute of Biochemistry, Martinsried, Germany

[2] Institute of Innate Immunity, Department of Systems Immunology and Proteomics, Medical Faculty, University of Bonn, Bonn, Germany

Identifying interactions of intercellular signaling proteins with cell surface proteins is fundamental to understanding their mechanistic functions and roles in biology. However, the unique localization and biophysical properties of integral membrane proteins pose technical challenges that often make these interactions difficult to study with established protein-protein interaction (PPI) screening methods[137-139]. Consequently, there is a need for specialized methods that facilitate robust and effective analysis of PPIs at the cell surface.

We and others have identified proximity labeling (PL) as a highly attractive approach for capturing extracellular ligand-receptor interactions *in situ*, as well as mapping the topologic arrangement of receptors, co-receptors, and other membrane proteins involved in modifying signal reception and transduction. However, the reliable distinction of proteins systematically associated with a protein of interest from co-captured proteins localized in the same compartment is an unresolved challenge in the field, often requiring sophisticated control strategies that need to be optimized on a case-by-case basis. This is aggravated by the comparably long half-life of reactive probes generated in widely used peroxidase PL reactions, resulting in larger labeling radii than previously anticipated, especially in less molecular crowded environments like the cell surface[177]. Research aimed at addressing these challenges has been focused on alternative PL chemistries producing extremely short-lived labeling probes to increase the spatial resolution[182,184].

Here, we find that horse-radish peroxidase (HRP) PL can be very effectively modulated by the addition of scavenger molecules, achieving results comparable to those produced by recently developed high resolution cell surface PL techniques like µMap[184] and LUX-MS[182]. Moreover, by applying scavenger-mediated PL modulation, we explore enrichment profiles of proteins across varying labeling radii. Compared to single radius PL, we demonstrate

that such enrichment profiles can significantly increase the accuracy of identifying proteins directly interacting with a protein of interest, while offering additional insights on the spatial relationships of less tightly associated proteins in the proximity, and clearly rejecting background, thereby addressing one of the key challenges of PL proteomics. Applying this approach to EGF-guided PL on HeLa cells successfully captured its primary receptor EGFR, along with its well-described co-receptor ERBB2. LRP1, a membrane receptor with recently found functional connections to EGFR signaling, is identified as a candidate EGFR interactor.

We have developed a comprehensive suite of experimental protocols to streamline sample processing for this method. We detail a chemical ligand-modification protocol that circumvents the need for genetic fusion to a peroxidase. A plate reader-based companion assay facilitates screening for target cell types and rapid protocol optimization, if required. Partial automation and sample processing in multi-well plate format mediates high throughput and precise control of time-sensitive reaction steps.

Contribution:

I designed and conducted experiments and supervised experimental work by Felix Kühner and Alexander Henrici. I analyzed and visualized data for all figures. Felix Meissner and I co-wrote the manuscript.

A Scalable Approach to Capturing Ligand-Receptor Interactions and Mapping Cell Surface Protein Assemblies via Proximity Labeling with Radius Modulation

Jonathan J Swietlik[1], Benedikt O Gansen[1,2], Felix Kühner[1], Alexander Henrici[1], Jonathan Jakob Scheler[2], Felix Meissner[1,2]

Affiliations
[1]Experimental Systems Immunology, Max Planck Institute of Biochemistry, Martinsried, Germany
[2]Institute of Innate Immunity, Department of Systems Immunology and Proteomics, Medical Faculty, University of Bonn, Bonn, Germany
lead contact: felix.meissner@uni-bonn.de

Abstract

Intercellular communication relies on signal transduction through protein interactions and the assembly of receptor complexes at the plasma membrane. Proximity labeling (PL) is emerging as a powerful tool for mapping proteins in sub-cellular compartments, including the cell surface. However, differentiating closely associated proteins from those more distant or spatially dispersed remains challenging. Here, we introduce a peroxidase-based PL strategy that resolves spatial relationships of proteins at the cell surface by gradually modulating the labeling radius through reaction scavengers. Using chemically tagged extracellular signaling proteins, our approach effectively captures previously validated direct ligand-receptor and lateral receptor interactions, identifies new interactor candidates, and differentiates them from unrelated co-enriched surface proteins. A colorimetric companion assay enables rapid pre-screening of ligand binding on intact cells, together, providing a flexible and scalable solution for the systematic mapping of signaling protein assemblies at the cell surface, with broad applications in both basic research and drug development.

Introduction

Cells in multicellular organisms communicate with neighboring and distant cells. Understanding how intercellular signaling proteins regulate physiological and pathological processes requires detailed insights into their context-dependent release, cell surface expression, and the signaling functions conveyed through their interactions and assemblies of signaling complexes at the cell surface. Mass spectrometry (MS)-based proteomics offers unsupervised, comprehensive approaches to analyze intercellular protein functions. For example, MS-based secretomics experiments capture release dynamics of known signaling proteins like cytokines[1,2] and facilitate the discovery of proteins or protein variants with previously undescribed extracellular signaling functions[3-5]. However, for many newly discovered and well-known intercellular signaling proteins, including high-profile drug target candidates[6-8], their corresponding receptors have yet to be identified. Moreover, the spatial arrangement of receptors, co-receptors, and other lateral interactors, such as tetraspandins[9] or receptor activity-modifying proteins (RAMPs)[10], can strongly influence signal integration and specificity[11], thus shaping cell type-specific responses[12]. Despite this, these interactions remain understudied, hindered by the unique properties and localization of transmembrane proteins, leading to strong underrepresentation in conventional protein-protein interaction screens with methods like affinity purification mass spectrometry (AP-MS)[13].

The growing awareness of the critical role of protein nanoorganization for signal transduction in human biology and drug design has sparked an interest in tailored methods that map spatial protein assemblies at the cell surface[12,14]. Several specialized techniques have been developed to improve the detection of extracellular ligand-receptor interactions[13,15,16] specifically. Among the most promising approaches are ligand-guided proximity labeling (PL) techniques, which capture neighboring, potentially interacting proteins and provide information about the lateral receptor environment. Like APEX, which has become widely used for characterizing intracellular protein environments[17], horseradish peroxidase (HRP) can efficiently generate reactive phenoxy radicals and tag proteins in the extracellular space. Early applications using antibody-HRP conjugates (e.g., EMARS[18] and SPPLAT[19]) or genetically encoded HRP-fusion proteins[20] have given unique insights into the protein composition of specific plasma membrane subdomains such as excitatory and inhibitory synaptic clefts[21]. Due to fast reaction kinetics, HRP provides effective labeling with high temporal resolution. However, the generated radicals have a comparably long solution half-life time, typically resulting in a large labeling radius of a few hundred nm[22]. This complicates the discrimination of directly interacting proteins from functionally unrelated proteins within the same sub-cellular compartment and has sparked affords to improve the spatial resolution. Novel proximity labeling approaches based on light-controlled singlet oxygen[23] or carbene[24] generators have very concise labeling radii that offer higher specificity for more confident detection of cognate receptors in ligand-guided reactions. Nonetheless, distinguishing interactors from merely co-localized proteins remains a significant challenge.

Here, we introduce a cell surface proximity labeling strategy that combines the advantages of HRP PL with the benefits of high spatial resolution in a single assay with extended capabilities. Instead of using a single concise labeling reaction, we modulate the large HRP PL radius through titration of scavenger molecules to generate surface protein enrichment profiles that correlate with their spatial relationship to an HRP-conjugated protein of interest. We demonstrate both expansive mapping of receptor environments, exemplified by antibody-based targeting of the T-cell receptor, and highly specific ligand-guided receptor identification on intact cells, where labeling radius modulation effectively distinguishes directly associated proteins from co-localized, independently diffusing

neighbors. Combined with a colorimetric companion assay for high throughput target cell screening, we introduce a flexible and comprehensive platform for systematically characterizing signaling proteins and their interactions at the cell surface.

Results

Peroxidase-based proximity labeling techniques have been successfully used to detect protein interactions in diverse contexts and offer unique advantages compared to conventional affinity-purification methods[17]. We adapted this principle to systematically characterize interactions of ligands with proteins at the cell surface.

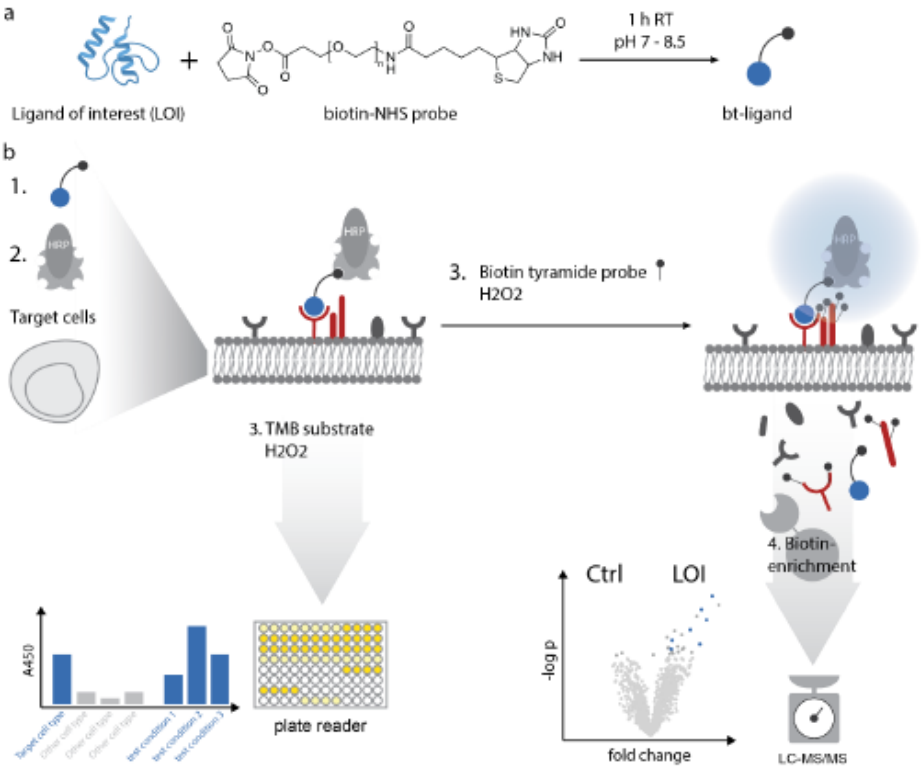

Figure 1: A peroxidase conjugation-based technology platform enables comprehensive evaluation of ligand-receptor interactions at the cell surface. a) Purified ligands are conjugated with bifunctional NHS-biotin adapter molecules that react with free primary amino groups. b) Modified ligands are then incubated with living cells and bind to their corresponding target receptor(s) on the cell surface. Subsequently, horse radish peroxidase (HRP)-NeutrAvidin conjugates are added and bind to the ligand adapter. During these steps, cells are suspended in PBS at physiological pH to maintain native protein folding, and kept cold at a maximum of 4 degrees to suppress potential receptor internalization. For sensitive, semiquantitative and high throughput detection of ligand binding to the cell surface, 3,3',5,5'-Tetramethylbenzidine (TMB) substrate is added and substrate conversion by HRP is measured with a microplate spectrophotometer. For target receptor capture and the characterization of the lateral receptor environment, HRP is used to generate phenoxy radicals that react with neighboring proteins and tag them for affinity purification. After the proximity labeling reaction, cells are lysed, biotinylated proteins are enriched, digested on-resin, and analyzed by MS-based proteomics. Quantified proteins are then compared to control samples, for example, capture reactions guided by unrelated ligands or negative controls without a guiding ligand. We integrated both workflows with a liquid-handling robot system for semi-automated parallel processing of samples in a multi-well plate format and highly precise time control of PL reaction steps.

Horse-radish peroxidase (HRP) is incompatible with reducing environments such as the cytosol; however, it has excellent extracellular activity[25]. In the presence of H2O2, it catalyzes the oxidation of tyramide probes to form phenoxy radicals that react with neighboring proteins and tag them for affinity purification. While HRP can be linked to a protein of interest through genetic fusion or conjugated antibodies, we employ bifunctional NHS-biotin adapter molecules to provide a modular workflow that accommodates any purified protein. This facilitates, for example, the streamlined screening of recombinantly expressed intercellular signaling protein candidates (Fig. 1a). Modified ligands incubated with living target cells bind their corresponding receptors in their native environment and are then linked to NeutrAvidin-HRP fusion proteins *in situ* (Fig. 1b). During the PL reaction, biotin-tyramide radicals generated by HRP form stable covalent bonds with proteins that are nearby. Cells are afterward lysed with strong detergents that efficiently extract and solubilize transmembrane proteins, and biotin-tyramide-labeled proteins are enriched and then quantified by mass spectrometry.

A ligand-guided, HRP-based colorimetric companion assay facilitates semi-quantitative detection of specific cell surface-binding with high throughput

Cell-based assays ensure correct folding, post-translational modification states, sub-cellular localization, and organization of all components required for ligand binding and signal transduction. However, target cell types, receptors, or co-receptors involved in signal transduction may be unknown for a given extracellular ligand. For rapid screening of potential ligand-binding cells, we developed a colorimetric companion assay that shortcuts proximity labeling and MS analysis and detects HRP-mediated 3,3',5,5'-Tetramethylbenzidine (TMB) substrate conversion in a plate reader. (Fig. 1b and 2a).

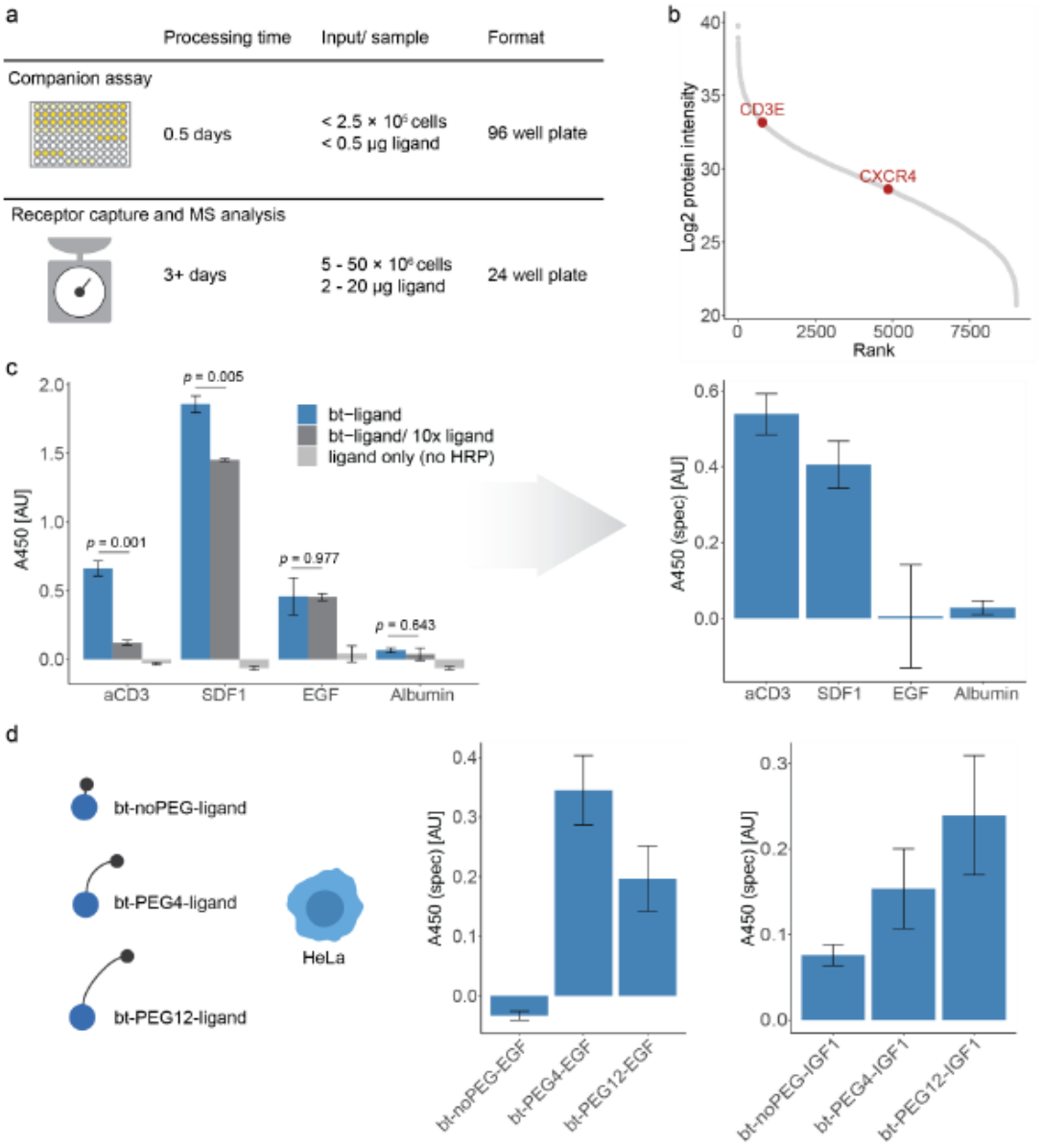

Figure 2: A colorimetric companion assay enables efficient target cell screening for novel signaling protein candidates and ligand-specific protocol optimization. a) Throughput and input material comparison between colorimetric surface binding detection and receptor identification by MS. b) Jurkat proteome intensity rank plot. Corresponding receptors for tested ligands are highlighted. c) (Left) HRP-mediated TMB substrate conversion quantified by absorption at 450 nm (A450) for surface binding detection of biotinylated ligand proteins on Jurkat cells (mean ± SE, n = 4). Student's t-test p-values between biotinylated-ligand samples and ligand competition controls are indicated. (Right) Signal after substraction of competition controls (A450 (spec)) corresponding to potential specific receptor binding. d) Quantification of specific receptor binding of EGF and IGF1 modified by short, medium, or long biotinylation probes (mean ± SE, n = 4).

First, we evaluated the binding of proteins with well-characterized interactions at the surface of Jurkat cells, an immortalized human T lymphocyte line. We targeted a T-cell co-receptor subunit with an anti-CD3 antibody, and the chemokine receptor CXCR4 with the chemokine SDF-1, both of which are expressed by Jurkat cells (Fig. 2b). In contrast, Jurkat cells lack expression of known cognate receptors for epidermal growth factor (EGF), which was used as a negative control in addition to

5

bovine serum albumin. To differentiate specific from non-specific binding, we used control samples supplemented with a tenfold excess of unmodified ligand incapable of HRP binding, assuming competition for specific and excess capacity for non-specific binding sites. Our results show large differences in specific and non-specific binding signals across ligands, underlining the importance of thorough controls: While cells incubated with bt-SDF1 produced the strongest overall signal, and bt-albumin barely exceeded HRP-free controls, total signal levels of bt-anti-CD3 and bt-EGF were similar (Fig 2c). For EGF and albumin, both lacking specific receptors on Jurkat cells, competition controls closely matched bt-ligand signals, whereas bt-anti-CD3 and bt-SDF1 signals were significantly decreased upon competition with unmodified ligand (Fig 2c). Binding competition, therefore, effectively differentiated specific and non-specific binding signals and allowed the robust distinction of ligands with and without corresponding receptors on Jurkat cells.

Next, we used the companion assay to optimize ligand modification for minimal binding interference, for example, by testing NHS-biotin adapters with varying linker lengths. The small signaling proteins EGF (6.2 kDa, 53 amino acids) and IGF-1 (7.7 kDa, 70 amino acids) modified with NHS-biotin probes without a PEG linker yielded only a weak surface binding signal on target cells or no specific signal at all (Fig. 2d). For both ligands, longer linkers significantly increased the specific binding signal, however, with individual differences in optimal tether length. While probes with both medium and long PEG linkers were compatible with all tested ligands in this study, the companion assay offers a rapid solution for optimizing signal-to-noise ratios, which may be critical for ligands with low corresponding receptor abundance or weak receptor affinity. Since the principal steps before PL are identical, insights from linker optimization can be directly applied to proximity labeling-based receptor capture experiments.

Radical scavengers effectively modulate proximity labeling

While PL can effectively capture even transient and low-affinity interactors in situ, defining precise protein interactomes poses challenges. Recent studies have shown that HRP PL radii at the cell surface extend to over 200 nanometers under standard labeling conditions[22]. This wide reach typically results in the labeling and co-enrichment of hundreds of co-localized proteins around a protein of interest, which hampers the discovery of high-confidence interactor candidates[22,23].

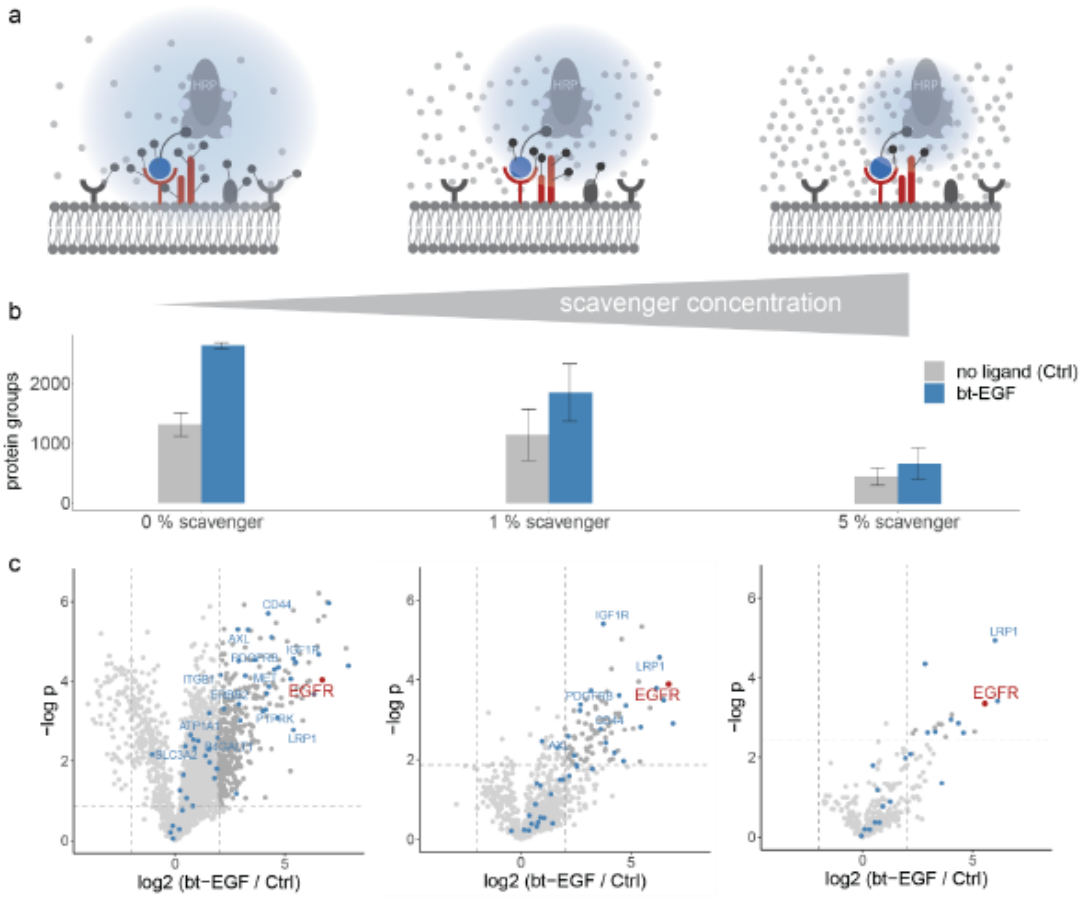

Figure 3: Scavenger molecules effectively control the radius of HRP-mediated proximity labeling at the cell surface. a) Scheme of proximity labeling radius modulation using scavenger molecules. b) Identified protein groups (mean ± SD, n = 3) after bt-EGF-guided receptor capture on HeLa cells, control reactions at different scavenger concentrations, and c) corresponding volcano plots. Significantly regulated proteins are highlighted in dark grey (two-sided Student's t-test, permutation-based FDR = 0.05). Previously described lateral receptor interactors listed in the BioGRID[26] database are highlighted in blue and labeled with gene names if reported in at least three independent studies.

This is exemplified by an EGF-guided proximity labeling experiment (Fig. 3a - c, left): Following the above-described procedure, we biotinylated recombinant EGF and conjugated HRP upon engagement of corresponding receptors on living HeLa cells. After a 90s labeling pulse and enrichment of labeled proteins, we identified, on average, 2269 proteins using 70 min data-dependent acquisition (DDA) LC-MS measurements. Samples without bt-ligand treatment controlled for proteins labeled by unspecifically bound HRP or unspecifically enriched in the downstream procedure and showed around 45 % fewer identifications. EGFR, the primary EGF receptor expressed by HeLa cells[27], was successfully captured and among the proteins with the strongest fold-changes and smallest p-values compared to controls. Along with EGFR, 35 surface proteins with previous experimental evidence for EGF or EGFR interaction curated in BioGRID[26] were significantly co-enriched with a 4-fold minimum fold-change, in addition to 328 proteins without obvious connection to EGF or EGFR. These results highlight the strengths and challenges of peroxidase PL at the cell surface: Endogenous ligands can be derivatized to capture corresponding receptors and associated surface-exposed proteins effectively. However, due to its low spatial resolution, HRP PL produces noisy data that requires tedious follow-ups to prioritize and validate interactor candidates. Previous

antibody-guided PL experiments targeting EGFR suggest that employing suitable reference control samples can reduce background noise by more accurately reflecting potential unspecific ligand interactions[22]. Nonetheless, even in isotope-controlled antibody-guided experiments, EGFR was co-enriched with more than a hundred other candidate proteins, and around half showed stronger fold changes[22]. Moreover, especially with poorly characterized ligands, finding suitable control ligands that exhibit similar non-specific binding properties but do not overlap in target binding can be challenging. Consequently, a PL approach compatible with neutral and universal reference controls is highly desirable.

Given that the PL radius critically depends on the half-life of generated reactive probes, we hypothesized that increasing the concentration of molecules that readily react with tyramide radicals and serve as scavengers could enhance the spatial resolution of HRP PL. Among other additives, we tested supplementing complex peptide mixtures like tryptone, a commonly available media component from casein digestion. Intriguingly, tryptone effectively modulated EGF-guided PL and was well tolerated by cells throughout the duration of labeling pulses. Although raw peptide yields in cell lysates remained constant, the number of detected proteins after streptavidin enrichment significantly decreased with the addition of tryptone during the labeling reaction (Fig. 3b). While EGFR consistently showed strong enrichment, the overall number of co-enriched proteins with differential abundance compared to controls was substantially reduced. With 5 % (w/w) supplemented tryptone, only 18 proteins reached statistical significance (17 with an enrichment fold change greater than 4-fold), EGFR ranking 4th in p-value and 3rd in enrichment fold change (Fig. 3c). These results closely resemble those observed with newly developed PL methods with ultra-short labeling radii such as µMap[22,24], supporting that tryptone additives facilitate effective modulation of the half-life and diffusion radius of tyramide radicals.

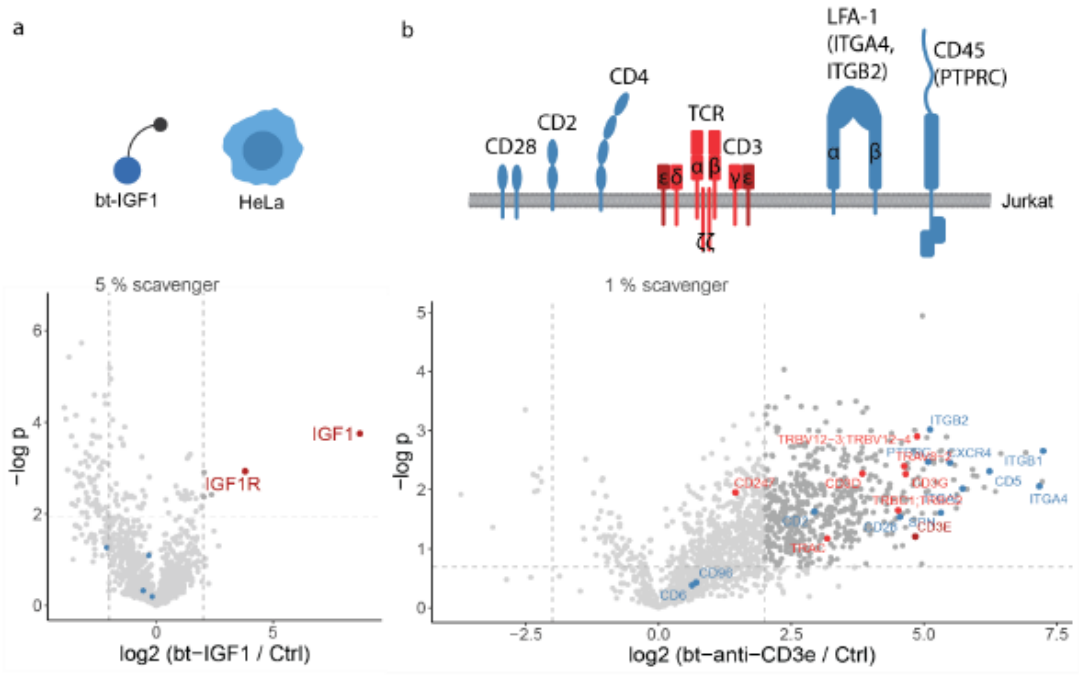

Figure 4: Ligand-guided proximity labeling with radius modulation allows highly specific receptor identification and comprehensive characterization of large signaling complexes. a) Volcano plot of IGF-1-guided PL on HeLa cells in 5% trypton compared to unguided (no-ligand) controls (n = 3). Significantly regulated proteins are highlighted in dark grey (two-sided Student's t-test, permutation-based FDR = 0.05). b) (Top) Scheme of the T-cell receptor complex and principal

components of the immunological synapse according to[28]. (Bottom) Volcano plot of anti-CD3ε-guided PL on Jurkat cells in 1 % trypton compared to unguided (no-ligand) controls (n = 3). Significantly regulated proteins are highlighted in dark grey (two-sided Student's t-test, permutation-based FDR = 0.05). Previously described components of the TCR complex are highlighted in red and immunological synapse components in blue.

Our data suggests that scavenger additives may be used to optimize PL radii to specific research questions, overcoming limitations of noisy HRP PL experiments under standard conditions while providing flexibility to adjust labeling reactions to larger structures of interest or broader coverage of lateral receptor environments and membrane domains. To investigate this, we profiled IGF1 binders on HeLa cells in the presence of high scavenger concentrations (Fig. 4a). A concise labeling radius enabled precise capture and identification of its target receptor IGF1R, which was, together with IGF1 itself, the most strongly enriched protein compared to no-ligand controls. Conversely, we used anti-CD3ε to guide HRP and label proteins of the T cell receptor (TCR) complex and its wider lateral environment (Fig. 4b and c). In addition to successfully capturing CD3ε and associated CD3γ, CD3δ, as well as CD3ζ (CD247), and TCR alpha and beta chains (TRA and TRB), labeling in the presence of low scavenger concentrations provided a wider view of co-localized and functionally related plasma membrane proteins. Among the most strongly enriched proteins were receptors and adhesion proteins with key roles in T cell activation. These included CD2, CD5, CD28, CD45, and LFA-1, core components of immunological synapses, concentric supramolecular clusters that form around TCR when engaged with cognate peptide bound major histocompatibility complex (MHC) of antigen-presenting cells[29-31]. Although the co-receptor CD4 was expected to be co-localized with TCR (Fig. 4b), it was not detected after enrichment of labeled proteins, likely due to its low abundance in Jurkat cells, as previously described[32].

PL radius modulation differentiates proteins based on their spatial organization relative to the source

Because a simple buffer additive achieves PL radius modulation, reactions with changes in labeling ranges can be conducted in a highly controlled and parallelized manner. We anticipated that analyzing protein labeling across multiple scavenger concentrations, as opposed to single PL snapshots, could offer deeper insights into spatial relationships, given the expected variations in protein enrichment profiles based on their relative distributions and distances to the PL source.

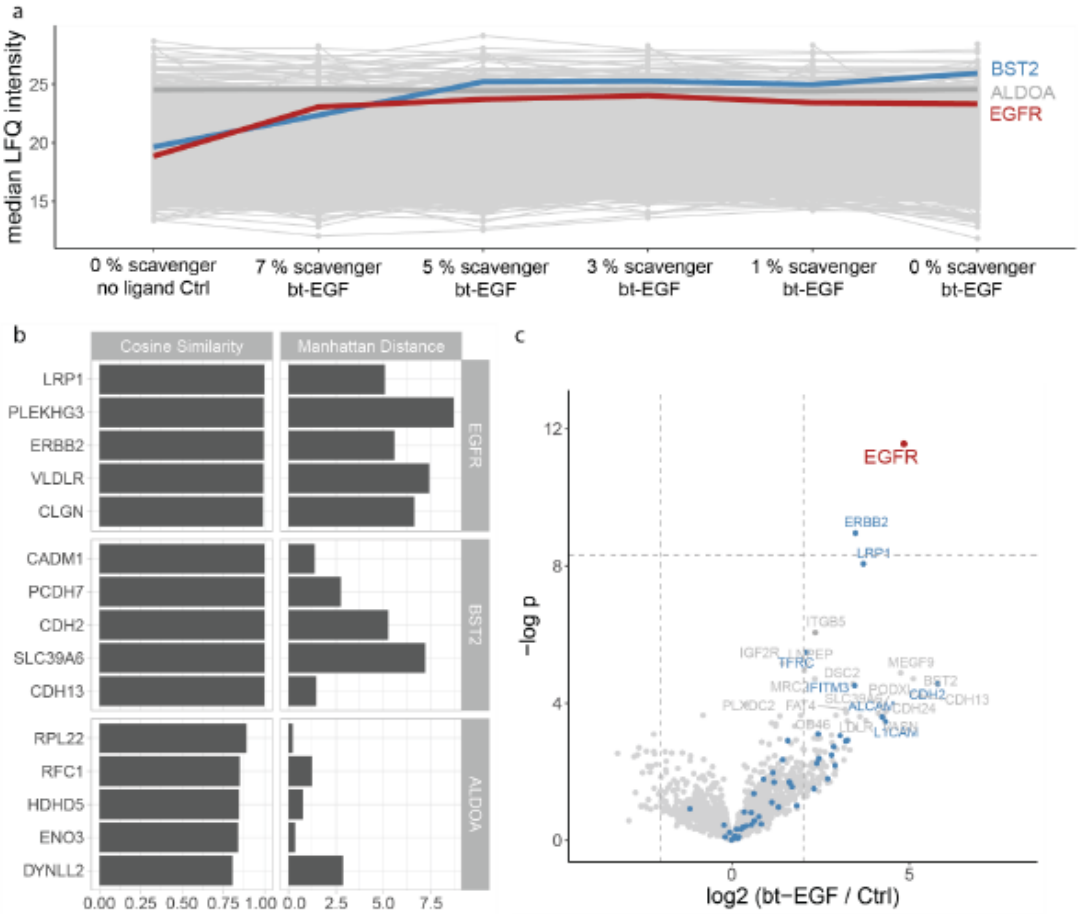

Figure 5: Modulation of proximity labeling enhances insights into the spatial context of labeled proteins. a) Median intensity profiles of enriched proteins from control or EGF-guided capture reactions across different scavenger concentrations (n = 3). b) Overview of the top 5 proteins ranked by fold change profile similarity to EGFR, BST2, and ALDOA references in EGF-guided capture across different scavenger concentrations relative to controls. c) Volcano plot comparing combined samples of EGF-guided capture across 0 - 7 % scavengers and control samples without an HRP-guiding ligand (two-sided Student's t-tests, permutation-based FDR = 0.05). Previously described lateral receptor interactors in the BioGRID[26] database are highlighted in blue.

To explore enrichment profiles across varying scavenger concentrations, we performed EGF-guided PL on HeLa cells with tryptone additives that decreased from 7 % to 0 % in 5 increments. Extending the MS acquisition time to 100 min and using data-independent acquisition significantly increased protein coverage and data completeness, yielding 4030 proteins quantified at least once in every sample group.

Background proteins that were non-specifically labeled or unlabeled and carried over through the enrichment protocol showed consistent abundance in all sample groups including controls, exemplified by abundant cytosolic proteins like aldolase A (ALDOA) (Fig. 5a). In contrast, EGFR exhibited a large fold change compared to negative controls and reached abundance saturation already at small labeling radii, indicative of a close and systematic association with the radical emitting enzyme. Interestingly, groups of other proteins displayed distinctly different profiles, such as bone marrow stromal antigen 2 (BST2), characterized by low enrichment at very small labeling radii and a plateau with high enrichment across medium scavenger concentrations. BST2, also

referred to as tetherin, is associated with lipid rafts and plays key roles in the spatial organization of proteins within plasma membrane microdomains[33-35]. EGFR is known to dynamically associate with different membrane partitions and partially localizes in lipid rafts[36], where downstream signaling upon ligand binding is strongly reduced[36,37]. A recent study identified BST2 as a crucial regulator of EGFR release from lipid rafts, strongly impacting EGF signaling and proliferation, thus presenting it as a potential drug target for cancer therapy[38].

Using profiles of ALDOA as a generic background reference, and BST2 - a distinctly localized plasma membrane protein that regulates EGFR signaling - along with EGFR, we set out to identify proteins with similar enrichment patterns and presumably similar spatial relationships to the PL source EGF. We converted protein abundance profiles to fold changes against no-ligand controls and ranked proteins by their cosine similarities to the three reference profiles. We excluded profiles with a Manhattan distance greater than ten to deprioritize proteins with strong differences in total enrichment. Proteins closely matching the ALDOA profile included other abundant cellular proteins, such as ribosomal proteins, cytoskeletal proteins, and various metabolic enzymes (Fig. 5b), and lacked known cell surface exposition or physical association with EGF or EGFR. Conversely, proteins most similar to BST2 were exclusively plasma membrane proteins and consistently showed functional and spatial connections shared with BST2, including roles in cell adhesion and association with lipid rafts[33,39-41]. Intriguingly, ERBB2, the only other ERBB/HER receptor family member we detected in HeLa cells, shared highly similar enrichment profiles with EGFR. Unlike EGFR, ERBB2 has a restricted ligand-binding domain and lacks a known direct endogenous ligand[42]. Nonetheless, it is crucial as a co-receptor in EGF-mediated signaling, tightly associating with other ligand-bound ERBB members like EGFR to form heterodimeric complexes that trigger signaling cascades that differ from those of ligand-bound homodimers[43]. While the high cosine similarities of averaged enrichment profiles for PLEKHG3 and CLGN were driven by measurements in no-ligand controls with high standard deviations, low-density lipoprotein receptor-related protein 1 (LRP-1) was robustly quantified across all conditions and showed a profile strikingly alike to those of EGFR and ERBB2. LRP-1 is a multifunctional plasma membrane protein and a member of the LDLR family with roles in receptor-mediated endocytosis, lipid metabolism, cell motility, and cell signaling, among others[44,45]. Its extracellular domain features four complement-type elements interspersed with EGF-like repeats[46] and is reported to bind to dozens of ligands[44]. Although validated evidence for direct interactions with EGFR is currently lacking, recent research has shown that LRP-1 stabilizes activated EGFR at the cell surface through a yet unknown mechanism[47].

Unlike the results from a small radius EGF-guided PL experiment alone (Fig. 3c), a t-test between grouped samples from PL experiments across multiple scavenger concentrations and control samples clearly differentiated EGFR based on p-values from other strongly co-enriched proteins with large fold changes (Fig. 4c). Notably, ERBB2 and LRP-1 were the second and third most significantly enriched proteins, respectively. These were followed by a distinct set of proteins exclusively localized to the plasma membrane, comprising many proteins known to associate with lipid rafts, including BST2 and proteins with similar enrichment profiles.

Discussion

In-depth knowledge of intercellular signaling protein interactions with cell surface proteins is essential for a mechanistic understanding of intercellular communication and lays an important foundation for drug development. In this study, we combined horse radish peroxidase (HRP)-based

PL with novel methodological concepts to capture both the association of intercellular signaling proteins with their cognate receptors and the landscape of spatially associated proteins on the surface of living cells.

We provide a methodological framework to systematically interrogate orphaned intercellular signaling proteins or newly discovered signaling protein candidates, for example, derived from large-scale secretomics experiments. In the early stages of evaluating candidates, the specific cell types expressing cognate receptors may not yet be identified. Our colorimetric companion assay offers a rapid method for screening potential target cell types with basic laboratory equipment and no specialized training, making it significantly more accessible than alternative screening methods like high-throughput flow cytometry. Notably, the companion assay workflow is designed to closely mirror our PL capture protocol for MS-based receptor identification, allowing for efficient and translatable optimization of ligand tagging parameters to mitigate binding interference when necessary.

PL has become highly valuable for mapping the molecular environment of proteins within their native cellular contexts. Nonetheless, distinguishing genuine interactors and closely associated proteins from those merely co-localized within the same cellular compartment remains a significant challenge. Recent advancements have introduced innovative PL strategies that generate extremely short-lived probes with small labeling radii to minimize noise. Methods like μMap[24] and LUX-MS[23] have shown substantial improvements in spatial precision over conventional HRP-PL. Here, we demonstrate that the labeling radius of HRP-PL can be effectively reduced by supplementing scavenger molecules that decrease the half-life of probe radicals in the labeling reaction buffer. Our workflow utilizes readily available off-the-shelf reagents, and reactions are controlled by simple buffer additions, making experiments both accessible and scalable for a broad community. Labeling radii can be seamlessly adjusted to suit specific research needs, from precise capture of direct interactors to expansive profiling of target protein environments. However, our results provide evidence that profiling enrichment across different labeling radii reveals additional insights into the spatial relationships of detected proteins, making PL experiments with varying scavenger concentrations the preferred method for both ligand-guided detection of target receptors and characterization of the lateral environment of targeted membrane proteins. Importantly, our radius modulation concept is not confined to HRP PL applications; it is likely translatable to other PL strategies as needed, such as in cases where HRP-induced steric hindrance presents a challenge.

In the example of EGF-guided PL on HeLa cells, comprehensive radius modulation experiments clearly differentiated between EGFR, the only known direct and specific binding partner detectable on the surface of HeLa cells[48], ERBB2, a validated co-receptor, and less tightly associated proteins. The enrichment profile of LRP1, a cell surface receptor with recently discovered functional connections to EGFR[47] but an undefined spatial relationship, stood out with striking similarities to both EGFR and ERBB2, suggesting direct association. Moreover, distinct groups of proteins showed specific enrichment profiles that indicated a larger but defined distance to EGF and EGFR, with many of these proteins known to be organized in lipid rafts.

State-of-the-art mass spectrometry instruments offer significantly enhanced detection limits and fast scan rates[49,50], likely enabling substantial miniaturization of HRP PL experiments and reduced acquisition times while maintaining high protein coverage. The increased sensitivity and throughput open new avenues for large-scale radius modulation experiments beyond ligand-guided receptor capture. For instance, this could include the comprehensive characterization of membrane protein

organization in rare primary cell types or the time-resolved tracking of dynamic rearrangements within signaling clusters upon stimulation.

Methods

Cell culture

Jurkat cells were acquired from DSMZ (ACC 282) and HeLa cells from ATCC (CCL-2). They were cultured in RPMI 1640 and DMEM media, respectively, each supplemented with 10 % heat inactivated fetal bovine serum (FBS HI). Cells were maintained at 37 °C with 5 % CO_2.

For live cell experiments, adherent cells were washed once in PBS, and then detached by incubation in 10 mM EDTA in PBS for 30 min. After collecting detached cells or suspension cells, cells were kept on ice when possible and handled in pre-chilled, ice-cold buffers. Cells were washed twice with PBS, and resuspended in PBS supplemented with 1 % BSA.

Cell lines underwent regular mycoplasma contamination tests using PCR.

Ligand biotinylation

Lyophilized ligand proteins were reconstituted in PBS pH 8 at 2 mg/ml final concentration. Biotin NHS-ester probes were reconstituted in ddH2O at 20 mM final concentration and added to ligand protein solutions at a molar probe-to-protein ratio of 5 - 10x. Reaction mixes were incubated at room temperature, 800 rpm for 45 min. Biotinylated ligands were subsequently diluted with PBS to 1 mg/ml, snap frozen in liquid nitrogen and stored at -20 °C.

Colorimetric companion assay

For each sample, a suspension of 2.5 x 10^5 washed cells in 300 µl PBS, 1 % BSA was dispensed into a 96-well plate. 250 ng biotinylated ligand or vehicle was added. In competition control samples, an additional 2.5 µg unbiotinylated ligand was added. Cells and ligands were incubated for 90 min at 4 °C with shaking at 500 rpm on a thermomixer. Afterwards, cells were washed twice in 300 µl PBS, 1 % BSA, and 1 µg Neutravidin-HRP was added and incubated with cells for 90 min at 500 rpm. Cells were washed again thrice in 300 µl PBS, 1 % BSA, and 300 µl TMB substrate were added. Cells were incubated in the dark for 4 - 20 min until an intense color development was detectable by eye, and then centrifuged at 400 x g for 4 min. 100 µl of cell supernatants were transferred into a clear, flat-bottom 96-well plate using an Agilent BRAVO liquid handling robot. Reactions were terminated by adding 50 µl 2 N sulfuric acid. Colorimetric read-out was performed at 450 nm with correction at 570 nm using a Tecan Infinite 200 microplate reader.

Ligand-guided proximity labeling

Per sample, 1 - 5 x 10^7 washed cells suspended in 3 ml PBS, 1 % BSA were dispensed into a round-bottom 24 deep-well plate and kept on ice. 20 µg biotinylated ligand or vehicle was added to each sample, and incubated with cells for 90 min at 4 °C with shaking at 550 rpm on a thermomixer. Cells

were washed as described above, then 15 µg Neutravidin-HRP were added and incubated with cells for 90 min at 4 °C with shaking at 550 rpm. Afterwards cells were washed thrice in PBS, 1 % BSA, and resuspended in 2 ml PBS, 1 % BSA, supplemented with 0 - 7 % tryptone. 500 µM Biotin-AEEA-tyramide was added and incubated with cells for 5 minutes at 550 rpm. An Agilent BRAVO liquid handling robot was used for precise control of the proximity labeling reaction. To start labeling, 40 µl H_2O_2 were added to each sample, and labeling was allowed to proceed for 90 seconds while shaking cells at 550 rpm. The reaction was stopped by adding a 2x quencher solution (PBS supplemented with 20 mM sodium ascorbate, and 10 mM Trolox). Subsequently, cells were washed twice in 1x quencher solution, supernatants were removed and cell pellets were frozen and stored at -80 °C.

Neutravidin enrichment of labeled proteins

After proximity labeling, cells were lysed in 1 ml RIPA buffer, supplemented with 10 mM TCEP, 30 mM CAA, and 1x Roche complete EDTA-free protease inhibitors. Cell lysates were transferred into 1.5 ml reaction tubes and heated for 5 min at 95 °C, 1000 rpm. Afterwards, lysates were sonicated using a Bioruptor sonicator for 15 min with 30s pulses and breaks. Lysates were then clarified by centrifugation at 20,000 x g for 10 min.

To enrich biotinylated proteins, 100 µl high capacity NeutrAvidin agarose bead slurry were washed thrice with PBS, combined with clarified lysates, and incubated for 2.5 h at RT with end-over-end mixing. Beads were transferred to empty Bio-Spin chromatography columns and washed with 10 ml RIPA buffer, 10 ml urea wash buffer (4 M urea, 100 mM Tris/ HCl pH 7.5), and 10 ml PBS. Washed beads were resuspended in 500 µl 50 mM ammonium bicarbonate (ABC) buffer and transferred to 2 ml protein LoBind reaction tubes. After centrifugation for 1 min at 1000 x g, supernatants were discarded, beads were resuspended in 100 µl ABC buffer, supplemented with 1 µg trypsin/Lys-C mix, and incubated for 16 h at 37 °C. After digestion and pelleting beads by centrifugation for 1 min at 1000 x g, supernatants were transferred to new reaction tubes and acidified to pH 2-3 using trifluoracetic acid (TFA).

Peptide desalting

Peptide samples were desalted by solid phase extraction using 100 mg Sep-Pak tC18 cartridges. Cartridges were equilibrated with 1 ml acetonitrile (ACN), 1 ml 50 % ACN, 0.1 % TFA, and 2x 1 ml 0.1 % TFA. Samples were loaded on equilibrated cartridges, washed twice with 0.1 % TFA, and eluted with 700 µl 50 % ACN, 0.1 % TFA. Eluates were dried in a SpeedVac vacuum concentrator. To prepare samples for MS acquisition, dried peptides were reconstituted in 20 µl 0.1 % formic acid (FA). Peptide concentrations were determined with a Nanodrop spectrophotometer and adjusted to 0.1 mg/ml.

LC-MS/MS analysis

Samples were analyzed with an Orbitrap Exploris 480 (Thermo Fisher Scientific) mass spectrometer coupled to an EASY-nLC 1200 system (Thermo Fisher Scientific). For each sample, 300 ng of peptide were injected and separated on 50 cm columns packed in-house with 1.9 µm ReproSil C18 beads (Dr. Maisch GmbH). Peptides were eluted at 60 °C and a flow rate of 300 nl/min using a 70 min

nonlinear gradient of 0.1 % FA (buffer A) and 80 % ACN, 0.1 % FA (buffer B) starting at 3 % buffer B and increasing to 98 % buffer B. For data-dependent acquisition, MS1 scans were acquired from 300 to 1650 m/z (AGC target 300 %, maximum injection time 25 ms, resolution 60,000 at 200 m/z), followed by higher-energy collisional dissociation (HCD) and MS2 scans using a Top10 method (normalized collision energy 30 %, AGC target 100 %, maximum injection time 28 ms, resolution 15,000 at 200 m/z).

LC-MS/MS data processing and statistical analysis

Raw MS data were processed using MaxQuant (version 2.0.1.0.) with default orbitrap instrument parameters and 1 % FDR at the peptide and protein level. MaxLFQ was enabled with a minimum ratio count of two. Spectra were matched against the human UniProt FASTA database (79,276 entries, June 2022).

Statistical analyses were performed using R (version 4.1.2) and Perseus (version 1.6.10.43).

References

1 Rieckmann, J. C. *et al.* Social network architecture of human immune cells unveiled by quantitative proteomics. *Nat Immunol* **18**, 583-593, doi:10.1038/ni.3693 (2017).

2 Meissner, F., Scheltema, R. A., Mollenkopf, H. J. & Mann, M. Direct proteomic quantification of the secretome of activated immune cells. *Science* **340**, 475-478, doi:10.1126/science.1232578 (2013).

3 Deshmukh, A. S. *et al.* Proteomics-Based Comparative Mapping of the Secretomes of Human Brown and White Adipocytes Reveals EPDR1 as a Novel Batokine. *Cell Metab* **30**, 963-975 e967, doi:10.1016/j.cmet.2019.10.001 (2019).

4 Blanco, M. A. *et al.* Global secretome analysis identifies novel mediators of bone metastasis. *Cell Res* **22**, 1339-1355, doi:10.1038/cr.2012.89 (2012).

5 Phulphagar, K. *et al.* Proteomics reveals distinct mechanisms regulating the release of cytokines and alarmins during pyroptosis. *Cell Rep* **34**, 108826, doi:10.1016/j.celrep.2021.108826 (2021).

6 Kontos, F. *et al.* B7-H3: An Attractive Target for Antibody-based Immunotherapy. *Clin Cancer Res* **27**, 1227-1235, doi:10.1158/1078-0432.CCR-20-2584 (2021).

7 Zhou, W. T. & Jin, W. L. B7-H3/CD276: An Emerging Cancer Immunotherapy. *Front Immunol* **12**, 701006, doi:10.3389/fimmu.2021.701006 (2021).

8 Podojil, J. R. & Miller, S. D. Potential targeting of B7-H4 for the treatment of cancer. *Immunol Rev* **276**, 40-51, doi:10.1111/imr.12530 (2017).

9 Termini, C. M. & Gillette, J. M. Tetraspanins Function as Regulators of Cellular Signaling. *Front Cell Dev Biol* **5**, 34, doi:10.3389/fcell.2017.00034 (2017).

10 Hay, D. L. & Pioszak, A. A. Receptor Activity-Modifying Proteins (RAMPs): New Insights and Roles. *Annu Rev Pharmacol Toxicol* **56**, 469-487, doi:10.1146/annurev-pharmtox-010715-103120 (2016).

11 Nussinov, R., Jang, H. & Tsai, C. J. Oligomerization and nanocluster organization render specificity. *Biol Rev Camb Philos Soc* **90**, 587-598, doi:10.1111/brv.12124 (2015).

12 Bausch-Fluck, D., Milani, E. S. & Wollscheid, B. Surfaceome nanoscale organization and extracellular interaction networks. *Curr Opin Chem Biol* **48**, 26-33, doi:10.1016/j.cbpa.2018.09.020 (2019).

13 Wood, L. & Wright, G. J. Approaches to identify extracellular receptor-ligand interactions. *Curr Opin Struct Biol* **56**, 28-36, doi:10.1016/j.sbi.2018.10.002 (2019).

14 Santos, R. *et al.* A comprehensive map of molecular drug targets. *Nat Rev Drug Discov* **16**, 19-34, doi:10.1038/nrd.2016.230 (2017).

15 Frei, A. P. *et al.* Direct identification of ligand-receptor interactions on living cells and tissues. *Nat Biotechnol* **30**, 997-1001, doi:10.1038/nbt.2354 (2012).

16 Sobotzki, N. *et al.* HATRIC-based identification of receptors for orphan ligands. *Nat Commun* **9**, 1519, doi:10.1038/s41467-018-03936-z (2018).

17 Qin, W., Cho, K. F., Cavanagh, P. E. & Ting, A. Y. Deciphering molecular interactions by proximity labeling. *Nat Methods* **18**, 133-143, doi:10.1038/s41592-020-01010-5 (2021).

18 Jiang, S. *et al.* A proteomics approach to the cell-surface interactome using the enzyme-mediated activation of radical sources reaction. *Proteomics* **12**, 54-62, doi:10.1002/pmic.201100551 (2012).

19 Li, X. W. *et al.* New insights into the DT40 B cell receptor cluster using a proteomic proximity labeling assay. *J Biol Chem* **289**, 14434-14447, doi:10.1074/jbc.M113.529578 (2014).

20 Li, J. *et al.* Cell-Surface Proteomic Profiling in the Fly Brain Uncovers Wiring Regulators. *Cell* **180**, 373-386 e315, doi:10.1016/j.cell.2019.12.029 (2020).

21 Loh, K. H. *et al.* Proteomic Analysis of Unbounded Cellular Compartments: Synaptic Clefts. *Cell* **166**, 1295-1307 e1221, doi:10.1016/j.cell.2016.07.041 (2016).

22 Oakley, J. V. *et al.* Radius measurement via super-resolution microscopy enables the development of a variable radii proximity labeling platform. *Proc Natl Acad Sci U S A* **119**, e2203027119, doi:10.1073/pnas.2203027119 (2022).

23 Muller, M. *et al.* Light-mediated discovery of surfaceome nanoscale organization and intercellular receptor interaction networks. *Nat Commun* **12**, 7036, doi:10.1038/s41467-021-27280-x (2021).

16

24 Geri, J. B. *et al.* Microenvironment mapping via Dexter energy transfer on immune cells. *Science* **367**, 1091-1097, doi:10.1126/science.aay4106 (2020).
25 Chen, C. L. & Perrimon, N. Proximity-dependent labeling methods for proteomic profiling in living cells. *Wiley Interdiscip Rev Dev Biol* **6**, doi:10.1002/wdev.272 (2017).
26 Oughtred, R. *et al.* The BioGRID database: A comprehensive biomedical resource of curated protein, genetic, and chemical interactions. *Protein Sci* **30**, 187-200, doi:10.1002/pro.3978 (2021).
27 Itzhak, D. N., Tyanova, S., Cox, J. & Borner, G. H. Global, quantitative and dynamic mapping of protein subcellular localization. *Elife* **5**, doi:10.7554/eLife.16950 (2016).
28 Al-Aghbar, M. A., Jainarayanan, A. K., Dustin, M. L. & Roffler, S. R. The interplay between membrane topology and mechanical forces in regulating T cell receptor activity. *Commun Biol* **5**, 40, doi:10.1038/s42003-021-02995-1 (2022).
29 Capitani, N. & Baldari, C. T. The Immunological Synapse: An Emerging Target for Immune Evasion by Bacterial Pathogens. *Front Immunol* **13**, 943344, doi:10.3389/fimmu.2022.943344 (2022).
30 Onnis, A. & Baldari, C. T. Orchestration of Immunological Synapse Assembly by Vesicular Trafficking. *Front Cell Dev Biol* **7**, 110, doi:10.3389/fcell.2019.00110 (2019).
31 Dustin, M. L. The immunological synapse. *Cancer Immunol Res* **2**, 1023-1033, doi:10.1158/2326-6066.CIR-14-0161 (2014).
32 Yu, J., Liang, C. & Liu, S. L. CD4-Dependent Modulation of HIV-1 Entry by LY6E. *J Virol* **93**, doi:10.1128/JVI.01866-18 (2019).
33 Billcliff, P. G. *et al.* CD317/tetherin is an organiser of membrane microdomains. *J Cell Sci* **126**, 1553-1564, doi:10.1242/jcs.112953 (2013).
34 Zhao, X. *et al.* Tetherin/BST2, a physiologically and therapeutically relevant regulator of platelet receptor signalling. *Blood Adv* **5**, 1884-1898, doi:10.1182/bloodadvances.2020003182 (2021).
35 Lingwood, D. & Simons, K. Lipid rafts as a membrane-organizing principle. *Science* **327**, 46-50, doi:10.1126/science.1174621 (2010).
36 Bag, N., Huang, S. & Wohland, T. Plasma Membrane Organization of Epidermal Growth Factor Receptor in Resting and Ligand-Bound States. *Biophys J* **109**, 1925-1936, doi:10.1016/j.bpj.2015.09.007 (2015).
37 Coskun, U., Grzybek, M., Drechsel, D. & Simons, K. Regulation of human EGF receptor by lipids. *Proc Natl Acad Sci U S A* **108**, 9044-9048, doi:10.1073/pnas.1105666108 (2011).
38 Braun, J. *et al.* Neocarzilin Inhibits Cancer Cell Proliferation via BST-2 Degradation, Resulting in Lipid Raft-Trapped EGFR. *JACS Au* **4**, 1833-1840, doi:10.1021/jacsau.4c00039 (2024).
39 Yang, D. *et al.* Increased plasmin-mediated proteolysis of L1CAM in a mouse model of idiopathic normal pressure hydrocephalus. *Proc Natl Acad Sci U S A* **118**, doi:10.1073/pnas.2010528118 (2021).
40 Hunte, R. *et al.* CADM1 is essential for KSHV-encoded vGPCR-and vFLIP-mediated chronic NF-kappaB activation. *PLoS Pathog* **14**, e1006968, doi:10.1371/journal.ppat.1006968 (2018).
41 Staebler, S. *et al.* The Role of T-Cadherin (CDH13) in Treatment Options with Garcinol in Melanoma. *Cancers (Basel)* **16**, doi:10.3390/cancers16101853 (2024).
42 Kovacs, T., Zakany, F. & Nagy, P. It Takes More than Two to Tango: Complex, Hierarchal, and Membrane-Modulated Interactions in the Regulation of Receptor Tyrosine Kinases. *Cancers (Basel)* **14**, doi:10.3390/cancers14040944 (2022).
43 Garrett, T. P. *et al.* The crystal structure of a truncated ErbB2 ectodomain reveals an active conformation, poised to interact with other ErbB receptors. *Mol Cell* **11**, 495-505, doi:10.1016/s1097-2765(03)00048-0 (2003).
44 Kuhbandner, K., Herz, J. & Pohlkamp, T. in *Biochemistry of lipids, lipoproteins and membranes* 583-622 (Elsevier, 2021).
45 Dieckmann, M., Dietrich, M. F. & Herz, J. Lipoprotein receptors--an evolutionarily ancient multifunctional receptor family. *Biol Chem* **391**, 1341-1363, doi:10.1515/BC.2010.129 (2010).

46 Bres, E. E. & Faissner, A. Low Density Receptor-Related Protein 1 Interactions With the Extracellular Matrix: More Than Meets the Eye. *Front Cell Dev Biol* **7**, 31, doi:10.3389/fcell.2019.00031 (2019).
47 Chang, C. *et al.* LRP-1 receptor combines EGFR signalling and eHsp90alpha autocrine to support constitutive breast cancer cell motility in absence of blood supply. *Sci Rep* **12**, 12006, doi:10.1038/s41598-022-16161-y (2022).
48 Uhlen, M. *et al.* Proteomics. Tissue-based map of the human proteome. *Science* **347**, 1260419, doi:10.1126/science.1260419 (2015).
49 Heil, L. R. *et al.* Evaluating the Performance of the Astral Mass Analyzer for Quantitative Proteomics Using Data-Independent Acquisition. *J Proteome Res* **22**, 3290-3300, doi:10.1021/acs.jproteome.3c00357 (2023).
50 Ctortecka, C. *et al.* Automated single-cell proteomics providing sufficient proteome depth to study complex biology beyond cell type classifications. *Nat Commun* **15**, 5707, doi:10.1038/s41467-024-49651-w (2024).

4. Discussion

Exploring the molecular mechanisms of intercellular communication is essential for advancing our understanding of biology and developing targeted therapies for disease. Proteins are key players in intercellular communication, functioning as signals and signal receptors, making mass spectrometry-based proteomics methods excellent tools for their investigation. Yet, important aspects of intercellular signaling remain understudied due to unresolved technical challenges. In my thesis, I applied state-of-the-art proteomics methods to investigate intercellular communication in the immune system and cancer, and focused on developing new approaches to address existing technological gaps and limitations.

Building on one of the earliest comprehensive studies of activation-state-dependent immune cell secretomes[40], our group has extensively researched cellular protein secretion across various biological contexts. Despite their importance, many key classes of communication signals, such as chemokines, are often among the least abundant cell-released proteins, making them challenging to detect. Article 4 demonstrates the strengths of our latest serum-free secretome profiling workflow. While relying on isolated cells cultured *in vitro*, this approach typically offers the lowest detection limits and deepest insights into released signaling proteins of all MS-based secretomics methods. An in-depth analysis of cancer cell-secreted immunomodulatory proteins enabled a detailed assessment of treatment-induced changes in communication pathways between cancer and immune cells, successfully identifying key factors driving therapy-induced remodeling of the tumor microenvironment. Analyzing signaling protein expression and secretion directly, rather than inferring from transcript levels, accounts for the numerous layers of post-transcriptional and post-translational regulation, thereby providing accurate quantitative insights into cell communication[40]. Beyond that, proteomics methods offer unique opportunities for discovering proteins with unexpected roles in intercellular signaling or cell-release pathways that are hard to predict[258]. The latter is highlighted in Article 5, where serum-free secretomics combined with biochemical and genetic tools has systematically deconvoluted protein release dynamics and exit routes in the highly complex process of pyroptosis, a form of programmed cell death with crucial immune signaling functions. The straightforward workflow, low input material requirements, scalability, and deep signaling protein coverage establish serum-free secretomics as the current gold standard for global analyses of cellular protein release. However, given the

highly dynamic adaptions of cell secretomes to environmental factors and the critical role of reciprocal communication with neighboring cells, secretomics approaches that capture protein secretion in its native context are highly desirable.

Outlined in Articles 2 and 3, we introduced new workflows aimed at capturing cell-selective protein secretion as close to native contexts as possible to address the limitations of conventional serum-free secretomics. After extensive method development that significantly enhanced specific yields and protein coverage, we successfully employed MetRS*-based azidonorleucine (Anl) protein labeling for detailed cell-selective analyses of intercellular signaling proteins in heterocellular model systems of various complexity. While currently requiring at least 10fold higher input material and more intricate sample preparation than typical serum-free experiments, MetRS*-based *in vitro* secretomics offers detailed cell type-resolved insights into reciprocal intercellular signaling between co-cultured cells. The ability to specifically enrich labeled proteins sets this method apart from alternative techniques, such as cell-selective labeling with amino acid precursors (CTAP), supporting full serum compatibility *in vitro* and ensuring effectiveness within tissue environments *in vivo*. We showed that MetRS*-based whole tissue analysis captures proteins in the extracellular space in addition to cell-intrinsic proteins, significantly increasing the coverage of important signaling proteins compared to cell sorting-based analyses. Applied to mouse models of pancreatic ductal adenocarcinoma (PDAC), we contributed to the urgently needed characterization of major molecular subtypes, uncovering immunomodulatory signals that shaped the distinct microenvironments of mesenchymal and classical PDAC tumors. Moreover, a comprehensive analysis of extracellular matrix (ECM) proteins produced by cancer cells revealed striking subtype-specific differences, including proteins recently identified as promising drug targets[249-251]. Notably, Anl-labeling also allowed enrichment and quantification of more than 1600 cancer cell-derived proteins from the blood of tumor-bearing mice, capturing 64 CellPhoneDB-annotated[66] messengers for intercellular communication, and clearly differentiating between cancer subtypes. This exemplifies how the technology opens new avenues for exploring processes that involve long-distance cell communication, such as pre-metastatic niche formation, and suggests high value for biomarker discovery.

Until recently, no cell-selective secretomics method effective *in vivo* was available, but newly developed proximity labeling-based approaches now provide an alternative to our

MetRS*-based method. Proof-of-concept studies granted valuable insights, for example, into diet-dependent changes to hepatocyte secretomes in living mice[120]. So far, however, signaling protein coverage has been very limited, and toxicity, immunogenicity, and other potential side effects remain to be evaluated. While MetRS*-based cell-selective proteomics and secretomics methods compare favorably to other approaches, ongoing developments will help make them more widely applicable and accessible. Recent advances in the automation of click chemistry workflows[259] have laid the groundwork for streamlining sample preparation and increasing throughput, facilitating larger scale studies. Moreover, technical breakthroughs in ultra-high sensitivity MS instruments[78,95,96] significantly decrease input material requirements, enabling the effective application of MetRS*-based cell-selective proteomics and secretomics to small cell populations.

Growing data on comprehensive cell secretomes across diverse biological contexts advance our understanding of intercellular communication while also revealing gaps in our knowledge of signaling pathways. Cell secretomes harbor secreted proteins with unknown functions or mechanisms of action, dynamically modified proteoforms with unclear functional roles, and proteins lacking conventional secretion signals that may moonlight as intercellular signals through unconventional secretion pathways. Yet, the lack of a clear roadmap for efficiently evaluating new signaling protein candidates has left this 'dark matter' of secretomes underexplored. Article 6 introduces a scalable proximity labeling (PL)-based technology platform for the identification of candidate target cells and their corresponding surface receptor proteins, key steps in uncovering their potential roles in intercellular communication. Recently, PL has emerged as a particularly powerful approach for both the systematic profiling of cell surface protein interactions *in situ*[173] and elucidating the spatial arrangement of the surfaceome[260] - an important, yet often neglected aspect of signal reception and transmission. Newly developed specialized PL approaches minimize steric hindrance using small catalysts and offer high spatial resolution through the activation of short-lived labeling probes[182,184]. However, a critical challenge remained: PL experiments often fail to reliably differentiate between functionally associated proteins and those that are simply co-localized within the same cellular compartment, necessitating elaborate control strategies and extensive follow-up experiments to validate the often large number of identified candidates. A key feature of our novel PL approach directly addresses this challenge. By quantifying captured proteins across experiments with incrementally varied PL radii, modulated with scavenger additives, we generated characteristic enrichment profiles that closely correlated with their spatial relationships to the PL source. Using the example of EGF, its cognate receptor,

and associated proteins expressed on the HeLa cell surface, we demonstrated how this method significantly simplifies the reliable detection of surface protein-protein interactions and offers valuable insights for mapping proteins systematically clustered in membrane microdomains. Furthermore, leveraging the high temporal resolution of peroxidase PL, we anticipate that this approach will facilitate the monitoring of protein rearrangements in signaling complexes, providing a deeper understanding of protein dynamics at the cell surface in response to stimulation. Although protocols cannot be directly applied to cell-intrinsic applications, the principles of analyzing enrichment profiles across incrementally varied PL radii may be transferrable when using membrane-permeable radical scavengers or other means of radius modulation. Likewise, the approach is not limited to peroxidase-based labeling and could potentially be applied to alternative PL techniques like uMap[184] and MS-Lux[182]. Therefore, broader adoption of these concepts should be evaluated in future studies and may provide significant advantages in the field of PL.

In conclusion, this thesis presents advancements that bridge previous technological gaps in the study of intercellular communication, establishing new benchmarks for analyzing cell-selective secretomes and signaling protein interactions in their native environment. Applications of these approaches revealed novel insights into innate immune cell signaling and contributed to the molecular characterization of pancreatic ductal adenocarcinoma subtypes. Collectively, the findings of this work will accelerate future research into the molecular mechanisms of cellular interactions.

5. References

1 Alvarez-Castelao, B. *et al.* Cell-type-specific metabolic labeling of nascent proteomes in vivo. *Nat Biotechnol* **35**, 1196-1201, doi:10.1038/nbt.4016 (2017).

2 Swietlik, J. J. *et al.* Cell-selective proteomics segregates pancreatic cancer subtypes by extracellular proteins in tumors and circulation. *Nat Commun* **14**, 2642, doi:10.1038/s41467-023-38171-8 (2023).

3 Swietlik, J. J. & Meissner, F. MetRS*-based deep cell-selective tissue proteomics and secretomics in vivo. (2024).

4 Swietlik, J. J., Sinha, A. & Meissner, F. Dissecting intercellular signaling with mass spectrometry-based proteomics. *Curr Opin Cell Biol* **63**, 20-30, doi:10.1016/j.ceb.2019.12.002 (2020).

5 de Visser, K. E. & Joyce, J. A. The evolving tumor microenvironment: From cancer initiation to metastatic outgrowth. *Cancer Cell* **41**, 374-403, doi:10.1016/j.ccell.2023.02.016 (2023).

6 Crouigneau, R. *et al.* Mimicking and analyzing the tumor microenvironment. *Cell Rep Methods* **4**, 100866, doi:10.1016/j.crmeth.2024.100866 (2024).

7 Hanahan, D. & Weinberg, R. A. Hallmarks of cancer: the next generation. *Cell* **144**, 646-674, doi:10.1016/j.cell.2011.02.013 (2011).

8 Hanahan, D. Hallmarks of Cancer: New Dimensions. *Cancer Discov* **12**, 31-46, doi:10.1158/2159-8290.CD-21-1059 (2022).

9 Winkler, J., Abisoye-Ogunniyan, A., Metcalf, K. J. & Werb, Z. Concepts of extracellular matrix remodelling in tumour progression and metastasis. *Nat Commun* **11**, 5120, doi:10.1038/s41467-020-18794-x (2020).

10 Hanahan, D. & Weinberg, R. A. The hallmarks of cancer. *Cell* **100**, 57-70, doi:10.1016/s0092-8674(00)81683-9 (2000).

11 Bhowmick, N. A., Neilson, E. G. & Moses, H. L. Stromal fibroblasts in cancer initiation and progression. *Nature* **432**, 332-337, doi:10.1038/nature03096 (2004).

12 Sahai, E. *et al.* A framework for advancing our understanding of cancer-associated fibroblasts. *Nat Rev Cancer* **20**, 174-186, doi:10.1038/s41568-019-0238-1 (2020).

13 Kalluri, R. The biology and function of fibroblasts in cancer. *Nat Rev Cancer* **16**, 582-598, doi:10.1038/nrc.2016.73 (2016).

14 Liu, Z. L., Chen, H. H., Zheng, L. L., Sun, L. P. & Shi, L. Angiogenic signaling pathways and anti-angiogenic therapy for cancer. *Signal Transduct Target Ther* **8**, 198, doi:10.1038/s41392-023-01460-1 (2023).

15 Hanahan, D. & Folkman, J. Patterns and emerging mechanisms of the angiogenic switch during tumorigenesis. *Cell* **86**, 353-364, doi:10.1016/s0092-8674(00)80108-7 (1996).

16 Lugano, R., Ramachandran, M. & Dimberg, A. Tumor angiogenesis: causes, consequences, challenges and opportunities. *Cell Mol Life Sci* **77**, 1745-1770, doi:10.1007/s00018-019-03351-7 (2020).

17 Weis, S. M. & Cheresh, D. A. Tumor angiogenesis: molecular pathways and therapeutic targets. *Nat Med* **17**, 1359-1370, doi:10.1038/nm.2537 (2011).

18 Zitvogel, L., Tesniere, A. & Kroemer, G. Cancer despite immunosurveillance: immunoselection and immunosubversion. *Nat Rev Immunol* **6**, 715-727, doi:10.1038/nri1936 (2006).

19 Shankaran, V. *et al.* IFNgamma and lymphocytes prevent primary tumour development and shape tumour immunogenicity. *Nature* **410**, 1107-1111, doi:10.1038/35074122 (2001).

20 Schreiber, R. D., Old, L. J. & Smyth, M. J. Cancer immunoediting: integrating immunity's roles in cancer suppression and promotion. *Science* **331**, 1565-1570, doi:10.1126/science.1203486 (2011).
21 van Weverwijk, A. & de Visser, K. E. Mechanisms driving the immunoregulatory function of cancer cells. *Nat Rev Cancer* **23**, 193-215, doi:10.1038/s41568-022-00544-4 (2023).
22 Shields, J. D., Kourtis, I. C., Tomei, A. A., Roberts, J. M. & Swartz, M. A. Induction of lymphoidlike stroma and immune escape by tumors that express the chemokine CCL21. *Science* **328**, 749-752, doi:10.1126/science.1185837 (2010).
23 Binnewies, M. *et al.* Understanding the tumor immune microenvironment (TIME) for effective therapy. *Nat Med* **24**, 541-550, doi:10.1038/s41591-018-0014-x (2018).
24 Garner, H. & de Visser, K. E. Immune crosstalk in cancer progression and metastatic spread: a complex conversation. *Nat Rev Immunol* **20**, 483-497, doi:10.1038/s41577-019-0271-z (2020).
25 Coussens, L. M. & Werb, Z. Inflammation and cancer. *Nature* **420**, 860-867, doi:10.1038/nature01322 (2002).
26 Valastyan, S. & Weinberg, R. A. Tumor metastasis: molecular insights and evolving paradigms. *Cell* **147**, 275-292, doi:10.1016/j.cell.2011.09.024 (2011).
27 Fares, J., Fares, M. Y., Khachfe, H. H., Salhab, H. A. & Fares, Y. Molecular principles of metastasis: a hallmark of cancer revisited. *Signal Transduct Target Ther* **5**, 28, doi:10.1038/s41392-020-0134-x (2020).
28 Paget, S. The distribution of secondary growths in cancer of the breast. 1889. *Cancer Metastasis Rev* **8**, 98-101 (1989).
29 Kaplan, R. N. *et al.* VEGFR1-positive haematopoietic bone marrow progenitors initiate the pre-metastatic niche. *Nature* **438**, 820-827, doi:10.1038/nature04186 (2005).
30 Peinado, H. *et al.* Pre-metastatic niches: organ-specific homes for metastases. *Nat Rev Cancer* **17**, 302-317, doi:10.1038/nrc.2017.6 (2017).
31 Couzin-Frankel, J. Breakthrough of the year 2013. Cancer immunotherapy. *Science* **342**, 1432-1433, doi:10.1126/science.342.6165.1432 (2013).
32 Ishida, Y., Agata, Y., Shibahara, K. & Honjo, T. Induced expression of PD-1, a novel member of the immunoglobulin gene superfamily, upon programmed cell death. *EMBO J* **11**, 3887-3895, doi:10.1002/j.1460-2075.1992.tb05481.x (1992).
33 Leach, D. R., Krummel, M. F. & Allison, J. P. Enhancement of antitumor immunity by CTLA-4 blockade. *Science* **271**, 1734-1736, doi:10.1126/science.271.5256.1734 (1996).
34 Iwai, Y. *et al.* Involvement of PD-L1 on tumor cells in the escape from host immune system and tumor immunotherapy by PD-L1 blockade. *Proc Natl Acad Sci U S A* **99**, 12293-12297, doi:10.1073/pnas.192461099 (2002).
35 Ishida, Y. PD-1: Its Discovery, Involvement in Cancer Immunotherapy, and Beyond. *Cells* **9**, doi:10.3390/cells9061376 (2020).
36 Tan, S., Li, D. & Zhu, X. Cancer immunotherapy: Pros, cons and beyond. *Biomed Pharmacother* **124**, 109821, doi:10.1016/j.biopha.2020.109821 (2020).
37 Vesely, M. D., Zhang, T. & Chen, L. Resistance Mechanisms to Anti-PD Cancer Immunotherapy. *Annu Rev Immunol* **40**, 45-74, doi:10.1146/annurev-immunol-070621-030155 (2022).
38 Kraehenbuehl, L., Weng, C. H., Eghbali, S., Wolchok, J. D. & Merghoub, T. Enhancing immunotherapy in cancer by targeting emerging immunomodulatory pathways. *Nat Rev Clin Oncol* **19**, 37-50, doi:10.1038/s41571-021-00552-7 (2022).
39 Uhlen, M. *et al.* The human secretome. *Sci Signal* **12**, doi:10.1126/scisignal.aaz0274 (2019).

40 Meissner, F., Scheltema, R. A., Mollenkopf, H. J. & Mann, M. Direct proteomic quantification of the secretome of activated immune cells. *Science* **340**, 475-478, doi:10.1126/science.1232578 (2013).
41 Tanzer, M. C. *et al.* Quantitative and Dynamic Catalogs of Proteins Released during Apoptotic and Necroptotic Cell Death. *Cell Rep* **30**, 1260-1270 e1265, doi:10.1016/j.celrep.2019.12.079 (2020).
42 Uhlen, M. *et al.* Proteomics. Tissue-based map of the human proteome. *Science* **347**, 1260419, doi:10.1126/science.1260419 (2015).
43 Kayagaki, N. *et al.* Caspase-11 cleaves gasdermin D for non-canonical inflammasome signalling. *Nature* **526**, 666-671, doi:10.1038/nature15541 (2015).
44 Shi, J. *et al.* Cleavage of GSDMD by inflammatory caspases determines pyroptotic cell death. *Nature* **526**, 660-665, doi:10.1038/nature15514 (2015).
45 Cypryk, W., Nyman, T. A. & Matikainen, S. From Inflammasome to Exosome-Does Extracellular Vesicle Secretion Constitute an Inflammasome-Dependent Immune Response? *Front Immunol* **9**, 2188, doi:10.3389/fimmu.2018.02188 (2018).
46 Lopez-Castejon, G. & Brough, D. Understanding the mechanism of IL-1beta secretion. *Cytokine Growth Factor Rev* **22**, 189-195, doi:10.1016/j.cytogfr.2011.10.001 (2011).
47 Zhang, M. *et al.* A Translocation Pathway for Vesicle-Mediated Unconventional Protein Secretion. *Cell* **181**, 637-652 e615, doi:10.1016/j.cell.2020.03.031 (2020).
48 Jang, D. I. *et al.* The Role of Tumor Necrosis Factor Alpha (TNF-alpha) in Autoimmune Disease and Current TNF-alpha Inhibitors in Therapeutics. *Int J Mol Sci* **22**, doi:10.3390/ijms22052719 (2021).
49 Palladino, M. A., Bahjat, F. R., Theodorakis, E. A. & Moldawer, L. L. Anti-TNF-alpha therapies: the next generation. *Nat Rev Drug Discov* **2**, 736-746, doi:10.1038/nrd1175 (2003).
50 Parameswaran, N. & Patial, S. Tumor necrosis factor-alpha signaling in macrophages. *Crit Rev Eukaryot Gene Expr* **20**, 87-103, doi:10.1615/critreveukargeneexpr.v20.i2.10 (2010).
51 Lichtenthaler, S. F., Lemberg, M. K. & Fluhrer, R. Proteolytic ectodomain shedding of membrane proteins in mammals-hardware, concepts, and recent developments. *EMBO J* **37**, doi:10.15252/embj.201899456 (2018).
52 Laurent, S. A. *et al.* gamma-Secretase directly sheds the survival receptor BCMA from plasma cells. *Nat Commun* **6**, 7333, doi:10.1038/ncomms8333 (2015).
53 Bianchi, M. E. DAMPs, PAMPs and alarmins: all we need to know about danger. *J Leukoc Biol* **81**, 1-5, doi:10.1189/jlb.0306164 (2007).
54 Chen, R., Kang, R. & Tang, D. The mechanism of HMGB1 secretion and release. *Exp Mol Med* **54**, 91-102, doi:10.1038/s12276-022-00736-w (2022).
55 Li, S., Wong, A. H. & Liu, F. Ligand-gated ion channel interacting proteins and their role in neuroprotection. *Front Cell Neurosci* **8**, 125, doi:10.3389/fncel.2014.00125 (2014).
56 Hubbard, S. R. & Miller, W. T. Receptor tyrosine kinases: mechanisms of activation and signaling. *Curr Opin Cell Biol* **19**, 117-123, doi:10.1016/j.ceb.2007.02.010 (2007).
57 Lemmon, M. A. & Schlessinger, J. Cell signaling by receptor tyrosine kinases. *Cell* **141**, 1117-1134, doi:10.1016/j.cell.2010.06.011 (2010).
58 Trenker, R. & Jura, N. Receptor tyrosine kinase activation: From the ligand perspective. *Curr Opin Cell Biol* **63**, 174-185, doi:10.1016/j.ceb.2020.01.016 (2020).
59 Leonard, W. J. & Lin, J. X. Cytokine receptor signaling pathways. *J Allergy Clin Immunol* **105**, 877-888, doi:10.1067/mai.2000.106899 (2000).

60 Morris, R., Kershaw, N. J. & Babon, J. J. The molecular details of cytokine signaling via the JAK/STAT pathway. *Protein Sci* **27**, 1984-2009, doi:10.1002/pro.3519 (2018).
61 Wootten, D., Christopoulos, A., Marti-Solano, M., Babu, M. M. & Sexton, P. M. Mechanisms of signalling and biased agonism in G protein-coupled receptors. *Nat Rev Mol Cell Biol* **19**, 638-653, doi:10.1038/s41580-018-0049-3 (2018).
62 Yang, D. *et al.* G protein-coupled receptors: structure- and function-based drug discovery. *Signal Transduct Target Ther* **6**, 7, doi:10.1038/s41392-020-00435-w (2021).
63 Rosenbaum, D. M., Rasmussen, S. G. & Kobilka, B. K. The structure and function of G-protein-coupled receptors. *Nature* **459**, 356-363, doi:10.1038/nature08144 (2009).
64 Wieduwilt, M. J. & Moasser, M. M. The epidermal growth factor receptor family: biology driving targeted therapeutics. *Cell Mol Life Sci* **65**, 1566-1584, doi:10.1007/s00018-008-7440-8 (2008).
65 Smith, J. S., Lefkowitz, R. J. & Rajagopal, S. Biased signalling: from simple switches to allosteric microprocessors. *Nat Rev Drug Discov* **17**, 243-260, doi:10.1038/nrd.2017.229 (2018).
66 Efremova, M., Vento-Tormo, M., Teichmann, S. A. & Vento-Tormo, R. CellPhoneDB: inferring cell-cell communication from combined expression of multi-subunit ligand-receptor complexes. *Nat Protoc* **15**, 1484-1506, doi:10.1038/s41596-020-0292-x (2020).
67 Jin, S. *et al.* Inference and analysis of cell-cell communication using CellChat. *Nat Commun* **12**, 1088, doi:10.1038/s41467-021-21246-9 (2021).
68 Rieckmann, J. C. *et al.* Social network architecture of human immune cells unveiled by quantitative proteomics. *Nat Immunol* **18**, 583-593, doi:10.1038/ni.3693 (2017).
69 International Human Genome Sequencing, C. Finishing the euchromatic sequence of the human genome. *Nature* **431**, 931-945, doi:10.1038/nature03001 (2004).
70 Wang, E. T. *et al.* Alternative isoform regulation in human tissue transcriptomes. *Nature* **456**, 470-476, doi:10.1038/nature07509 (2008).
71 Pan, Q., Shai, O., Lee, L. J., Frey, B. J. & Blencowe, B. J. Deep surveying of alternative splicing complexity in the human transcriptome by high-throughput sequencing. *Nat Genet* **40**, 1413-1415, doi:10.1038/ng.259 (2008).
72 Schluter, H., Apweiler, R., Holzhutter, H. G. & Jungblut, P. R. Finding one's way in proteomics: a protein species nomenclature. *Chem Cent J* **3**, 11, doi:10.1186/1752-153X-3-11 (2009).
73 UniProt, C. Reorganizing the protein space at the Universal Protein Resource (UniProt). *Nucleic Acids Res* **40**, D71-75, doi:10.1093/nar/gkr981 (2012).
74 Smith, L. M., Kelleher, N. L. & Consortium for Top Down, P. Proteoform: a single term describing protein complexity. *Nat Methods* **10**, 186-187, doi:10.1038/nmeth.2369 (2013).
75 Yang, X. *et al.* Widespread Expansion of Protein Interaction Capabilities by Alternative Splicing. *Cell* **164**, 805-817, doi:10.1016/j.cell.2016.01.029 (2016).
76 Bowler, E. & Oltean, S. Alternative Splicing in Angiogenesis. *Int J Mol Sci* **20**, doi:10.3390/ijms20092067 (2019).
77 Aebersold, R. *et al.* How many human proteoforms are there? *Nat Chem Biol* **14**, 206-214, doi:10.1038/nchembio.2576 (2018).
78 Guzman, U. H. *et al.* Ultra-fast label-free quantification and comprehensive proteome coverage with narrow-window data-independent acquisition. *Nat Biotechnol*, doi:10.1038/s41587-023-02099-7 (2024).

79 Tanzer, M. C., Bludau, I., Stafford, C. A., Hornung, V. & Mann, M. Phosphoproteome profiling uncovers a key role for CDKs in TNF signaling. *Nat Commun* **12**, 6053, doi:10.1038/s41467-021-26289-6 (2021).
80 Hansen, F. M. *et al.* Data-independent acquisition method for ubiquitinome analysis reveals regulation of circadian biology. *Nat Commun* **12**, 254, doi:10.1038/s41467-020-20509-1 (2021).
81 Zecha, J. *et al.* Decrypting drug actions and protein modifications by dose- and time-resolved proteomics. *Science* **380**, 93-101, doi:10.1126/science.ade3925 (2023).
82 Meissner, F., Geddes-McAlister, J., Mann, M. & Bantscheff, M. The emerging role of mass spectrometry-based proteomics in drug discovery. *Nat Rev Drug Discov* **21**, 637-654, doi:10.1038/s41573-022-00409-3 (2022).
83 Steger, M., Karayel, O. & Demichev, V. Ubiquitinomics: History, methods, and applications in basic research and drug discovery. *Proteomics* **22**, e2200074, doi:10.1002/pmic.202200074 (2022).
84 Eckert, S. *et al.* Decrypting the molecular basis of cellular drug phenotypes by dose-resolved expression proteomics. *Nat Biotechnol*, doi:10.1038/s41587-024-02218-y (2024).
85 Deshmukh, A. S. *et al.* Proteomics-Based Comparative Mapping of the Secretomes of Human Brown and White Adipocytes Reveals EPDR1 as a Novel Batokine. *Cell Metab* **30**, 963-975 e967, doi:10.1016/j.cmet.2019.10.001 (2019).
86 Vanheule, V., Metzemaekers, M., Janssens, R., Struyf, S. & Proost, P. How post-translational modifications influence the biological activity of chemokines. *Cytokine* **109**, 29-51, doi:10.1016/j.cyto.2018.02.026 (2018).
87 Liu, Y., Beyer, A. & Aebersold, R. On the Dependency of Cellular Protein Levels on mRNA Abundance. *Cell* **165**, 535-550, doi:10.1016/j.cell.2016.03.014 (2016).
88 Bausch-Fluck, D. *et al.* A mass spectrometric-derived cell surface protein atlas. *PLoS One* **10**, e0121314, doi:10.1371/journal.pone.0121314 (2015).
89 Schwanhausser, B. *et al.* Global quantification of mammalian gene expression control. *Nature* **473**, 337-342, doi:10.1038/nature10098 (2011).
90 Wollscheid, B. *et al.* Mass-spectrometric identification and relative quantification of N-linked cell surface glycoproteins. *Nat Biotechnol* **27**, 378-386, doi:10.1038/nbt.1532 (2009).
91 Fang, J. *et al.* The target atlas for antibody-drug conjugates across solid cancers. *Cancer Gene Ther* **31**, 273-284, doi:10.1038/s41417-023-00701-3 (2024).
92 Mandal, K. *et al.* Structural surfaceomics reveals an AML-specific conformation of integrin beta(2) as a CAR T cellular therapy target. *Nat Cancer* **4**, 1592-1609, doi:10.1038/s43018-023-00652-6 (2023).
93 Hosen, N. *et al.* The activated conformation of integrin beta(7) is a novel multiple myeloma-specific target for CAR T cell therapy. *Nat Med* **23**, 1436-1443, doi:10.1038/nm.4431 (2017).
94 Uniken Venema, W. T. C. *et al.* Gut mucosa dissociation protocols influence cell type proportions and single-cell gene expression levels. *Sci Rep* **12**, 9897, doi:10.1038/s41598-022-13812-y (2022).
95 Brunner, A. D. *et al.* Ultra-high sensitivity mass spectrometry quantifies single-cell proteome changes upon perturbation. *Mol Syst Biol* **18**, e10798, doi:10.15252/msb.202110798 (2022).
96 Heil, L. R. *et al.* Evaluating the Performance of the Astral Mass Analyzer for Quantitative Proteomics Using Data-Independent Acquisition. *J Proteome Res* **22**, 3290-3300, doi:10.1021/acs.jproteome.3c00357 (2023).
97 Mund, A. *et al.* Deep Visual Proteomics defines single-cell identity and heterogeneity. *Nat Biotechnol*, doi:10.1038/s41587-022-01302-5 (2022).

98 Rosenberger, F. A. *et al.* Spatial single-cell mass spectrometry defines zonation of the hepatocyte proteome. *Nat Methods* **20**, 1530-1536, doi:10.1038/s41592-023-02007-6 (2023).
99 Ong, S. E. *et al.* Stable isotope labeling by amino acids in cell culture, SILAC, as a simple and accurate approach to expression proteomics. *Mol Cell Proteomics* **1**, 376-386, doi:10.1074/mcp.m200025-mcp200 (2002).
100 Jorgensen, C. *et al.* Cell-specific information processing in segregating populations of Eph receptor ephrin-expressing cells. *Science* **326**, 1502-1509, doi:10.1126/science.1176615 (2009).
101 Gauthier, N. P. *et al.* Cell-selective labeling using amino acid precursors for proteomic studies of multicellular environments. *Nat Methods* **10**, 768-773, doi:10.1038/nmeth.2529 (2013).
102 Tape, C. J. *et al.* Cell-specific labeling enzymes for analysis of cell-cell communication in continuous co-culture. *Mol Cell Proteomics* **13**, 1866-1876, doi:10.1074/mcp.O113.037119 (2014).
103 Tape, C. J. *et al.* Oncogenic KRAS Regulates Tumor Cell Signaling via Stromal Reciprocation. *Cell* **165**, 910-920, doi:10.1016/j.cell.2016.03.029 (2016).
104 Dieterich, D. C., Link, A. J., Graumann, J., Tirrell, D. A. & Schuman, E. M. Selective identification of newly synthesized proteins in mammalian cells using bioorthogonal noncanonical amino acid tagging (BONCAT). *Proc Natl Acad Sci U S A* **103**, 9482-9487, doi:10.1073/pnas.0601637103 (2006).
105 Eichelbaum, K., Winter, M., Berriel Diaz, M., Herzig, S. & Krijgsveld, J. Selective enrichment of newly synthesized proteins for quantitative secretome analysis. *Nat Biotechnol* **30**, 984-990, doi:10.1038/nbt.2356 (2012).
106 Yang, A. C. *et al.* Multiple Click-Selective tRNA Synthetases Expand Mammalian Cell-Specific Proteomics. *J Am Chem Soc* **140**, 7046-7051, doi:10.1021/jacs.8b03074 (2018).
107 Ngo, J. T. *et al.* Cell-selective metabolic labeling of proteins. *Nat Chem Biol* **5**, 715-717, doi:10.1038/nchembio.200 (2009).
108 Mahdavi, A. *et al.* Engineered Aminoacyl-tRNA Synthetase for Cell-Selective Analysis of Mammalian Protein Synthesis. *J Am Chem Soc* **138**, 4278-4281, doi:10.1021/jacs.5b08980 (2016).
109 Erdmann, I. *et al.* Cell Type-specific Metabolic Labeling of Proteins with Azidonorleucine in Drosophila. *Bio Protoc* **7**, e2397, doi:10.21769/BioProtoc.2397 (2017).
110 Alvarez-Castelao, B., Schanzenbacher, C. T., Langer, J. D. & Schuman, E. M. Cell-type-specific metabolic labeling, detection and identification of nascent proteomes in vivo. *Nat Protoc* **14**, 556-575, doi:10.1038/s41596-018-0106-6 (2019).
111 Drescher, H., Weiskirchen, S. & Weiskirchen, R. Flow Cytometry: A Blessing and a Curse. *Biomedicines* **9**, doi:10.3390/biomedicines9111613 (2021).
112 Azizian, N. G. *et al.* Selective Labeling and Identification of the Tumor Cell Proteome of Pancreatic Cancer In Vivo. *J Proteome Res* **20**, 858-866, doi:10.1021/acs.jproteome.0c00666 (2021).
113 Prabhakar, P. *et al.* Monitoring regional astrocyte diversity by cell type-specific proteomic labeling in vivo. *Glia* **71**, 682-703, doi:10.1002/glia.24304 (2023).
114 Evans, H. T., Bodea, L. G. & Gotz, J. Cell-specific non-canonical amino acid labelling identifies changes in the de novo proteome during memory formation. *Elife* **9**, doi:10.7554/eLife.52990 (2020).
115 Muller, A., Stellmacher, A., Freitag, C. E., Landgraf, P. & Dieterich, D. C. Monitoring Astrocytic Proteome Dynamics by Cell Type-Specific Protein Labeling. *PLoS One* **10**, e0145451, doi:10.1371/journal.pone.0145451 (2015).

116 Rayaprolu, S. *et al.* Cell type-specific biotin labeling in vivo resolves regional neuronal and astrocyte proteomic differences in mouse brain. *Nat Commun* **13**, 2927, doi:10.1038/s41467-022-30623-x (2022).
117 Soto, J. S., Jami-Alahmadi, Y., Wohlschlegel, J. A. & Khakh, B. S. In vivo identification of astrocyte and neuron subproteomes by proximity-dependent biotinylation. *Nat Protoc* **19**, 896-927, doi:10.1038/s41596-023-00923-7 (2024).
118 Enstrom, A., Carlsson, R., Buizza, C., Lewi, M. & Paul, G. Pericyte-Specific Secretome Profiling in Hypoxia Using TurboID in a Multicellular in Vitro Spheroid Model. *Mol Cell Proteomics* **23**, 100782, doi:10.1016/j.mcpro.2024.100782 (2024).
119 Sunna, S. *et al.* Cellular Proteomic Profiling Using Proximity Labeling by TurboID-NES in Microglial and Neuronal Cell Lines. *Mol Cell Proteomics* **22**, 100546, doi:10.1016/j.mcpro.2023.100546 (2023).
120 Wei, W. *et al.* Cell type-selective secretome profiling in vivo. *Nat Chem Biol* **17**, 326-334, doi:10.1038/s41589-020-00698-y (2021).
121 Kim, K. E. *et al.* Dynamic tracking and identification of tissue-specific secretory proteins in the circulation of live mice. *Nat Commun* **12**, 5204, doi:10.1038/s41467-021-25546-y (2021).
122 Liu, J., Jang, J. Y., Pirooznia, M., Liu, S. & Finkel, T. The secretome mouse provides a genetic platform to delineate tissue-specific in vivo secretion. *Proc Natl Acad Sci U S A* **118**, doi:10.1073/pnas.2005134118 (2021).
123 Droujinine, I. A. *et al.* Proteomics of protein trafficking by in vivo tissue-specific labeling. *Nat Commun* **12**, 2382, doi:10.1038/s41467-021-22599-x (2021).
124 Nurk, S. *et al.* The complete sequence of a human genome. *Science* **376**, 44-53, doi:10.1126/science.abj6987 (2022).
125 Walhout, A. J. *et al.* Protein interaction mapping in C. elegans using proteins involved in vulval development. *Science* **287**, 116-122, doi:10.1126/science.287.5450.116 (2000).
126 Uetz, P. *et al.* A comprehensive analysis of protein-protein interactions in Saccharomyces cerevisiae. *Nature* **403**, 623-627, doi:10.1038/35001009 (2000).
127 Stelzl, U. *et al.* A human protein-protein interaction network: a resource for annotating the proteome. *Cell* **122**, 957-968, doi:10.1016/j.cell.2005.08.029 (2005).
128 Rual, J. F. *et al.* Towards a proteome-scale map of the human protein-protein interaction network. *Nature* **437**, 1173-1178, doi:10.1038/nature04209 (2005).
129 Luck, K. *et al.* A reference map of the human binary protein interactome. *Nature* **580**, 402-408, doi:10.1038/s41586-020-2188-x (2020).
130 Rolland, T. *et al.* A proteome-scale map of the human interactome network. *Cell* **159**, 1212-1226, doi:10.1016/j.cell.2014.10.050 (2014).
131 Michaelis, A. C. *et al.* The social and structural architecture of the yeast protein interactome. *Nature* **624**, 192-200, doi:10.1038/s41586-023-06739-5 (2023).
132 Hein, M. Y. *et al.* A human interactome in three quantitative dimensions organized by stoichiometries and abundances. *Cell* **163**, 712-723, doi:10.1016/j.cell.2015.09.053 (2015).
133 Huttlin, E. L. *et al.* Architecture of the human interactome defines protein communities and disease networks. *Nature* **545**, 505-509, doi:10.1038/nature22366 (2017).
134 Huttlin, E. L. *et al.* Dual proteome-scale networks reveal cell-specific remodeling of the human interactome. *Cell* **184**, 3022-3040 e3028, doi:10.1016/j.cell.2021.04.011 (2021).

135 Orchard, S. *et al.* The MIntAct project--IntAct as a common curation platform for 11 molecular interaction databases. *Nucleic Acids Res* **42**, D358-363, doi:10.1093/nar/gkt1115 (2014).
136 Dimitrakopoulos, G. N., Klapa, M. I. & Moschonas, N. K. How Far Are We from the Completion of the Human Protein Interactome Reconstruction? *Biomolecules* **12**, doi:10.3390/biom12010140 (2022).
137 Wood, L. & Wright, G. J. Approaches to identify extracellular receptor-ligand interactions. *Curr Opin Struct Biol* **56**, 28-36, doi:10.1016/j.sbi.2018.10.002 (2019).
138 Kotlyar, M. *et al.* In silico prediction of physical protein interactions and characterization of interactome orphans. *Nat Methods* **12**, 79-84, doi:10.1038/nmeth.3178 (2015).
139 Braun, P. *et al.* An experimentally derived confidence score for binary protein-protein interactions. *Nat Methods* **6**, 91-97, doi:10.1038/nmeth.1281 (2009).
140 Wright, G. J. Signal initiation in biological systems: the properties and detection of transient extracellular protein interactions. *Mol Biosyst* **5**, 1405-1412, doi:10.1039/B903580J (2009).
141 Wright, G. J., Martin, S., Bushell, K. M. & Sollner, C. High-throughput identification of transient extracellular protein interactions. *Biochem Soc Trans* **38**, 919-922, doi:10.1042/BST0380919 (2010).
142 Bushell, K. M., Sollner, C., Schuster-Boeckler, B., Bateman, A. & Wright, G. J. Large-scale screening for novel low-affinity extracellular protein interactions. *Genome Res* **18**, 622-630, doi:10.1101/gr.7187808 (2008).
143 Martinez-Martin, N. *et al.* An Unbiased Screen for Human Cytomegalovirus Identifies Neuropilin-2 as a Central Viral Receptor. *Cell* **174**, 1158-1171 e1119, doi:10.1016/j.cell.2018.06.028 (2018).
144 Crosnier, C. *et al.* Basigin is a receptor essential for erythrocyte invasion by Plasmodium falciparum. *Nature* **480**, 534-537, doi:10.1038/nature10606 (2011).
145 Lin, H. *et al.* Discovery of a cytokine and its receptor by functional screening of the extracellular proteome. *Science* **320**, 807-811, doi:10.1126/science.1154370 (2008).
146 Shalem, O. *et al.* Genome-scale CRISPR-Cas9 knockout screening in human cells. *Science* **343**, 84-87, doi:10.1126/science.1247005 (2014).
147 Wang, T., Wei, J. J., Sabatini, D. M. & Lander, E. S. Genetic screens in human cells using the CRISPR-Cas9 system. *Science* **343**, 80-84, doi:10.1126/science.1246981 (2014).
148 Sharma, S. & Wright, G. J. Cell Surface Receptor Identification Using Genome-Scale CRISPR/Cas9 Genetic Screens. *J Vis Exp*, doi:10.3791/60803 (2020).
149 Sharma, S., Bartholdson, S. J., Couch, A. C. M., Yusa, K. & Wright, G. J. Genome-scale identification of cellular pathways required for cell surface recognition. *Genome Res* **28**, 1372-1382, doi:10.1101/gr.231183.117 (2018).
150 Frei, A. P. *et al.* Direct identification of ligand-receptor interactions on living cells and tissues. *Nat Biotechnol* **30**, 997-1001, doi:10.1038/nbt.2354 (2012).
151 Frei, A. P., Moest, H., Novy, K. & Wollscheid, B. Ligand-based receptor identification on living cells and tissues using TRICEPS. *Nat Protoc* **8**, 1321-1336, doi:10.1038/nprot.2013.072 (2013).
152 Sobotzki, N. *et al.* HATRIC-based identification of receptors for orphan ligands. *Nat Commun* **9**, 1519, doi:10.1038/s41467-018-03936-z (2018).
153 Frey, K., Goetze, S., Rohrer, L., von Eckardstein, A. & Wollscheid, B. Decoding Functional High-Density Lipoprotein Particle Surfaceome Interactions. *Int J Mol Sci* **23**, doi:10.3390/ijms23169506 (2022).
154 Johnston, R. J. *et al.* VISTA is an acidic pH-selective ligand for PSGL-1. *Nature* **574**, 565-570, doi:10.1038/s41586-019-1674-5 (2019).

155 Roux, K. J., Kim, D. I., Raida, M. & Burke, B. A promiscuous biotin ligase fusion protein identifies proximal and interacting proteins in mammalian cells. *J Cell Biol* **196**, 801-810, doi:10.1083/jcb.201112098 (2012).
156 Branon, T. C. *et al.* Efficient proximity labeling in living cells and organisms with TurboID. *Nat Biotechnol* **36**, 880-887, doi:10.1038/nbt.4201 (2018).
157 Uezu, A. *et al.* Identification of an elaborate complex mediating postsynaptic inhibition. *Science* **353**, 1123-1129, doi:10.1126/science.aag0821 (2016).
158 Roux, K. J., Kim, D. I., Burke, B. & May, D. G. BioID: A Screen for Protein-Protein Interactions. *Curr Protoc Protein Sci* **91**, 19 23 11-19 23 15, doi:10.1002/cpps.51 (2018).
159 Alwash, M. & Gariepy, J. Labeling Cell Surface Receptors with Ligand.BirA* Bispecifics. *ACS Pharmacol Transl Sci* **5**, 62-69, doi:10.1021/acsptsci.1c00192 (2022).
160 Liu, Q. *et al.* A proximity-tagging system to identify membrane protein-protein interactions. *Nat Methods* **15**, 715-722, doi:10.1038/s41592-018-0100-5 (2018).
161 Takano, T. *et al.* Chemico-genetic discovery of astrocytic control of inhibition in vivo. *Nature* **588**, 296-302, doi:10.1038/s41586-020-2926-0 (2020).
162 Takano, T. & Soderling, S. H. Tripartite synaptomics: Cell-surface proximity labeling in vivo. *Neurosci Res* **173**, 14-21, doi:10.1016/j.neures.2021.05.002 (2021).
163 Martell, J. D. *et al.* Engineered ascorbate peroxidase as a genetically encoded reporter for electron microscopy. *Nat Biotechnol* **30**, 1143-1148, doi:10.1038/nbt.2375 (2012).
164 Lobingier, B. T. *et al.* An Approach to Spatiotemporally Resolve Protein Interaction Networks in Living Cells. *Cell* **169**, 350-360 e312, doi:10.1016/j.cell.2017.03.022 (2017).
165 Rhee, H. W. *et al.* Proteomic mapping of mitochondria in living cells via spatially restricted enzymatic tagging. *Science* **339**, 1328-1331, doi:10.1126/science.1230593 (2013).
166 Lam, S. S. *et al.* Directed evolution of APEX2 for electron microscopy and proximity labeling. *Nat Methods* **12**, 51-54, doi:10.1038/nmeth.3179 (2015).
167 Polacco, B. J. *et al.* Profiling the proximal proteome of the activated mu-opioid receptor. *Nat Chem Biol* **20**, 1133-1143, doi:10.1038/s41589-024-01588-3 (2024).
168 Paek, J. *et al.* Multidimensional Tracking of GPCR Signaling via Peroxidase-Catalyzed Proximity Labeling. *Cell* **169**, 338-349 e311, doi:10.1016/j.cell.2017.03.028 (2017).
169 Honke, K. & Kotani, N. Identification of cell-surface molecular interactions under living conditions by using the enzyme-mediated activation of radical sources (EMARS) method. *Sensors (Basel)* **12**, 16037-16045, doi:10.3390/s121216037 (2012).
170 Li, X. W. *et al.* New insights into the DT40 B cell receptor cluster using a proteomic proximity labeling assay. *J Biol Chem* **289**, 14434-14447, doi:10.1074/jbc.M113.529578 (2014).
171 Bar, D. Z. *et al.* Biotinylation by antibody recognition-a method for proximity labeling. *Nat Methods* **15**, 127-133, doi:10.1038/nmeth.4533 (2018).
172 Ogawa, Y. *et al.* Antibody-directed extracellular proximity biotinylation reveals that Contactin-1 regulates axo-axonic innervation of axon initial segments. *Nat Commun* **14**, 6797, doi:10.1038/s41467-023-42273-8 (2023).
173 Loh, K. H. *et al.* Proteomic Analysis of Unbounded Cellular Compartments: Synaptic Clefts. *Cell* **166**, 1295-1307 e1221, doi:10.1016/j.cell.2016.07.041 (2016).
174 Li, J. *et al.* Cell-Surface Proteomic Profiling in the Fly Brain Uncovers Wiring Regulators. *Cell* **180**, 373-386 e315, doi:10.1016/j.cell.2019.12.029 (2020).

175 Shuster, S. A. *et al.* In situ cell-type-specific cell-surface proteomic profiling in mice. *Neuron* **110**, 3882-3896 e3889, doi:10.1016/j.neuron.2022.09.025 (2022).
176 Qin, W., Cho, K. F., Cavanagh, P. E. & Ting, A. Y. Deciphering molecular interactions by proximity labeling. *Nat Methods* **18**, 133-143, doi:10.1038/s41592-020-01010-5 (2021).
177 Oakley, J. V. *et al.* Radius measurement via super-resolution microscopy enables the development of a variable radii proximity labeling platform. *Proc Natl Acad Sci U S A* **119**, e2203027119, doi:10.1073/pnas.2203027119 (2022).
178 Mayer, G. & Bendayan, M. Amplification methods for the immunolocalization of rare molecules in cells and tissues. *Prog Histochem Cytochem* **36**, 3-85, doi:10.1016/s0079-6336(01)80002-4 (2001).
179 Zimmerman, S. B. & Trach, S. O. Estimation of macromolecule concentrations and excluded volume effects for the cytoplasm of Escherichia coli. *J Mol Biol* **222**, 599-620, doi:10.1016/0022-2836(91)90499-v (1991).
180 Zimmerman, S. B. & Minton, A. P. Macromolecular crowding: biochemical, biophysical, and physiological consequences. *Annu Rev Biophys Biomol Struct* **22**, 27-65, doi:10.1146/annurev.bb.22.060193.000331 (1993).
181 Kotani, N. *et al.* Biochemical visualization of cell surface molecular clustering in living cells. *Proc Natl Acad Sci U S A* **105**, 7405-7409, doi:10.1073/pnas.0710346105 (2008).
182 Muller, M. *et al.* Light-mediated discovery of surfaceome nanoscale organization and intercellular receptor interaction networks. *Nat Commun* **12**, 7036, doi:10.1038/s41467-021-27280-x (2021).
183 Kuimova, M. K., Yahioglu, G. & Ogilby, P. R. Singlet oxygen in a cell: spatially dependent lifetimes and quenching rate constants. *J Am Chem Soc* **131**, 332-340, doi:10.1021/ja807484b (2009).
184 Geri, J. B. *et al.* Microenvironment mapping via Dexter energy transfer on immune cells. *Science* **367**, 1091-1097, doi:10.1126/science.aay4106 (2020).
185 Admasu, A. *et al.* A laser flash photolysis study of p-tolyl(trifluoromethyl)carbene. *Journal of the Chemical Society, Perkin Transactions 2*, 1093-1100, doi:10.1039/A707586C (1998).
186 Lander, E. S. *et al.* Initial sequencing and analysis of the human genome. *Nature* **409**, 860-921, doi:10.1038/35057062 (2001).
187 Venter, J. C. *et al.* The sequence of the human genome. *Science* **291**, 1304-1351, doi:10.1126/science.1058040 (2001).
188 Fenn, J. B., Mann, M., Meng, C. K., Wong, S. F. & Whitehouse, C. M. Electrospray ionization for mass spectrometry of large biomolecules. *Science* **246**, 64-71, doi:10.1126/science.2675315 (1989).
189 Tanaka, K. *et al.* Protein and polymer analyses up to m/z 100 000 by laser ionization time-of-flight mass spectrometry. *Rapid Communications in Mass Spectrometry* **2**, 151-153, doi:https://doi.org/10.1002/rcm.1290020802 (1988).
190 Karas, M. & Hillenkamp, F. Laser desorption ionization of proteins with molecular masses exceeding 10,000 daltons. *Anal Chem* **60**, 2299-2301, doi:10.1021/ac00171a028 (1988).
191 Cox, J. & Mann, M. MaxQuant enables high peptide identification rates, individualized p.p.b.-range mass accuracies and proteome-wide protein quantification. *Nat Biotechnol* **26**, 1367-1372, doi:10.1038/nbt.1511 (2008).
192 Yates, J. R., 3rd. Pivotal role of computers and software in mass spectrometry - SEQUEST and 20 years of tandem MS database searching. *J Am Soc Mass Spectrom* **26**, 1804-1813, doi:10.1007/s13361-015-1220-0 (2015).

193 Demichev, V., Messner, C. B., Vernardis, S. I., Lilley, K. S. & Ralser, M. DIA-NN: neural networks and interference correction enable deep proteome coverage in high throughput. *Nat Methods* **17**, 41-44, doi:10.1038/s41592-019-0638-x (2020).
194 Compton, P. D., Zamdborg, L., Thomas, P. M. & Kelleher, N. L. On the scalability and requirements of whole protein mass spectrometry. *Anal Chem* **83**, 6868-6874, doi:10.1021/ac2010795 (2011).
195 Toby, T. K. *et al.* A comprehensive pipeline for translational top-down proteomics from a single blood draw. *Nat Protoc* **14**, 119-152, doi:10.1038/s41596-018-0085-7 (2019).
196 Hein, M. Y., Sharma, K., Cox, J. & Mann, M. in *Handbook of Systems Biology* 3-25 (2013).
197 Olsen, J. V., Ong, S. E. & Mann, M. Trypsin cleaves exclusively C-terminal to arginine and lysine residues. *Mol Cell Proteomics* **3**, 608-614, doi:10.1074/mcp.T400003-MCP200 (2004).
198 Swaney, D. L., Wenger, C. D. & Coon, J. J. Value of using multiple proteases for large-scale mass spectrometry-based proteomics. *J Proteome Res* **9**, 1323-1329, doi:10.1021/pr900863u (2010).
199 Huang, Y. *et al.* Statistical characterization of the charge state and residue dependence of low-energy CID peptide dissociation patterns. *Anal Chem* **77**, 5800-5813, doi:10.1021/ac0480949 (2005).
200 Swaney, D. L., McAlister, G. C. & Coon, J. J. Decision tree-driven tandem mass spectrometry for shotgun proteomics. *Nat Methods* **5**, 959-964, doi:10.1038/nmeth.1260 (2008).
201 Glatter, T. *et al.* Large-scale quantitative assessment of different in-solution protein digestion protocols reveals superior cleavage efficiency of tandem Lys-C/trypsin proteolysis over trypsin digestion. *J Proteome Res* **11**, 5145-5156, doi:10.1021/pr300273g (2012).
202 Hughes, C. S. *et al.* Single-pot, solid-phase-enhanced sample preparation for proteomics experiments. *Nat Protoc* **14**, 68-85, doi:10.1038/s41596-018-0082-x (2019).
203 Liu, J. J. *et al.* In vivo brain GPCR signaling elucidated by phosphoproteomics. *Science* **360**, doi:10.1126/science.aao4927 (2018).
204 Mertins, P. *et al.* Reproducible workflow for multiplexed deep-scale proteome and phosphoproteome analysis of tumor tissues by liquid chromatography-mass spectrometry. *Nat Protoc* **13**, 1632-1661, doi:10.1038/s41596-018-0006-9 (2018).
205 Frauenstein, A. *et al.* Identification of covalent modifications regulating immune signaling complex composition and phenotype. *Mol Syst Biol* **17**, e10125, doi:10.15252/msb.202010125 (2021).
206 Lundberg, E. & Borner, G. H. H. Spatial proteomics: a powerful discovery tool for cell biology. *Nat Rev Mol Cell Biol* **20**, 285-302, doi:10.1038/s41580-018-0094-y (2019).
207 Altelaar, A. F. & Heck, A. J. Trends in ultrasensitive proteomics. *Curr Opin Chem Biol* **16**, 206-213, doi:10.1016/j.cbpa.2011.12.011 (2012).
208 Sinitcyn, P. *et al.* Global detection of human variants and isoforms by deep proteome sequencing. *Nat Biotechnol* **41**, 1776-1786, doi:10.1038/s41587-023-01714-x (2023).
209 Bekker-Jensen, D. B. *et al.* An Optimized Shotgun Strategy for the Rapid Generation of Comprehensive Human Proteomes. *Cell Syst* **4**, 587-599 e584, doi:10.1016/j.cels.2017.05.009 (2017).
210 El-Aneed, A., Cohen, A. & Banoub, J. Mass Spectrometry, Review of the Basics: Electrospray, MALDI, and Commonly Used Mass Analyzers. *Appl Spectrosc Rev* **44**, 210-230, doi:Pii 909281413

10.1080/05704920902717872 (2009).
211 Prudent, M. & Girault, H. H. Functional electrospray emitters. *Analyst* **134**, 2189-2203, doi:10.1039/b910917j (2009).
212 Taylor, G. Disintegration of Water Drops in an Electric Field. *Proceedings of the Royal Society of London Series A* **280**, 383-397, doi:10.1098/rspa.1964.0151 (1964).
213 Wilm, M. Principles of electrospray ionization. *Mol Cell Proteomics* **10**, M111 009407, doi:10.1074/mcp.M111.009407 (2011).
214 Denisov, E., Damoc, E. & Makarov, A. Exploring frontiers of orbitrap performance for long transients. *Int J Mass Spectrom* **466**, doi:ARTN 116607

10.1016/j.ijms.2021.116607 (2021).
215 Sinha, A. & Mann, M. A beginner's guide to mass spectrometry–based proteomics. *The Biochemist* **42**, 64-69, doi:10.1042/bio20200057 (2020).
216 Makarov, A. Electrostatic axially harmonic orbital trapping: a high-performance technique of mass analysis. *Anal Chem* **72**, 1156-1162, doi:10.1021/ac991131p (2000).
217 Steen, H. & Mann, M. The ABC's (and XYZ's) of peptide sequencing. *Nat Rev Mol Cell Biol* **5**, 699-711, doi:10.1038/nrm1468 (2004).
218 Olsen, J. V. & Mann, M. Improved peptide identification in proteomics by two consecutive stages of mass spectrometric fragmentation. *Proc Natl Acad Sci U S A* **101**, 13417-13422, doi:10.1073/pnas.0405549101 (2004).
219 Lin, D., Tabb, D. L. & Yates, J. R., 3rd. Large-scale protein identification using mass spectrometry. *Biochim Biophys Acta* **1646**, 1-10, doi:10.1016/s1570-9639(02)00546-0 (2003).
220 Patterson, S. D. & Aebersold, R. H. Proteomics: the first decade and beyond. *Nat Genet* **33 Suppl**, 311-323, doi:10.1038/ng1106 (2003).
221 Frese, C. K. *et al.* Improved peptide identification by targeted fragmentation using CID, HCD and ETD on an LTQ-Orbitrap Velos. *J Proteome Res* **10**, 2377-2388, doi:10.1021/pr1011729 (2011).
222 van Bentum, M. & Selbach, M. An Introduction to Advanced Targeted Acquisition Methods. *Mol Cell Proteomics* **20**, 100165, doi:10.1016/j.mcpro.2021.100165 (2021).
223 Wichmann, C. *et al.* MaxQuant.Live Enables Global Targeting of More Than 25,000 Peptides. *Mol Cell Proteomics* **18**, 982-994, doi:10.1074/mcp.TIR118.001131 (2019).
224 Remes, P. M., Yip, P. & MacCoss, M. J. Highly Multiplex Targeted Proteomics Enabled by Real-Time Chromatographic Alignment. *Anal Chem* **92**, 11809-11817, doi:10.1021/acs.analchem.0c02075 (2020).
225 Yu, Q. *et al.* Sample multiplexing for targeted pathway proteomics in aging mice. *Proc Natl Acad Sci U S A* **117**, 9723-9732, doi:10.1073/pnas.1919410117 (2020).
226 Zhang, Y., Wen, Z. H., Washburn, M. P. & Florens, L. Effect of Dynamic Exclusion Duration on Spectral Count Based Quantitative Proteomics. *Analytical Chemistry* **81**, 6317-6326, doi:10.1021/ac9004887 (2009).
227 Lou, R. & Shui, W. Acquisition and Analysis of DIA-Based Proteomic Data: A Comprehensive Survey in 2023. *Mol Cell Proteomics* **23**, 100712, doi:10.1016/j.mcpro.2024.100712 (2024).
228 Rost, H. L. *et al.* OpenSWATH enables automated, targeted analysis of data-independent acquisition MS data. *Nat Biotechnol* **32**, 219-223, doi:10.1038/nbt.2841 (2014).
229 Bekker-Jensen, D. B. *et al.* Rapid and site-specific deep phosphoproteome profiling by data-independent acquisition without the need for spectral libraries. *Nat Commun* **11**, 787, doi:10.1038/s41467-020-14609-1 (2020).

230 Muntel, J. *et al.* Surpassing 10 000 identified and quantified proteins in a single run by optimizing current LC-MS instrumentation and data analysis strategy. *Mol Omics* **15**, 348-360, doi:10.1039/c9mo00082h (2019).
231 Sinitcyn, P., Rudolph, J. D. & Cox, J. Computational Methods for Understanding Mass Spectrometry–Based Shotgun Proteomics Data. *Annual Review of Biomedical Data Science* **1**, 207-234, doi:https://doi.org/10.1146/annurev-biodatasci-080917-013516 (2018).
232 Chen, C., Hou, J., Tanner, J. J. & Cheng, J. Bioinformatics Methods for Mass Spectrometry-Based Proteomics Data Analysis. *Int J Mol Sci* **21**, doi:10.3390/ijms21082873 (2020).
233 Elias, J. E. & Gygi, S. P. Target-decoy search strategy for increased confidence in large-scale protein identifications by mass spectrometry. *Nat Methods* **4**, 207-214, doi:10.1038/nmeth1019 (2007).
234 Strauss, M. T. *et al.* AlphaPept: a modern and open framework for MS-based proteomics. *Nat Commun* **15**, 2168, doi:10.1038/s41467-024-46485-4 (2024).
235 Kall, L., Canterbury, J. D., Weston, J., Noble, W. S. & MacCoss, M. J. Semi-supervised learning for peptide identification from shotgun proteomics datasets. *Nat Methods* **4**, 923-925, doi:10.1038/nmeth1113 (2007).
236 Tsou, C. C. *et al.* DIA-Umpire: comprehensive computational framework for data-independent acquisition proteomics. *Nat Methods* **12**, 258-264, 257 p following 264, doi:10.1038/nmeth.3255 (2015).
237 Searle, B. C. *et al.* Generating high quality libraries for DIA MS with empirically corrected peptide predictions. *Nat Commun* **11**, 1548, doi:10.1038/s41467-020-15346-1 (2020).
238 Sinitcyn, P. *et al.* MaxDIA enables library-based and library-free data-independent acquisition proteomics. *Nat Biotechnol* **39**, 1563-1573, doi:10.1038/s41587-021-00968-7 (2021).
239 Heil, L. R. *et al.* Building Spectral Libraries from Narrow-Window Data-Independent Acquisition Mass Spectrometry Data. *J Proteome Res* **21**, 1382-1391, doi:10.1021/acs.jproteome.1c00895 (2022).
240 Thielert, M. *et al.* Robust dimethyl-based multiplex-DIA doubles single-cell proteome depth via a reference channel. *Mol Syst Biol* **19**, e11503, doi:10.15252/msb.202211503 (2023).
241 Thompson, A. *et al.* Tandem mass tags: a novel quantification strategy for comparative analysis of complex protein mixtures by MS/MS. *Anal Chem* **75**, 1895-1904, doi:10.1021/ac0262560 (2003).
242 Virreira Winter, S. *et al.* EASI-tag enables accurate multiplexed and interference-free MS2-based proteome quantification. *Nat Methods* **15**, 527-530, doi:10.1038/s41592-018-0037-8 (2018).
243 Nesvizhskii, A. I., Keller, A., Kolker, E. & Aebersold, R. A statistical model for identifying proteins by tandem mass spectrometry. *Anal Chem* **75**, 4646-4658, doi:10.1021/ac0341261 (2003).
244 Savitski, M. M., Wilhelm, M., Hahne, H., Kuster, B. & Bantscheff, M. A Scalable Approach for Protein False Discovery Rate Estimation in Large Proteomic Data Sets. *Mol Cell Proteomics* **14**, 2394-2404, doi:10.1074/mcp.M114.046995 (2015).
245 Tyanova, S. *et al.* The Perseus computational platform for comprehensive analysis of (prote)omics data. *Nat Methods* **13**, 731-740, doi:10.1038/nmeth.3901 (2016).
246 Santos, A. *et al.* A knowledge graph to interpret clinical proteomics data. *Nat Biotechnol* **40**, 692-702, doi:10.1038/s41587-021-01145-6 (2022).
247 Mueller, S. *et al.* Evolutionary routes and KRAS dosage define pancreatic cancer phenotypes. *Nature* **554**, 62-68, doi:10.1038/nature25459 (2018).

248 Falcomata, C. *et al.* Selective multi-kinase inhibition sensitizes mesenchymal pancreatic cancer to immune checkpoint blockade by remodeling the tumor microenvironment. *Nat Cancer* **3**, 318-336, doi:10.1038/s43018-021-00326-1 (2022).
249 Tian, C. *et al.* Proteomic analyses of ECM during pancreatic ductal adenocarcinoma progression reveal different contributions by tumor and stromal cells. *Proc Natl Acad Sci U S A* **116**, 19609-19618, doi:10.1073/pnas.1908626116 (2019).
250 Tian, C. *et al.* Cancer Cell-Derived Matrisome Proteins Promote Metastasis in Pancreatic Ductal Adenocarcinoma. *Cancer Res* **80**, 1461-1474, doi:10.1158/0008-5472.CAN-19-2578 (2020).
251 Tian, C. *et al.* Suppression of pancreatic ductal adenocarcinoma growth and metastasis by fibrillar collagens produced selectively by tumor cells. *Nat Commun* **12**, 2328, doi:10.1038/s41467-021-22490-9 (2021).
252 Siegel, R. L., Miller, K. D., Fuchs, H. E. & Jemal, A. Cancer statistics, 2022. *CA Cancer J Clin* **72**, 7-33, doi:10.3322/caac.21708 (2022).
253 Connor, A. A. & Gallinger, S. Pancreatic cancer evolution and heterogeneity: integrating omics and clinical data. *Nat Rev Cancer* **22**, 131-142, doi:10.1038/s41568-021-00418-1 (2022).
254 Rahib, L. *et al.* Projecting cancer incidence and deaths to 2030: the unexpected burden of thyroid, liver, and pancreas cancers in the United States. *Cancer Res* **74**, 2913-2921, doi:10.1158/0008-5472.CAN-14-0155 (2014).
255 Kleeff, J. *et al.* Pancreatic cancer. *Nat Rev Dis Primers* **2**, 16022, doi:10.1038/nrdp.2016.22 (2016).
256 Morrison, A. H., Byrne, K. T. & Vonderheide, R. H. Immunotherapy and Prevention of Pancreatic Cancer. *Trends Cancer* **4**, 418-428, doi:10.1016/j.trecan.2018.04.001 (2018).
257 Broz, P. & Dixit, V. M. Inflammasomes: mechanism of assembly, regulation and signalling. *Nat Rev Immunol* **16**, 407-420, doi:10.1038/nri.2016.58 (2016).
258 Poschmann, G. *et al.* Secretomics-A Key to a Comprehensive Picture of Unconventional Protein Secretion. *Front Cell Dev Biol* **10**, 878027, doi:10.3389/fcell.2022.878027 (2022).
259 Bortecen, T., Muller, T. & Krijgsveld, J. An integrated workflow for quantitative analysis of the newly synthesized proteome. *Nat Commun* **14**, 8237, doi:10.1038/s41467-023-43919-3 (2023).
260 Bausch-Fluck, D., Milani, E. S. & Wollscheid, B. Surfaceome nanoscale organization and extracellular interaction networks. *Curr Opin Chem Biol* **48**, 26-33, doi:10.1016/j.cbpa.2018.09.020 (2019).

6. Acknowledgements

I am deeply grateful to all the great people who contributed to this work, offered their support, and made this journey both joyful and rewarding. In particular, I would like to acknowledge:

Felix Meissner, for being an exceptional mentor, granting freedom to explore, offering unwavering support and trust, and fostering an environment where creativity could thrive.

Matthias Mann, for being an inexhaustible source of inspiration, invaluable advice, and constant support and encouragement to push boundaries within an exceptionally stimulating research environment.

Henrik Daub, for being a wonderful mentor in my master's program and staying in touch as an member of my thesis advisory committee, and for introducing me to the world of proteomics, planting the seed for this research.

Ankit Sinha, for brilliant thoughts, insightful discussions, countless answers to my questions, and unforgettable road trips.

Meera Phulphagar, for thoughtful conversations about science and life, and for inspiring me to read more. I look forward to our continued paths crossing.

Johannes Müller-Reif, for innovative thinking, column packing machine adventures, shared love of music, and a memorable Michelin-star restaurant deal.

Jakob Bader, for many thought-provoking brainstorming sessions, relentless curiosity, and a crash course in winemaking.

Jan Rudolph, for invaluable bioinformatics advice and jam sessions in the most unexpected corners of our institute.

Felix Kühner and Alex Henrici, for their quick learning, smart ideas, hard work, and successful experiments. For balcony barbecues and spotting lifts.

Jingyuan Cheng, for great teamwork, R programming support, and dumpling dinners.

The Sen office (and extensions): Annika Frauenstein, Stefan Ebner, Benedikt Gansen, Diana Fink, Steven Dewitz, Alexander Ullrich, Victoria Böck, Franziska Brüning, Tanja Bange, Sandra Mitzkus, Shannon Schreier; For scientific discussions, feedback, and invaluable experimental support. For making lab life both efficient and fun, boat tours, Currywurst breaks.

Sebastian Virreira Winter, for his inspiration. Sophia Mädler, for hosting mind-boggling board games. André Michaelis, for iced coffees and financial advice. Max Zwiebel, for traditions. Lisa Schweizer, for rainbow cake. And the entire Mann group, for being my foster family after the Meissners ventured to new grounds.

Dieter Saur, Chiara Falcomatà, Stefanie Bärthel, for such a fruitful and exciting collaboration, and regular excursions to Munich's finest beer gardens.

The new Meissner group in Bonn, especially Anushka – Nushi – Kudaliyanage and Sebastian Kallabis, for their fantastic help with paper revision, which made collaboration across a 6,000 km distance feel seamless.

Peter Landgraf and Daniela Dieterich, for their warm welcome and expert introduction to cell-selective protein labeling.

Ute Sackers, Medini Steger, Alison Dalfovo, Theresa Schneider, Bianca Splettstößer, Igor Paron, Mario Oroshi, Christian Deiml, Tim Heymann, and the column teams in the Mann department. For all of your support, training, and advice, for memorable retreats, book recommendations, and DIY project adventures.

Alexandra Swietlik, for your love, patience and constant encouragement throughout this journey. For standing by my side through every triumph and challenge, keeping me grounded, and being my true partner in life.